Advanced Understanding of the Electronic Properties of Perovskite Solar Cells

Contact Formation, Band Energy Diagrams and involved Surface Photovoltages

Grundlegendes Verständnis der elektronischen Eigenschaften von Perowskit-Solarzellen – Bandanpassung, Bandenergiediagramme und resultierende Photospannungen

Zur Erlangung des akademischen Grades Doktor der Naturwissenschaften (Dr. rer. nat.)
Dissertation von Tim Hellmann aus Gelnhausen
Darmstadt, August 2021
Fachbereich Materialwissenschaft, Fachgebiet Oberflächenforschung

1. Gutachten: Prof. Dr. Wolfram Jaegermann
2. Gutachten: Prof. Dr. Wolfgang Ensinger

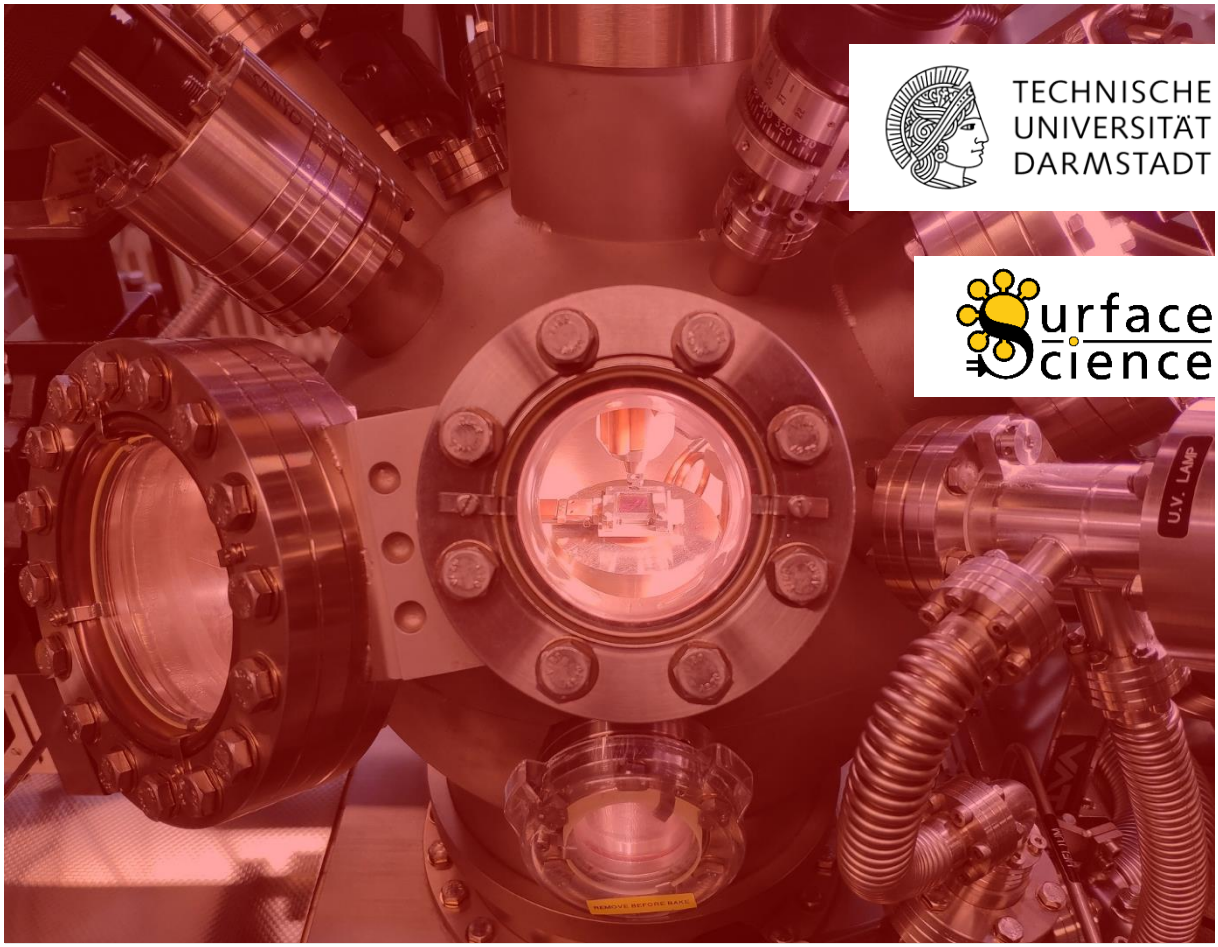

Advanced Understanding of the Electronic Properties of Perovskite Solar Cells:
Contact Formation, Band Energy Diagrams and involved Surface Photovoltages

Grundlegendes Verständnis der elektronischen Eigenschaften von Perowskit-Solarzellen:
Bandanpassung, Bandenergiediagramme und resultierende Photospannungen

1. Gutachten: Prof Dr. Wolfram Jaegermann
2. Gutachten: Prof. Dr. Wolfgang Ensinger

Genehmigte Dissertation von Tim Hellmann aus Gelnhausen
Darmstadt, Technische Universität Darmstadt,
Fachbereich Materialwissenschaft, Fachgebiet Oberflächenforschung

Jahr der Veröffentlichung der Dissertation auf TUprints: 2021
Tag der mündlichen Prüfung: 22.10.2021
URN: urn:nbn:de:tuda-tuprints-198039

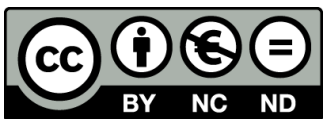

Erklärung zur Dissertation

Hiermit versichere ich, die vorliegende Dissertation ohne Hilfe Dritter nur mit den angegebenen Quellen und Hilfsmitteln angefertigt zu haben. Alle Stellen, die aus Quellen entnommen wurden, sind als solche kenntlich gemacht. Diese Arbeit hat in gleicher oder ähnlicher Form noch keiner Prüfungsbehörde vorgelegen.

Darmstadt, den 27.08.2021

_____

(Tim Hellmann)

Zusammenfassung

Solarzellen mit organisch-anorganischen Metallhalogenid-Perowskiten als Absorber-Material haben nach nur wenigen Jahren in der Forschung Wirkungsgrade von über 25% erreicht. Die rasante Steigerung des Wirkungsgrads von Perowskit-Solarzellen im Vergleich zu etablierten Absorber-Materialien wie beispielsweise Silizium, Cadmium-Tellurid oder Gallium-Arsenid resultiert hauptsächlich aus der Möglichkeit einer einfachen und kostengünstigen Flüssigprozessierung bei niedrigen Temperaturen, beispielsweise durch eine Rotationsbeschichtung. Um den Wirkungsgrad von Perowskit-Solarzellen weiter erhöhen zu können, ist es notwendig ein fundmentales Verständnis des Funktionsprinzips zu entwickeln.

Der Fokus dieser Arbeit liegt daher auf der Charakterisierung der Bandenergiediagramme von Perowskit-Solarzellen im Dunklen und unter Beleuchtung unter Leerlaufspannungs-Bedingungen. Als Analysemethode wird hierbei hauptsächlich Photoelektronen-Spektroskopie (PES) verwendet. Es werden zwei verschiedene Solarzellen-Architekturen untersucht und miteinander verglichen: i) die klassische Architektur, bei welcher der Perowskit-Absorber auf der Elektron-Extraktionsschicht abgeschieden wird und ii) die invertierte Struktur bei welcher der Perowskit auf der Loch-Extraktionsschicht gewachsen wird.

In ersten Experimenten konnte aufgezeigt werden, dass Perowskit-Absorber extrem sensitiv auf Beleuchtung reagieren, sodass bereits geringe Mengen an Restlicht in der Kammer, zum Beispiel das sichtbare Licht, welches von der Röntgenquelle emittiert wird, ausreichen, um eine Photospannung in dem Perowskiten zu induzieren. Solch eine Photospannung beeinflusst PES-Messungen erheblich, da als Folge sämtliche Spektren zu höheren oder niedrigen Bindungsenergien verschoben werden. Um die Probe, während der PES-Messung von dem sichtbaren Licht der Röntgenröhre abzuschirmen, wurde das in dieser Arbeit verwendete PES-Spektrometer zunächst durch den Einbau eines Aluminiumfensters zwischen Probe und Röntgenquelle aufgerüstet.

Im nächsten Schritt wurden verschiedene Perowskit-Absorber auf n-dotiertem SnO_2- (klassische Struktur) und p-dotierten NiO_x-Substraten (invertierte Architektur) hinsichtlich ihrer Dotierung miteinander verglichen, da in der Literatur ein Einfluss des Substrats auf die Dotierung des Perowskit-Absorbers abgeleitet wird. Es wurde nachgewiesen, dass das Substrat keinen direkten Einfluss auf die Dotierung des Perowskit-Absorbers hat und dass der Perowskit unabhängig von seinem Substrat n-dotiert vorliegt. Es wurde angenommen, dass der in der Literatur beschriebene Substrat-Effekt aus einer unzureichenden Abschirmung des Perowskiten gegenüber Restlicht in der Messkammer resultiert, welches eine Photospannung induziert, wodurch Messergebnisse falsch interpretiert worden sind. Für beide Architekturen bildet sich ein Großteil der Photospannung, das heißt die offene Klemmspannung der Solarzelle, an der Grenzfläche zwischen dem n-dotierten Perowskiten und der p-dotierten Loch-Extraktionsschicht. Anschließend wurden die Grenzflächen zwischen dem Perowskiten und den jeweiligen Loch-Extraktionssichten (klassisch: Spiro-MeOTAD und invertiert: NiO_x) für beide Architekturen im Detail analysiert.

Im Falle der Perowskit-Spiro-MeOTAD-Grenzfläche wurde ein klassisches Grenzflächenexperiment durchgeführt. Da Spiro-MeOTAD-Schichten üblicherweise mit LiTFSI dotiert sind, wurde zunächst ein Vakuumabscheidungsprozess von LiTFSI-dotiertem Spiro-MeOTAD durch ein Co-Verdampfen beider Materialien entwickelt. Die Grenzflächenanalyse belegt, dass im Dunkeln eine Bandverbiegung vorliegt, die unter Beleuchtung durch Ausbildung einer Photospannung in eine Flachband-Situation übergeht. Für die invertierte Architektur wurde die Perowskit-NiO_x-Grenzfläche mittels „tapered cross-section PES“ untersucht, wobei im Dunkeln ebenfalls eine Bandverbiegung nachgewiesen wurde. In beiden Architekturen ist damit die energiewandelnde Grenzfläche am Lochkontakt nachgewiesen.

Schließlich wurden die Ergebnisse der Photospannung-Messungen und der Grenzflächenexperimente kombiniert und es konnten Bandenergiediagramme für beide Architekturen im Dunkeln und unter Beleuchtung abgeleitet werden.

Abstract

Solar cells incorporating organic-inorganic metal halide perovskites as the absorber material have achieved power conversion efficiencies of more than 25% after only a decade of research. The extremely rapid improvement in efficiency of perovskite solar cells compared to pre-established absorber materials, such as silicon, cadmium telluride, or gallium arsenide, is mainly due to their cheap and easy low-temperature, solution-processing preparation techniques such as spin-coating. To further improve the power conversion efficiency of perovskite solar cells, it is still necessary to develop a fundamental understanding of the device physics.

The focus of this work lies, therefore, on investigating the energy band diagram of perovskite solar cells, both in the dark and under illumination at open-circuit conditions, predominantly using photoelectron spectroscopy (PES). Two different architectures are investigated and compared: i) the classical architecture where the perovskite absorber is deposited onto the electron extraction layer and ii) the inverted architecture where the perovskite is deposited onto the hole extraction layer.

Initial experiments showed that perovskite absorbers are extremely light-sensitive, meaning that even small intensities of background light, like the visible light emitted from the X-ray source, can induce a photovoltage which will significantly affect the PES measurements by shifting all spectra to higher or lower binding energies. To shield the sample from the visible light emitted by the X-ray source, the setup of the X-ray photoelectron spectroscopy (XPS) system used in this work was improved by installing an aluminum window in between the sample and the X-ray source.

In the next step, a comparative study of several different perovskite absorbers on n-type SnO_2 (classical) and p-type NiO_x substrates (inverted architecture) was performed. It was proven that the underlying substrate has no effect on the doping level of the perovskite absorbers, as it has previously been proposed in the literature. The perovskite absorbers are always measured to be n-doped. It is suggested that the literature-reported substrate effect originates from background light during the measurement. This leads to an unnoticed photovoltage resulting in a binding energy shift of all spectra, which leads to the determination of incorrect doping levels. For both architectures, the majority of the photovoltage and hence the open-circuit voltage of the full device is identified at the n-type perovskite | p-type hole extraction layer interface.

The interfaces between the perovskite and the respective hole extraction layer (classical: spiro-MeOTAD and inverted: NiO_x) were then investigated in detail. For the perovskite | spiro-MeOTAD interface a classical step-by-step interface experiment was performed. Since spiro-MeOTAD films used in perovskite solar cell devices are usually doped with LiTFSI, at first a vacuum deposition process of LiTFSI-doped spiro-MeOTAD through co-evaporation of both materials was developed. The interface characterization proved that a band bending occurs in the dark, which changes to a flat-band situation under illumination, corresponding to a surface photovoltage. For the inverted architecture, the perovskite | NiO_x interface was investigated using the tapered cross-section PES method, which demonstrated the presence of a band bending in the dark as well.

Finally, the results from the photovoltage measurements and the detailed interface characterizations were combined to derive complete energy band diagrams for both architectures under dark and illuminated open-circuit conditions.

Table of contents

Relevant symbols and abbreviations

A	Absorbance
A_m	Measured area
A_n	Normalized area
α	Absorption coefficient
$c(x)$	Atomic concentration of element *x*
d	Thickness
$D_{e/h}$	Diffusion coefficient of electrons/holes
δ	Interface dipole
e	Electron charge
E	Energy
E_B	Binding energy
$E_{core\ level}$	Energy of core-level electrons
$E_{free\ electron}$	Energy of free electrons
E_g	Bandgap
E_{CBM}	Conduction band minimum energy
E_F	Fermi level
E_{kin}	Kinetic energy
E_{VAC}	Vacuum level
E_{VBM}	Valence band maximum
φ	Work function
φ_{sample}	Work function of the sample
φ_{spec}	Work function of the spectrometer
γ	Incident angle with respect to the surface normal
h	Planck constant
hv	Photon energy
I_0	Initial intensity
$I(d)$	Transmitted intensity at a distance of d
I_P	Ionization potential
J	Current density
J_0	Dark saturation current
J_{MPP}	Current density at MPP
J_{SC}	Short-circuit current density
J_{ph}	Photocurrent density
$L_{E>Eg}$	Incident light with energy larger than E_g
$L_{e/h}$	Diffusion length of electrons / holes
λ	Wavelength
N_A	Acceptor concentration
N_D	Donor concentration
P_{MAX}	Maximum power output
V_{MPP}	Voltage at MPP
V_{OC}	Open-circuit voltage
V_{bb}	Band bending
d_{hkl}	Distance between the lattice planes with the Miller indices hkl
$d_{n/p}$	Space charge region width on n-/p-side
k_B	Boltzmann's constant
m^*	Effective mass
R	Reflectance

r_A	Radius of the A-cation in ABX_3
r_B	Radius of the B-cation in ABX_3
r_X	Radius of the X-anion in ABX_3
T	Temperature
T_M	Transmittance
t	Goldschmidt's tolerance factor
$\tau_{e/h}$	Lifetime of electrons/holes
θ	Scattering angle in XRD
U	Voltage
$\mu_{e/h}$	Mobility of electrons/holes
v	Photon frequency
χ	Electron affinity
ΔE_{CBM}	Conduction band offset
ΔE_{VBM}	Valence band offset
ACF	Analyzer compensation factor
AM	Air mass
ASF	Atomic sensitivity factor
BCP	Bathocuproine
C_{60}	Fullerene
CBM	Conduction band minimum
CsFAPI	Cesium formamidinium lead iodide
CsMAFAPI	Cesium methylammonium formamidinium lead iodide
DAISY-BAT	Darmstadt's integrated system for battery research
DAISY-SOL	Darmstadt's integrated system for solar cell research
DFT	Density functional theory
DOS	Density of states
EBIC	Electron beam induced current
ECF	Energy compensation factor
EEL	Electron extraction layer
ESCA	Electron spectroscopy for chemical analysis
FAI	Formamidinium iodide
FAPI	Formamidinium lead iodide
FASI	Formamidinium tin iodide
FTO	Fluorine-doped tin oxide
HEL	Hole extraction layer
HID	High-intensity discharge
HOMO	Highest occupied molecular orbital
IMFP	Inelastic mean free path
IPES	Inverse photoelectron spectroscopy
ITO	Indium tin oxide
KPFM	Kelvin probe force microscopy
LiTFSI	Lithium bis(trifluoromethanesulfonyl)imide
LUMO	Lowest unoccupied molecular orbital
MAFAPI	Methylammonium formamidinium lead iodide
MAI	Methylammonium iodide
MAPI	Methylammonium lead iodide
MASI	Methylammonium tin iodide
MPP	Maximum power point
P3HT	Poly(3-hexylthiophene)
PCE	Power conversion efficiency
PEDOT:PSS	Poly(3,4-ethylenedioxythiophene) polystyrene sulfonate
PES	Photoelectron spectroscopy

PICS	Photoionization cross-section
PolyTPD	Poly(N,N'-bis-4-butylphenyl-N,N'-bisphenyl)benzidine
PTAA	Poly-[bis-(4-phenyl)-(2,4,6-trimethylphenyl)-amine
PV	Photovoltage
QCM	Quartz Crystal Microbalance
SC	Semiconductor
SEC	Secondary Electron Cutoff
Spiro-MeOTAD	2,2',7,7'-Tetrakis[N,N-di(4-methoxyphenyl)amino]-9,9'-spirobifluorene
SPV	Surface Photovoltage
tBP	4-tert-Butylpyridine
TCO	Transparent conductive oxide
TCS-XPS	Tapered cross-section X-ray photoelectron spectroscopy
TXFN	Transmission function
UPS	Ultraviolet photoelectron spectroscopy
UV	Ultraviolet
UV-Vis	Ultraviolet-Vis (spectroscopy)
VBM	Valence band maximum
WF	Work function
XPS	X-ray photoelectron spectroscopy
XRD	X-ray diffraction

1. Fundamentals

1.1. Organic-inorganic metal halide perovskite absorbers

Crystal structure and Goldschmidt's tolerance factor

The term perovskite has two different definitions: it i) describes the mineral $CaTiO_3$ and ii) is used for any material that crystallizes in the same structure as $CaTiO_3$. The perovskite crystal structure was first discovered by Gustav Rose in 1839 and is named after Lev Perovski [1]. The unit cell of a perovskite with its ABX_3 composition is shown in Figure 1.1. The A-cations are forming a primitive cubic system with the B-cations positioned on the body-centered positions and the X-anions on the face-centered positions. In the case of hybrid organic-inorganic metal halide-perovskites, the X-site is usually occupied by an iodide or bromide ion and therefore an anion with the oxidation state of -1. The cations on the A-site and B-site must therefore have an total charge of +3, which is usually achieved by putting a large cation with an oxidation state of +1 on the A-site, and a smaller cation with an oxidation state of +2 on the B-site. Since the A-site is usually partly occupied by organic cations and the B-site by inorganic cations, the description "hybrid organic-inorganic" is used. Whether a material with the composition ABX_3 crystallizes in the perovskite structure, can be estimated with Goldschmidt's tolerance factor, which is calculated from the ratio of the different ionic radii r_A, r_B and r_X (see equation 1.1) [2].

$$t = \frac{r_A + r_X}{\sqrt{2} \cdot (r_B + r_X)} \qquad 1.1$$

The tolerance factor basically describes how well the cation on the A-site can fit into the octahedron formed by the X-anions (see Figure 1.1). According to Goldschmidt, the perovskite structure is formed when the tolerance factor is between 0.8 and 1.0. Outside this range, the A-site cation is either too small ($t < 0.8$) or too large ($t > 1.0$), resulting in the system crystallizing in a

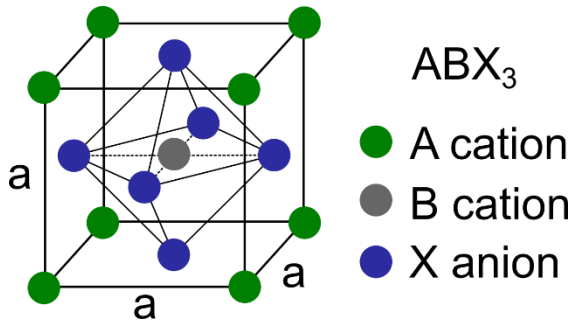

Figure 1.1: The perovskite crystal structure (ABX_3) with the A-cations in green, the B-cations in grey and the X-anions in blue. In the center of the unit cell the octahedron formed by the X-anions with the B-cation it its center is shown.

structure with lower symmetry. While Goldschmidt's tolerance factor is quite successful in predicting whether oxide-based materials (ABO_3) are crystallizing in the perovskite structure, it is less accurate when being applied to metal halide perovskites [3]. Since the metal-halide bonds are more covalent compared to metal-oxide bonds, it was proposed to use cation radii depending on the used anion, resulting in more precise predictions of the tolerance factor [3].

Varying the A-cation

In 2009, Kojima *et al.* [4] reported the first solar cell, where the perovskites methylammonium lead iodide ($CH_3NH_3PbI_3$, MAPI) and methylammonium lead bromide ($CH_3NH_3PbBr_3$) were used as absorber materials. They reported power conversion efficiencies (PCE) of 3.1% and 3.8% for MAPI and $CH_3NH_3PbBr_3$, respectively. Especially MAPI has been intensively studied in the first years after the publication from Kojima *et al.* in 2009 and PCE values of up to 20.4% have been reported [5]. However, a crucial issue of MAPI, limiting its application as absorber material in solar cells, is its low intrinsic thermal and chemical stability and the resulting poor long-term stability of MAPI devices. Two different degradation mechanism have been reported for MAPI at elevated temperatures: the degradation into lead iodide (PbI_2) and i) methylamine (CH_3NH_2) + hydrogen iodide (HI)[6–8] (see equation 1.2) or ii) CH_3I (methyl iodide) + NH_3 (ammonia) (see equation 1.3) [7–9].

$$CH_3NH_3PbI_3 \rightarrow PbI_2 + CH_3NH_3 + HI \quad (1.2)$$

$$CH_3NH_3PbI_3 \rightarrow PbI_2 + CH_3I + NH_3 \quad (1.3)$$

Both degradation reactions have been reported to take place in between 40 °C and 100 °C [6,8–11], which is above or in the range of the temperature of degradation tests proposed for organic solar cells (ISOS protocols) [12] that have also been recommended to be applied for perovskite solar cells [13]. While other degrading factors like humidity [14,15], UV light [16,17] or a catalytic effect of the substrate [18,19] may still be prevented by an encapsulation of the device or by introducing UV filters, the low intrinsic thermal stability of MAPI will most likely be a killing factor for potential commercialization. When the stability of full devices is compared, the situation becomes much more complex, since not only the used charge extraction layers play a role [20], but also the measurement protocol of the devices, i.e. whether it is kept for example at open-circuit conditions or its maximum power point (MPP) [21]. A recent study has shown that MAPI devices could retain 90% or 85% of their PCE when being kept for 500 hours (0.06 years) at 65 °C or 95 °C at constant illumination at their MPP [22], which is still far too low compared to the stability of commercial silicon solar cells. A meta-analysis of the degradation rate of silicon solar cells estimated an efficiency loss of around 0.5% per year, which would mean that silicon solar cells can still retain more than 85% of their initial efficiency after 30 years [23].

To increase the thermal stability of MAPI, the MA^+ cation can be replaced with the larger formamidinium ($CH(NH_2)_2^+$, FA^+), the smaller Cs^+, or with mixtures of both cations. The bandgap of formamidinium lead iodide (FAPI) is with 1.45 eV to 1.51 eV [24,25] slightly lower compared to MAPI (1.58 eV) [24] and therefore close to the ideal bandgap, based on the Shockley-Queisser-Limit [26].

Cesium lead iodide ($CsPbI_3$) exhibits a slightly increased bandgap of 1.73 eV [27]. While FAPI seems to be only slightly more stable compared to MAPI [28], the fully inorganic $CsPbI_3$ is reported to be stable up to temperatures of around 350 °C [29]. However, due to the FA^+ cation being slightly too large, the thermodynamically stable phase of FAPI at room temperature is a non-perovskite hexagonal phase (space group $P6m3c$) with a bandgap of 2.43 eV, which is also referred to as "yellow phase" or δ-phase [30]. The bandgap of the δ-phase is too large to efficiently absorb the sun's light, making it unsuitable as an absorber material for solar cells. The desired photoactive cubic perovskite phase (space group $Pm\bar{3}m$), also called α-phase or "black phase", forms only at elevated temperatures of at least 60 °C [31] or even higher [32,33]. Similarly, the photoactive "black" cubic perovskite phase of $CsPbI_3$ (space group $Pm\bar{3}m$) forms only at temperatures above 305 °C [34], while below that, the materials crystallize in an orthorhombic non-perovskite "yellow phase" (space group $Pnma$) as well. The yellow phase of $CsPbI_3$ exhibits a bandgap of 2.82 eV [27], which is, similarly to that of the yellow phase of FAPI, is too large to be used as absorber material in a solar cell as well. For both materials – FAPI and especially $CsPbI_3$ [27] – the transformation from the black to the yellow phase is accelerated when they are being exposed to humid atmosphere [35]. Different strategies to kinetically trap the black phase of FAPI or $CsPbI_3$ at room temperature have been developed, for example through quick quenching of the annealed black phase or different additives in the perovskite film [36–38]. However, the thermodynamic instability of the black phases of FAPI and $CsPbI_3$ perovskites at room temperature, related to the too large FA^+ / too small Cs^+ cations and therefore a too large / too small Goldschmidt tolerance factor, cannot be avoided. To overcome the issue of the thermodynamically unstable black phases of FAPI and $CsPbI_3$ perovskites at room temperature, mixed systems containing FA^+ and Cs^+ cations at the same time have been reported. Compositions like $Cs_{0.15}FA_{0.85}PbI_3$ [39] or $Cs_{0.1}FA_{0.9}PbI_3$ [40] showed a stable black phase at room temperature, in the case of $Cs_{0.1}FA_{0.9}PbI_3$ even down to temperatures of -93 °C. Since for mixed-cation perovskites like MAFAPI or CsMAFAPI degradation at elevated temperatures has been linked to the release of MA^+ from the perovskite material, methylammonium should, in general, be avoided for perovskites solar cells [41]. Turren-Cruz *et al.* reported methylammonium-free triple-cation perovskites with the composition $Rb_{0.05}Cs_{0.1}FA_{0.85}PbI_3$ that achieved PCE values of up to 20.35% and retained more than 90% of its initial efficiency after a constant illumination for 1000 hours (0.12 years) [42]. Further improvement of the stability of methyl-ammonium free perovskite solar cells is therefore still required.

Varying the B-cation [a)]

Another concern about metal halide perovskites absorbers is the neurotoxicity of lead [43], which combined with the high water solubility of the perovskite materials may lead to a high bioavailability of lead. The bioavailability of a substance describes how easily the substance can enter living organisms. If perovskite solar cells are produced commercially, exposure of lead from perovskite solar panels to the environment must be avoided during their manufacturing, their full lifetime, and after use, applying a potential recycling process. An often-discussed alternative to lead is tin, even though it is controversially discussed whether the tin in tin-based perovskite solar cells is less toxic than lead [44–47]. Li *et al.* [48] who directly compared the bioavailability of SnI_2 and PbI_2, discovered that the lead-uptake of plants is ten times higher compared to tin. They related the lower bioavailability of SnI_2 compared to PbI_2 to the much easier oxidation of Sn^{2+} to SnO_2, which is insoluble in water. However, the low chemical stability of the Sn^{2+} ions compared to Sn^{4+} is also the reason for the experimentally more challenging synthesis of pure tin-based perovskites and their increased sensitivity to ambient atmosphere [49,50]. The highest achieved efficiency of tin-based perovskite is with 13.4% for formamidinium tin iodide (FASI) [51] therefore still considerably lower compared to the pure lead-based materials. High PCE values for tin-based perovskite solar cells are usually achieved by the addition of tin fluoride (SnF_2) during the preparation of the perovskite film, which suppresses the oxidation of Sn^{2+} to Sn^{4+} [52,53]. Tin halide perovskites materials are still of interest due to their lowered bandgap compared to lead-containing perovskites, [54] which allows them to theoretically achieve higher efficiencies based on the Shockley-Queisser-Limit (see Figure 1.6) [26]. In addition, the smaller bandgap opens the possibility to use them as low bandgap material in full perovskite tandem devices [55,56]. While MAPI has a bandgap of around 1.55 eV [54], the bandgap of methylammonium tin iodide ($CH_3NH_3SnI_3$, MASI) is reduced to 1.30 eV [54]. The decrease in bandgap can be explained by the Sn *5s* states being positioned at lower [a)] binding energies (closer to the Fermi level) compared to the Pb *6s* states and a resulting stronger interaction between the Sn *5s* and I *5p* states (as compared to the interaction between Pb *6s* and I *5p* states) [57]. The Sn *5s* states being positioned at lower binding energies, which is caused by the relativistic inert-pair effect described by Sidgwick [58], can also explain the reduced chemical stability of the Sn^{2+} states in MASI compared to the Pb^{2+} states in MAPI, as the higher-lying Sn *5s* states are more likely to participate in a bonding. Interestingly, the bandgap of mixed lead-tin-perovskites is even lower than the pure materials, meaning that Vegard's law of calculating the bandgap of mixed semiconductor systems cannot be applied. The mixed lead-tin perovskite absorber with the composition $MASn_{0.5}Pb_{0.5}I_3$ shows for example a bandgap of 1.17 eV [54]. Mixed lead-tin systems are not suffering from the stability issues as pure tin-based perovskites, which makes them an interesting alternative as well. PCE values of up to 21.1% have been achieved for the perovskite composition $MA_{0.3}FA_{0.7}Pb_{0.5}Sn_{0.5}I_3$ [56]. Instead of lead or tin, germanium-based perovskite

a) The binding energy is here defined according to a photoelectron spectroscopy spectrum: The Fermi level resembles the zero, and the binding energy increases towards the core electrons, meaning that all binding energies values are positive. In the energy band diagrams shown in this work, the binding energy is therefore increasing downwards. This definition will always be applied throughout the whole thesis. See also Figure 1.2 and Figure 1.12 for schematic representations.

absorbers have been synthesized as well, although the highest reported PCE value is much lower with 0.6%, most likely due to the even lower stability and therefore easier oxidation of the Ge^{2+} state [59].

Varying the X-anion

On the X-anion site (see Figure 1.1) the commonly used iodine ion can be completely or partially replaced with bromine or sometimes also chlorine, which leads to an increased bandgap. By increasing the bromine content in mixed iodine-bromine perovskites ($CH_3NH_3PbI_{3-x}Br_x$) the bandgap can be gradually increased from 1.58 eV (MAPI) up to 2.29 eV for methylammonium lead bromide ($CH_3NH_3PbBr_3$, $MAPbBr_3$) [60]. The larger bandgap of $MAPbBr_3$ compared to MAPI partially results by a downward-shifted [a)] VBM and an upward-shifted [a)] conduction band maximum (CBM) as depicted in Figure 1.2. The downward-shifted VBM comes from the Br *4p* states being positioned at higher binding energies compared to the I *5p* states. The upward-shifted CBM is caused by an upward shift of the Pb *6p* states, which is related to a decrease in the Pb-Br bond length in $MAPbBr_3$ compared to the Pb-I bond in MAPI [61]. The wide control of the bandgap in mixed methylammonium lead iodine-bromine perovskites ($CH_3NH_3PbI_{3-x}Br_x$) allows potential applications as wide bandgap materials in multi-junction solar cells or as an absorber material for photocatalytic water splitting. Unfortunately, a light-induced phase segregation into an iodine-rich and a bromine-rich phase has been reported, limiting the device performance of mixed iodine-bromine perovskite absorbers. Theoretical calculations have shown that a solid solution over the complete iodine to bromine range is only possible for temperatures above 70 °C and that at room temperature a miscibility gap is present for $0.2 < x < 0.7$ [62]. A similar range for the miscibility gap ($0.29 < x < 0.92$) was determined by Lehmann based on experimental evidence [63].

Nowadays, the highest certified PCE for perovskite solar cells according to the NREL efficiency chart is 25.5%, even though the exact composition is not revealed yet. Complex compositions like $FA_{0.95}MA_{0.05}Pb(I_{0.95}Br_{0.05})_3$ or $Rb_{0.05}(Cs_{0.05}(MA_{0.17}FA_{0.83})_{0.95})_{0.95}Pb(I_{0.83}Br_{0.17})_3$ have achieved PCE values higher than 20% [64,65].

Electronic structure and charge carrier transport properties

Most of the information regarding the charge carrier transport properties of metal halide perovskite absorbers that are discussed in the following are based on the review papers of Brenner *et al.* and Herz [66,67]. The electronic structure of metal halide perovskite absorbers – meaning the contribution of the atomic orbitals of the different elements to the total density of states (DOS) – has been repeatedly investigated through theoretical calculations. In the case of MAPI, it was predicted

a) The binding energy is here defined according to a photoelectron spectroscopy spectrum: The Fermi level resembles the zero, and the binding energy increases towards the core electrons, meaning that all binding energies values are positive. In the energy band diagrams shown in this work, the binding energy is therefore increasing downwards. This definition will always be applied throughout the whole thesis. See also Figure 1.2 and Figure 1.12 for schematic representations.

that the valence band is mainly comprised of I *5p* states with some Pb *6s* contributions, while the conduction band is made of Pb *6p* states with some I *5p* contributions [68–70]. The metal cation orbitals (Pb *6p*) are therefore dominating the conduction band states and the halide anion orbitals (I *5p*) the valence band states, as one would expect it from a simple linear combination of the atomic orbital (LCAO) approach. The organic MA^+ cation has no relevant contribution to the DOS of the valence or conduction band. Tao *et al.* [61] calculated the DOS of 18 different perovskite absorbers (A = MA^+, FA^+ and Cs^+ | B = Pb^{2+} and Sn^{2+} | C = I^-, Br^- and Cl^-) and compared their theoretical calculations to experimental ultraviolet photoelectron spectroscopy (UPS) and inverse photoelectron spectroscopy (IPES) data. They confirmed that the A-site cation is not involved in the bonding and has only minor influences on the band structure through varying the size of the unit cell or by distortions of the perovskite lattice, caused by the different cation sizes. The contribution of the different halide and metal orbitals to the valence and conduction band, determined by Tao *et al.*, are shown in Figure 1.2.

For MAPI, theoretical calculations predicted the effective mass of electrons and holes to be around $m^* \approx 0.15 m_e$, with m_e being the electron rest mass [71,72]. Such values are reasonable since they are comparable to what has been observed for other semiconductor materials like silicon, GaAs, or CdTe, which are used as absorbers materials in solar cells as well [73–75]. The reported charge carrier mobilities of electrons (μ_e) and holes (μ_h) of MAPI are scattered over a wide range. Electron mobilities of $\mu_{e,tf} = (0.7 \text{ to } 1.4)\,\frac{\text{cm}^2}{\text{Vs}}$ and $\mu_{e,sc} = (2.5 \text{ to } 105)\,\frac{\text{cm}^2}{\text{Vs}}$ and hole mobilities of $\mu_{h,tf} = (0.4 \text{ to } 0.9)\,\frac{\text{cm}^2}{\text{Vs}}$ and $\mu_{e,sc} = (2.5 \text{ to } 164)\,\frac{\text{cm}^2}{\text{Vs}}$ have been reported for measurements performed on thin film (tf) and

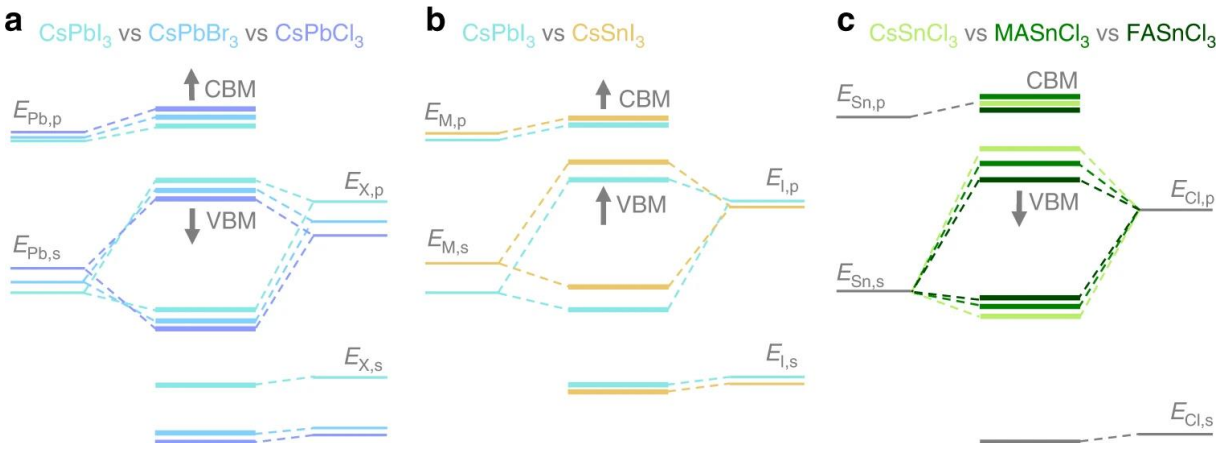

Figure 1.2: Contribution of the atomic orbitals to the valence band and conduction band energy levels of different metal halide perovskite absorbers. In a) the variation of the X-anion, in b) the variation of the metallic B-cation and in c) the variation of the organic / inorganic A-cation is shown.

single-crystal (sc) samples, respectively. The lower determined mobility values for polycrystalline materials indicate that grain boundaries are having a negative effect on the charge transport. Herz [67] also emphasized that carrier mobility values determined by long-range measurements techniques as

photoluminescence quenching (PLQ) are generally lower compared to values determined by short-range techniques such as Terahertz-probe conductivity and microwave conductivity, therefore implying as well that grain boundaries are impeding the charge carrier transport properties [67]. Even though the mobility values determined in literature are scattered over a wide range, they are lower than typical mobilities reported for semiconductors like Si or GaAs (see Table 1.1). Given that the diffusion coefficient D is proportional to the mobility (see equation 1.4), rather low diffusion coefficients are expected for MAPI as well.

$$D_{e/h} = \frac{\mu_{e/h} \cdot k_B \cdot T}{e} \qquad 1.4$$

Brenner *et al.* [66] related the low mobilities in metal halide perovskites absorbers to scattering processes. However, since metal halide perovskites absorbers still exhibit large diffusion lengths and therefore excellent charge carrier collection, the scattering centers are most likely no recombination centers. As dominating scattering mechanisms Brenner *et al.* proposed phonons and dynamic disorder scattering. The large diffusion lengths L of up to 175 µm reported for MAPI single crystals must therefore be connected to long carrier lifetimes τ to cancel the rather low diffusion coefficients (see equation 1.5).

$$L_{e/h} = \sqrt{D_{e/h} \cdot \tau_{e/h}} \qquad 1.5$$

A summary of reported mobilities, carrier lifetimes, diffusion lengths, and effective masses for MAPI and a comparison to silicon and gallium arsenide is given in Table 1.1. Detailed lists including all values with references and the characterization techniques used to determine the values are given in the appendix in Table 9.1 and Table 9.2.

Table 1.1: Diffusion lengths, carrier lifetimes, and mobility values of thin-film and single-crystalline MAPI samples compared to silicon and gallium arsenide semiconductors. The values are adapted from Brenner *et al.* [66] and extended with additional references. Detailed lists including all values with references and the characterization techniques used to determine the values are given in the appendix in Table 9.1 and Table 9.2.

Material	Charge carriers	Mobility / $\frac{cm^2}{Vs}$	Carrier lifetime / µs	Diffusion length / µm	Effective mass / m_e
thin film MAPI	electrons holes	0.7 to 1.4 0.4 to 0.9	0.004 to 0.01	0.1 to 1.9 0.1 to 1.5	0.15 [71,72]
single-crystal MAPI	electrons holes	2.5 to 105 2.5 to 164	0.02 to 95	1.8 to 175	
Si [75]	electrons holes	1450 500	≈ 1000	1000 600	0.19 0.16
GaAs [75,76]	electrons holes	8000 400	≈ 0.01 to 1	7 1.6	0.063 0.076

1.2. Characterization techniques

X-ray diffraction

X-ray diffraction (XRD) is a technique that can be used to determine the crystal structure of a material by the diffraction of incident X-rays at the electron clouds of the periodically arranged atoms of a sample material. During an XRD measurement one usually records the intensity of the diffracted X-radiation in dependence of the scattering angle 2θ, which is also called a diffraction pattern or diffractogram. In the simple Bragg model, a path difference between two parallel incident X-rays, that is equal to a multiple n of the X-rays wavelength λ, results in constructive interference and therefore a peak in the diffraction pattern. The diffraction with constructive interference can be described using Bragg's law (see equation 1.6). Figure 1.3 shows a schematic representation of the diffraction process.

$$n\lambda = 2d_{hkl}\sin(\theta) \qquad 1.6$$

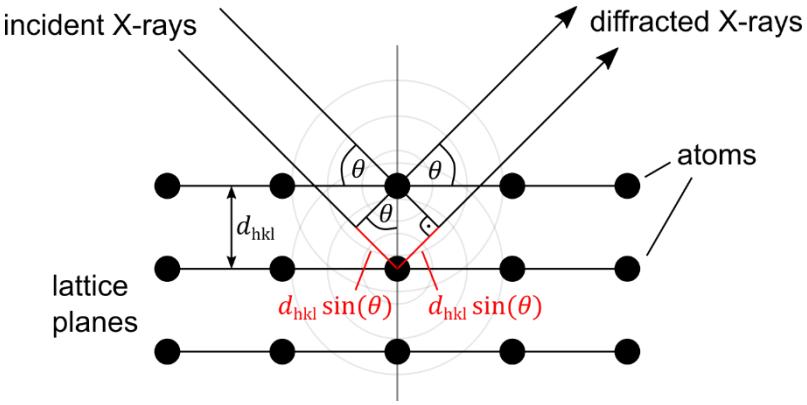

Figure 1.3: Diffraction of incident parallel X-rays beams at two parallel lattice planes. The path difference between both X-ray beams is marked in red.

Ultraviolet-visible spectroscopy

Ultraviolet-visible spectroscopy (UV-Vis) allows determining the investigated sample's absorbance, transmittance, and reflectance of electromagnetic radiation in the ultraviolet and visible light ranges. The experimental setup usually includes two different light sources and detectors, one for the UV-range and one for the Vis-range, and additional optical components like gratings, lenses, or mirrors, which are exchanged depending on the energy that is measured. The optics system allows to monochromatize the light and direct it onto the sample. To account for the energy-dependent variation of intensity reaching the sample, at first usually, a baseline measurement is performed. Then, the sample is positioned in the path of the beam of light, usually tilted so that the angle γ between the incident light and the surface normal of the sample is around 5° (see Figure 1.4). For transmittance

measurements, the detector is positioned behind the sample in direction of the light. The reflectance can be recorded with the detector positioned at two times the angle between the incident light and the surface normal of the sample. The setup is sketched in Figure 1.4. It can now be assumed that the intensity of the transmitted $I(d)$, reflected I_R and absorbed light $I_A(d)$ is equal to the intensity of the incident light I_0. Since the incident light intensity is known from the baseline measurement and the reflected and transmitted light intensities are measured, the absorbed light intensity can be determined. By normalizing the incident light intensity to 1, equation 1.7 results. T_M, R and A are the transmittance, reflectance and absorbance, respectively. For equation 1.7 it is assumed that all the reflection occurs at an angle of 2γ, which is not true, especially for rough samples. For a more precise determination of the reflectance an Ulbricht sphere can be used as detector [77,78].

$$T_M(E) + R(E) + A(E) = 1 \qquad 1.7$$

The intensity decay of the light while traveling through the sample can be described using the Beer-Lambert law (see equation 1.8) with $\alpha(E)$ being the absorption coefficient for a specific energy E and d being the effective thickness. The absorption coefficient describes how far electromagnetic radiation can travel through a solid until it is attenuated to an intensity of $1/e \approx 36.8\%$.

$$I(d,E) = I_0(E) \cdot \exp\left(-\alpha(E) \cdot d\right) \qquad 1.8$$

From the transmittance and reflectance data, the energy-dependent absorption coefficient $\alpha(E)$ can be calculated using equation 1.9 [79].

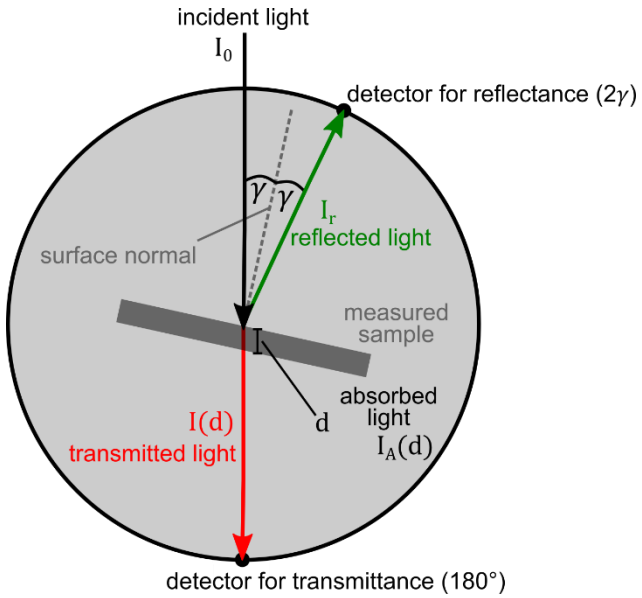

Figure 1.4: Position of the sample and the detector during a UV/Vis measurement when the transmitted (red) and reflected (green) light intensity is recorded.

$$\alpha(E) = -ln\left(\frac{T_M(E)}{1 - R(E)}\right) \cdot \frac{1}{d} \qquad 1.9$$

Solar simulator measurements

To compare the performance of photovoltaic devices, their current-voltage curves (I-V-curves) are recorded using a solar simulator. The recorded current I is usually divided by the active surface area of the device A, and the resulting current density J is plotted in dependence on the voltage V. An exemplary JV-curve and the corresponding power density curve of a CsFAPI perovskite solar cell produced in this work are shown in Figure 1.5.

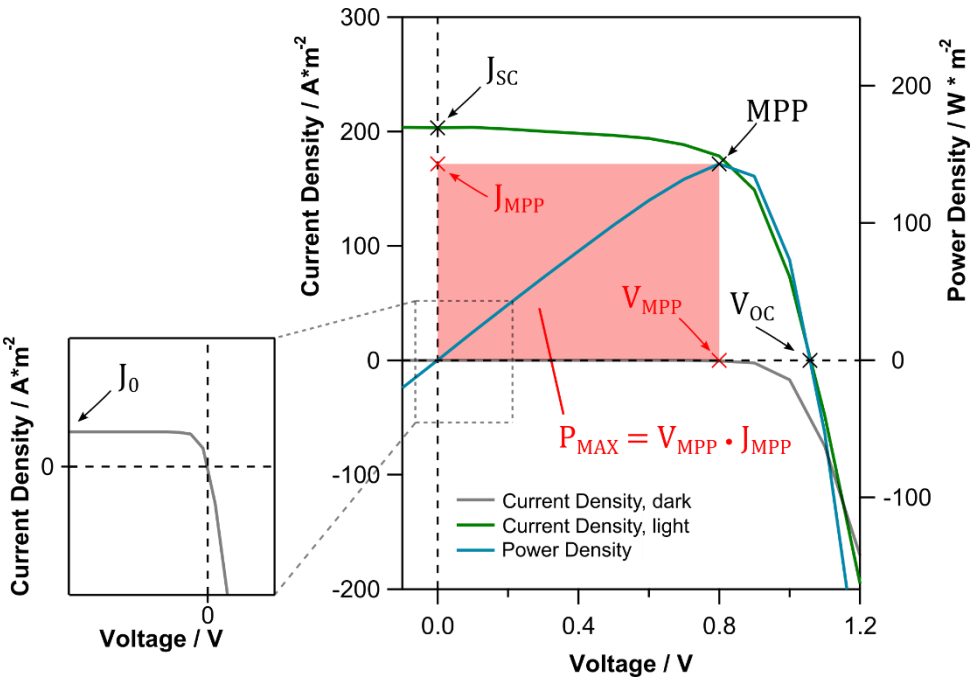

Figure 1.5: Current density (green) and power density (blue) of a CsFAPI perovskite solar cell produced in this work with the open-circuit voltage and (V_{OC}), the short-circuit current (J_{SC}) and the maximum power point (MPP) highlighted. V_{MPP}, J_{MPP} and P_{MAX} are the voltage, the current density and the power density that can be extracted when the device is operated at the MPP.

From the J-V-curve the open-circuit voltage (V_{OC}) and short-circuit current (J_{SC}) can be directly extracted as the intersection of the J-V-curve with the voltage- and the current-axis, respectively. The Shockley diode equation [80] for an ideal solar cell with an additional term that accounts for the photocurrent (J_{ph}) provides a mathematical description of the J-V curve of a solar cell (see equation 1.10). J_0 is in this case the dark saturation current density, e the elementary charge, k_B the Boltzmann constant and T the temperature.

$$J(U) = J_0 \cdot \left[exp\left(\frac{eU}{k_B T}\right) - 1\right] - J_{ph} \qquad 1.10$$

By setting the current density to zero ($J(U) = 0$) and solving equation 1.10 for the voltage U, an expression for the open-circuit voltage can be derived (see equation 1.11) [81].

$$U_{OC} = \frac{k_B T}{e} \cdot ln\left(\frac{J_{ph}}{J_0}\right) \qquad 1.11$$

The open-circuit voltage shows a logarithmic dependence on the photocurrent density and therefore also on the short-circuit current density. Since the short-circuit current density is proportional to the intensity of the incident light with an energy larger than the bandgap of the absorber material ($L_{E>Eg}$), the open-circuit voltage depends logarithmically on $L_{E>Eg}$ (see equation 1.12). The dependence between the open-circuit voltage and the incident light intensity will be of importance for the later-presented photovoltage experiments.

$$U_{OC} \sim ln(L_{E>Eg}) \qquad 1.12$$

It is commonly accepted to use the standardized AM 1.5 spectrum (ISO 9845-1) with an irradiance of 1000 $\frac{\mathrm{W}}{\mathrm{m}^2}$ to illuminate a solar cell during J-V-measurements. “AM” stands in this case for “air mass” and the number 1.5 describes how far the light travels through the atmosphere before reaching the solar cell. While AM 0 (1367 $\frac{\mathrm{W}}{\mathrm{m}^2}$) is the spectrum outside the earth’s atmosphere, AM 1 is at the earth’s surface when the sun is in zenith and AM 1.5 at the earth's surface when the sun is at an angle of 48.2°, meaning that the light travels through 1.5-times the earth’s atmosphere. While the light passes through the atmosphere, it is attenuated mainly due to scattering and absorption at the atmosphere's gas molecules like O_2, H_2O, or CO_2. To mimic the AM 1.5 spectrum, laboratory solar simulators are

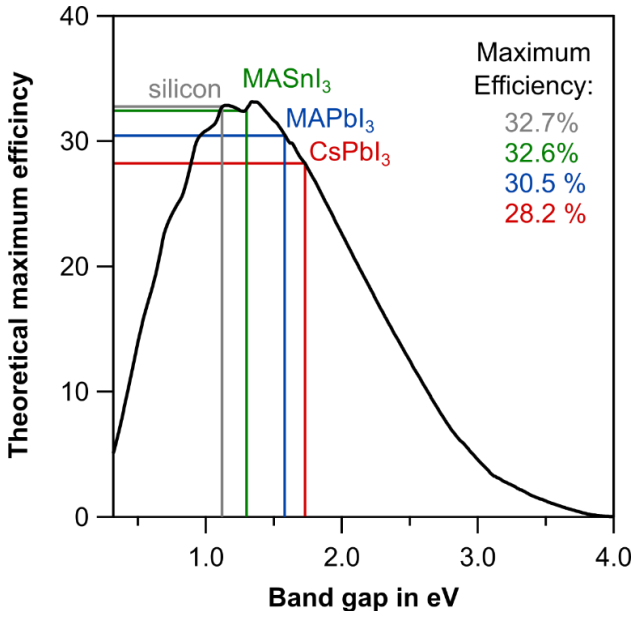

Figure 1.6: The Shockley-Queisser limit for the AM 1.5G spectrum with highlighted bandgaps of silicon (1.12 eV), MASI (1.30 eV), MAPI (1.58 eV) and $CsPbI_3$ (1.73 eV).

often using gas-discharge lamps or multiple LEDs. Additional filters are usually positioned in between the light source and the measured device. With the irradiance of the AM 1.5 being 1000 $\frac{\mathrm{W}}{\mathrm{m}^2}$, the power conversion efficiency (PCE) of the measured device can be calculated using equation 1.13.

$$PCE = \frac{P_{MAX}}{1000\,\frac{W}{m^2}} = \frac{V_{MPP} \cdot J_{MPP}}{1000\,\frac{W}{m^2}} \qquad 1.13$$

The maximum PCE that a solar cell can achieve depending on its bandgap if only radiative combination is considered can be described by the detailed balance limit, or also called Shockley-Queisser limit [26]. It was first calculated by William Shockley and Hans Queisser in 1961, approximating the solar spectrum as a black body with a temperature of 6000 K. The detailed balance limit, calculated from the AM 1.5G spectrum and plotted after tabulated values of Rühle [82] is shown in Figure 1.6. The bandgaps of silicon (1.12 eV), MASI (1.30 eV), MAPI (1.58 eV), and $CsPbI_3$ (1.73 eV) are highlighted in grey, green blue, and red, respectively.

1.3. Photoelectron spectroscopy

Photoelectron Spectroscopy (PES) belongs to the surface-sensitive characterization techniques. The fundamental principle of PES is the photoelectric effect [83]: incident electromagnetic radiation is absorbed by electrons, which are emitted as photoelectrons out of the surface of the investigated material. Depending on whether X-ray radiation or UV light is used, one can distinguish between XPS (X-ray photoelectron spectroscopy) or UPS (ultraviolet photoelectron spectroscopy). The kinetic energy of the emitted photoelectrons allows determining the binding energy of the electrons before their removal from the sample material, providing information about the sample. In the case of XPS, the chemical composition and the oxidation state of the different elements of the investigated material can be determined. The XPS method was developed by Kai Siegbahn who first named the method Electron Spectroscopy for Chemical Analysis (ESCA). [84–86]

1.3.1. The photoemission process and the resulting XPS spectrum

The photoemission process in XPS can be pictured with the so-called three-step model developed by Spicer in 1958 [87] and is sketched in Figure 1.8. In the first step, the energy of the incident X-rays is transferred to the electrons of the material, which are then excited from their orbitals (initial state, $E_{initial}$) into a higher non-occupied state (final state, E_{final}), that is still inside the material. The transition probability between the initial and the final states, which is proportional to the intensity of the later-measured XPS peak can theoretically be described by Fermi's golden rule [88,89]. While the photoelectrons are traveling to the surface of the sample (step 2), secondary electrons are created due to the collision of some of the excited photoelectrons with other electrons in the material. Only unscattered or elastically scattered photoelectrons, those that did not change their kinetic energy, will contribute to the peak in the finally received XPS spectrum. The kinetic energy of the secondary electrons is lower than the kinetic energy of the unscattered or elastically scattered photoelectrons, as it is depicted by the blue and grey areas below the final state in step 2 of Figure 1.8. If an electron wants to escape from the sample, it must overcome the samples work function φ_{sample}, meaning that only secondary electrons with $E_{kin} > \varphi_{sample}$ can escape (blue area) while secondary electrons with $E_{kin} < \varphi_{sample}$ are trapped (grey area). When the electrons escape from the sample into the vacuum (step 3), the secondary electrons are therefore cut at $E_{kin} = \varphi_{sample}$. The resulting XPS spectrum, the intensity of the photoelectrons in dependence of their binding energy, is sketched in Figure 1.8 on the right. The secondary electron-cutoff (SEC) allows to determine the work function of the sample φ_{sample} through equation 1.14. hv is the energy on the incident electromagnetic radiation.

$$\varphi_{sample} = hv - SEC \qquad 1.14$$

The photoelectrons emitted from the sample are passing through a system of electrical and magnetic lenses that focus the electrons into the spectrometer. The spectrometer, often a so-called hemispherical deflection analyzer, allows only electrons of a specific kinetic energy, the pass energy

(E_{pass}), to be transmitted. Behind the analyzer, the electrons are being counted by a detector system, which in commercial XPS systems are often channel electron multipliers (CEM, channeltrons). If the energy of the incident X-ray radiation hv is fixed, the kinetic energy of the excited photoelectrons can be calculated using equation 1.15, where E_B is the binding energy of electrons inside the sample and φ_{sample} the work function of the sample (see Figure 1.7).

$$E_{kin} = hv - E_B - \varphi_{sample} \quad 1.15$$

Equation 1.15 can be rewritten as 1.16, to obtain an expression for the binding energy of the electrons.

$$E_B = hv - E_{kin} - \varphi_{sample} \quad 1.16$$

In XPS the binding energy axis is usually referenced with respect to the Fermi level ($E_F = 0$). If the sample is now electrically grounded, and all electrical potentials of the electrostatic lens system and the spectrometer are referenced to the ground as well, a contact potential determined by the difference of the work functions of the sample and the spectrometer is formed $(\varphi_{sample} - \varphi_{spec})$ [90]. The work function difference between the sample and the spectrometer $(\varphi_{sample} - \varphi_{spec})$ is therefore the kinetic energy change that the photoelectron experiences due to the contact potential between sample and analyzer after it has left the sample until it has travelled through the lens optics to the entrance of the analyzer. For a concentric hemispherical analyzer, the spectrometer work function is the (average) work function of the hemisphere surfaces, since the voltages applied to the

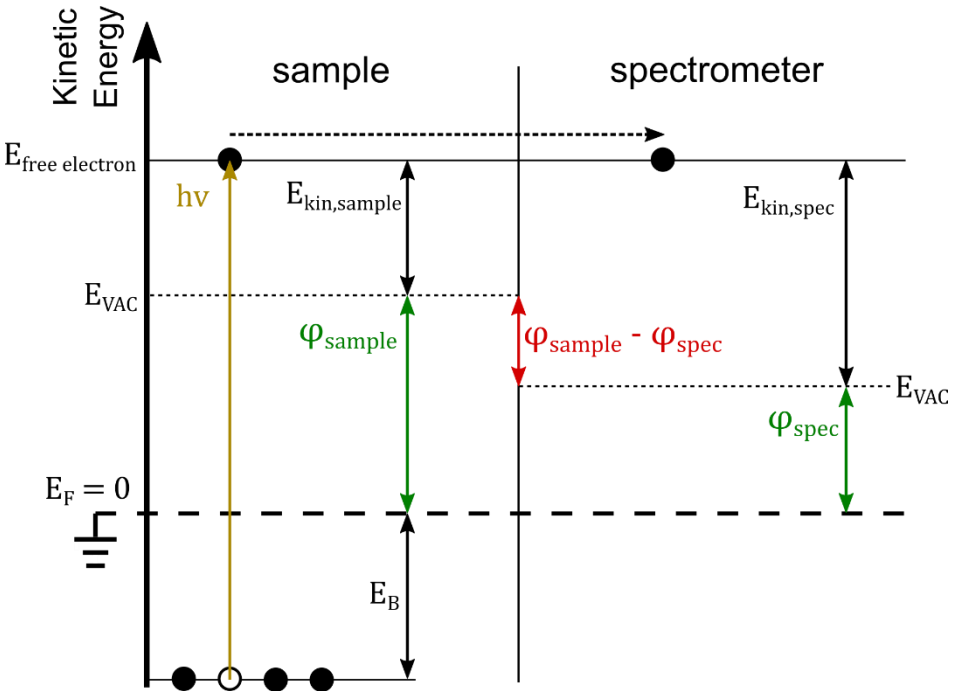

Figure 1.7: The energy levels of the sample (left) and the spectrometer (right) when they are both electrically connected to the ground so that the Fermi levels of them are aligned. Due to the work function difference of the sample and the spectrometer, a contact potential $(\varphi_{sample} - \varphi_{spec})$ is formed.

hemispheres define the kinetic energy an electron must have, so it can pass through the spectrometer and be detected. It can for example change due to adsorption of molecules from the gas phase onto the surface of the hemispheres [91]. The binding energy in equation 1.16 becomes now independent of the sample work function (φ_{sample}) and only the work function of the spectrometer (φ_{spec}) must be considered, as expressed by equation 1.17.

$$E_B = h\nu - E_{kin} - \varphi_{sample} + (\varphi_{sample} - \varphi_{spec}) = h\nu - E_{kin} - \varphi_{spec} \qquad 1.17$$

The spectrometer work function is usually calibrated from reference measurements of metal surfaces. The spectrometer of the Thermo Fisher Escalab 250 XPS system mainly used in this work was calibrated using the Fermi level as the zero of the binding energy scale and the Ag $3d_{5/2}$ emission line of a metallic silver sample, the Au $4f_{7/2}$ emission line of a metallic gold sample, and the Cu $2p_{3/2}$ emission line of a metallic copper sample.

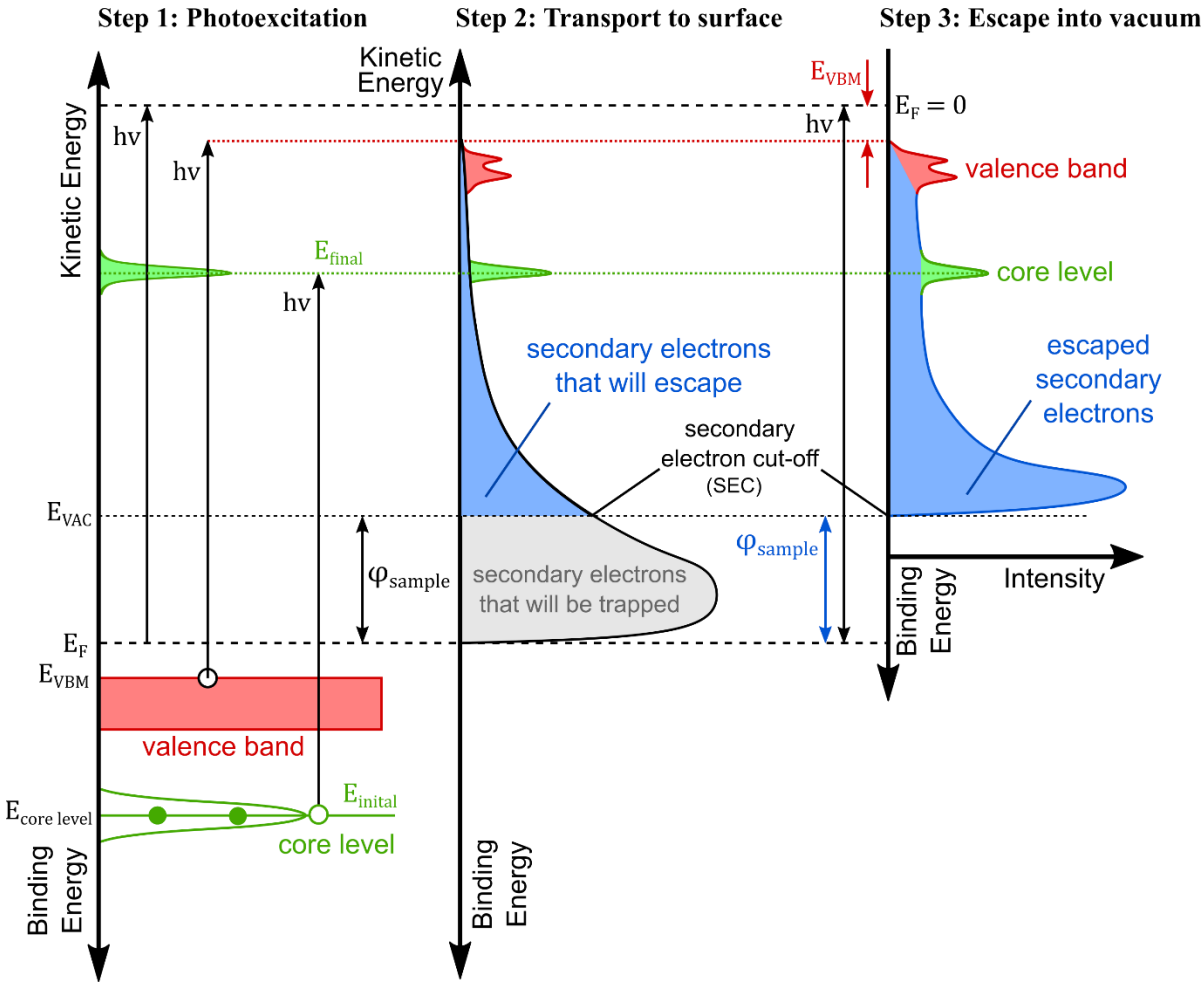

Figure 1.8: The photoemission process in XPS based on the three-step model. On the left, the energy levels of an atom are shown. The curve in the middle shows the energy distribution of the photoelectrons after the photoexcitation took place and before the electrons have left the sample. On the right, the resulting XPS spectrum is shown. The energy of the incident X-ray radiation is equal to $h\nu$.

1.3.2. Qualitative analysis and chemical states determination

Since the binding energies of the atomic orbitals of each element are characteristic, they can act as a fingerprint allowing to identify the elements present in the surface of the investigated sample. The binding energies of all elements are tabularized, for example in the "Handbook of X-ray photoelectron spectroscopy" by Moulder et al [92]. In addition to the qualitative analysis, XPS allows a determination of the chemical state of an element since the binding energy of an emission line is influenced by the local electron density of the investigated atom. The local electron density can be influenced for example by the bonding partner of the atom or by the atom's oxidation states. The emission lines of an element appear usually shifted to higher or lower binding energies, depending on whether the electronegativity of the element's bonding partner is higher or lower. Exceptions to this rule, such as silver, where the oxidized form ($Ag^{2+}O$) appears at lower binding energies compared to metallic silver (Ag^0), exist as well, due to strong shifts of the sample's work function [93]. Binding energy shifts related to a change in the chemical environment are usually considered as "chemical shifts". As an example for a chemical shift, the Si2p emission line of a Si wafer sample with a native SiO_2 on top is shown in Figure 1.9. The oxide layer is thin enough so that both the metallic bulk as well as the oxide surface layer are visible. The silicon atoms of the substrate have an oxidation state of 0 and the

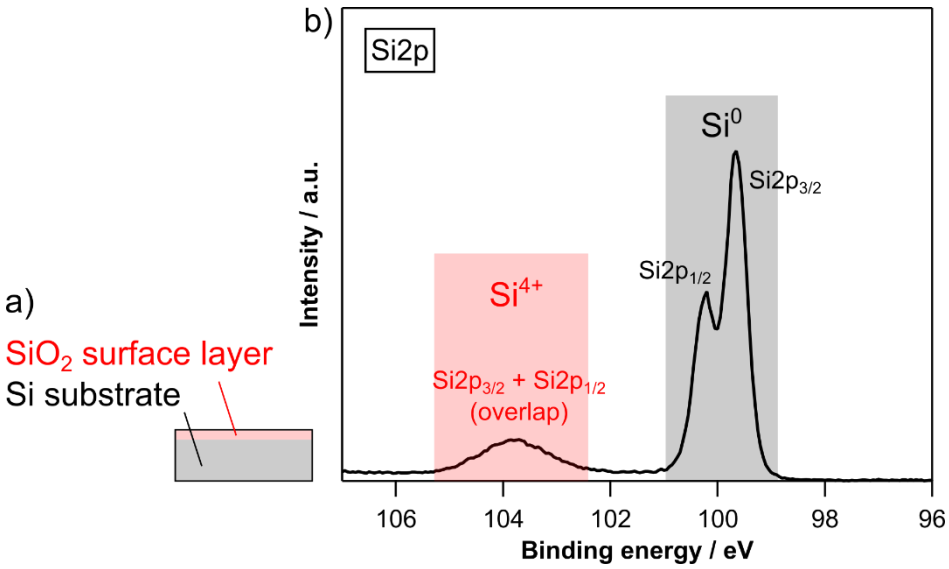

Figure 1.9: a) Sketch of a silicon wafer sample with a native oxide layer on the surface and b) Si2p emission line of the sample by XPS. At around 100 eV (black) the Si^0 oxidation state of the Si substrate is visible. The Si^{4+} state of the native SiO_2 surface appears shifted to higher binding energies by around 4 eV (red).

corresponding Si2p emission line appears at around 100 eV, here highlighted in black. The silicon atoms of the oxide layer have an oxidation state of +4 and appear shifted to higher binding energies by around 4 eV, highlighted in red in Figure 1.9.

Besides chemical shifts, which are related to a change in the local chemical environment, a binding energy shift can also be related to a change of the Fermi level position (work function), for example, due to a doping effect. When a material is being n-doped or p-doped, its Fermi level will shift

towards its CBM or VBM. Since the XPS spectrum is calibrated in such a way, that the Fermi level is fixed at 0 eV, an n-doping will shift all core levels to higher binding energies and a p-doping to lower binding energies, respectively. Binding energy shifts that are related to doping are described as "electronic shifts". Other causes of a binding energy shift might be an electrical charging due to an insufficient grounding of the sample, a voltage that is applied to the sample as it is done in UPS work function measurements, or the presence of a surface photovoltage (SPV). More details regarding SPVs in XPS measurements are given in chapter 1.6.3.

1.3.3. Surface sensitivity and thickness determination of surface layers

The information depth in PES is limited by the escape depth of the excited photoelectrons from the sample material, also called inelastic mean free path (IMFP). The IMFP describes the distance that the electrons will travel through a solid material before they are being attenuated to an intensity of $^1/_e \approx 36.8\%$ and can be expressed by a universal curve (see equation 1.18), first described by Seah *et al.* [94] in 1979. Seah *et al.* provide different universal curve shapes depending on the material class the electron is traveling through (Au, elements, inorganic or organic). Equation 1.18 is valid for pure elements and is plotted in the range from 10 eV to 2000 eV in Figure 1.10.

$$IMFP = \frac{143}{(E_{kin})^2} + 0.054 \cdot \sqrt{E_{kin}} \qquad 1.18$$

The typical energy range of the photoelectrons in XPS, when Al Kα radiation is used, is highlighted in Figure 1.10 in green. It is usually assumed that the information depth is three times the mean free path since this would result in an attenuation of the signal to $^1/_{e^3} \approx 5.0\%$. The information depth of XPS, when using Al Kα radiation (1486.6 eV), would therefore fall in the range of 3.2 nm to 6.0 nm, depending on the kinetic energy of the photoelectrons and therefore the binding energy of the investigated energy level. For He I or He II radiation, which is commonly used for ultraviolet photoelectron spectroscopy (UPS), an information depth of 1.71 nm and 1.29 nm results, respectively. UPS is therefore much more surface sensitive compared to XPS.

By knowing the IMFP, it is possible to determine the thickness of thin surface layers, such as native oxide films or the adsorbate films deposited during a step-by-step interface experiment (see chapter 1.6.1). The intensity decay of the signal of a substrate emission line caused by the scattering

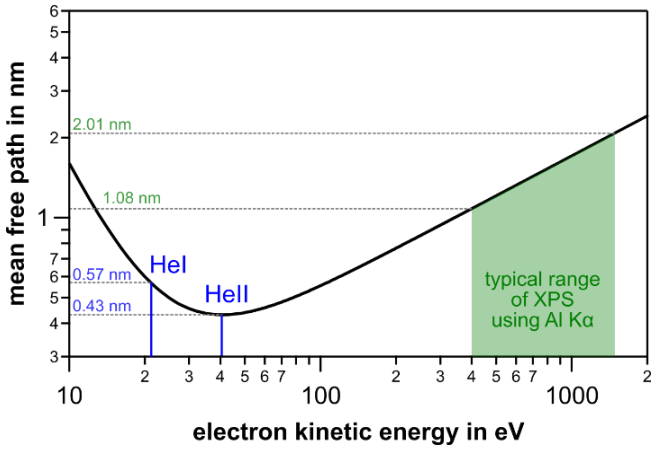

Figure 1.10: The universal curve for the inelastic mean free path (IMFP) of an electron after Seah *et al.*, plotted in the range from 10 eV to 2000 eV. In blue the energies of HeI and HeII and in green the typical energy range of XPS is highlighted, when Al Kα radiation is used.

of the photoelectrons while traveling through the surface layer can be described using the Beer-Lambert law [95] (see equation 1.19).

$$\mathrm{I}_{sub}(d_{ads}) = I_{sub,0} \cdot \exp\left(-\frac{d_{ads}}{IMFP_{ads} \cdot \cos(\gamma)}\right) \qquad 1.19$$

$\mathrm{I}_{sub,0}$ is the substrate intensity measured without the surface layer, $\mathrm{I}_{sub}(d_{ads})$ the attenuated signal at a distance $\frac{d_{ads}}{\cos(\gamma)}$ (corresponding to a surface layer thickness of d_{ads}), $IMFP_{ads}$ the IMFP of the photoelectrons inside the adsorbate and γ the angle between the incident X-rays and the electron take-off direction. This expression can be solved for d_{ads} to determine the surface layer thickness.

1.3.4. Quantitative analysis

XPS allows performing a quantitative analysis of the measured sample by comparing the integrated peak areas of the photoemission lines of the different elements. Before comparing the integrated peak areas, they must be weighed by dividing them by element-specific photoionization cross-sections (PICS) or by atomic sensitivity factors (ASFs). The PICSs are theoretically calculated values, that describe the probability that a photoelectron is excited. They depend on the initial state (the orbital) and the energy of the incident X-ray radiation. ASFs are determined from real measurements of reference samples, which means that they contain the PICS, but also in addition the probability that the electron escapes from the sample and is transmitted through the analyzer so it can be detected. Depending on which kind of factors (PICSs or ASFs) are chosen, the peak areas must be additionally divided by the spectrometer transmission function $TXFN(E_{kin})$ and an energy compensation factor $ECF(E_{kin})$ (when using PICSs) or by an analyzer correction factor (for ASFs).

Energy compensation factor:

The energy compensation factor (ECF) accounts for the kinetic-energy-dependent escape depth of the photoelectrons. As depicted in the three-step model in Figure 1.8, while traveling to the surface of the sample, the photoelectrons are scattered depending on their kinetic energy. Since scattered electrons will not contribute to the peak, but to the background or secondary electrons of the XPS spectrum, the ECF must be considered. Often, the IMFP is used as ECF, determined by different methods, such as the universal curve by Seah *et al.* [94] discussed in chapter 1.3.2., or the empirically calculated TPP-2M formula [96]. Another frequently-used way of calculating the ECF is the kinetic energy raised to the 0.6th power ($E_{Kin}{}^{0.6}$).

Photoionization cross-sections / atomic sensitivity factors:

The most frequently used PICSs are the ones calculated by Scofield [97], even though other databases exist as well [98,99]. They describe the element-specific and orbital-specific probability for an excitation of the photoelectron. In addition, the cross-sections depend on the used excitation source, for example, Al Kα or Mg Kα. In the case of Scofield sensitivity factors, they are normalized, so the PICS of the C1s emission line is equal to 1.

AFSs are based on real measurements of reference samples. The most used ASFs are the ones by Wagner et al [100], although a variety of other databases exists as well [101,102]. The Wagner sensitivity factors are normalized so that the ASF of F1s is equal to 1. For the ASFs, the ECF and the transmission function are already included in the sensitivity factors and are therefore not part of the normalization. However, since the reference measurements of Wagner have been performed on an XPS machine using a cylindrical mirror analyzer, an analyzer correction factor (ACF) must be applied, if another analyzer type is used. Modern XPS machines are usually equipped with hemispherical deflection analyzers.

In addition, it must be considered that the angular distribution of the photoelectrons depends on their kinetic energy. Only at an angle of 54.74° (also called the magic angle), the angular distribution is independent of the kinetic energies [103]. If the angle between the incident X-rays and the electron take-off-direction is therefore different from the magic angle, the PICSs must be further modified. For many commercially available XPS machines, the angle between the X-rays and the emitted electrons is 45° or 90°, which means that corrections are required. The ASFs of Wagner have been recorded at two different instruments with the electrons collected at angles of 90° and 50°. However, in his original publication Wagner states “that the angular effects are below the level expected to be significant, relative to other factors” [100].

Transmission function:

The transmission function (TXFN) is the probability of a photoelectron to travel from the surface of the sample through the lens optics and the analyzer up to the detector unit and depends on the kinetic energy of the photoelectron, the used lens mode, and the pass energy. It can be determined by

measuring two or more core levels of the same element, ideally with largely different binding energies, and comparing the ratio of the measured intensities to the ratio of the Scofield sensitivity factors. The different IMFPs of both emission lines must be considered as well. A pure sputter-cleaned elemental sample like for example metallic copper should be used. In the case of copper, one can compare the $Cu2p_{3/2}$ and $Cu3p_{3/2}$ emission lines at binding energies of 933 eV and 77 eV. Usually, the TXFN is already provided by the XPS manufacturer in the measurement software of the XPS machine, and it is not required to be further adjusted.

Stoichiometry determination:

The calculation of the normalized peak areas $A_n(x)$ from the measured peak areas $A_m(x)$ at the magic angle for an element x is described in equations 1.20 and 1.21 for PICSs and ASFs, respectively.

$$A_{n,PICS}(x) = \frac{A_m(x)}{TXFN(E_{kin}) \cdot ECF(E_{kin}) \cdot PICS(x)} \quad 1.20$$

$$A_{n,ASF}(x) = \frac{A_m(x)}{ACF \cdot ASF(x)} \quad 1.21$$

The atomic percentages of an element x can then be calculated from the normalized peak areas using equation 1.22.

$$c(x) = \frac{A_n(x)}{\sum_x A_n(x)} \quad 1.22$$

Stoichiometry calculations with the above-described method are only precise when the investigated sample has a homogeneous elemental distribution. Surface layers with a different stoichiometry compared to the bulk, like for example a native oxide film or adventitious carbon contaminations, can lead to inaccurate results. The photoelectrons emitted from the bulk of the sample must travel through the surface layer to leave the sample, which means that they are scattered in the surface layer depending on their kinetic energy and therefore the binding energy of the measured orbitals. If the binding energy of the orbitals of the investigated materials differ stronger from each other, the error in the determination of the stoichiometry will be larger.

TXFN and IMFP canceling each other out:

When determining stoichiometries by XPS it is occasionally assumed that the TXFN and the IMFP are approximately canceling out each other's energy-dependency and can therefore be ignored. It is argued that the TXFN and IMFP show a $E_{kin}{}^{-0.5}$ and a $E_{kin}{}^{0.5}$ dependence, respectively [104]. The peak areas are then simply normalized by dividing them by the PICS values, for example, the factors provided by Scofield. While the assumption that the TXFN shows a $E_{kin}{}^{-0.5}$-dependence can be made for older XPS system with more simple lens towers and without magnetic lenses [105,106], it is not necessarily valid anymore for more modern systems [104]. The TXFN of the Thermo Fisher Escalab 250 system, which was

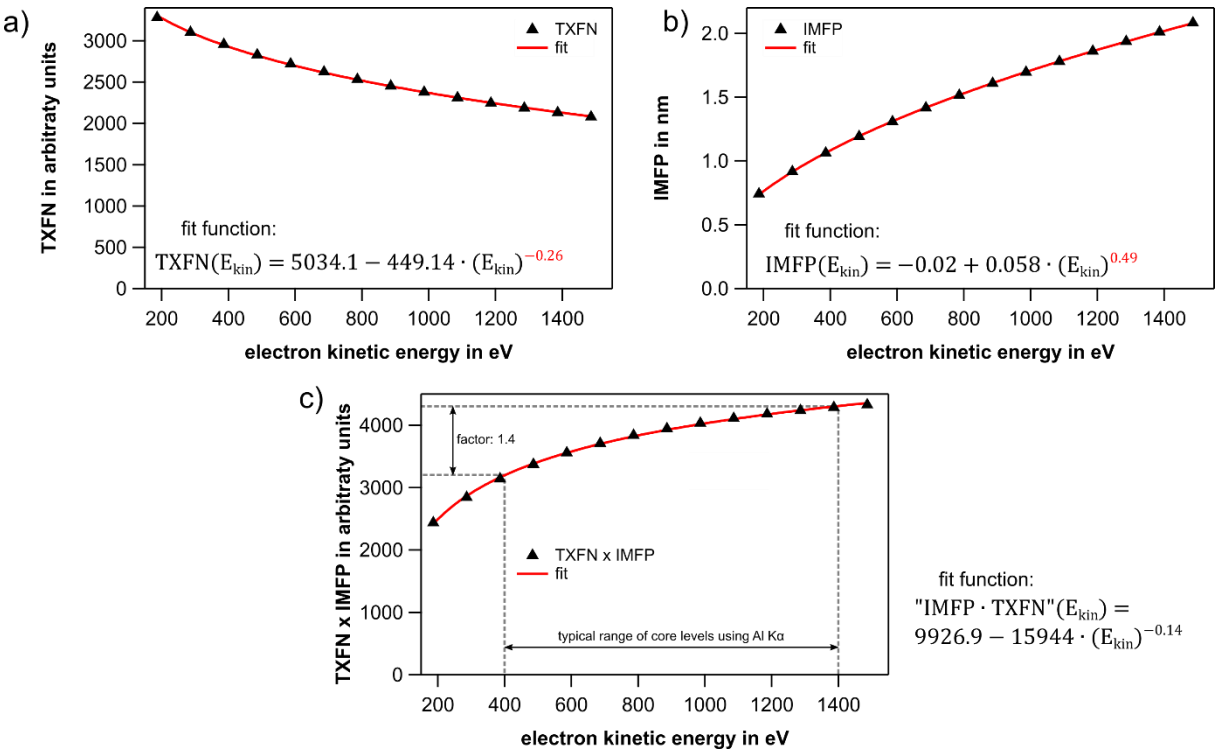

Figure 1.11: a) The TXFN of the Thermo Fisher Escalab 250 used in this work, b) the IMFP after Seah at al. and c) the product of the IMFP and the TXFN plotted against the kinetic energy of the photoelectrons. In the binding energy range that is usually investigated using Al Kα ($E_B \approx 80eV$ to $1080eV$) the product of IMFP and TXFN can vary by a factor of around 1.4, showing that the assumption that the IMFP and TXFN cancel each other out should not be applied.

mainly used in this work, shows a TXFN with a $E_{kin}{}^{-0.26}$ dependency, (see Figure 1.11 a) when it is operated at a pass energy of 50 eV in the lens mode "LargeAreaXL". Along with the IMFP by Seah *et al.* [94] (see Figure 1.11 b) the product between both can vary by a factor up to 1.4, demonstrating that the assumption that the IMFP and the TXFN are canceling out should not be applied without knowing the exact $E_{kin}{}^{-n}$-behavior of the TXFN of the used XPS system.

1.4. Energy band alignment at semiconductor interfaces

The energy band alignment at material interfaces can be determined through a model proposed by Anderson in 1960, also called “Anderson’s rule” [107]. It will be presented in the following at the example of the alignment of an n-type semiconductor (SC) with a smaller bandgap (labeled “n”) and a p-type SC with a larger bandgap (labeled “p”). For more details regarding the physical background of the energy band alignment at interfaces, the reader is referred to the books of Hunklinger [108] and Sze. [75]

Both materials are shown in Figure 1.12 a) before contact with their vacuum levels E_{vac} aligned. Three different material properties are shown for each SC: i) the work function, which is the difference between E_{vac} and the Fermi level E_F, ii) the electron affinity χ, which is the difference between E_{vac}

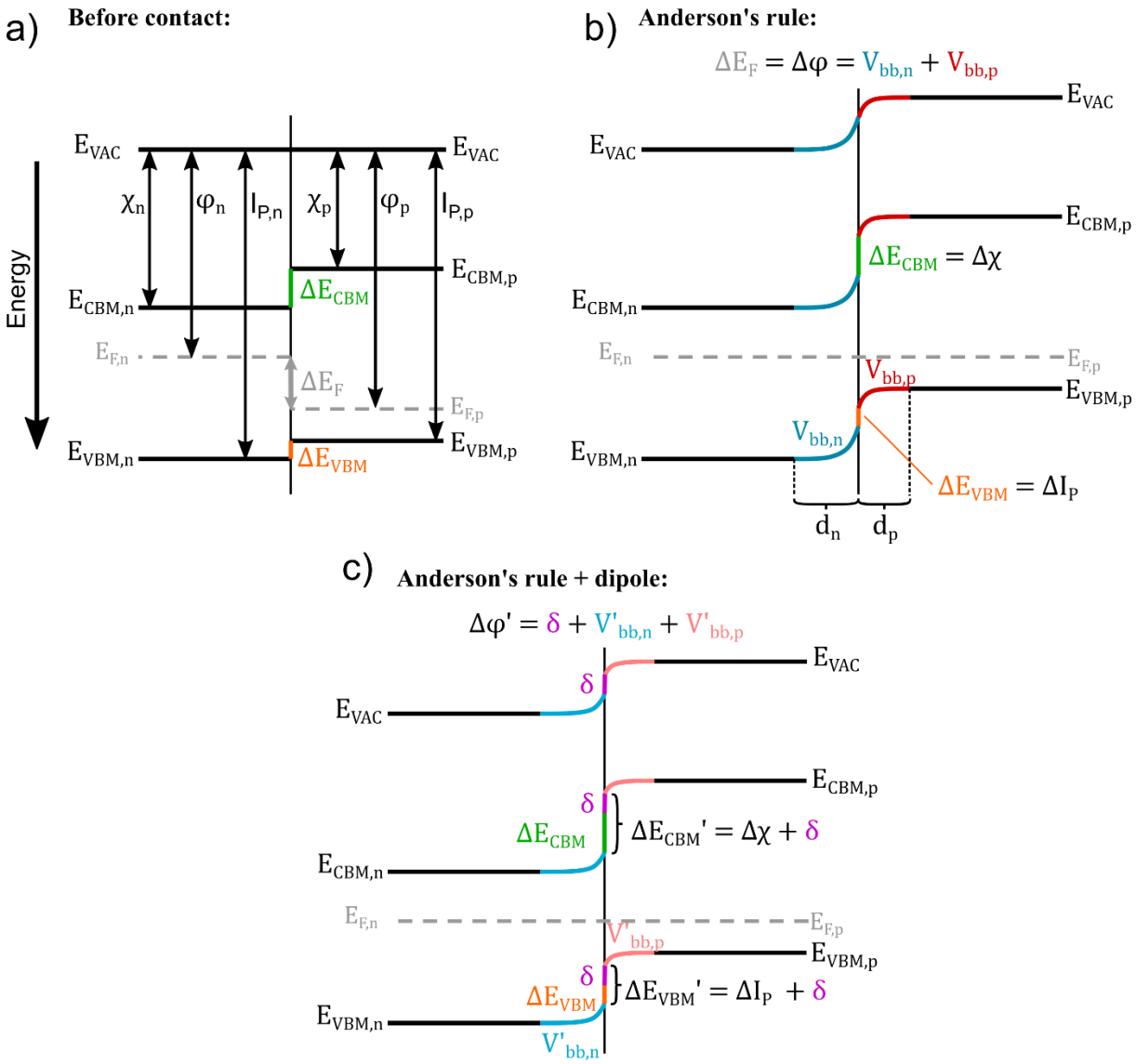

Figure 1.12: a) Two semiconductor materials before contact with their vacuum levels aligned and b) after contact aligned at their Fermi levels according to Anderson’s rule. In c) an additional dipole is assumed, which reduces the band bending and increases the offsets between the VBM and CBM of both materials.

and the conduction band minimum (CBM) and iii) the ionization potential I_P, which is the difference between E_{vac} and the valence band maximum (VBM). Anderson stated that without any interface states being present, the built-in potential (V_{bb}, the band bending) that will form upon contacting both materials is defined by the difference of their Fermi levels and therefore their work function difference $\Delta\varphi$. This dependence is expressed below in equation 1.23, with $V_{bb,n}$ being the band bending in the n-type SC and $V_{bb,p}$ the band bending in p-type SC.

$$\Delta\varphi = V_{bb} = V_{bb,n} + V_{bb,p} \qquad 1.23$$

Due to the different Fermi levels of both materials, electrons are transferred from the material with a lower work function (higher E_F) to the material with a higher work function (lower E_F) and holes are transferred in the other direction. Both charge carriers recombine in the center and leave behind charged ions, causing an electric field (and therefore a built-in potential or band bending). In thermal equilibrium, the diffusion current caused by the difference in carrier concentration and drift current cause by the formed electric field are canceling each other out. The extension of the band bending into the n-side (d_n) or p-side (d_p) SC and the amount of band bending on each side of the interface ($V_{bb,n}$ / $V_{bb,p}$) can be determined using equations 1.24 and 1.25, where N_A and N_D are the acceptor and donor concentrations [75].

$$\frac{d_n}{d_p} = \frac{N_A}{N_D} \qquad 1.24$$

$$\frac{V_{bb,n}}{V_{bb,p}} = \frac{N_A}{N_D} \qquad 1.25$$

The materials in contact, with their Fermi levels aligned, are shown in Figure 1.13 b). The offsets between the CBM (ΔE_{CBM}) and VBM (ΔE_{VBM}) of both SCs are sketched in green and orange, respectively, and can be determined from the electron affinity $\Delta\chi$ and ionization potential differences ΔI_P (see equation 1.26 and 1.27).

$$\Delta E_{CBM} = \Delta\chi \qquad 1.26$$

$$\Delta E_{VBM} = \Delta I_P \qquad 1.27$$

The valence band and conduction band offsets can either act as a barrier for a charge carrier that is trying to overcome it or as a "cliff" so that the charge carrier will "fall down", resulting in an energy loss for the charge carriers. In the band diagram sketched in Figure 1.13 b), ΔE_{CBM} would be a barrier for an electron travelling from the n-type SC to the p-type SC (left to right) and result in an energy loss for an electron traveling in the opposite direction. A hole traveling from the left to the right would lose energy when it falls down the valence band offset ΔE_{VBM}, while it must overcome the valence band offset ΔE_{CBM} when it is moving from the right SC to the left SC. Identifying barriers and cliffs at energy

band diagrams of solar cells is therefore of interest since they can reveal efficiency-limiting factors of the device. A more detailed discussion on the effect of offsets on the device performance of solar cells is given in chapter 1.5.

The model of Anderson can often fail to predict the exact energy band alignment since it does not consider the possibility of the formation of an interface dipole. At the surface and at the interface between two materials the symmetry of the crystal lattice is usually disturbed which can either lead to asymmetric charge distributions or result in dangling bonds and therefore lead to interface states. These interface states can take up charge carriers and can therefore reduce the amount of band bending at the interface. Compared to a band bending where the potential is extended over a distance of several nm or even further, the interface dipole δ causes an abrupt potential change within atomic dimensions, which is visible as an offset in the vacuum level. Figure 1.13 c) shows again the band alignment of the same materials as in Figure 1.13 b), but with an additional interface dipole that has formed.

The Fermi level difference of both materials before contact is now partially compensated by the interface dipole, which reduces the total band bending, as described by equation 1.28.

$$\Delta\varphi' = {V_{bb,1}}' + {V_{bb,2}}' + \delta \qquad 1.28$$

At the same time, also the valence band and conduction band offsets are modified as well (see equations 1.29 and 1.30).

$${\Delta E_{CBM}}' = \Delta\chi + \delta \qquad 1.29$$

$${\Delta E_{VBM}}' = \Delta I_P + \delta \qquad 1.30$$

Since also the band offsets are influenced, a dipole that is appearing at an interface between two materials inside a solar cell can affect the device performance. Whether an interface dipole is formed cannot be predicted easily, which is why the exact energy band alignment at interfaces is usually determined from experiments. In chapters 1.6.1 and 1.6.2 two different experimental approaches will be presented for determining such energy band alignments: i) classical step-by-step interface experiments and ii) tapered cross-section XPS (TCS-XPS).

1.5. Comparison of p-n-based and p-i-n-based solar cells

The requirement for a photovoltaic device to generate power is the separation of the excited electron-hole pairs. Two different device structures for the separation of the charge carriers will be discussed in the following: i) a p-n-junction as it is for example used in crystalline silicon solar cells and ii) a p-i-n-junction, which is for example used in amorphous silicon solar cells and is often claimed to be the type of junction used in perovskite solar cells (see chapter 2.4 for a discussion on the working principle of perovskite solar cells).

A p-n-homojunction device in the dark and under illumination at open-circuit conditions is depicted in Figure 1.13 a) and b), respectively. In the dark, the junction is in electronic equilibrium and the Fermi level is constant over the whole device. The band bending on the n-side and the p-side is marked in blue and red, respectively. Upon illumination, electron-hole pairs are created. The number of electrons in the conduction band (n) and holes in the valence band (p) can now not be described with a single Fermi distribution anymore and separate Fermi levels for the electrons ($E_{F,n}$) and holes ($E_{F,p}$) must be defined, also called quasi-Fermi level splitting. The amount of quasi-Fermi level splitting is the potential difference of the electrons in the conduction band and the holes in the valence band

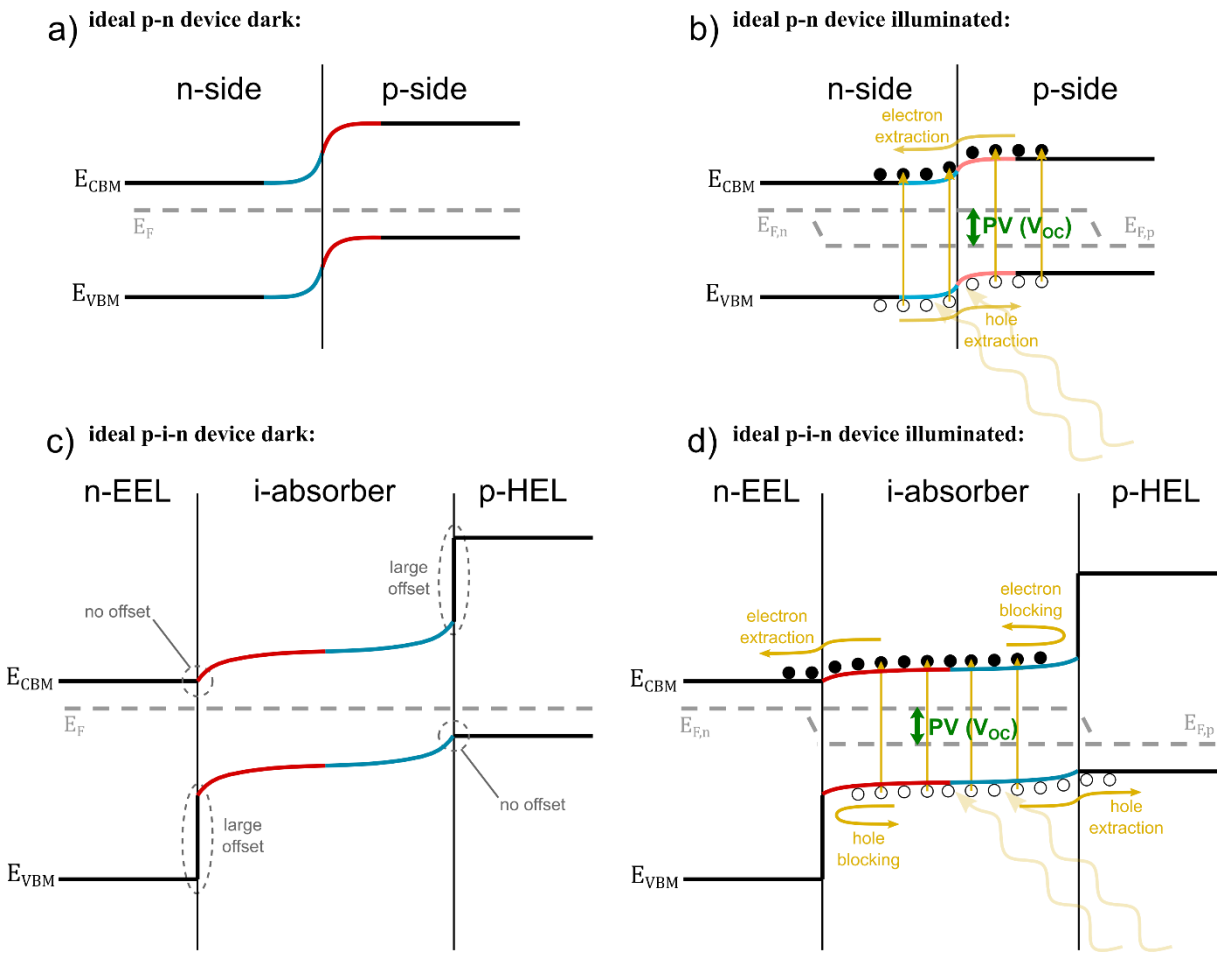

Figure 1.13: Comparison of energy band diagrams of p-n solar cells and p-i-n solar cells in the dark (left) and under illumination (right) at open-circuit conditions.

and is therefore equal to the generated maximum photovoltage (PV) or the open-circuit voltage (V_{OC}) of the device. Following the theoretical discussion of Würfel [109], the separation is caused by the gradient of the Fermi levels, which is equivalent to the electrochemical potentials and therefore the sum of the potential and concentration gradient. Electrons are moving to the n-side while holes are moving to the p-side. Under open-circuit-conditions, the separation of the charge carriers reduces the built-in potential towards a flat-band situation, as depicted by the light blue and light red sketched band bending in Figure 1.13 b). Even at open-circuit conditions, usually, part of the band bending will remain and the full flat-band conditions will not be reached. The band bending in the dark is therefore limiting the open-circuit voltage of the device under illumination. It becomes now evident, that an interface dipole that will reduce the band bending, will also limit the photovoltage (the V_{OC}) that can be extracted from the junction.

Figure 1.13 c) and d) are showing a p-i-n-junction device in the dark and under illumination at open-circuit conditions, respectively. The intrinsic absorber material is positioned in between two wide bandgap semiconductors, a low work function electron extraction layer (EEL) which blocks the holes, and a large work function hole extraction layer (HEL) which blocks electrons. Both charge extraction layers are usually highly doped. Since the absorber material is intrinsic, its intrinsic carrier concentration is rather low compared to the electron concentration n in the EEL and the hole concentration p inside the HEL. It is therefore assumed that the band bending appears only inside the absorber material and that it is ideally extended throughout the full thickness of the material. Compared to a p-n-junction device, every electron-hole pair is excited inside the built-in potential, meaning that the charge carriers can be separated more efficiently. Ideally, the CBM of the EEL and the absorber and the VBM of the HEL and the absorber are exactly aligned, so no offset that could act as a barrier or a voltage loss would result. The choice of the right charge extraction layers that form suitable contacts to the absorber material is therefore essential. Since the exact energy band alignment cannot be predicted from comparing the individual materials before contact (see chapter 1.4 on Anderson's rule and its limitations), an experimental determination of the band alignment is necessary. The following three chapters will discuss how the energy band alignment at the interface between two materials can be determined experimentally from PES measurements, both in the dark and under illumination when a photovoltage is formed.

1.6. Energy band alignment at material interfaces using PES

The energy band alignment at the interface between two different materials can be determined using PES. In the following, two different approaches, which are both applied in this work will be discussed: i) classical step-by-step interface experiments which are performed by depositing thin films of increasing thickness of an adsorbate material on top of the substrate and PES measurements in between each deposition step and ii) tapered cross-section XPS (TCS-XPS), where the interface between both materials is extended to a range of several mm by preparing a small-angle wedge so that a PES line scan can be performed along the incline. Since for photoactive materials, illumination may induce photovoltages which will affect the PES measurements and band diagram, the effect of light on PES measurements and how this translates into an illuminated energy band diagram are discussed as well.

1.6.1. Classical step-by-step interface experiments

The idea behind a classical step-by-step interface experiment is that the interface between the two investigated materials is built up gradually by depositing extremely thin layers of the adsorbate materials on top of the substrate and performing PES measurements in between each deposition step so that the built-in potentials (the band bending) inside both materials can be tracked. The width of the space charge region between two different materials depends mainly on their majority charge carrier concentrations and is usually in the range of 3 to 50 nm. The first deposition step of the adsorbate material should therefore be in the range of one monolayer since otherwise already a too large part of the space charge region has built up when the first PES measurement is performed. The adsorbate material should preferentially be deposited by a method that allows depositing very thin homogeneous films like thermal evaporation so that a controlled deposition of such low thickness is possible. Sputter deposition is also possible, although care must be taken that no chemical changes are induced to the substrate. The principle of classical step-by-step interface experiments will be explained at the example of an np-heterojunction and is depicted in Figure 1.14. At first, the band bending inside the substrate and adsorbate is determined. The band bending (or also called built-in potential) at the interface between substrate and adsorbate is caused by a charge transfer between both materials related to the equalization of their Fermi levels. For more details regarding the band energy alignment at the interface between two semiconductors, the reader is referred to the publication of Anderson [107].

Since the VBM to core level binding energy difference is a material's constant for non-reactive materials, the core levels are shifting parallel to the VBM (and therefore also the CBM). The binding energy shift of the substrate and the adsorbate core levels are therefore resembling the VBM and CBM shifts, which is the band bending. Figure 1.14 a) shows the variation of a substrate core level (left) and an adsorbate core level (right) with increasing adsorbate thickness. The measured substrate shift ($\Delta E_{sub,m}$) and adsorbate shift ($\Delta E_{ads,m}$) are depicted in light blue and light red. Subfigure b) shows the binding energy shift of both emission lines in dependence on the thickness of the deposited adsorbate

layer. The thickness of the adsorbate layer can be calculated from the intensity damping of the substrate emission lines as it is explained in chapter 1.3.2. Since after the first deposition step already some of the space charge region has built up, the binding energy shift of the adsorbate should ideally be extrapolated back to a thickness of 0 nm. This is depicted in Figure 1.14 b) with the red dotted line that is labeled with "extrapolated". The same extrapolation should also be performed for the binding energy shift of the substrate emission lines. As a result, the total binding energy shifts of the substrate ($\Delta E_{sub,t}$) and adsorbate emission lines ($\Delta E_{ads,t}$) can be determined. Now, the band bending inside the substrate ($V_{bb,sub}$) and the adsorbate ($V_{bb,ads}$) can be calculated using equation 1.31 and 1.32.

$$V_{bb,sub} = \Delta E_{sub,t} \qquad 1.31$$

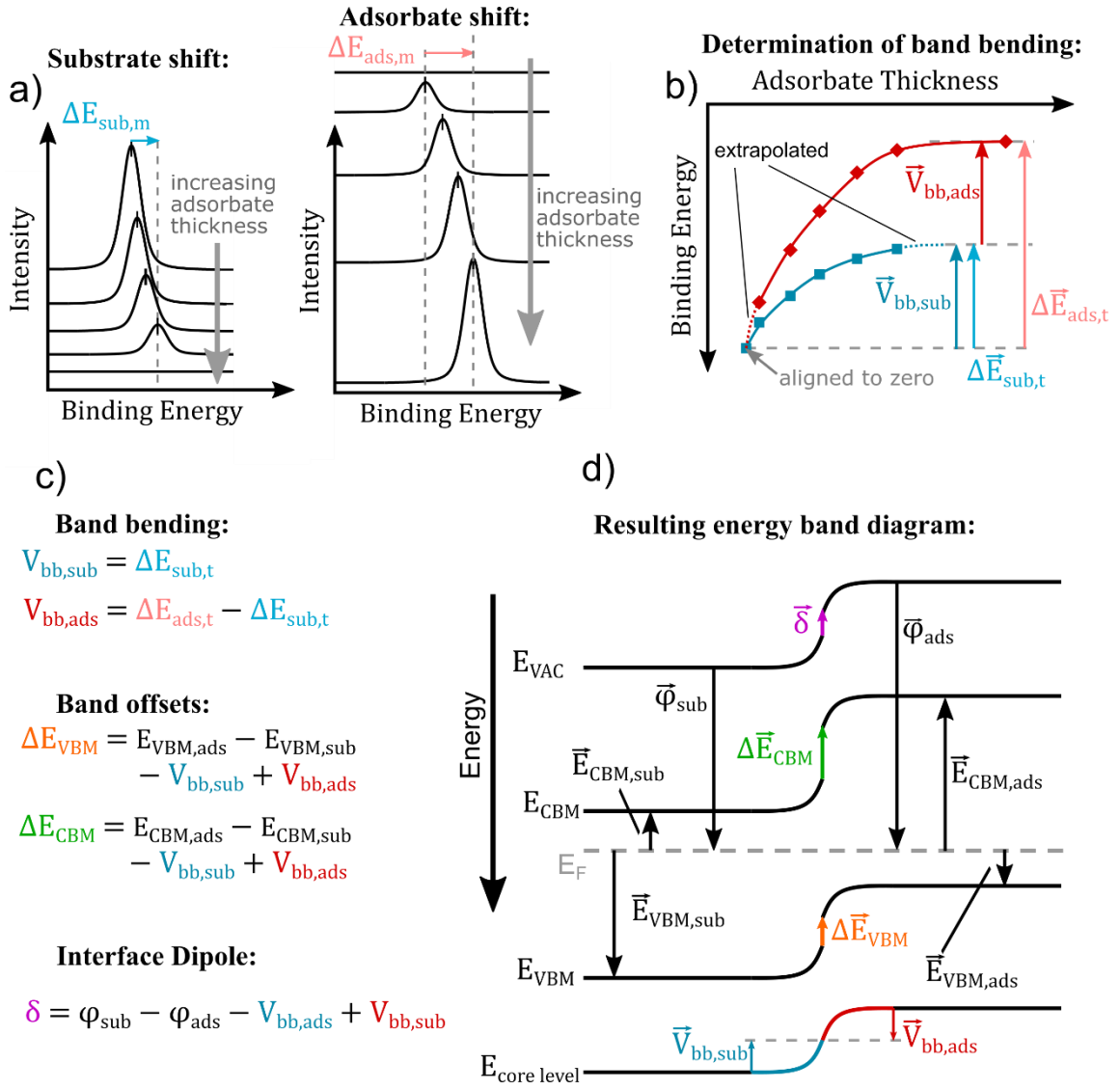

Figure 1.14: Illustration of how the energy band diagram at the interface between two materials is determined from a classical step-by-step interface experiment. a) Core level emissions line of the substrate material (left) that are decreasing in intensity and of the adsorbate material (right) that are increasing in intensity. b) Determination of the band bending values from the core level shifts. The dotted parts of the lines are extrapolated. c) The determination of the offsets between the VBMs, the CBMs, and the vacuum levels and d) the resulting energy band diagram at the interface between both materials.

$$V_{bb,ads} = \Delta E_{ads,t} - \Delta E_{sub,t} \quad (1.32)$$

Since the direction of the adsorbate and substrate bending can change – it can either be an upward (substrate in Figure 1.14 d) or a downward band bending (adsorbate in Figure 1.14 d) – also the sign of the band bending value can be either positive or negative. This can easily lead to confusion. The formulas derived in this chapter will define the band bending value coming from the bulk of the substrate/adsorbate and going towards the interface. Since in PES the binding energy is increasing when going from the Fermi level towards the core levels (see Figure 1.14 d), an upward band bending induces a decrease in binding energy and an downward band bending an increase in binding energy.

In addition to the band bending values, it is necessary to determine the VBM values, the work function values (φ), and the energy bandgap (E_g) of both the substrate and the adsorbate. The VBM values can be determined from XPS or UPS by applying a linear fit to the onset of the valence band edge and determining the point of intersection with zero counts. Work function values can be determined from UPS measurements with an applied bias and the energy gaps can for example be determined from UV/Vis measurements. With the bandgap values, the difference between the Fermi level and the CBM can be calculated using equation 1.33.

$$CBM_{sub/ads} = VBM_{sub/ads} - E_{g,sub/ads} \quad (1.33)$$

Since the vectors of the CBM to Fermi level differences are pointing upwards, the CBM values are always negative, unless the material is degenerately doped, meaning that the Fermi level is positioned above the CBM. When the VBM and work function values of the substrate and adsorbate are known, the valence band and conduction band offsets between both materials can be calculated as followed:

$$\Delta E_{VBM} = E_{VBM,ads} - E_{VBM,sub} - V_{bi,sub} + V_{bi,ads} \quad (1.34)$$

$$\Delta E_{CBM} = E_{CBM,ads} - E_{CBM,sub} - V_{bi,sub} + V_{bi,ads} \quad (1.35)$$

The dipole at the interface can be determined using equation 1.36.

$$\delta = \varphi_{sub} - \varphi_{ads} - V_{bb,sub} + V_{bb,ads} \quad (1.36)$$

The VBM and CBM offsets and the dipole at the interface are defined in such a way that the vectors are following the path when coming from the substrate and going towards the adsorbate. The derived band diagram is schematically shown in Figure 1.14 d).

The here-discussed derivation of the band diagram resembles the situation in the dark, where the system is in thermodynamic equilibrium. Under illumination, generated electron-hole-pairs can be separated at the built-in-potential, which will give rise to an SPV. The formation of an SPV will affect the PES spectra as well as the resulting energy band diagram. Chapter 1.6.3 will discuss how the PES spectra and the energy band diagram will be affected when the interface experiment is performed while the sample is being illuminated.

1.6.2. Tapered cross-section XPS

Besides the described step-by-step interface experiments, TCS-XPS is another method to determine the energetic alignment at material interfaces. TCS-XPS allows determining the energy band alignment at all interfaces inside a multi-layer stack using an XPS line scan on a single sample, which can be, for example, a solar cell. The basic idea of TCS-XPS is the transfer of the cross-section of the multi-layer stack, which in the case of a solar cell has a thickness of around 1 µm (see Figure 1.15 b) to a range of several mm, by preparing a low-angle wedge (see Figure 1.15 c). Since the lateral resolution of a laboratory XPS system can only be reduced to around 10 µm, it is not possible to perform an XPS line scan along the original cross-section of the multi-layer stack in direction of the surface normal. In the case of a metal halide perovskite solar cell, the tapered cross-section is typically prepared through mechanical polishing. If an XPS line scan is now performed over the extended cross-section, the band energy diagram of all interfaces inside the multilayer stack can be measured at once, making TCS-XPS much less time-consuming compared to the classical step-by-step interface approach, since no intermediate film deposition is required. For such experiments and valid evaluations of the measured built-in potentials, no additional potential changes should be caused by the newly formed surfaces. This seems to be the case for organic semiconductors. If the XPS line scan is performed while the sample is being illuminated, TCS-XPS is also able to identify SPVs. To determine the energy band diagram, the data acquired during a TCS-XPS experiment can be analyzed in the same way as for the

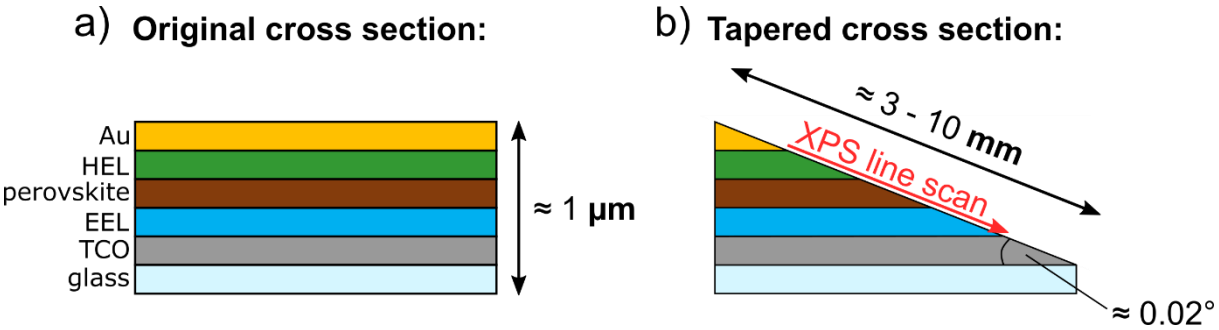

Figure 1.15: a) Side view of a perovskite solar cell. The typical thickness of such a device is around 1 µm, which is much higher than the lowest possible resolution during a PES measurement. b) The prepared tapered cross-section through polishing the sample at an extremely low angle of around 0.02°. The cross-section is now extended from 1 µm to several mm, so that an XPS line scan can be performed.

step-by-step interface experiment. For further details, the reader is referred to the publications of Wussler *et al.* [110] and Das *et al.* [111], who performed TCS-XPS experiments on full perovskite solar cell devices.

The difficulty of TCS-XPS lies in the preparation of the tapered cross-section sample, which is not always straight-forward depending on the investigated sample, especially when the hardness of the layers in the material stack differ strongly from each other. In addition, it may not be possible to measure extremely thin layers, like for example self-assembled monolayers (SAMs) or passivation layers, as they are often used in metal halide perovskite solar cells. Also, cross-contamination between the different layers can sometimes not be avoided. Nevertheless, TCS-XPS has proven to be a versatile

method for recording the energy band diagram of full devices in the dark and under illumination, especially when the investigated materials cannot be thermally evaporated.

1.6.3. Photovoltages in XPS and their effect on the energy band diagram

In chapter 1.6.1 it was described how the energy band alignment at material interfaces can be determined from PES interface measurements, using an exemplary np-homojunction in the dark without the formation of an SPV. In the following, it will be discussed how the acquired PES spectra of a step-by-step interface experiment and the resulting energy band diagram are affected by light illumination which causes the formation of an SPV [112,113].

The requirement for the formation of an SPV during an XPS measurement is a proper grounding of the measured sample, as it is depicted in Figure 1.16 a). The sample must be connected to the electrical ground of the XPS machine at the underlying substrate, so that all layers on top – where the SPV will build up under illumination – are electrically floating. In the shown example of an np-junction, the SPV will obviously build up at the interface between the n-side and the p-side, where also the band bending in the dark is present. The influence of the illumination on a PES measurement of a core level is shown in Figure 1.16 b): the formed SPV results in a shift of the core level to higher binding energies. The development of the substrate and adsorbate core levels are shown in Figure 1.16 a), with increasing adsorbate thickness when going from bottom to top. Black solid and colored broken lines represent the dark and light measurements, respectively. The green arrows indicate the light-induced shift caused by the formation of the SPV. By tracking the shifts of the core levels with increasing adsorbate thicknesses, it is noticeable that the band bending observed in the dark is flattened under the illumination of light. The lowered band bending is further shown in Figure 1.16 b), where the change of the absolute binding energy positions of the substrate and adsorbate are shown in dependence on the adsorbate thickness. With these values, the resulting band diagrams can be determined as described in chapter 1.6.1 and as shown in Figure 1.16 c) and d) for the dark and the illuminated case, respectively. The dark blue arrow ($E_{core,sub,D}$) shows the binding energy of the substrate core level at the point where the full substrate band bending, and therefore part of the total band bending of the np-junction, is developed. Under illumination, electron-hole pairs are separated at the np-junction, resulting in the formation of the SPV, a flattening of the band bending, and a splitting of the quasi-Fermi levels. In PES, the SPV shifts the substrate core level position to higher binding energy, here indicated by the light blue arrow ($E_{core,sub,L}$). The bulk of the n-type side of the np-junction, outside of the space charge region is not affected by the SPV, which means that the core level binding energy ($E_{core,sub,below}$) is identical for the dark and illuminated situation. The red arrows indicate the adsorbate core level binding energy at the bulk of the adsorbate, and therefore at the position where the full band bending (substrate + adsorbate) is developed. The dark red ($E_{core,ads,D}$) and light red arrow ($E_{core,ads,L}$) are indicating again the PES-measured core level binding energies. The SPV-induced shift ($\Delta E_{SPV,ads,max}$) measured at the bulk of the adsorbate is now larger compared to what has been observed for the substrate ($\Delta E_{SPV,sub,max}$), since the full band bending has built up at this position.

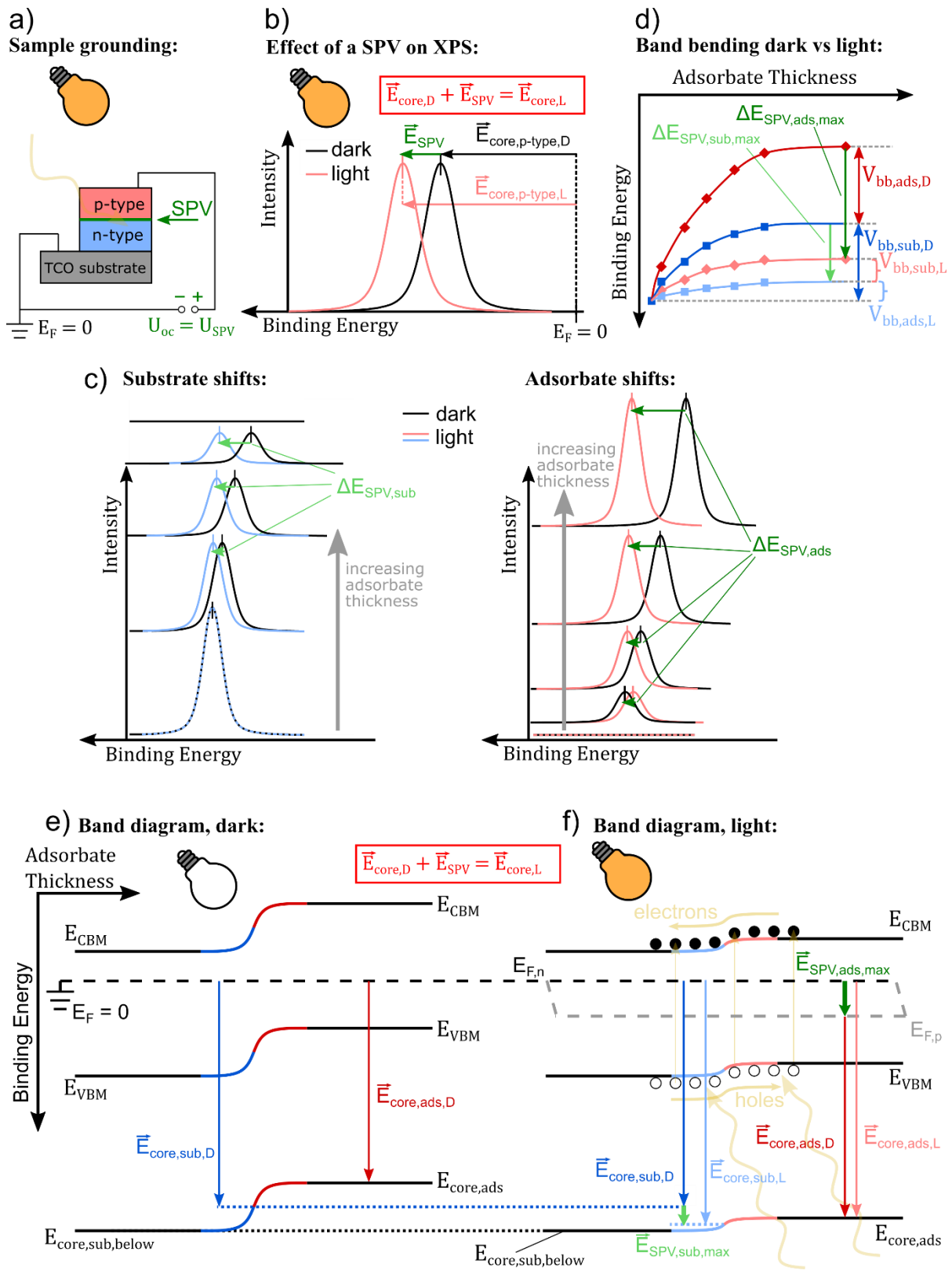

Figure 1.16: Illustration of a classical step-by-step interface experiment and the resulting energy band diagram in the dark where a band bending is present and under illumination with the formation of an SPV. a) A sample under illumination with the electrical ground connected to the TCO, so that an SPV can build up and b) the resulting shift in PES due to the SPV. c) Change of the substrate and adsorbate core level shifts for the dark case (black curves) and the illuminated case (colored curves) and d) the summarized core level shifts in dependence of the adsorbate thickness. The resulting energy band diagrams in the dark and under illumination are shown in d) and e), respectively.

2. Literature review and motivation

After the first reported use of organic-inorganic metal halide perovskites as an absorber material for photovoltaic devices by Kojima *et al.* in 2009, perovskite solar cells have been studied extensively over the past decade, resulting in an improvement of their PCE up to values of over 25% [114]. While it took perovskite solar cells only 11 years to go from Kojima's first reported efficiency of 3.8% to the current world record of 25.5%, the increase in PCE of silicon and cadmium telluride solar cells has been much slower. From 1980 until today, silicon and cadmium-telluride-based solar cells improved from around 15% and 8% to current record values of 26.1% and 22.1%, respectively [114]. The faster development of perovskite solar cells is due to their quick, simple, and cheap processing using low-temperature solution-based preparation techniques, resulting in a much higher sample throughput. This resulted in research focusing on improved device performance, usually on an empirical basis without generalized guidelines and a lack of understanding the underlying device physics. To be able to perform more specific experiments to further improve the PCE of perovskite solar cells, understanding the device physics is of fundamental interest. A key aspect of understanding the working principle of photovoltaic devices lies in accurately investigating and understanding their energy band diagram (see chapter 1.4). A prerequisite is therefore knowing the absorber material's Fermi level position inside the energy bandgap and understanding how it is influenced by doping. This chapter will give an overview of the current state of research on the Fermi level position of perovskite absorbers and the resulting energy band diagrams when they are used in a photovoltaic device. How the doping of perovskite absorbers is affected by their stoichiometry and the underlying substrate will be discussed. The reported results from different characterization techniques like i) PES, which allows to determine the position of the VBM with respect to the material's Fermi level and provides therefore direct information about the doping, and ii) indirect measurements like Kelvin probe force microscopy (KPFM) or Hall measurements, will be discussed. In addition, the proposed working principle of full perovskite solar cell devices based on electron-beam-induced current (EBIC) and KPFM measurements will be presented. Based on the current state of research and initial results from the beginning of this Ph.D. thesis, a set of experiments will be proposed to i) address inconsistencies among reported results in the literature and ii) expand the knowledge of how perovskite solar cells function.

2.1. The effect of the stoichiometry of MAPI on its Fermi level position: PES measurements

The first PES measurements of MAPI were published by Umbebayashi *et al.* in 2003 [115], 6 years before MAPI was first used as absorber material in a photovoltaic device. By performing UPS measurements and density functional theory (DFT) calculations they could show that the valence band of MAPI is mainly composed of σ-antibonding states of Pb 6*s* and I 5*p* orbitals, which was later confirmed by other studies [61,116]. Given the growing interest in organic-inorganic metal halide perovskite, they have been extensively studied by PES. This resulted in a research update by Olthof [116] in 2016 and a review article by Béchu *et al.* [117] in 2020 that focus on reported PES measurements on perovskite surfaces and interfaces to adjacent charge extraction layers. A notable publication is from Tao and coworkers [61], who used UPS measurements and DFT calculations to perform a systematic study on the electronic structure of 18 different perovskite materials, through exchanging the monovalent cation ($A = MA^+$, FA^+, Cs^+), the metal cation ($B = Pb^{2+}, Sn^{2+}$) and the halide anion ($X = I^-, Br^-, Cl^-$). They reported that the investigated perovskites mainly differ in their VBM and that the VB states are determined by hybridization of the metal *s* and the halide *p* states. When going from I to Br and Cl, the halide *p* states and therefore the VBM are shifting to lower binding energies [a)], which increases the energy gap. By exchanging lead with tin, the bandgap is lowered, since the Sn,*s* states are positioned at lower binding energies compared to the Pb,*s* states.

With the increasing number of PES studies on halide perovskites, researchers realized that the reported ionization potential values for this kind of material vary over a wide range from around 5.1 eV to 6.6 eV (see Figure 2.1 a) [116]. Such a wide range of ionization potential values is quite unusual and much higher than the measurement uncertainty of a typical PES instrument or the influence of possible surface contaminations for *ex-vacuo* prepared samples. In 2014, Wang *et al.* [118] were the first to experimentally prove, that the ratio between MAI and PbI_2 in MAPI perovskites films influences the Fermi level position inside the bandgap. Using UPS, they observed a shift of the work function from 4.1 eV to 4.8 eV and of the VBM from 1.2 eV (n-doped) to 0.7 eV (intrinsic / p-doped) when changing the PbI_2 to MAI ratio of the precursor solution from 1.7 (PbI_2-rich) to 0.3 (MAI-rich) (see Figure 2.1 d). Furthermore, they performed Hall-measurements and observed that by going from a PbI_2-rich perovskite to an MAI-rich perovskite, the electron concentration decreases, and transforms the material from n-type to p-type. However, they did not perform XPS measurements and therefore could not investigate a potential shift of the core levels, which would further confirm the doping effect. The finding of Wang *et al.*, that the doping of the MAPI perovskite can be tuned depending on its stoichiometry, confirmed what had been predicted by density-functional calculations a few months earlier by two other research groups [119,120]. Yin *et al.* [119] proposed that lead vacancy defects (V_{Pb}) are responsible for p-doping and that methylammonium interstitial defects (MA_i) will result in n-doping.

a) see footnote on page 4.

Kim *et al.* [120] predicted that V_{Pb} and V_{MA} defects will result in p-doping, while they proposed that V_I defects will result in n-doping. Both authors emphasize that defects with low formation energies are resulting in shallow states near the band edges, while defects that result in energy states in the middle of the bandgap have high formation energies. It is therefore possible to p-dope and n-dope MAPI over a wide range without impairing charge carrier lifetimes caused Shockley-Read-Hall recombination at deep-level trap states.

Shortly after the work of Wang *et al.* [118] was published, Kim *et al.* [121] reported similar observation for MAPI, $MAPbI_{3-x}Br_x$, and $MAPbI_{3-x}Cl_x$, perovskites in 2015: the ratio between the metal salt (PbI_2, $PbBr_2$, and $PbCl_2$,) and the organic halide salt (MAI) will strongly influence the ionization potential. This is at first sight surprising, as doping should only change a material's work function and not its electron affinity or ionization potential. They discovered a higher ionization potential for Pb^{2+}-rich films and a lower ionization potential for MAI-rich films. The same trend for MAPI perovskites was confirmed again by Xie *et al.* in late 2015 [122], Emara *et al.* in 2016 [123] and, Hawash *et al.* in 2017 [124]. The work of Emara *et al.* [123] is especially noteworthy since they compare the electronic structure of 40 different MAPI perovskites films, using different ratios of the PbI_2 to MAI precursors prepared by both vacuum deposition and spin-coating. This huge number of samples is making their

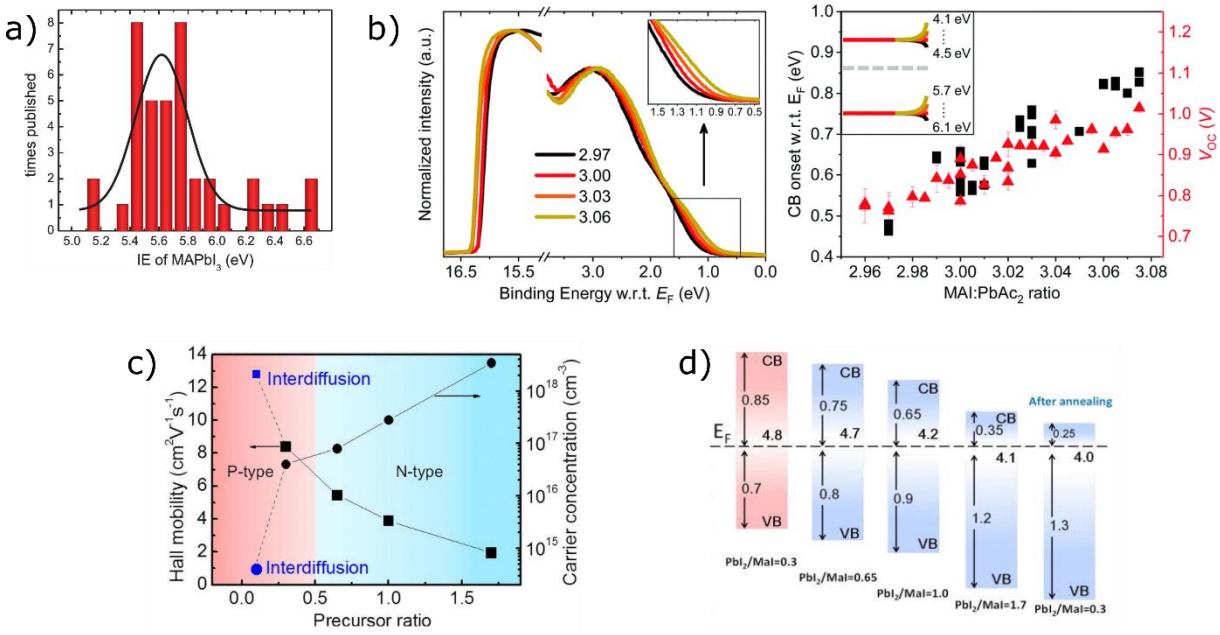

Figure 2.1: Selected PES and Hall measurements from the literature. a) Statistical distribution of ionization potential values for MAPI reported in literature from Olthof *et al.* b) UPS measurements of MAPI films prepared from solution with varying MAI to $PbAc_2$ content and the determined conduction band onset values from Fassl *et al.* c) Charge carrier concentrations values determined by Hall measurements of MAPI films prepared from solution with varying PbI_2 to MAI concentrations, taken from Wang *et al.* d) Fermi level positions with respect to the VBM determined by UPS, also taken from Wang *et al.*

conclusions less prone to statistical errors and therefore much more reliable compared to earlier studies, which often investigated only a few samples. Furthermore, Emara *et al.* [123] also prepared devices and showed that a slightly higher amount of PbI_2 in the perovskite film will give the highest PCE. Until 2017, all studies that investigated the effect of the PbI_2 to MAI ratio on the electronic structure of the perovskite only used UPS to determine the doping or, in case of XPS measurements, only reported small numbers of samples. In 2018, Fassl *et al.* [125] presented an extensive study of MAPI perovskite films prepared by spin-coating with different MAI to $PbAc_2$ ratios in the precursor solution (see Figure 2.1 b). Compared to previous reports, they performed several different characterization techniques (XPS, XRD, SEM, JV-measurements and stability measurements) and were able to precisely control the stoichiometry of the precursor solution, resulting in more obvious trends. By XPS, they observed a parallel shift of the core emission lines to higher (lower) binding energies for PbI_2-rich (MAI-rich) films and a parallel shift of the VBM in UPS measurements. However, the work function remained constant at a value of 5.0 ± 0.1 eV, which led them to the conclusion that the bulk of the perovskite remains unchanged and that only the surface exposed to the vacuum changes from n-type to p-type when going from a PbI_2-rich to MAI-rich material.

In summary, several different studies have shown that the stoichiometry of metal halide perovskites like $MAPbI_3$, $MAPbBr_3$, and $MAPbCl_3$ directly influences their doping. An excess of the lead halide salt is proven to result in n-doping while an excess of the respective methylammonium halide leads to p-doping of the perovskite. Theoretical measurements propose that n-doping is caused by V_{Pb} and V_{MA} defects and p-doping by V_I defects. However, it is not yet clear how the defect concentrations influence the band edge positions as given for example, by the ionization potential.

2.2. The effect of the stoichiometry of MAPI on its Fermi level position: Hall and KPFM measurements

The effect of the stoichiometry on the Fermi level position in metal halide perovskites discussed in the previous chapter has also been confirmed by Hall measurements. In 2014, Wang *et al.* [118] reported a combined PES and Hall measurement study on samples prepared from precursor solutions with systemically controlled PbI_2 to MAI ratios where they related the Fermi level position, from PES measurements to the charge carrier concentration from their Hall measurements (see Figure 2.1 c) and d). For a PbI_2-rich precursor with a PbI_2 to MAI ratio of 1.7, they observed a VBM of 1.2 eV and an electron concentration of 3.5×10^{18} cm^{-3}. When decreasing the PbI_2 to MAI ratio to 1.0 and 0.65 they observed a decrease in the VBM to 0.9 eV and 0.8 eV, respectively. At the same time, the electron concentration determined by Hall measurements decreased to 2.8×10^{17} cm^{-3} and 8.1×10^{16} cm^{-3}. For an MAI-rich precursor with a PbI_2 to MAI ratio of 0.3, they reported a VBM of 0.7 eV and a change of the conductivity from n-type to p-type with a hole concentration of 4.0×10^{16} cm^{-3}, respectively. In addition, they showed that thermally annealing a MAPI film deposited from a MAI-rich solution transforms the film from p-type to n-type with a VBM of 1.3 eV and an extremely high electron concentration of 7.6×10^{20} cm^{-3}. They explained this change from p-type to n-type with the evaporation of MAI from the film, which changes the stoichiometry of the film and therefore also its doping. The effect of an annealing process on the Fermi level position of MAPI was further investigated by Song *et al.* in 2015 [126]. Like Wang *et al.*, they performed PES measurements and Hall measurements on annealed MAPI films. Without any thermal annealing, they observed a VBM of 0.4 eV and a hole concentration of 5.0×10^{17} cm^{-3}. After annealing at 60 °C, 100 °C, 130 °C, and 160 °C the VBM increased to 0.6 eV, 0.7 eV, 0.8 eV, and 0.95 eV, respectively. At the same time, the hole concentration decreased to 1.5×10^{17} cm^{-3}, 3.4×10^{16} cm^{-3} and 2.8×10^{16} cm^{-3} for 60 °C, 100 °C, and 130 °C annealed samples. For the samples annealed at 160 °C, the conductivity changed from p-type to n-type with an electron concentration of 6.3×10^{16} cm^{-3}. In 2017, Cai *et al.* [127] performed KPFM measurements on cross-sections of MAPI-containing perovskite solar cells, using different PbI_2 to MAI ratios in the MAPI precursor solution, to investigate the distribution of the electric potential throughout the device. For their experiments, they used an fluorine-doped tin oxide (FTO) | TiO_2 | MAPI | spiro-MeOTAD | Au stack. They discovered that the position of the built-in potential can be shifted from the front contact (TiO_2 | MAPI) to the back contact (MAPI | spiro-MeOTAD) when changing the stoichiometry of the precursor solution from MAI-rich to PbI_2-rich. Even though they did not measure the doping or the Fermi level position of the perovskite directly, their results are in agreement with previous publications, which show that PbI_2-rich MAPI is n-doped while MAI-rich MAPI is p-doped. For a p-doped perovskite, one would expect the built-in potential to form at the interface with the EEL, in this case TiO_2, and for an n-doped perovskite at the interface with the HEL, i.e. spiro-MeOTAD.

To summarize it can be said that Hall measurements of MAPI films reported in literature seem to confirm the observations made by PES. The stoichiometry has a direct influence on the type of doping: MAI-rich films have a p-type conductivity and PbI_2-rich films have an n-type conductivity.

2.3. The effect of the substrate on the Fermi level position of MAPI

Besides the effect of the stoichiometry of metal halide perovskites on their electronic structure, it has also been reported that the underlying substrate will directly influence the perovskites doping. In a photovoltaic device, the perovskite absorber is usually incorporated between an n-type EEL and a p-type HEL. The first reported perovskite solar cell devices used TiO_2 as an EEL below the perovskite absorber and spiro-MeOTAD as an HEL on top of it [4,128,129]. Later, devices were developed where the perovskite absorber is deposited on top of the p-type HEL and below the n-type EEL [130,131]. Since the glass | transparent conductive oxide (TCO) | EEL | perovskite | HEL | back electrode structure was reported first, it is often referred to as the *classical architecture*, while the glass | TCO | HEL | perovskite | EEL | back electrode structure is described as the *inverted architecture*. In literature, it is reported that perovskite absorbers deposited on n-type EELs tend to be n-type as well, wheres they are intrinsic when deposited on p-type HELs [127,132–134].

Such a substrate effect was first proposed by Miller *et al.* [132] in 2014, who determined the VBM and the work function of MAPI perovskite films deposited on various n-type and p-type substrates using XPS and UPS. The perovskite films deposited on p-type substrates (Cu_2O, NiO, and Poly(3,4-ethylenedioxythiophene) polystyrene sulfonate (PEDOT:PSS) showed VBM values varying from 0.9 eV to 1.38 eV and work function values between 4.9 eV and 4.43 eV and can therefore be considered an intrinsic or slightly p-type semiconductor. In comparison, the perovskites deposited on n-type substrates (FTO, Al_2O_3, ZnO, TiO_2, and ZrO_2) showed a larger VBM (1.69 eV to 1.77 eV) and a smaller work function (4.22 eV to 3.86 eV), implying an n-type semiconductor. In 2015, Schulz *et al.* [133] reported a substrate-dependent doping of MAPI as well. MAPI deposited on p-type NiO_x showed a VBM of 0.7 eV and a work function of 4.7 eV and therefore p-type behavior, while MAPI deposited on TiO_2 showed a VBM of 1.4 eV and a work function of 4.0 eV, resulting in a more n-type material. They also reported a CBM shift of 0.7 eV to higher binding energies when depositing MAPI onto the NiO_x substrates. In the supplementary information of their manuscript, they show that after exposing their p-type perovskite films (deposited on NiO_x) to X-ray radiation, the VBM determined by UPS changes to 1.4 eV, making the film n-type and therefore similar to the MAPI film deposited on TiO_2. Zou *et al.* in 2016 [135] and Olthof *et al.* in 2017 [136] reported similar substrate dependent doping levels of the perovskite for other n-type and p-type materials. In the two review papers of Olthof *et al.* [116] and Béchu *et al.* [117] from 2016 and 2020, such a substrate effect is also discussed. In general, the idea of a substrate-dependent electronic structure of the perovskite absorber seems to be commonly accepted by the perovskite community, even though no physical explanation has been given so far. For n-type substrates, MAPI is reported to be n-type, with a VBM of approximately 1.5 eV and a low work function of around 4.0 eV. For p-type substrates, MAPI is reported to be intrinsic or slightly p-type, with a VBM of around 1 eV and a work function of around 4.7 eV.

In 2019, Zu *et al.* [134] discovered the PES measurements of metal halide perovskite are quite sensitive to illumination. It is emphasized here, that the results of Zu *et al.* had not yet been published when the initial experiments of this Ph.D. work were planned. Zu *et al.* reported that when MAPI surfaces are illuminated with visible light or UV light, an SPV can form which can shift the work function and the energy levels, including the VBM, by values of up to 700 meV to lower binding energies (see Figure 2.2 a). They deposited different perovskite absorbers (MAPI, MAFAPI, CsMAFAPI, and RbCsMAFAPI) on (p-type) poly(triaryl amine) (PTAA) substrates and performed Kelvin probe measurements and UPS measurements with varying UV flux and while illuminating the perovskite surface with visible light. When performing a UPS measurement with low UV flux and no additional visible light, they determined for MAPI a VBM value of 1.75 eV. From Kelvin probe measurements they determined a work function of 4.22 eV. This is a quite surprising result, since other researchers reported MAPI to appear intrinsic on p-type substrates like PTAA and not strongly n-type MAPI like Zu *et al.* By increasing the UV flux and illuminating the perovskite surface with visible light, Zu *et al.* could

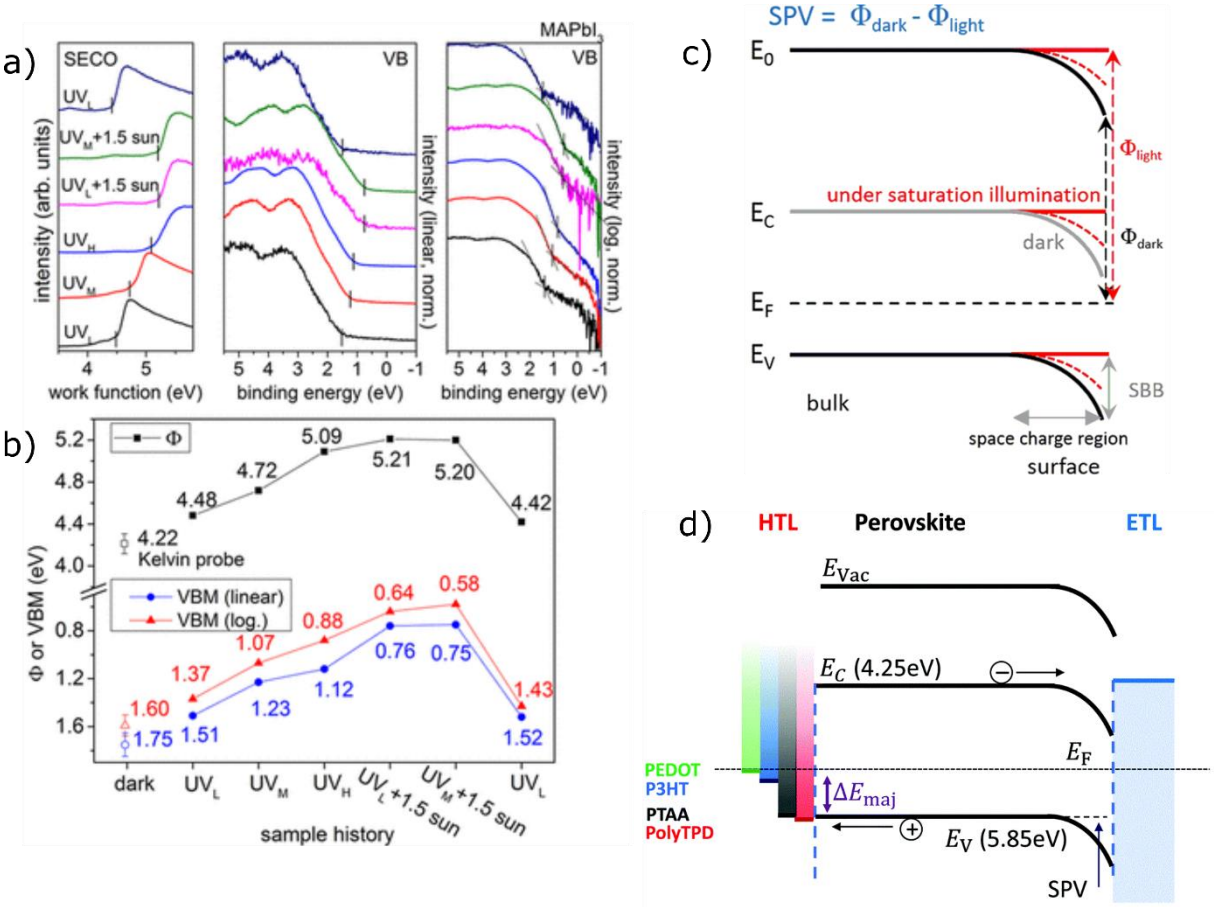

Figure 2.2: Work of Zu *et al.* a) UPS measurements and b) their resulting VBM and work function values for a MAPI film deposited on a p-type PTAA substrate with different fluxes of UV light and visible light. c) The model of Zu *et al.* which correlates the SPV to a band bending at the perovskite | vacuum interface. d) The model of Stolterfoht *et al.*, like the one of Zu *et al.* shown in c).

shift the VBM to lower binding energies and at the same time decrease the work function. When using a maximum UV flux and illuminating the sample at the same time with 1.5 suns of visible light, the VBM decreases and the work function increases to values of 0.75 eV and 5.20 eV, respectively. Zu *et al.* explained this light-induced shift by the formation of an SPV at the perovskite | vacuum interface as displayed in Figure 2.2 (c). In the dark, they assume a downward band bending induced by surface defects, which makes the surface appear to be n-type. Under illumination, they claim that the space-charge-region at the MAPI | vacuum interface results in a separation of the excited charge carries and the band bending is reduced, making the surface appear intrinsic. However, this model is just a hypothesis without any experimental evidence. The SPV could also form by the separation of the charge carriers at any other interface in the sample stack below, such as the PTAA | MAPI interface. Zu *et al.* only supported their claim of the SPV being formed at the MAPI | vacuum interface by referring to Hall measurements in the literature, which have shown that the perovskite is p-type [137,138]. Nevertheless, even without knowing the exact origin of the SPV, the results of Zu *et al.* are show that the metal halide perovskite surfaces are sensitive to illumination during PES measurements, since even low intensities of light can result in an unnoticed SPV which will shift the entire spectrum.

Shortly after that the publication of Zu *et al.*, Stolterfoht *et al.* [139] also reported a light-dependent electronic structure of MAPI as well (see Figure 2.2 d). They used UPS to measure MAPI perovskite films deposited on p-type substrates such as PEDOT:PSS, Poly(3-hexylthiophene) (P3HT), PTAA, and Poly(N,N'-bis-4-butylphenyl-N,N'-bisphenyl)benzidine (PolyTPD). In the dark, they measure a VBM of 1.35 eV for MAPI, which shifts to 0.80 eV under illumination. Like Zu *et al.*, they claim that the bulk of the perovskite is intrinsic, with a downward band bending towards its surface, resulting in the surface being n-type. They argue that under illumination, the band bending is flattened by the formation of an SPV, which allows for the measurement of the VBM of the bulk.

To summarize, several reports in the literature observe an influence of the substrate on the electronic structure of MAPI perovskite films. On n-type substrates MAPI is reported to grow as an n-type material, while on p-type substrates MAPI is reported to grow as an intrinsic material [127,132–134].

2.4. The working principle of MAPI-based perovskite solar cell devices

Given the substrate effect discussed in the previous chapter (n-type MAPI on n-EEL substrates and intrinsic MAPI on p-HEL substrates) it is quite surprising, that various publications focusing on device performance refer to their devices as “n-i-p-devices” in the case of the classical architecture and “p-i-n-devices” in the case of the inverted architecture, suggesting that the perovskite is intrinsic in both cases, independent of the substrate [140–149]. The terms “n-i-p” and “p-i-n” seem to be frequently used as synonyms for “classical” and “inverted”. This chapter will give a short overview of literature reports that investigate the working principle of perovskite solar cells. For a comparison of solar cells based on p-i-n-junctions and p-n-junctions, the reader is referred to chapter 1.5.

The first time that perovskite solar cell using MAPI as absorber material was described as having an-i-p-structure appears to be 2013, when Ball *et al.* reported a PCE of 12.3% (a remarkable value at this time) using Al_2O_3 nanoparticles between the MAPI absorber and the n-type compact TiO_2 layers [150]. On top of the perovskite absorber, they used spiro-MeOTAD as a p-type HTM and claim that this device “*could be described as a p-i-n heterojunction solar cell, where the intrinsic (i) is the perovskite absorber*” without providing any additional experimental evidence for this claim. Ball *et al.* did not perform any measurement on the perovskite absorber to determine its Fermi level position. Their work was later cited by several other publications, that focus on investigating the working principle of perovskite solar cells.

For example, in 2014 Edri *et al.* [151] reported EBIC measurements performed on cross-sections classical architecture devices with MAPI and $MAPbI_{3-x}Cl_x$ perovskite absorbers (see Figure 2.3 a), (A) for $MAPbI_{3-x}Cl_x$, and (B) for MAPI). They argued that their EBIC line profiles show a current generation throughout the absorber layer, but not in the selective contacts, which is characteristic for a p-i-n photovoltaic device. However, assuming the diffusion length of electrons and holes in the perovskite is high enough so that both charge carriers can reach the EEL and HEL such an EBIC pattern could simply result from a perovskite absorber of any doping (n-type, p-type, or intrinsic) in between two selective contacts (EEL and HEL).

Bergmann *et al.* [152] performed KPFM measurements on cross-sections of full perovskite solar cell devices and claimed that their electric field distribution is constant throughout the full device, which resembles a p-i-n junction (see Figure 2.3 b). From the FTO front contact to the Au back contact they observe a total contact potential difference of around 600 mV. Surprisingly, 200 mV of this 600 mV appears inside the FTO and an additional 250 mV appears inside the TiO_2 layer and not inside the perovskite absorber as one would it expect it for a p-i-n junction. Inside a highly-doped TCO like FTO, a built-in potential of 200 mV should not be able to exist, which makes the conclusion of Bergmann *et al.* questionable.

In 2018, Hermes *et al.* [153] also performed KPFM measurements on cross-sections of full perovskite solar cell devices as well, and compared ITO | TiO_2 | MAPI | spiro-MeOTAD | Au with ITO | C_{60} | MAPI | spiro-MeOTAD | Au devices to investigate the effect of these two different EELs (see

Figure 2.3 c). The so-called *photo-potential* shown in Figure 2.3 c) is the difference between the measured contact potential difference under open-circuit conditions (FTO front contact grounded and Au back contact floating) and under short-circuit conditions (both contacts grounded) and should

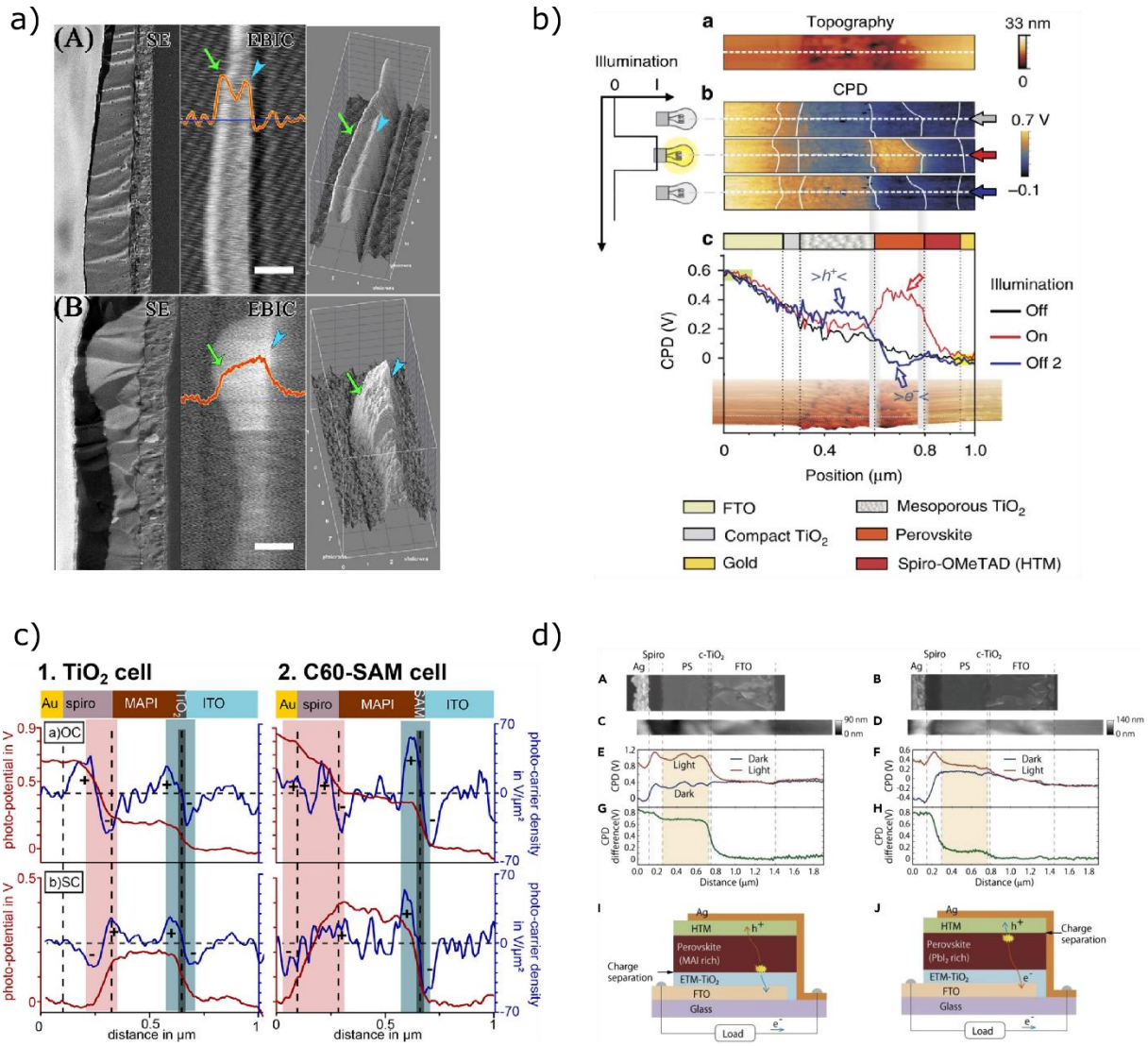

Figure 2.3: a) EBIC measurements of Edri *et al.* of devices with $MAPbI_{3-x}Cl_x$ (A) and MAPI (B) as absorber material. b) KPFM measurement of Bergmann *et al.* performed on a full perovskite device showing the contact potential distribution (CPD). c) KPFM measurements of Hermes *et al.* on two different device structures suing TiO_2 as EEL (left) and using C_{60} as EEL (right). d) KPFM measurements of Cai *et al.* comparing MAI-rich (left) and PbI_2-rich (right) perovskite absorbers. The built-in potential is shifting from the EEL | perovskite to the perovskite | HEL interface when the perovskite absorber composition is changed from MAI-rich to PbI_2-rich.

therefore resemble the built-in potential throughout the device. For the devices with TiO_2 and C_{60} as EEL Hermes *et al.* observe a total built-in potential of around 650 meV and 850 meV, respectively. For both device types, approximately 65% of the built-in potential appears at the MAPI | spiro-MeOTAD interface or throughout the spiro-MeOTAD layer and the remaining 35% at the EEL | MAPI interface. Such a potential distribution, where the built-in potential is split (almost evenly) between the EEL | MAPI and the MAPI | HEL contact would indeed point towards a n-i-p-device structure.

Another study using KPFM measurements on cross-sections of full devices was published by Cai *et al.* in 2018 [127]. The authors used devices in the classical architecture with TiO_2 as the EEL and spiro-MeOTAD as the HEL and compared the built-in potential throughout their devices for MAPI layers prepared from PbI_2-rich and MAI-rich precursor solutions. Even though they did not directly measure the composition of the final perovskite film, it seems reasonable that varying the PbI_2 to MAI ratio of the precursor solution would affect the composition of the deposited perovskite film. They discovered that for planar devices (no mesoporous TiO_2) with a PbI_2-rich MAPI layer, the built-in potential appears at the MAPI | spiro-MeOTAD interface and is switched to the TiO_2 | MAPI interface in the case of MAI-rich MAPI layers (see Figure 2.3 d). At the same time, they built devices for both perovskite compositions and found that their devices with PbI_2-rich MAPI layers can achieve slightly higher PCEs. This observation fits nicely with the fact that PbI_2-rich MAPI layers are reported to be n-type and MAI-rich layers p-type. For an n-type (PbI_2-rich) MAPI layer, one would expect the built-in potential to form at the MAPI | HEL interface, while it should appear at the EEL | MAPI interface for a p-type (MAI-rich) MAPI. The results of Cai *et al.* are therefore indicating that depending on the stoichiometry of MAPI their devices work either as an n-EEL | p-MAPI or an n-MAPI | p-HEL structure.

In conclusion, several publications claim a p-i-n-device architecture for perovskite solar cells based on KPFM and EBIC measurements [150–153]. However, these claims, like the one of Ball *et al.*, are sometimes without experimental evidence [150] and in other cases are not completely clear and conclusive [151,152]. The only study showing clear evidence of a p-i-n-device is the KPFM study of Hermes *et al.* [153], who find that the built-in potential is spit between the EEL | MAPI and MAPI | HEL interfaces. However, a more recent KPFM study from Cai *et al.* [127] seems to show that depending on the PbI_2 to MAI ratio of the perovskite absorber and therefore it's doping, the device functions either as an n-EEL | p-MAPI or an n-MAPI | p-HEL structure.

2.5. Summary: The Fermi level position of MAPI and the working principle of MAPI-based perovskite solar cells

The different literature reports on the Fermi level position of metal halide perovskites and the working principle of MAPI-based devices that were discussed in the previous sections can be summarized as follows:

i) **By changing the ratio between PbI_2 and MAI the doping level of MAPI can be controlled** from p-type (MAI-rich) to n-type (PbI_2-rich).

ii) The **underlying substrate, upon which MAPI is deposited, seems to influence the doping level of MAPI**. When grown on n-type substrates, MAPI appears to be n-type as well. On p-type substrates MAPI appears to be intrinsic instead.

iii) Several publications that investigate the device structure of perovskite solar cells claim that **perovskite solar cells function as n-i-p-devices,** although the experimental data is not always conclusive.

iv) In addition, a great majority of publications that focus on device performance are using the terms “n-i-p-devices” and “p-i-n-devices” for devices in the classical (MAPI on EEL) and inverted (MAPI on HEL) architecture. **“n-i-p-device” and “p-i-n-device” seem to be commonly accepted terms.**

Assuming that there is a substrate effect, and that MAPI tends to grow n-type on n-type substrates (see point i), this substrate effect would be in contradiction to the idea, that classical architecture devices (MAPI on n-type EEL) function as n-i-p-devices (see point iii and iv), where MAPI is intrinsic. Devices using the inverted architecture (MAPI on p-type HEL) could operate as p-i-n-structure, as this will be in agreement with the substrate effect, where MAPI is predicted to be intrinsic on p-type substrates. However, until now all literature studies that have investigated the working principle of perovskite solar cells focused on classical architecture devices. Devices with inverted architecture have not been studied so far.

The doping level of MAPI and its dependence on the substrate therefore remains an unsolved question. In addition, the exact working principles of perovskite solar cells are not clarified yet, especially for devices with an inverted architecture. Investigations into both these aspects, and hence clarification of the afore-mentioned issues will form part of this doctoral thesis. A set of initial experiments to acquire more experimental evidence is presented in the following chapter.

2.6. Initial results: extreme light sensitivity of metal halide perovskites

In the early stages of this Ph.D. work XPS measurements on different perovskite solar cell device stacks were performed, and often resulted in unexpected or unreproducible results regarding the binding energy position of core levels and VBM position. It was discovered that XPS measurements on metal halide perovskite absorbers are extremely sensitive to small amounts of unintentional illumination since such light can lead to an SPV which shifts the XPS spectra, resulting in a misinterpretation of the XPS spectra if the SPV remains unnoticed. In the following section, the measurement on the Au back electrode of a full device in the classical architecture with the layer stack ITO | SnO_2 | MAPI | spiro-MeOTAD | Au will be discussed. The XPS spectra of this sample provide a clear example of how easily unintentional background illumination can influence PES measurements of metal halide perovskite absorbers.

The XPS valence band measurements of the Au back electrode of the full device are depicted in Figure 2.4 a). The Au Fermi level appears at around 0.6 eV and therefore shifted from its equilibrium position of 0 eV. Since during XPS measurements the sample is grounded, the Fermi level of the sample and ground will align, meaning that the Fermi level of a metal will always appear at 0 eV. If this is not the case, the measured sample is not in electronic equilibrium, for example, due to a light-induced SPV. The shown measurements were performed with the chamber light turned off and all vacuum glass

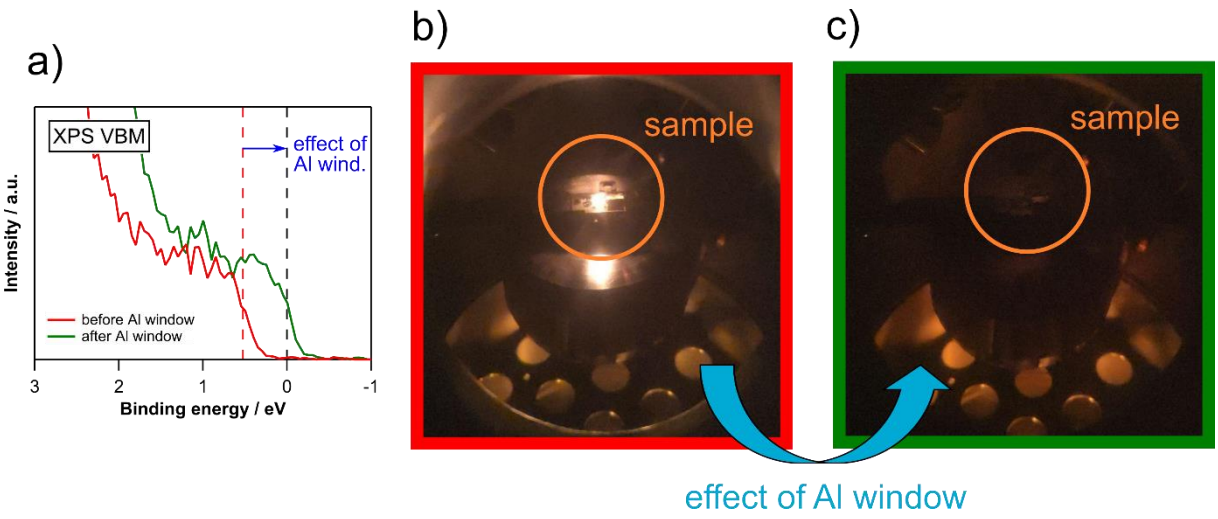

Figure 2.4: a) HeI and XPS VBM measurements of the Au back electrode of a full perovskite solar cell device in the classical architecture employing the following layer stack: ITO | SnO_2 | MAPI | spiro-MeOTAD | Au. The curve in red was recorded before installing the aluminum window. The Au Fermi level is shifted from its equilibrium position at 0 eV, indicating the presence of a light-induced surface photovoltage. The curves in green were recorded after installing the aluminum window. The Fermi level is now measured at 0 eV, proving that no photovoltage is present. b) A view inside the measurement chamber with the chamber light turned off and the glass view ports covered so that no light from outside will reach the sample. The bright light spot on the sample is the light emitted from the heated cathode of the X-ray source hat is reflected onto the sample. c) The same view as in b) but with an installed aluminum window in between the X-ray source and the sample to shield the sample from the light emitted by the cathode of the X-ray source.

viewports covered, so that no light from outside could reach the sample. A look into the XPS chamber shown in Figure 2.4 b) reveals that there is still a light spot visible on the sample, which was later identified to be caused by the heated cathode of the X-ray source. Since the X-ray source is obviously required for XPS measurements it would not have been possible to perform measurements on metal halide perovskite samples in electronic equilibrium using this setup without the presence of a light-induced SPV. A solution to this problem was to install an aluminum window between the X-ray source and the sample. This windows is a 300 µm thin aluminum foil that blocks the visible light from the cathode, while the X-rays are transmitted (see Figure 2.5). After installing the aluminum window, the Fermi level of the Au back electrode is now measured at 0 eV (see Figure 2.4 a), green curve), proving that no SPV is present. A look into the XPS chambers shows that the light is efficiently blocked by the aluminum window (see Figure 2.4 c). Since the frame of the aluminum window is connected to a rotary feedthrough, measurements can be either performed with or without the aluminum window. The extreme light-sensitivity of the investigated perovskite solar cell elucidated the importance of being able to perform *real-dark measurements*, without any SPV caused by unintentional background light. Since literature reports of XPS measurements of metal halide perovskite absorbers are not always providing detailed measurement conditions, it is not clear whether they suffered from an unnoticed SPV. Since the SPV will result in a binding energy shift of all emission lines, including the valence band, an unnoticed SPV can easily lead to the misinterpretation of XPS spectra, meaning that wrong core level binding energy values and wrong doping levels will be determined. The XPS measurements presented in this Ph.D. work will therefore be compared for the real-dark situation and the light situation.

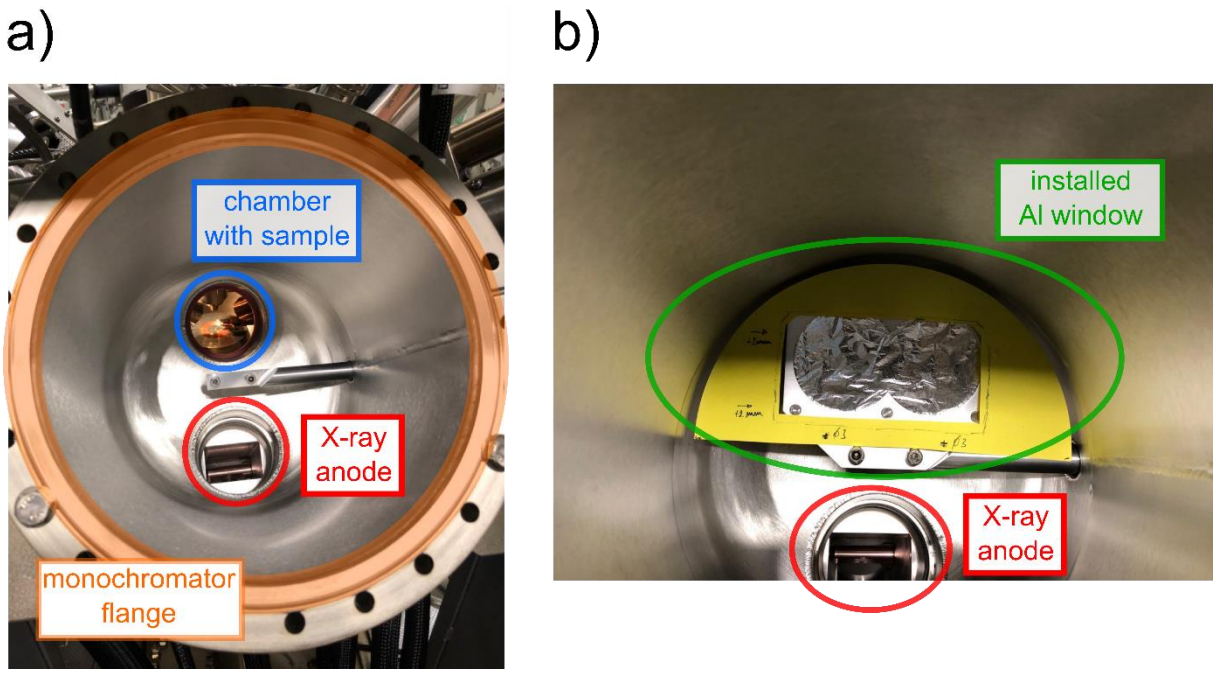

Figure 2.5: a) A look into the XPS chamber through the removed monochromator flange. The red circle shows the X-ray anode emitting the X-rays, that are diffracted at the monochromator, usually attached at the orange-highlighted flange. Only the desired Al Kα radiation will then reach into the measurement chamber, where the sample is positioned (blue circle). In b) the installed aluminum window (green circle) is shown. The yellow mask was positioned to take the inner dimensions of the flange and was removed before closing the system.

2.7. Performed experiments throughout this Ph.D. thesis

To investigate whether the doping of MAPI is dependent on the substrate and to clarify the working principle of perovskite solar cells, especially devices in the inverted architecture, the following experiments have been performed:

i) Firstly, different perovskite absorbers (including MAPI) were grown on n-type (classical architecture) and p-type (inverted architecture) substrates and were measured using PES to investigate the doping level of the perovskite. These measurements were performed in the dark and under illumination to investigate the effect of possible surface photovoltages.

ii) Next, devices were deposited layer-by-layer and PES measurements, again in the dark and under illumination, were performed at each intermediate step. The aim of this step was to identify the interface at which the photovoltage appears in the device hence help to draw conclusions about its working principle. [a)]

iii) The interfaces at which the photovoltages in ii) have been identified were then analyzed in detail by classical step-by-step interface experiments. If possible, these experiments were performed in the dark and under illumination. These experiments aimed to verify that a built-in potential is present in the dark and is then flattened out under illumination.

iv) Finally, the results from i) – iii) were combined with additional UPS measurements to determine the VBM and work function values for each layer in the device. Band diagrams of the completed devices with both classical and inverted architecture were constructed.

[a)] Since the step-by-step deposition of some materials (for example MAPI or doped spiro-MeOTAD) can be experimentally challenging, additional experiments were required at step ii).

3. Investigation of fundamental perovskite properties

3.1. Motivation and chapter overview

The main goal of this chapter is to i) investigate the effect of the substrate (n-type EEL or p-type HEL) on the doping of a perovskite absorber deposited on top of it and ii) to identify possible SPVs of such a layer stack. A so-called substrate effect has been mentioned several times before in the literature with the main conclusion that the perovskite will show an n-doping on n-type substrates and be intrinsic on p-type substrate [127,132–134]. In total, five different perovskite absorbers with varying cations (MAPI, FAPI, $MA_{0.5}FA_{0.5}PI$, $Cs_{0.15}FA_{0.85}PI$, and $Cs_{0.05}MA_{0.475}FA_{0.475}PI$) on top of two different charge extraction layers (n-type SnO_2 and p-type NiO_x) are investigated. The results provide evidence that the idea of a substrate-determined doping of the perovskite absorber is most likely not correct and caused by wrong interpretation of XPS data due to unnoticed SPVs. For both investigated substrates (n-type SnO_2 and p-type NiO_x), the perovskite absorber shows an n-doping when measured in the dark. Under illumination, for the perovskite absorbers deposited on p-type NiO_x a negative SPV arises, resulting in the shift of all emission lines including the VBM to lower binding energies, which makes the material appear intrinsic.

At first, the precursor materials MAI, FAI, PbI_2, and CsI which were used to synthesize the perovskite absorbers, are investigated by XPS. This will help to identify any possible leftovers of unreacted precursors in the final perovskite films and allow to define modified photoionization cross-sections (PICS) which will improve the accuracy of the stoichiometry determination of the final perovskite films. In the next step, the perovskite absorbers are investigated by XRD and UV/Vis to prove the presence of the perovskite phase, determine their bandgap values, and identify possible leftover precursors. JV-measurements to determine the PCE when the perovskite absorbers are used in devices are supplied as well. Then, XPS measurements of the perovskite absorbers performed in the dark and under illumination are presented. It will be discussed how critical it is to avoid unintentional illumination during XPS measurements by exposing an SPV-active sample to different light sources like the hot-ionization pressure gauge, the X-ray source, or the chamber lighting. To be able to measure photovoltages in XPS, the perovskite absorbers must show reasonable PCEs when incorporated into a photovoltaic device. The experiments on the perovskite absorbers were done in collaboration with the research group of Prof. Ulrich W. Paetzold at the Light Technology Institute at the Karlsruhe Institute of Technology, in the former cooperation in the Perosol project. The preparation of the perovskite samples and the SnO_2 and NiO_x substrates was performed by Dr. Jonas Schwenzer, who already optimized the spin-coating process in his Ph.D. work to achieve efficiencies of at least 17.5% for each perovskite type.

3.2. Experimental procedure

Synthesis of the precursor materials MAI, FAI, PbI_2, and CsI by thermal evaporation:

Pre-cut Pilkington NSG TEC™ 15A FTO glass substrates with a thickness of 2.2 mm and dimensions of 20 mm x 20 mm were used. Before the deposition of spiro-MeOTAD, the FTO substrates were consecutively cleaned with DI water and dishwashing soap, isopropanol, DI water, and finally dried under the flow of nitrogen gas. The precursor materials MAI (GreatCell Solar, 99.99% purity, CAS: 14965-49-2), FAI (GreatCell Solar, 99.99% purity, CAS: 879643-71-7), PbI_2 (AlfaAeser, 99.9985% purity, CAS: 10101-63-0), and CsI (AlfaAeser, purity: 99.999%, CAS: 7789-17-5) were thermally evaporated at the DAISY-SOL cluster tool (DArmstadt Integrated SYstem for SOLar Research) at the Technical University of Darmstadt. Effusion cells manufactured by CreaTec Fischer & Co. GmbH were used. To avoid cross-contamination between the different materials, separate effusion cells were used for each material. For the evaporation of MAI, PbI_2, and CsI, Single Filament Cell (SFC) effusion cells equipped with Al_2O_3 crucibles were operated at temperatures of 120 °C, 230 °C, and 400 °C, respectively. The deposition rate was monitored with a quartz crystal microbalance (QCM) at the position where also the sample is placed during the thin film deposition. Using the deposition rate, the deposition time was adjusted so that a film thickness of 30 nm results. The base pressure in the evaporation chamber was at around $5.0 \cdot 10^{-8}$ mbar and increases to values of around $5.0 \cdot 10^{-7}$ mbar and $2.0 \cdot 10^{-8}$ mbar for the deposition of PbI_2 and CsI, respectively. For the MAI thin film deposition, the chamber was kept at a pressure of around $1.0 \cdot 10^{-3}$ mbar by lowering the pumping speed of the turbopump. This was achieved by closing the plate valve which connects the chamber with the turbopump and pumping through a bypass with a smaller cross-section. The deposition procedure for MAI was adapted from Stöhr [154]. For the evaporation of FAI, an OLED Effusion Cell equipped with a quartz glass crucible was used. The OLED Effusion Cell is specifically designed to evaporate organic materials or materials with high vapor pressure and therefore low evaporation temperature. An evaporation temperature of 170 °C was chosen for FAI. It is noted here that comparing the evaporation temperature of FAI to the evaporation temperatures of the other materials might be misleading since different types of effusion cells were used. After the thin film deposition, the samples were transferred to the XPS measurement chamber without breaking the vacuum. The base pressure of the intermediate chambers and the XPS chamber were always kept between $5.0 \cdot 10^{-9}$ mbar and $5.0 \cdot 10^{-10}$ mbar.

Synthesis of the charge extraction layers and the perovskite absorbers by spin-coating:

The synthesis of the SnO_2 films, the NiO_x films, and the perovskite absorbers was performed by Dr. Jonas Schwenzer from the Light Technology Institute at the Karlsruhe Institute of Technology. The same is true for the photovoltaic devices discussed in chapter 3.4.2. The deposition processes will be discussed only briefly here. For the detailed experimental procedure, the reader is referred to chapter 4.3 of the Ph.D. work of Schwenzer [81].

Pre-patterned ITO substrates were cleaned in acetone and isopropanol in an ultrasonic bath for 10 min each. Before the deposition of the charge extracting layers, the substrates were exposed to an oxygen plasma for 3 minutes. For the classical architecture, the SnO_2 layers were spin-coated on top of the commercial ITO glass substrates using a colloidal dispersion containing SnO_2 nanoparticles as the precursor solution. For the inverted architecture, NiO_x was magnetron-sputtered on top of the ITO substrates. The sputtering process was performed in a PVD 75 PRO-Line system (Kurt J. Lesker). For the perovskite deposition, PbI_2 was dissolved in a mixture of dimethylformamide (DMF) and dimethyl sulfoxide (DMSO) and heated at 130 °C for several minutes before it was cooled to room temperature. Then, the respective organic halide salts (MAI, FAI, and CsI) were added to the solution. The solution was spin-coated on top of the SnO_2 and NiO_x substrates. During the spin-coating process, an antisolvent was pipetted on top of the rotating substrates (isopropanol for MAPI and chlorobenzene for all other perovskites). This antisolvent method is commonly used for the spin-coating of perovskite absorbers [155,156]. After the spin-coating process the samples were annealed again at temperatures varying between 100°C and 150°C depending on the perovskite type, to improve the crystallinity [81]. The spin-coating of the SnO_2 layers was performed in air. The preparation of NiO_x and perovskite samples took place in a nitrogen-purged glove box without any exposure to ambient atmosphere.

To complete the devices, a spiro-MeOTAD layer was deposited on top of the perovskite films. spiro-MeOTAD was dissolved in chlorobenzene, 4-tert-butylpyridine, and lithium bis(trifluoromethanesulfonyl)imide dissolved in acetone was used as dopant added to the solution. The spin-coating process was performed in a nitrogen atmosphere as well. The samples were stored overnight in an environment with 20 to 25% humidity, which will oxidize the hole extraction layer, and increases its conductivity. The gold back electrode was deposited by thermal evaporation. The active cell area is 10.5 mm² (3 mm x 3.5 mm).

Characterization techniques:

For the *XPS measurements,* the samples were sealed in an airtight container and shipped from Karlsruhe to Darmstadt. The container was then opened inside a nitrogen-filled glove box, the samples were mounted onto the XPS holder, and finally transferred to the XPS measurements chamber using a nitrogen-filled shuttle, so that any exposure to air in between the sample deposition and the XPS measurements is avoided. To be able to measure an SPV, the sample was contacted to the electrical ground of the XPS machine at the ITO front contact. The layers on top of the ITO were either scratched away using a doctor blade (in case of SnO_2 and the perovskites) or a mask was used during the deposition process (in case of NiO_x). All other layers on top of the ITO were therefore electrically floating so that an SPV can develop. The light measurements were always carried out before the dark measurements since the samples might degrade during the XPS measurements, which will lower the amount of SPV [157]. For the light measurements, a 50 W ECONLUX SolarRaptor tungsten high-intensity discharge (HID)-lamp was attached to one of the glass viewports of the measurements chamber at an 45° angle and a distance of around 50 cm. An estimation of the light intensity that will reach the

perovskite absorbers, when they are measured in the XPS chamber, is given in chapter 4.6. For the dark measurements the vacuum viewports were covered with aluminum foil and all light sources inside the measurement chamber were turned off. This included the hot-filament ionization gauge, which emits an amount of light that is not negligible during its operation. Since the heated cathode of the X-ray source will emit visible light as well, an aluminum window, which absorbs most of the visible light but will let the X-ray radiation pass, was installed in between the cathode and the sample (see chapter 2.6). All XPS measurements were acquired with a monochromatic XR6 X-ray source (Al Kα) with an excitation energy of around 1486.6 eV at a Thermo Fisher Escalab 250. The survey spectra were acquired with a pass energy of 50 eV, a step size of 0.5 eV, and a dwell time of 50 ms per measurement point. For each survey, only one scan was recorded. The detailed spectra were acquired with a pass energy of 10 eV, a step size of 0.05 eV, and a dwell time of 50 ms per measurement point. The number of scans was adjusted depending on the respective emission line so that a reasonable signal-to-noise ratio was achieved. The energy scale was calibrated using the Fermi level (0 eV), the Ag $3d_{5/2}$ emission line of metallic silver (368.26 eV), the Au $4f_{7/2}$ emission line of metallic gold (84.0 eV), and the Cu $2p_{3/2}$ emission line of metallic copper (932.67 eV). Before measuring the metallic samples, they were sputter-cleaned with an EX05 sputter gun using Argon ions at an energy of 3 kV. The VBM values of semiconductors were determined by applying a linear fit to the valence band onset and the background and taking the intersection between both lines. The Fermi level value of the Ag metal surface for the calibration was determined with a Sigmoid fit and taking the position where the intensity is 50%. Peak fitting was done in the Avantage software (v5.9911, Build 06601) by using a convolution between a Lorentzian and a Gaussian peak with a 30% ratio. For the background subtraction, the Smart Background was chosen in Avantage, which is a Shirley background with the additional constraint that the intensity of the background is always lower than the intensity of the measured data.

For the *XRD measurements,* the samples were removed from the glove box so that the measurements were performed in air. Measurements were performed at a Bruker D2Phaser system using Cu Kα radiation. A step size of 0.03° and a measurement time of 2 s per measurement point was chosen. All diffractograms were aligned with respect to the reflection of the underlying ITO substrate at 30.6°. The measurements were performed by Dr. Jonas Schwenzer at the Karlsruhe Institute of Technology and were already published in his Ph.D. thesis.

For the *UV/Vis measurements,* the samples had to be removed from the glove box and the measurement was performed in air. A Lambda 1050 spectrometer from PerkinElmer equipped with a deuterium arc lamp for the UV range and a halogen lamp for the visible and infrared range was employed. The measurement setup is equipped with an Ulbricht sphere, which allows recording the transmittance and reflectance. The absorbance is then calculated using the formula $A = 1 - T_M - R$. A step width of 2 nm was chosen for each measurement. The measurements were performed by Dr. Jonas Schwenzer at the Karlsruhe Institute of Technology and were already published in his Ph.D. thesis.

The *JV-measurements* were performed at an AAA LED solar simulator from Wavelabs with an approximate AM 1.5G spectrum. The irradiance of the AM 1.5G was calibrated by measuring a

calibrated Newport reference solar cell. A scan rate of 0.6 V/s was chosen, and the device was kept at a temperature of 25 °C during the measurement. For the measurement of the stabilized PCE values, the device was kept at a constant voltage, which means that no MPP tracking was performed. The measurements were performed by Dr. Jonas Schwenzer at the Karlsruhe Institute of Technology and were already published in his Ph.D. thesis.

3.3. Investigation of precursor materials

At first, the precursor materials used to synthesize the perovskite absorbers with varying cations will be analyzed using XPS. Knowing the binding energy positions of the precursor materials will help to confirm whether the synthesized perovskite films are phase pure or if they contain any leftovers of unreacted precursors. Furthermore, the XPS measurements of the precursor materials will be used as a reference to determine modified photoionization cross-section values to improve the accuracy of the stoichiometry calculation of the perovskite absorbers presented in the following chapters. The precursors used to synthesize the MAPI, FAPI, CsFAPI, MAFAPI, and CsMAFAPI perovskite absorbers are in this case lead iodide (PbI_2), cesium iodide (CsI), methylammonium iodide (CH_3NH_3I, MAI), and formamidinium iodide ($CH(NH_2)_2I$, FAI).

The XPS survey spectra of thermally evaporated PbI_2, CsI, MAI, and FAI films with an estimated thickness of around 30 nm, deposited on top of glass | FTO substrates, are presented in Figure 3.1. The grey shaded bars indicate the main emission lines of all elements present in the four precursor

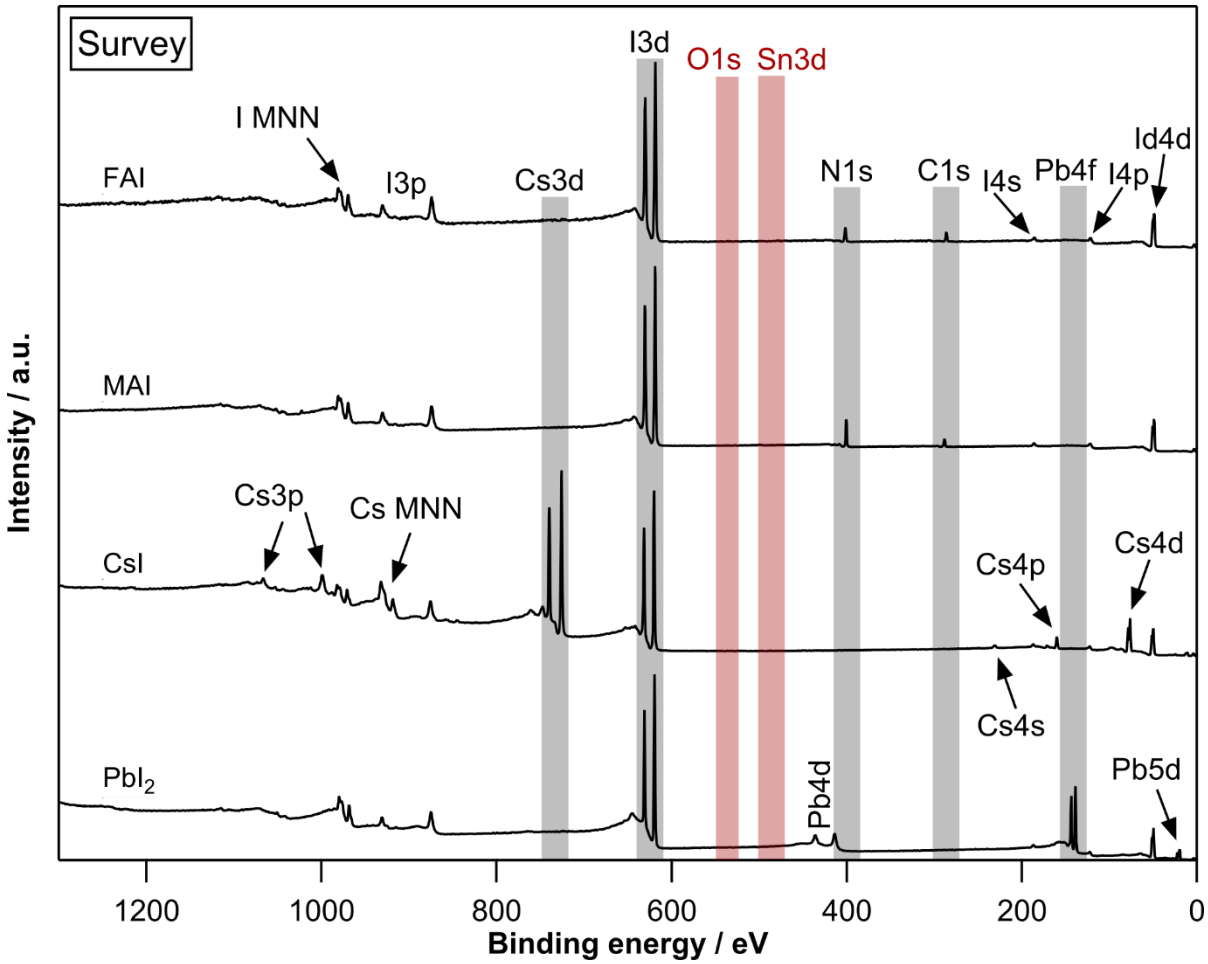

Figure 3.1: XPS survey spectra of thermally evaporated PbI_2, CsI, MAI and FAI films on top of FTO substrates measured without the samples being exposed to ambient atmosphere in between the film deposition and the measurement. The energetic position where an O1s and Sn3d emission line would be expected are marked in red. For a better comparison, the highest intensity of each spectrum has been normalized to 1 and an y-offset of 1.1 has been applied in between each spectrum.

Table 3.1: Emission line binding energy positions and valence band maximum positions of the four precursor materials used to deposit the MAPI, FAPI, MAFAPI, CsFAPI, and CsMAFAPI perovskite absorbers. All energy values are given in eV.

Material	$I3d_{5/2}$	N1s	C1s	$Cs3d_{5/2}$	$Pb4f_{7/2}$	VB
FAI	618.58	400.14	287.89	-	-	1.87
MAI	619.01	401.88	286.35	-	-	2.00
CsI	618.24	-	-	723.86	-	1.49
PbI_2	619.56	-	-	-	138.57	1.93

materials (Cs3d, I3d, N1s, C1s, and Pb4f). The energetic positions, where O1s and Sn3d emission lines would potentially appear are marked in red. Since no oxygen and tin are visible, it is assumed that for all four precursor materials a closed film without any pinholes has been achieved. Furthermore, the film thickness of each layer should be high enough to establish the bulk electronic properties so that a potential space charge region at the FTO | precursor interface does not affect the binding energy positions of the precursor film. For all deposited layers only the expected emission lines appear in the survey. The absence of carbon in the CsI and PbI_2 films and the absence of oxygen for all four materials confirm that the vacuum was always good enough so that an oxidation was avoided. The detailed spectra of the main emission lines along with the O1s emission line and the valence band regions are presented in Figure 3.3. Table 3.1 summarizes all emission line binding energy positions along with the valence band maximum positions.

The $I3d_{5/2}$ emission line and N1s emission line of MAI is shown in Figure 3.2 a) and b). Their symmetric line shape indicates that only one species of nitrogen and iodine is present in the thermally evaporated MAI layers. For MAI, the $I3d_{5/2}$ and N1s emission line appear at 619.01 eV and 401.88 eV, which means they only differ by 0.11 eV and 0.12 eV to the values reported by Dachauer [79] (618.9 eV for $I3d_{5/2}$ and 402.0 eV for N1s). Liu *et al.* [158] reported an $I3d_{5/2}$ emission line at around 619.8 eV and an N1s emission line at 403.0 eV, which is shifted by around 0.8 eV and 1.1 eV cases to higher binding energies compared to the values of Dachauer [79] and this work. Looking into a polymer database of Briggs *et al.* [159] the N1s binding energy position of a $-\boldsymbol{N}^{+}H_3$ functional group is reported to be positioned at around 401.46 eV, which is comparable to the value report in this work. The C1s emission line (see Figure 3.3 c) appears at 286.35 eV, which is close to the value of 286.50 eV reported by

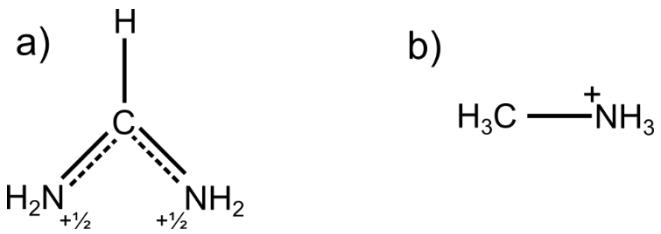

Figure 3.2: a) Hybrid structure of the FA^{+} cation where the positive charge is delocalized among both nitrogen atoms, resulting in a positive charge of +½ for each nitrogen atom, and b) Lewis structure of the MA^{+} cation where the single nitrogen atom carries a charge of +1.

Dachauer [79] and the binding energy of 286.22 eV of a carbon atom in a $\boldsymbol{C} - N^{+}H_3$ functional group reported by Briggs *et al*. [159].

To the best of our knowledge, XPS measurements of FAI have not been reported so far. The $I3d_{5/2}$ emission line of FAI appears at 618.58 eV, the N1s emission line at 400.14 eV, and the C1s emission line at 287.89 eV (see Figure 3.3 a) - c). Compared to MAI ($E_{\mathrm{B,MAI,N1s}} = 401.88$ eV), the N1s emission line of FAI is positioned at lower binding energies ($E_{\mathrm{B,FAI,N1s}} = 400.14$ eV), which allows to distinguish methylammonium from formamidinium by their N1s emission lines. The binding energy difference of 1.75 eV can be explained by the fact that both $\boldsymbol{C} - N$ bonds in the FA^{+} cation are equivalent, resulting in the positive charge being delocalized shared between both nitrogen atoms (see hybrid structure in Figure 3.2). Both nitrogen atoms carry therefore a net charge of +½, compared to the charge of +1 for the nitrogen atom in the MAI molecule and the N1s emission line of FA^{+} is shifted to lower binding energies.

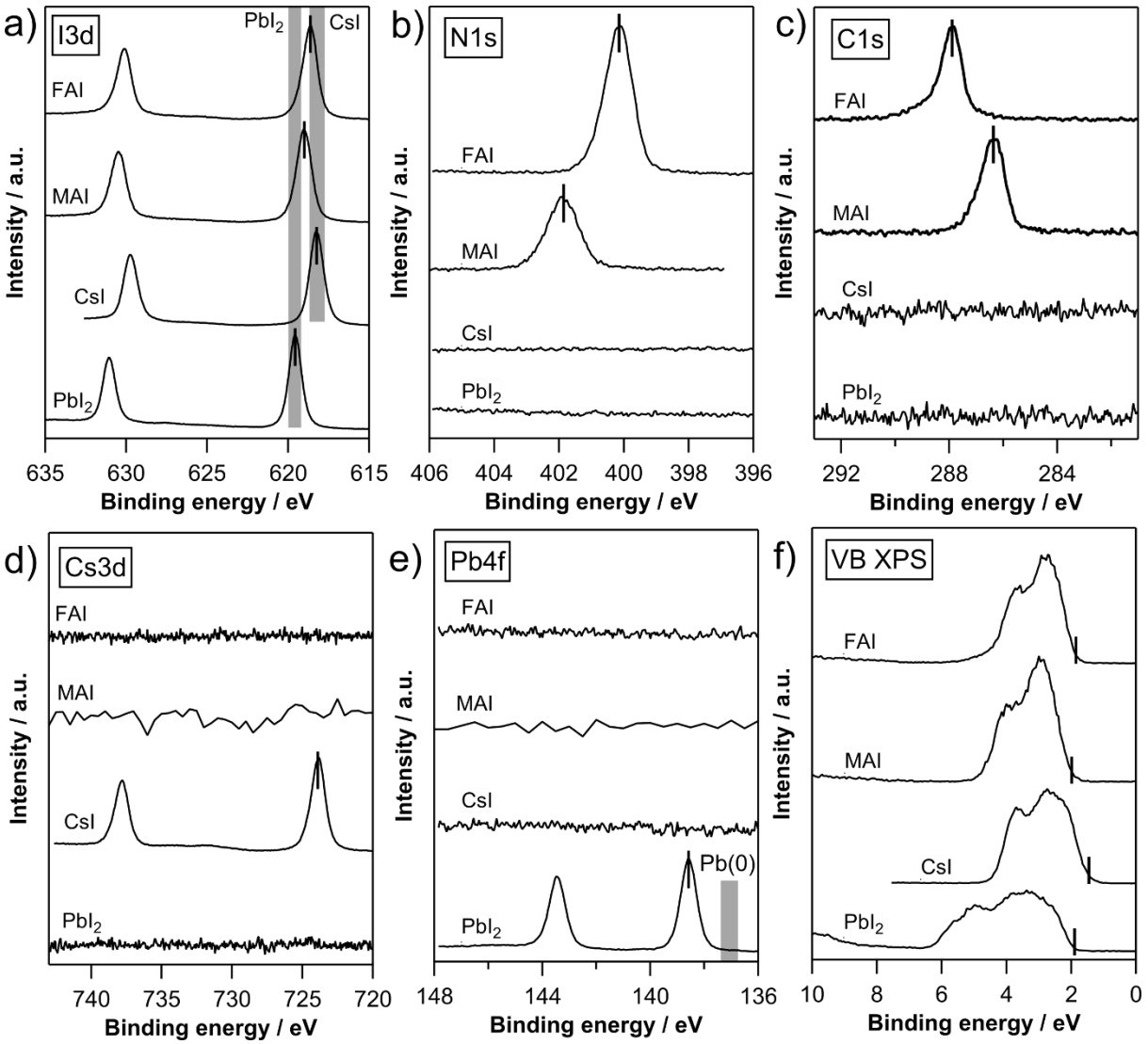

Figure 3.3: a) Detailed I3d, b) N1s, c) C1s, d) Cs3d, e) Pb4f emission lines and f) valence band regions of thermally evaporated PbI_2, CsI, MAI and FAI films on top of FTO substrates measured without the samples being exposed to ambient atmosphere. For a better comparison, all spectra have been normalized with respect to the I3d emission line.

The C1s emission line of FAI appears at higher binding energies of $E_{\mathrm{B,FAI,N1s}} = 287.89\ \mathrm{eV}$ compared to the C1s emission line of MAI ($E_{\mathrm{B,MAI,N1s}} = 286.25\ \mathrm{eV}$), due to the carbon forming two instead of one $C-N$ bonds with the more electronegative nitrogen atom (see Figure 3.2). The higher intensity of the N1s emission line of FAI compared to MAI can be explained by the fact that two nitrogen atoms instead of one are present in FAI. A more detailed discussion on the stoichiometry of the precursor materials is given below.

For PbI_2, the $Pb4f_{7/2}$ and $I3d_{5/2}$ emission lines appear at 138.57 eV and 619.56 eV (see Figure 3.3 a) and e), which agrees with previous XPS investigations reported in the literature [79,160]. The film appears to be free of any metallic lead, which is expected to appear at 136.9 eV (see Figure 3.3 e). Metallic lead has been frequently reported in lead halide materials [157,161–165]. For CsI the $Cs3d_{5/2}$ and $I3d_{5/2}$ emission line appear at 723.86 eV and 618.24 eV (see Figure 3.3 a) and d) which agrees with previous XPS investigations as well [166,167]. Compared to MAI and FAI, the $I3d_{5/2}$ emission line of PbI_2 appears at higher and the $I3d_{5/2}$ emission line of CsI at lower binding energies, which will allow discriminating residual PbI_2 and CsI in later-investigated mixed perovskites.

Besides identifying residual precursor materials, the reference measurements can also be used to optimize stoichiometry determination of metal halide perovskite samples. Determining stoichiometries from XPS measurements can be quite challenging since the intensity of the emission lines depends on multiple factors like the mean free path of the photoelectrons (IMFP), the transmission function of the spectrometer (TXFN), and the photoionization cross-sections (PICS) of the respective core level. (For a more extended discussion on the theoretical background of stoichiometry calculation using XPS the reader is referred to chapter 1.3.4.) If *ex-vacuo* samples with an adventitious carbon film on the surface are investigated, stoichiometry determination becomes even more complex, since the photoelectrons from each core level will be scattered inside the carbon layer, depending on their kinetic energy. The presented precursor materials are thermally evaporated and measured without exposing them to ambient atmosphere, meaning there is no detrimental influence of an adventitious carbon layer. Furthermore, the stoichiometry of MAI, FAI, PbI_2, and CsI is well defined, if no decomposition is observed. Since the N1s and the I3d emission lines appear symmetric for MAI and FAI it is assumed that the molecules did not decompose during the thermal evaporation.

Table 3.2 gives an overview of the calculated atomic percentages of the different precursor materials. An extended table that also includes the values for the energy correction ($KE^{0.6}$), the TXFN values, and the integrated and normalized peak areas is given in Table 9.3 in the Appendix. For PbI_2, the calculated atomic percentages (32.1% for Pb and 67.9% for I) are quite close to the expected values of 33.3% and 66.7%. A modified PICS for $Pb4f_{7/2}$ can now be determined so that the atomic percentages calculated using the modified PICS matches the expected atomic percentages. This results in a modified cross-section of 12.0 for the $Pb4f_{7/2}$ emission line. Looking at the two organic salts, a larger discrepancy between the calculated and the expected atomic percentages is observed (see Table 3.2). When using the classical Scofield factors, both materials appear nitrogen-deficient and show too much iodine. As for PbI_2, the cross-section of the $I3d_{5/2}$ emission line is kept the same and modified PICSs for N1s and C1s are determined. This results in a much lower modified PICS for N1s of 1.26 and 1.43 in the case of FAI and MAI, respectively, compared to the Scofield PICS of 1.8. The modified cross-sections of C1s

(0.844 for FAI and 0.929 for MAI) are slightly lower compared to the original value of 1.0. Average modified PICSs of 1.34 and 0.887 result for N1s and C1s, respectively. In chapter 3.5, the modified PICSs will be used to determine atomic ratios of different perovskite absorbers and the results will be compared to stoichiometry calculations by classical Scofield PICSs. It is emphasized that the modified PICSs are machine-specific and should only be applied for stoichiometry calculations of measurements that have been performed at the Escalab 250 XPS system at DAISY-SOL at the TU Darmstadt.

To summarize, the XPS measurements of the precursor materials have shown that it is possible to distinguish between the methylammonium (MA^+) and the formamidinium cation (FA^+) using XPS, due to a quite large binding energy difference for their N1s emission lines of 1.74 eV. This difference in binding energy could be explained by the molecular structure of both molecules. Furthermore, the measurements of PbI_2, MAI, and FAI were used to determine modified PICSs for the $Pb4f_{7/2}$, the C1s, and the N1s emission line, which, when applied to calculate the atomic percentages of MAI, FAI, and PbI_2, will give the atomic percentages expected from their molecular structure. In chapter 3.5 these modified PICSs will be used to determine atomic ratios of different perovskite absorbers and the results will be compared to stoichiometry calculations by classical Scofield PICSs.

Table 3.2: Calculated atomic percentages for the thermally evaporated precursor materials based on Scofield photoionization cross-sections (PICS) taken from the Avantage software and calculated modified PICS, that will give ideal stoichiometry when used to determine the atomic ratios of the thermally evaporated precursor materials. An extended table is given in the Appendix in Table 9.3. Values for the integrated areas are given in cps.

Sample	Emission Line	Scofield PICS	Calculated Atomic %	Ideal Atomic %	Modified PICS
PbI_2	$Pb4f_{7/2}$	12.73	32.1	33.3	12.0
	$I3d_{5/2}$	19.87	67.9	67.7	19.87
FAI	C1s	1.0	26.0	25	0.844
	N1s	1.8	43.1	50	1.26
	$I3d_{5/2}$	19.87	30.8	25	19.98
MAI	C1s	1.0	34.1	33.3	0.929
	N1s	1.8	29.2	33.3	1.43
	$I3d_{5/2}$	19.87	36.7	33.3	19.87
CsI	$Cs3d_{5/2}$	23.76	51.57	50	25.3
	$I3d_{5/2}$	19.87	48.43	50	19.87

3.4. Investigation of various perovskite absorbers on n-type and p-type substrates

In total, five different perovskite materials (MAPI, FAPI, MAFAPI, CsFAPI, and CsMAFAPI) on two different substrates (n-type SnO_2 and p-type NiO_x) are investigated. At first, XRD and UV/Vis measurements are performed, to confirm the presence of the perovskite phase. Then, XPS measurements of the perovskite absorbers on n-type SnO_2 are discussed and the influence of illumination during the XPS measurements is discussed to identify possible light-induced SPVs. The same XPS measurements are then repeated for perovskite absorbers deposited on p-type NiO_x. The XRD, UV/Vis, and XPS measurements are performed on separate perovskite samples, prepared with identical depositions parameters. As mentioned in the experimental part (see chapter 3.2) the XRD, UV/Vis, and JV-measurements were performed by Dr. Jonas Schwenzer at the Karlsruhe Institute of Technology and were already published in his Ph.D. thesis.

3.4.1. XRD and UV/Vis analysis

Figure 3.5 presents XRD measurements of the five different perovskite absorbers deposited on top of SnO_2. MAPI has been reported to show three different polymorphic structures: i) at low temperatures an orthorhombic crystal structure (space group $Pnma$) [168], that will ii) change at 162 K to a tetragonal crystal structure (space group $I4/mcm$) [169] and finally iii) at temperatures above 327 K a cubic crystal structure (space group $Pm\bar{3}m$) [169]. From a thermodynamic point of view, it is therefore expected that MAPI crystallizes at room temperature in the tetragonal phase, which has also been observed in the literature [125,170]. Even though most of the reflections of the cubic and tetragonal phases appear at similar angles, the tetragonal phase shows an additional (211) reflection at 23.5°. Another way to distinguish between both structures is in the range between 42.5° and 43.5°, where

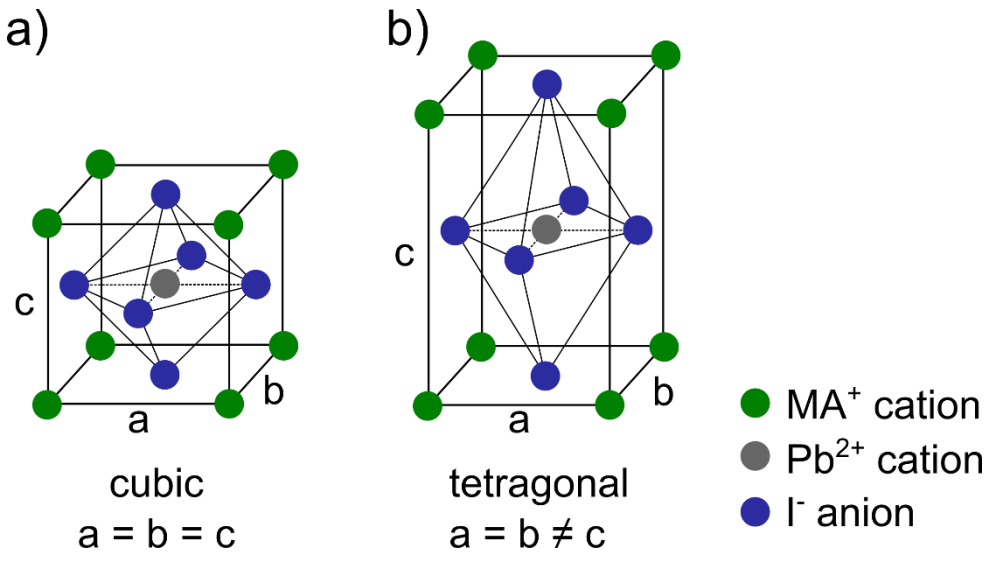

Figure 3.4: Illustration of the crystal structure of MAPI in the a) cubic phase and the b) tetragonal phase.

the cubic phase shows only one and the tetragonal phase two reflections. These areas, which help to distinguish between the cubic and the tetragonal phase, are highlighted in red in Figure 3.5.

The presented MAPI film crystallizes in the tetragonal crystal structure since the reflection at 23.5° is visible and two reflections are appearing between 42.5° and 43.5°. The reflection at 12.6° (yellow area) can be addressed to PbI_2 (hexagonal crystal structure with space group $P\bar{3}m1$) [171], most likely some residual material from the synthesis process. Interestingly, PbI_2 shows a strong (001) texture, since only the (001) reflection at 12.6° but not the main (101) reflection at 25.9° can be observed. Such a (001) texture has also been reported several times before in literature for various substrates [172–175]. Since this texture effect makes the (001) reflection appear stronger in intensity, comparing the absolute intensities of the (001) reflection of PbI_2 and the (110) reflection of MAPI will result in an overestimation of the amount of residual PbI_2. For determining the amount of residual PbI_2 inside the MAPI layer, the later-presented XPS measurement will only be considered (see Figure 3.10

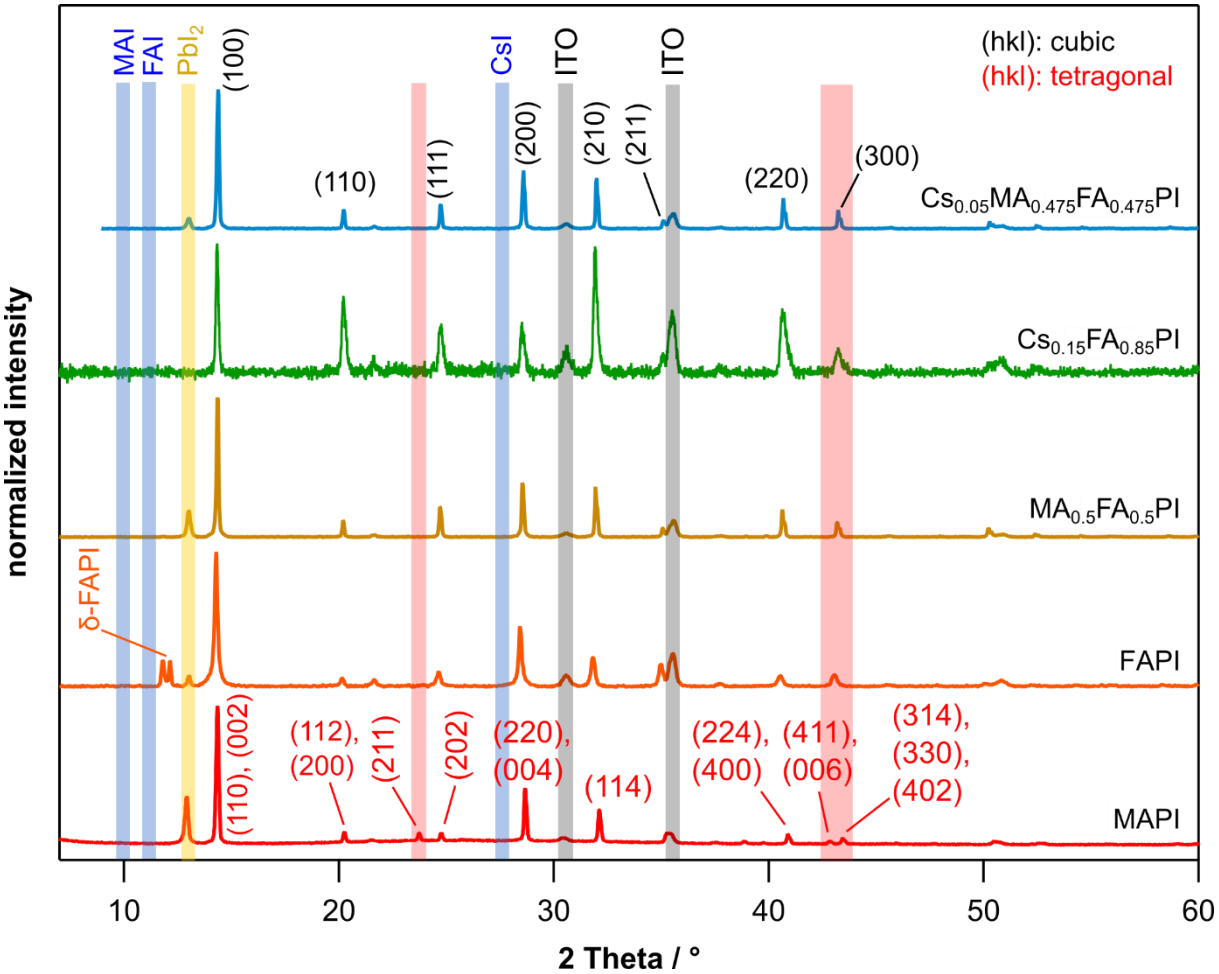

Figure 3.5: XRD measurements of MAPI, FAPI, MAFAPI, CsFAPI and CSMAFAPI perovskite absorbers. All XRD diffractograms have been normalized to 1 and an y-offset of 1.1 has been applied in between. The black (hkl) values on the top correspond to the tetragonal perovskite phase and the red (hkl) values at the bottom to the tetragonal perovskite phase. The areas marked in red at 23.5° and at 43.0° can be used to identify whether the perovskite crystallizes in the cubic or tetragonal phase. Measurements performed by Dr. Jonas Schwenzer.

and Figure 3.13). The synthesized MAPI crystallizes in the tetragonal crystal structure with small amounts of residual PbI_2 and no residual MAI.

For FAPI, the preferred photoactive cubic crystal structure (space group $Pm\bar{3}m$) forms only at elevated temperatures. This phase is also often referred to as α-phase or simply as "black phase", due to its color. Reported transitions temperatures are 60 °C [31], 127 °C [32], and 150 °C [33], in any case well above room temperature. The low-temperature δ-phase with a larger bandgap, also called "yellow phase", crystallizes in the non-perovskite hexagonal crystal structure (space group $P6m3c$). Through thermal annealing followed by rapid quenching of the FAPI films, the α-phase can be kinetically trapped at room temperature, even though it will transform back to the δ-phase eventually [176–178]. The cubic and hexagonal phases of FAPI can be well distinguished by XRD, since the main (100) reflection of the hexagonal phase appears at 11.8°, while the highest intensity (100) reflection of the cubic phase is found at 13.9°. The presented FAPI layers crystallize mainly in the preferred and photoactive cubic α-phase, visible through the strong (100) reflection appearing at 13.9°. A small amount of residual PbI_2 with a (001) texture can also be observed, however, even less than in the case of the MAPI perovskite. The weak reflections at 11.8° (labeled with δ-phase in Figure 3.5) indicate the presence of small amounts of the hexagonal FAPI phase. The second reflection at slightly higher angles (12.1°) could result from a second low-temperature hexagonal phase [32] but cannot be clearly identified. Thus, from the presented XRD data it can be concluded that the synthesized FAPI films are mainly forming the preferred photoactive cubic phase. Only small amounts of residual PbI_2 and the hexagonal FAPI phase are observed. As for the MAPI perovskite, no leftovers of the organic salt (FAI) can be observed in the XRD data.

Since for the mixed cation $MA_{0.5}FA_{0.5}PI$ perovskite a 1:1 molar ratio of MAI to FAI has been used during the synthesis, it can crystallize in either of the structures of the pure MAPI or FAPI perovskites, with the MA^+ and FA^+ cations both sitting on the A-site. To the best of our knowledge, it has not been reported that mixed cation perovskite will crystallize in a different structure than MAPI or FAPI. Since there is no reflection visible at around 23.5° (left red area) and only one reflection between 42.5° and 43.5° (right red area), it becomes evident that MAFAPI crystallizes in the cubic structure. Small amounts of residual PbI_2 with a (001) texture are also visible for the MAFAPI perovskite.

For $Cs_{0.15}FA_{0.85}PI$ and $Cs_{0.05}MA_{0.475}FA_{0.475}PI$ perovskite, the concentration of CsI in the precursor solution are much lower compared to MAI and FAI with 15% and 5%, respectively. It is therefore expected that both perovskites crystallize in the structure of MAPI or FAPI, with the MA^+, FA^+, and Cs^+ cations sitting on the A-site. For both perovskites, a cubic crystal structure is observed. For the CsFAPI perovskite, the (110) reflex at 20.3° and the (220) reflection at 41.3° are slightly stronger in intensity, indicating a slight texture. Small amounts of residual PbI_2 are identified for CsMAFAPI. No remaining halide salts (MAI, FAI, or CsI) appear in the XRD diffractogram. CsFAPI appears to be phase pure, without any leftover precursor material, not even PbI_2. The XRD analysis shows that all five perovskite materials have been successfully synthesized. Small amounts of residual PbI_2 have been detected for all samples, apart from CsFAPI.

To further confirm the presence of the perovskite phase and to determine the bandgaps, UV/Vis measurements have been performed (see Figure 3.6). For the single-cation perovskite absorbers MAPI

and FAPI, bandgap values of 1.59 eV and 1.51 eV are determined. This agrees well with previous measurements, where the bandgap of MAPI was reported to be 1.58 eV [24,135,179] and the bandgap of FAPI slightly lower, with values ranging between 1.45 eV and 1.51 eV [24,25]. The smaller bandgap of FAPI compared to MAPI is related to the FA^+ molecule being slightly larger than the MA^+ molecule, resulting in a distortion of the perovskite lattice [24] (see Figure 1.2 in chapter 1.1). For the mixed cation perovskites MAFAPI, CsFAPI, and CsMAFAPI, bandgap values of 1.53 eV, 1.53 eV, and 1.54 eV are determined, respectively. As expected, the bandgap values of the mixed cation perovskites are in between those of the pure MAPI and FAPI films. Figure 3.6 b) shows the recorded transmittance plotted against the wavelength of the incident light. Besides the absorption edge at around 780 nm (≈ 1.59 eV) which corresponds to the respective perovskite absorber, another feature at higher wavelengths of around 560 nm (≈ 2.32 eV) is visible. This second feature most likely results from residual PbI_2, which has already been observed in XRD measurements (see Figure 3.5). The optical bandgap of PbI_2 has been reported to be 2.35 eV (≈ 551 nm) [180]. Compared to the XRD measurements (see Figure 3.5), the second feature, which corresponds to residual PbI_2, appears therefore also for the CsFAPI perovskite.

The UV/Vis measurements are confirming the XRD results: in all five cases, the perovskite phase has been synthesized successfully. The measured bandgap values agree with values reported in the literature: MAPI shows the highest bandgap of 1.59 eV, FAPI the lowest bandgap of 1.51 eV, and the bandgaps of the mixed cation perovskites are positioned in between. Based on the Shockley-Queisser limit [26], perovskites solar cells employing FAPI as absorber material can theoretically achieve the highest PCE. Small amounts of residual PbI_2 can be observed in the XRD for all perovskite absorbers, except CsFAPI. UV/Vis shows an absorption feature at around 560 nm, corresponding to residual PbI_2 for all perovskite absorbers.

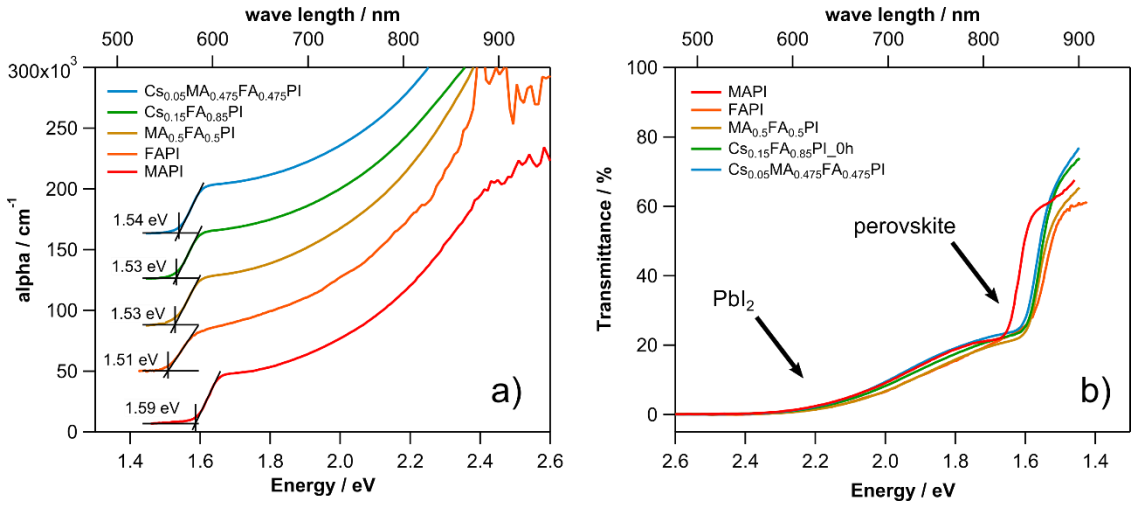

Figure 3.6: UV/Vis spectra of the five different perovskite thin films spin-coated on top of SnO_2. a) The absorption coefficient α, calculated from the measured transmittance and reflectance data after equation 1.9 plotted against the photon energy and b) the recorded transmittance plotted against the wavelength of the incident light. Measurements performed by Dr. Jonas Schwenzer.

3.4.2. Device performance

This chapter will shortly discuss the PCE values that can be reached when the perovskite absorbers are used in photovoltaic devices. As already discussed in the experimental procedure in chapter 3.2, the perovskite absorbers and the devices were prepared by Dr. Jonas Schwenzer from the Light Technology Institute at the Karlsruhe Institute of Technology. Figure 3.7 a) presents reverse and forward JV-scans for all five perovskites devices. Hysteresis is observed for all devices, which is a common problem for perovskite solar cells, making the comparison of the PCE of different devices more difficult. Factors that influence the hysteresis are for example the scanning direction and scanning speed [181,182], pre-treatments by illumination or applied bias [182,183], the device temperature [184], or the charge extraction layers used in the device [185–187]. Even though the origin of the hysteresis is still not completely resolved until now, several studies are indicating that the movement of ions and defects inside the perovskite absorber, most likely methyl-ammonium (MA^+) or iodine (I^-), might be the cause [188–193]. The PCE values were therefore determined from time-dependent PCE measurements that are shown in Figure 3.7 b). Since the measurements for the device with CsMAFAPI did not stabilize within 300 seconds, the data has been fitted using an exponential decay function PCE curve, and the stabilized value was determined by extrapolation. Details regarding the fitting method are given in Table 9.4 in the Appendix. Table 3.3 shows the stabilized PCE values, the J_{SC} values, and the V_{OC}values that were determined from the forward and reverse JV-scans. For all perovskite absorbers, PCEs of around 15% or higher can be achieved, proving that the perovskite layers are working reasonably well in solar cells. A direct comparison of PCE values to literature values is always complicated for perovskite

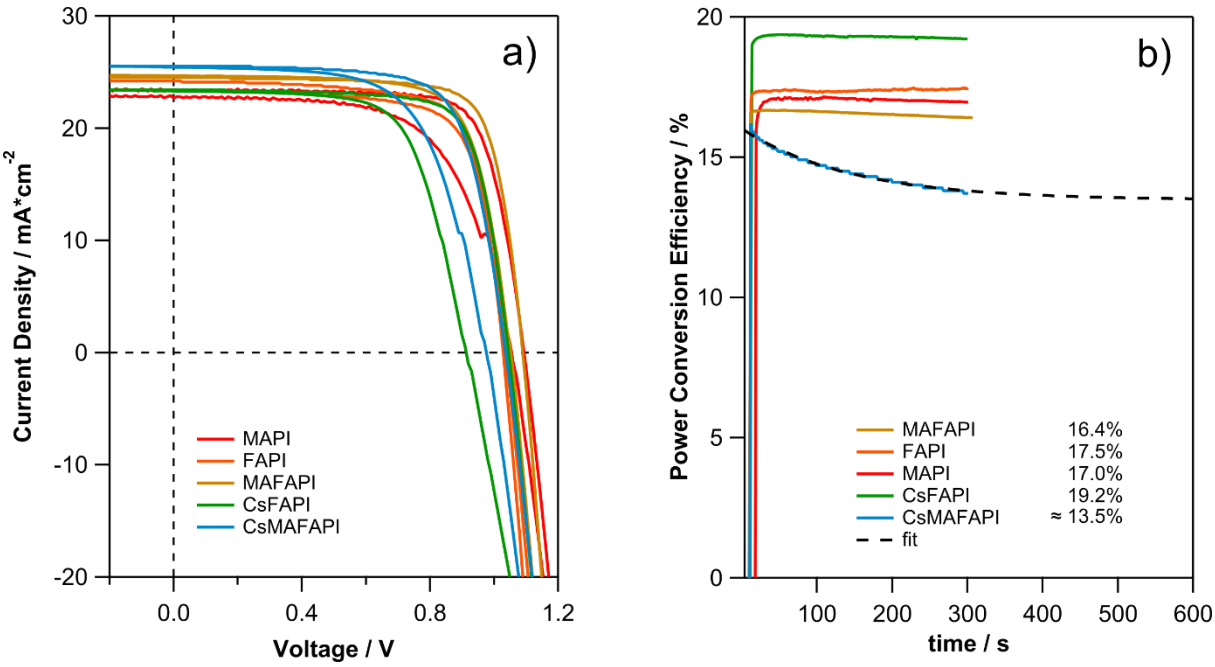

Figure 3.7: a) JV-scans of the of devices with the respective perovskite materials as absorber and b) the PCE measured over a duration of 300 seconds to determine the stabilized PCE values. The experimental data of CsMAFAPI has been fitted using an exponential decay function, the details of the fitting method are given in in the Appendix in Table 9.4. Measurements performed by Dr. Jonas Schwenzer.

solar cells since there is a huge variety of absorber compositions, deposition methods, charge transport materials, and other parameters like additives or buffer layers. Besides this, the PCE is strongly affected by the cell area. However, when simply comparing the PCE values to the world record of 24.1% from 2019 [114], the time when the devices were measured, the achieved PCE values seem satisfactory. It should be considered that record efficiencies are usually achieved for perovskite compositions with a mixture of iodine and bromide, instead of pure iodine as for the perovskites investigated in this work.

Table 3.3: PCE, short-circuit current, and open-circuit voltage values for devices with the different perovskite absorbers in the classical architecture with SnO_2 as substrate. The stabilized values for CsMAFAPI has been determined from an exponentially decaying fit function.

perovskite absorber	stabilized PCE	forward J_{SC} in $\frac{mA}{cm^2}$	reverse J_{SC} in $\frac{mA}{cm^2}$	forward V_{OC} in V	reverse V_{OC} in V
MAPI	17.0%	22.7	23.4	1.05	1.09
FAPI	17.5%	24.2	23.4	1.03	1.04
MAFAPI	16.4%	24.7	24.5	1.05	1.09
CsFAPI	19.2%	23.3	23.4	0.91	1.05
CsMAFAPI	≈ 13.5%*	25.4	25.5	0.98	1.04

3.4.3. How to perform real-dark measurements

As already mentioned in the motivation of this work in chapter 2.6, initial XPS measurements showed that even small amounts of background light can result in an SPV and therefore a shift of all PES emissions to higher or lower binding energies, depending on the polarity of the SPV. If this SPV remains unnoticed, PES spectra will eventually be misinterpreted, which is especially severe for valence band measurements. A wrong determination of the VBM will result in wrong doping levels. This chapter will therefore focus on systematically investigating the amount of SPV that can be induced by different light sources that are commonly appearing inside PES measurement chambers. The measurements were performed at the Escalab 250 system at DAISY-SOL since most of the XPS measurements discussed in this thesis were recorded there. For this experiment, a SnO_2 | MAPI | spiro-MeOTAD device stack is used. The SnO_2 layer was deposited by spin-coating and MAPI was deposited by thermal evaporation of PbI_2 and MAI as described in chapter 4.2. Finally, spiro-MeOTAD was deposited *in-vacuo* by thermal evaporation of spiro-MeOTAD and its dopant Li-TFSI. A detailed description of the experimental procedure is provided in chapter 5.2.

All UPS valence band measurements at different illumination conditions of the spiro-MeOTAD film are shown in Figure 3.8 a). The black curve shows the “real dark measurement”, where the sample is exposed to the lowest possible light intensity: the X-ray source, the ion gauge, and the chamber lightning are turned off and the glass viewports are covered with aluminum foil so that no light from outside the vacuum chamber can reach the measured sample. The VBM of spiro-MeOTAD appears in this case at 0.68 eV. When the same sample is measured with the ion gauge turned on (dark blue

curve), the VBM appears at 0.69 eV, showing that the light of the ion gauge can induce a small SPV. Figure 3.8 b) below shows a look into the XPS chamber through a glass viewport at the different illumination conditions. The red circle in the center of each image indicates the position of the measured sample. Since the ion gauge is positioned below the sample, only reflected light will reach the sample. After turning on the room lighting and removing the aluminum foil from the glass viewports (light blue curve), the VBM is shifted to 0.72 eV, which means that an SPV of 0.04 V is

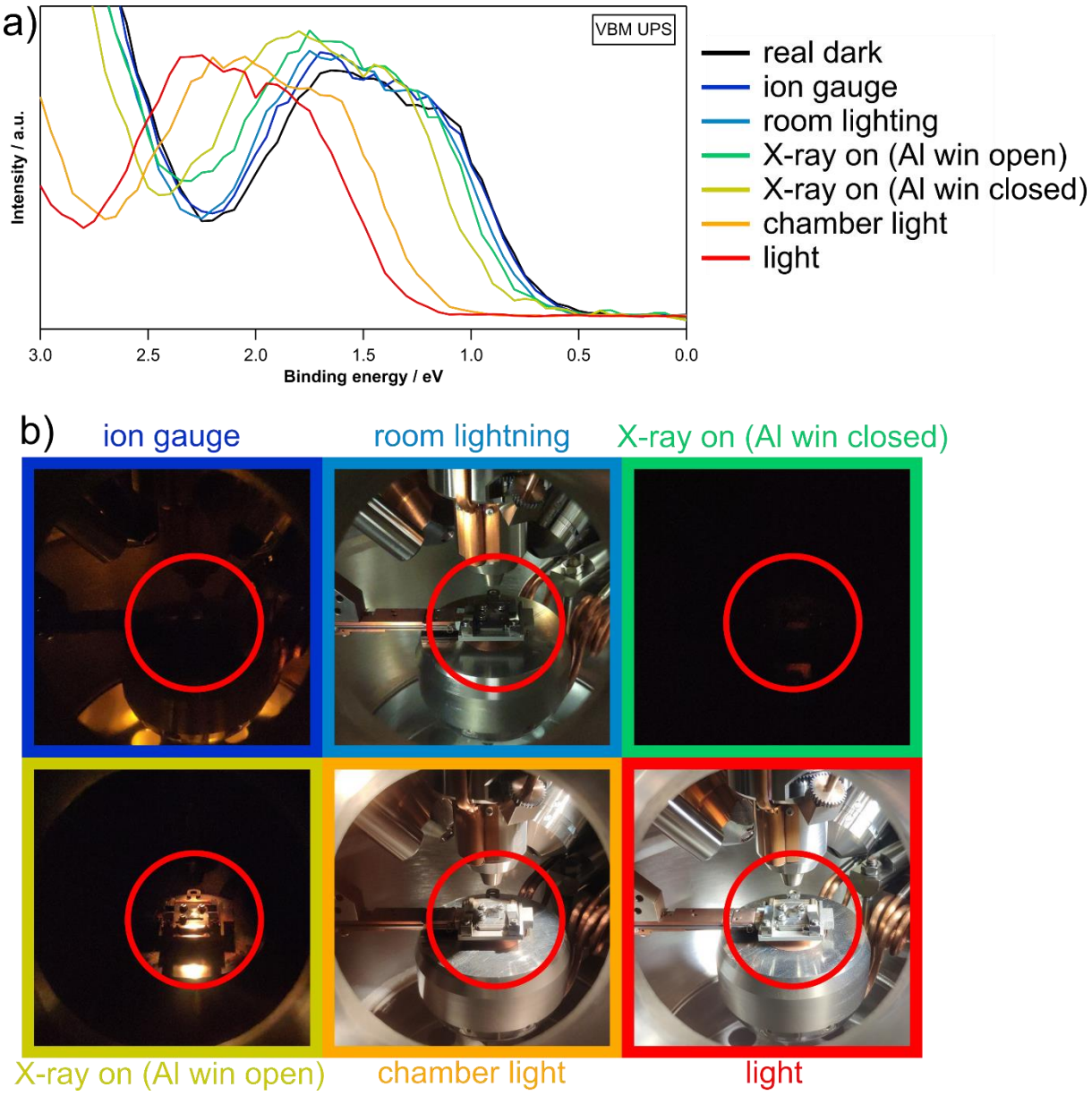

Figure 3.8: a) UPS valence band measurements of a SnO_2 | MAPI | spiro-MeOTAD sample that is showing an SPV at different illumination conditions and b) the look into the XPS chamber through a vacuum glass view port to visualize how the inside of the chamber looks like. The red circle in the center of each image indicates the sample positions. The dark blue color shows the situation with only the hot-filament ionization gauge turned on and the light blue color with the glass view ports uncovered so that the room lightning can shine into the chamber. Green and yellow represent the situation with the X-ray source turned on and the aluminum window closed and opened, respectively. Orange and red show the situation for the chamber light and the tungsten HID-lamp turned on.

present. Compared to the situation before, a small amount of light is now reaching the sample. With the X-ray source turned on during the measurement (green curve), but the aluminum window in between the cathode and the sample closed, the VBM is shifted even more and appears at 0.79 eV. When looking into the XPS chamber one can see that the amount of light reaching the sample is about the same as for the situation where only the ion gauge was turned on (dark blue). The larger shift of the VBM for the "X-ray on" compared to the "ion gauge on" situation proves that the X-ray radiation itself can induce an SPV which is not negligible with a value of 0.11 V. Even though source-induced SPVs have been reported frequently before [194–197], they are usually observed for measurements at synchrotrons, where the fluence is several orders of magnitudes higher than standard laboratory XPS machines. The yellow curve represents the same conditions as before but in addition with the aluminum window opened. The VBM appears at 0.88 eV and the induced SPV is increased to 0.20 V. The look into the chamber in Figure 3.8 b) shows that the light emitted by the cathode of the X-ray source will directly hit the sample when the aluminum window is not closed, explaining the strong induced SPV. When turning on the chamber light, which is usually used to position the sample in focus (orange curve), the VBM shifts drastically to a value of 1.20 eV, meaning that an SPV of 0.52 V is present. The sample is now directly illuminated with visible light. The red curve shows the "light measurement", with the tungsten HID-lamp turned on, pointing directly onto the sample. The same light source was also used for the light measurements of the SPV measurements presented in the following chapters of this work. The VBM appears now at 1.32 eV, which means that a maximum SPV of 0.64 V is present.

The presented results show that common light sources of standard laboratory XPS machines like the used Escalab 250 will induce significant SPVs and therefore binding energy shifts which can result in wrong data interpretation if the SPV remains unnoticed. Metal halide perovskite absorbers like MAPI are extremely sensitive to light, which is most likely caused by their exceptional high charge carrier lifetimes [66,67] (see chapter 1.1). The X-ray radiation of the X-ray source resulted in an SPV of 0.11 V, which corresponds to 17% of the SPV observed for maximum illumination. For XPS measurements of perovskite samples, it must therefore always be considered that an X-ray-induced SPV can be present. The X-ray-induced SPV value of 0.11 V was determined with an aluminum window positioned in between the heated cathode of the X-ray source and the measures sample. After removing the aluminum window, the SPV increased to 0.20 V and therefore 31% of the SPV that was observed for maximum illumination. It is therefore recommended to always perform XPS measurements with the aluminum window in the closed position. It is emphasized here, that laboratory XPS machines are not necessarily equipped with such an aluminum window. For the used Escalab 250 system, the Aluminum window was intentionally installed (see chapter 2.6), after it has been suspected that the light from the heated cathode induces an SPV. The chamber lightning did even result in an SPV of 0.52 V and therefore 81% of the SPV that was observed for maximum illumination. The SPV induced by the chamber lightning is therefore high enough, to make n-type perovskite absorbers on p-type substrates appear intrinsic and could be the reason why some research groups report a substrate-dependent doping of metal halide perovskite absorbers. It is not unreasonable to assume that an inexperienced experimentalist will run an XPS measurement with the chamber lightning stilled turned on. Finally, it

should be mentioned that the effects of the different light sources might vary depending on the XPS system that is used. Throughout this Ph.D. work, some measurements have been performed at a Physical Electronics VersaProbe 5000, where the hot-filament ionization gauge is positioned directly above the measured sample. This has the effect that much more light emitted from the ion gauge will reach the measured sample, which means that SPV induced by the ion gauge is also largely increased. In this case, the ion gauge must be switched off during the XPS measurements. Since the pressure value given by the ion gauge inside the XPS chamber is usually used as an interlock for powering the X-ray gun, additional modifications of the XPS system are required in this case.

By i) installing an aluminum window, ii) switching off the hot-filament ionization gauge, iii) switching of the chamber light, and iv) covering all windows of the XPS chamber, the amount of light inside the XPS chamber is now reduced to a minimum. For the dark measurements presented in the following chapters, the above-mentioned actions i) – iv) were always implemented.

It must be noted, however, that also the UV source in UPS measurements may induce an unknown SPV as well. In general, the amount of SPV induced by an illumination source does not only depend on the intensity of the illumination source, but also on the lifetime of the excited charge carriers and therefore the quality of the junction at which the charge carriers are separated. The amount of SPV induced by a certain illumination (compared to the maximum possible SPV) is therefore also sample-dependent. Measurements on high-efficient $MAPbBr_3$ perovskites presented in the Appendix of this work (see chapter 9.2) showed sometimes high UV-source-induced photovoltages. Any SPV can be estimated by shifts of the Fermi level of a metallic adsorbate layer, for example a gold film on top of the semiconductor device substrate, from its reference level $E_F = 0$.

For UPS measurements of full devices (of iodide-based perovskites) discussed in chapter 4.5 (see Figure 4.5), the Fermi level of the gold electrode appears at around 0 eV. It is therefore expected that the SPV induced by the UV source is rather small for the iodide-based perovskites investigated in this work.

3.4.4. XPS analysis of the classical architecture: dark measurements

After establishing that MAPI, FAPI, MAFAPI, CsFAPI, and CsMAFAPI perovskite absorbers have been synthesized successfully and showing that they perform reasonably well when used in photovoltaic devices, XPS measurements will be performed in the dark and under illumination, to determine the stoichiometries and the doping of each perovskite and to identify possible SPVs. This chapter will discuss perovskite absorbers in the classical architecture, with n-type SnO_2 as substrate. XPS measurements on the inverted architecture, with p-type NiO_x as substrate, will be presented in the following chapter. Figure 3.9 presents the valence band regions and Figure 3.10 the I3d, the N1s, the Pb4f, and the C1s emission line of all five different perovskite materials, along with the precursor materials PbI_2, CsI, MAI, and FAI. The measurements for the precursor materials are the same measurements that have been discussed before (see Figure 3.3). A summary of all binding energy

values of the core emission lines along with all differences between the core emission lines and the VBM values is given in Table 9.5 in the Appendix.

The VBM values of the presented XPS measurements will be determined using a logarithmic intensity scale. In the scientific community, it is still under debate whether a linear intensity scale, which is commonly used to determine the onset of the valence band for semiconductors, or a logarithmic intensity scale should be used for metal halide perovskites. Using a linear intensity plot for determining the VBM of MAPI and other metal halides perovskites gives in general a higher VBM value [135,198–200]. This can result in the unlikely case that the Fermi level is positioned inside the conduction band [136]. Endres *et al.* [199] have argued that in the case of metal halide perovskites an unusually low density of states exists at the onset of the valence band edge, which can be easily missed when a linear instead of logarithmic intensity scale is being used. For this reason, the valence band spectra of the perovskite absorbers in this work will be evaluated using a logarithmic intensity plot, since this method seems to give more reliable values. However, a disadvantage of using a logarithmic intensity plot is the fact that the background noise at energies below the VBM is largely increased, making it much more difficult to determine the onset. When looking at the valence band measurements of the different perovskite absorbers in Figure 3.9 it can be observed that the shape of the valence band region appears the same for all five materials and only small binding energy shifts are visible. Having the same shape of the valence band for all five perovskite materials indicates that the cation (MA^+, FA^+ or Cs^+) has no (or almost no) contribution to the valence band states. DFT calculations and UPS measurements in the literature have confirmed this observation: Tao *et al.* and Olthof *et al.* have both argued that the valence band of MAPI is mainly composed of I *5p* with some Pb *6s* hybridization and that the organic cation has only a minor influence [61,116]. The valence band onset for MAPI, MAFAPI, and CsMAFAPI appears at around 1.50 eV. For FAPI and CsFAPI it is slightly

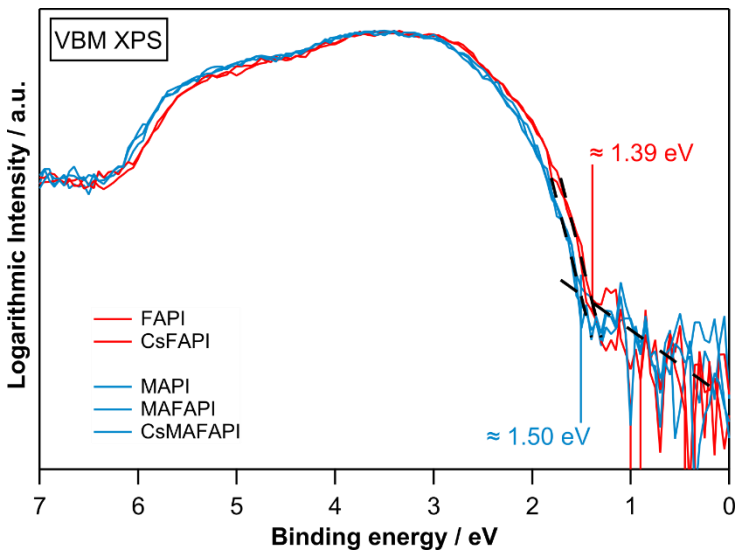

Figure 3.9: Normalized VBM measurements of the five different perovskites deposited by spin-coating on top of SnO_2 with a logarithmic intensity scale. FAPI and CsFAPI are shown in red and MAPI, FAPI and CsMAFAPI are shown in light blue. Due to the logarithmic plot, the background noise below 1.50 eV becomes much noisier, which makes a precise determination of the VBM more difficult.

shifted to lower binding energies, resulting in a VBM at around 1.39 eV. Given that the bandgaps of the perovskites are all around 1.5 to 1.6 eV (see Figure 3.6), the Fermi level is for all perovskite films quite close to the CBM, indicating an n-type semiconductor. This observation agrees with the substrate effect that has been proposed in the literature: on n-type substrates the perovskite grows as an n-type material as well. The different VBM values (1.39 eV vs. 1.50 eV) arise most likely due to slightly different defect doping levels of the respective perovskites. This can be verified by looking at the difference between the core levels and the VBM. Since this difference is a material constant, it will stay constant, even when the material is differently doped [201].

In the case of the $I3d_{5/2}$ emissions (see Figure 3.10 a), the difference to the VBM for the five different perovskite absorbers are almost identical with values of 618.14 eV, 618.16 eV, 618.14 eV, 618.13 eV, and 618.16 eV for MAPI, FAPI, MAFAPI, CsFAPI, and CsMAFAPI, respectively. The absolute binding energy positions are varying between 619.46 eV and 619.60 eV. For MAPI, MAFAPI, and CsMAFAPI they appear at 619.58 eV, 619.58 eV, and 619.60 eV, respectively. For FAPI and CsFAPI they are located at 619.49 eV and 619.46 eV, respectively. The binding energy position of MAPI is close to literature values that are typically reported for n-type MAPI [124,202,203]. All peaks appear to be symmetric without chemically shifted components, indicating the presence of only one oxidation state. Compared to the perovskite films, the $I3d_{5/2}$ emission line of MAI and FAI are located at lower binding energies (619.01 eV and 618.58 eV), which means that any residual MAI or FAI should be visible by an asymmetric peak with a shoulder to lower binding energies. Since the $I3d_{5/2}$ emission line of CsI is located at even lower binding energy values (618.20 eV), residual CsI will be even more evident. For PbI_2, the $I3d_{5/2}$ emission line is located at 619.56 eV and therefore almost exactly at the same binding energy position as the perovskites, making it impossible to identify residual PbI_2 through XPS by looking at the I3d orbitals. Based on the I3d emission lines, residual MAI, FAI or CsI can therefore be excluded; residual PbI_2 is possible but cannot be verified.

For the $Pb4f_{7/2}$ emission lines (see Figure 3.10 b), the differences to the VBM are quite similar as well with values of 137.21 eV, 137.27 eV, 137.23 eV, 137.23 eV, and 137.24 eV in the case of MAPI, FAPI, MAFAPI, CsFAPI, and CsMAFAPI, respectively. The absolute binding energy positions are 138.65 eV, 138.67 eV, and 138.68 eV for MAPI, MAFAPI, and CsMAFAPI, respectively. For FAPI and CsFAPI the $Pb4f_{7/2}$ emission lines are positioned at binding energies of 138.60 eV and 138.56 eV. For all five perovskites, the Pb4f emission lines are symmetric, which indicates once more the presence of only one oxidation state. Metallic lead, which is expected to appear at 136.9 eV [157,164], is not observed. The $Pb4f_{7/2}$ emission line of residual PbI_2 is located at 138.57 eV and therefore quite close to the binding energy positions of the perovskites, making it hard to identify residual PbI_2 based on the Pb4f core levels. Since also the I3d emission line of PbI_2 and the perovskites are quite close to each other, it is not possible to identify residual PbI_2 with XPS.

The N1s emission lines of the perovskite absorbers along with reference spectra of MAI and FAI are presented in Figure 3.10 c). For the MAPI and FAPI perovskite, a single symmetric peak can be observed which is located at a binding energy of 402.60 eV for MAPI and 400.85 eV for FAPI. The peak at higher binding energies corresponds to the MA^+ and the peak at lower binding energies to the FA^+ cation when they are incorporated into the perovskite structure [136,180,203]. This becomes even more

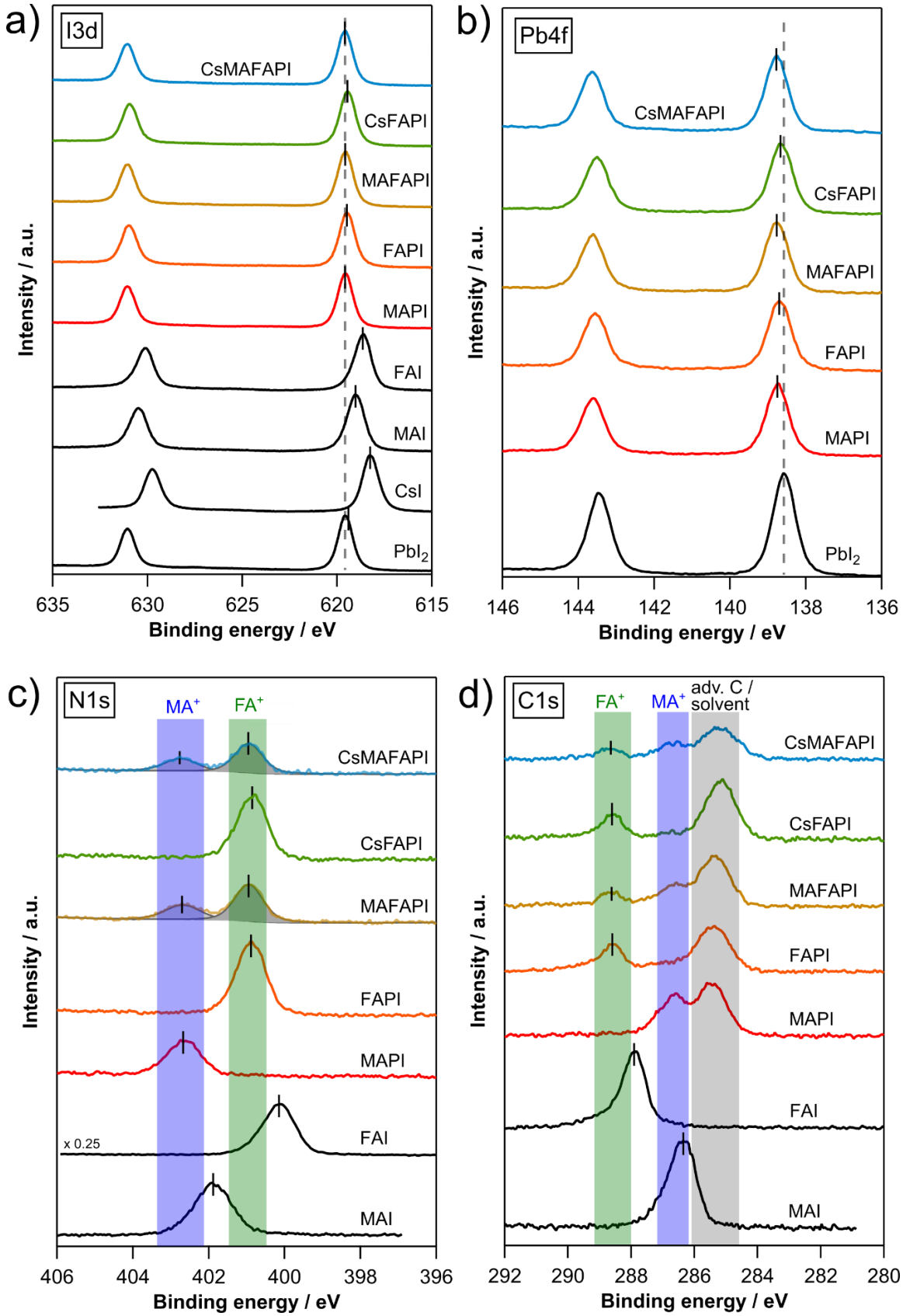

Figure 3.10: a) Detailed I3d b), N1s c), Pb4f and d) C1s emission lines of the five different perovskites deposited by spin-coating on top of SnO_2. The measurements of the thermally evaporated MAI, FAI, CsI and PbI_2 films from Figure 3.3 are shown on the bottom in black as reference. For a better comparison, all emission lines have been normalized with respect to I3d. The marker (1) indicates C1 emission from residual solvent material and / or adventitious carbohydrates, that do not appear in the thermally evaporated MAI and FAI thin films

evident when looking at the other perovskite materials: CsFAPI shows a single peak at 400.81 eV, MAFAPI two peaks at 400.91 eV, and 402.66 eV and CsMAFAPI two peaks as well, one at 400.90 eV and the second one at 402.71 eV. The binding energy difference between the N1s emission lines of the MA^+ and FA^+ cations when they are inside the perovskite matrix (MAPI vs. FAPI) compared to when they form the organic salts (MAI vs. FAI) are almost similar ($\Delta E_{\mathrm{B,N1s}} = 1.76$ eV for MAPI vs. FAPI and $\Delta E_{\mathrm{B,N1s}} = 1.74$ eV for MAI vs. FAI). When comparing the absolute binding energy positions of the N1s emission line of MAI to MAPI and FAI to FAPI they appear shifted by 0.74 eV and 0.76 eV to higher binding energies, respectively. These differences in binding energy of the N1s emission line of the halide salt compared to the perovskite may result from i) a chemical shift, caused by a different chemical environment of the MA^+/FA^+ cations inside the MAI/FAI and MAPI/FAPI matrices or ii) an electronic shift, due to different doping and therefore different Fermi level positions of the organic salts compared to the perovskites. To exclude the influence of an electronic shift, the emission lines of MAPI, FAPI, MAI, FAI are plotted in Figure 3.11 aligned with respect to the $I3d_{7/2}$ emission instead of the Fermi level as in Figure 3.10. The N1s line of MAI and MAPI appear now at the same binding energy

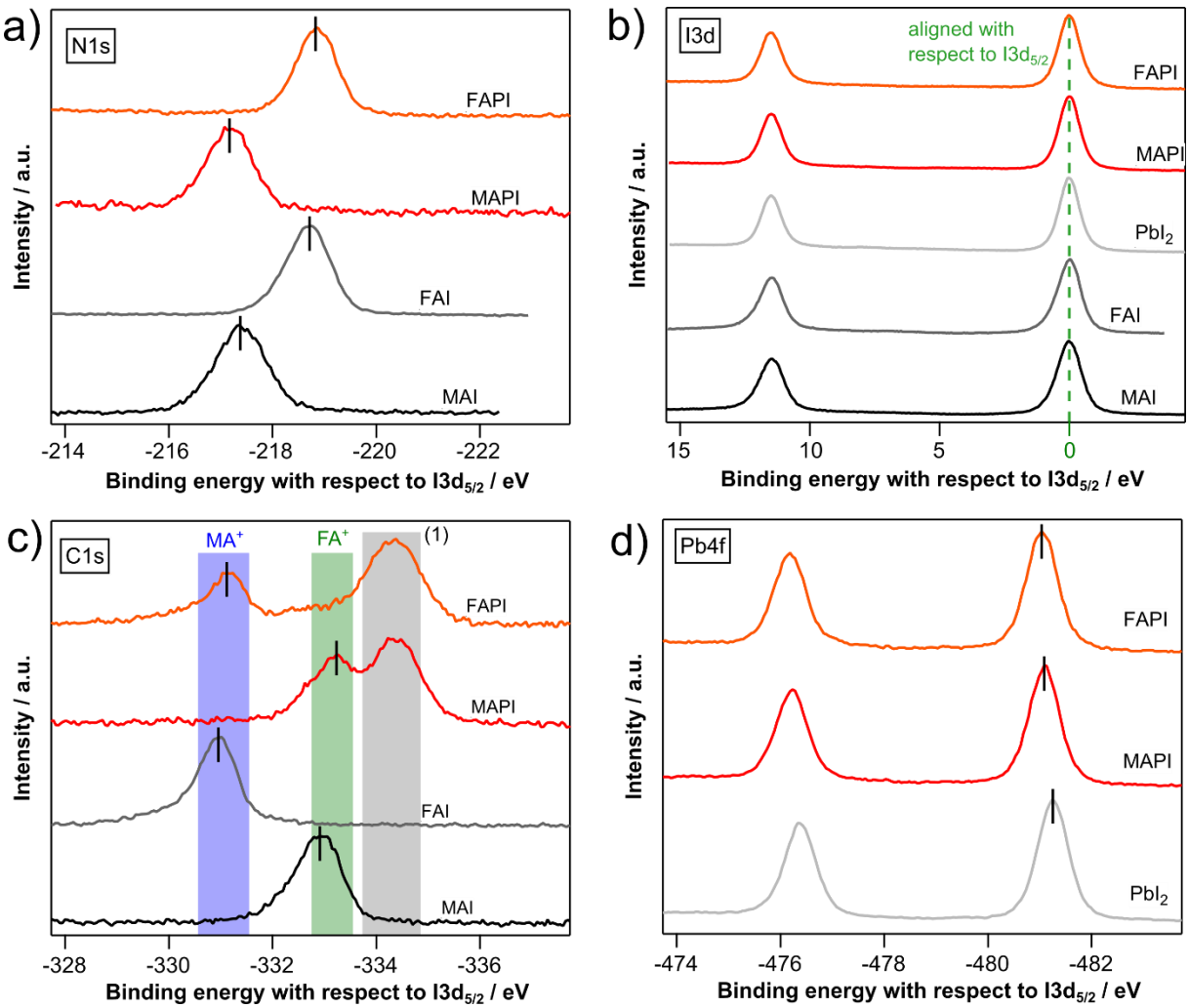

Figure 3.11: a) N1s, b) I3d, c) C1s and d) Pb4f emission lines of the spin-coated MAPI and FAPI perovskite films compared to the thermally evaporated MAI and FAI precursor materials. For reference all spectra are normalized to 1 and aligned to the $I3d_{7/2}$ emission line (see green dotted line in b).

position, indicating that there is no significant change in the chemical environment for the MA^+ cation, when it forms the MAI salt and when it forms the MAPI perovskite. The binding energy position is mainly a result of the intra-molecular bonding inside the MA^+ molecule. The same is true for the N1s emission line of the FAI salt when it is compared to the N1s emission line of the FAPI perovskite. By fitting the N1s emission lines that belong to both cations, the ratio between the number of MA^+ cations and FA^+ cations can be calculated. For MAFAPI an MA^+ to FA^+ ratio of 1.00 and for CsMAFAPI a ratio of 1.02 results, which is in both cases remarkably close to the 1:1 molar ratio of MAI to FAI inside the precursor solution used during the spin-coating process.

The C1s emission lines of the perovskite absorbers and the reference spectra of MAI and FAI are given in Figure 3.10 d) aligned with respect to the Fermi level. A broad feature at a binding energy of around 284.6 eV and 285.6 eV is visible for all five perovskite materials, here highlighted in grey and labeled with (1). This feature consists probably of more than one peak and originates from leftover solvent contributions of the spin-coating process and/or adventitious carbohydrate contaminations [203]. This is supported by the fact that no signal is observed in this binding energy region for the thermally evaporated and *in-vacuo* measured MAI and FAI films. For MAPI, a second emission at higher binding energies of around 286.6 eV is visible, which belongs to the MA^+ cation. This peak appears also for the $MA_{0.5}FA_{0.5}PI$, as well as the $Cs_{0.15}MA_{0.475}FA_{0.475}PI$ perovskite, in both cases, as expected from their stoichiometries, with lower intensity compared to MAPI. Similar values for the C1s binding energy position of MAPI have been reported in the literature [136,180,203]. FAPI shows a second peak at higher binding energies around 288.6 eV, which can be identified as the FA^+ cation. This peak can be observed for all other perovskite materials as well, except for MAPI. Figure 3.11 c) presents the C1s emission line of MAI, FAI, MAPI, and FAPI aligned with respect to the $I3d_{5/2}$ emission line. Similar to the N1s emission line, the peaks of the MA^+ and FA^+ cation in MAI/FAI and MAPI/FAPI are now situated at similar same binding energies.

To summarize, the XPS measurements of MAPI, FAPI, MAFAPI, CsFAPI, and CsMAFAPI grown on top of the EEL SnO_2 show an n-doping with VBM values ranging between 1.39 eV and 1.50 eV for all five perovskite absorbers. The absolute binding energy positions of the core level emissions of MAPI are in accordance with values that have been reported in the literature for n-type MAPI. For all other perovskite absorbers, literature reports of XPS measurements are limited, making a comparison of the binding energies of the core levels impossible. An n-doping of the perovskite absorbers when they are deposited on top of an n-type EEL like SnO_2 agrees with the theory of a “substrate effect”, which has been reported in literature several times before [127,132–134]. Since the parameters of the spin-coating process of the used perovskite absorbers have been optimized regarding achieving a maximum PCE, it is suggested that PCE-optimized perovskite absorbers tend to be n-doped. Besides that, it has been shown that exchanging the MA^+ cation with FA^+ or Cs^+ does not influence the shape of the valence band. This agrees with the predictions of DFT calculations in literature, where it is argued that the valence band is mainly composed of Pb 6*s* and I 5*p* orbitals and that the organic cation has only a minor influence [61,116]. Interestingly also the doping level is unintentionally similar for all five perovskites materials.

Furthermore, it was demonstrated that the MA^+ and FA^+ cations can be distinguished quite well in XPS from the binding energy position of their N1s and C1s emission lines. The difference in binding energy of the N1s and C1s emission lines in the MA^+ and FA^+ cations could be explained by their molecular structure. The comparison of the XPS measurements of the perovskite absorbers to the precursor materials MAI and FAI showed that residual MAI and FAI would be visible in XPS by evaluating the I3d and N1s emission lines. Residual PbI_2 is not that easy to identify, since the Pb4f and I3d emission lines of PbI_2 and n-doped perovskite absorbers are overlapping. The fact that no residual MAI or FAI has been observed in any of the five perovskite materials agrees with the XRD measurements presented before (Figure 3.5).

3.4.5. XPS analysis of the inverted architecture: dark measurements

In the previous chapter, XPS measurements have shown that several different perovskites absorbers (MAPI, FAPI, MAFAPI, CsFAPI, and CsMAFAPI) are n-doped when they are deposited on top of n-type SnO_2. The same perovskites will now be investigated on top of p-type NiO_x, meaning in the inverted architecture. Based on literature reports, it is expected that metal halide perovskites are intrinsic when they are deposited on p-type substrate, such as the investigated NiO_x. The respective XPS VBM and core level measurements of the five different perovskite absorbers in the dark are shown in Figure 3.12 and Figure 3.13. It is important to mention here, that prior to the dark measurements, the samples have already been measured while being illuminated, to determine a possible SPV. The light measurements have been performed before the dark measurements since metal halide perovskite samples tend to degrade during XPS measurements through releasing organic components

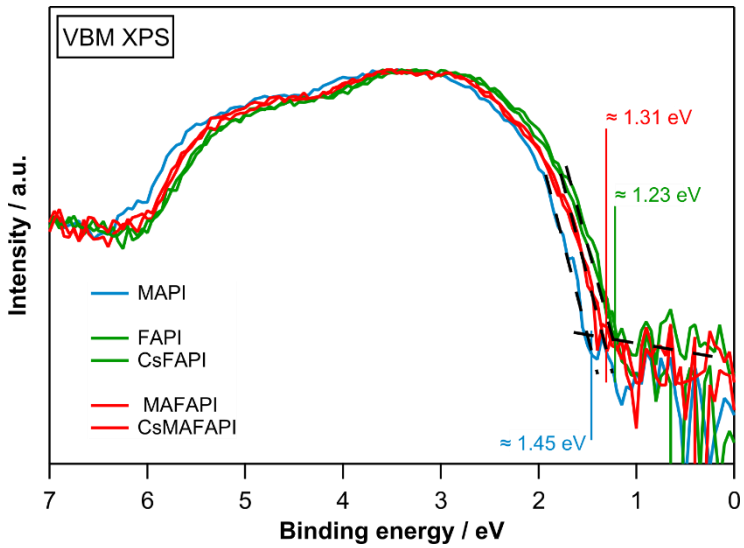

Figure 3.12: Normalized VBM measurements of the five different perovskites deposited by spin-coating on top of NiO_x with a logarithmic intensity scale. MAPI is shown in blue, FAPI and CsFAPI are shown in green and MAFAPI and CsMAFAPI are shown in red. Due to the logarithmic plot, the background noise below 1.50 eV is much noisier, which makes a precise determination of the VBM more difficult. For a better comparison, all spectra have been normalized.

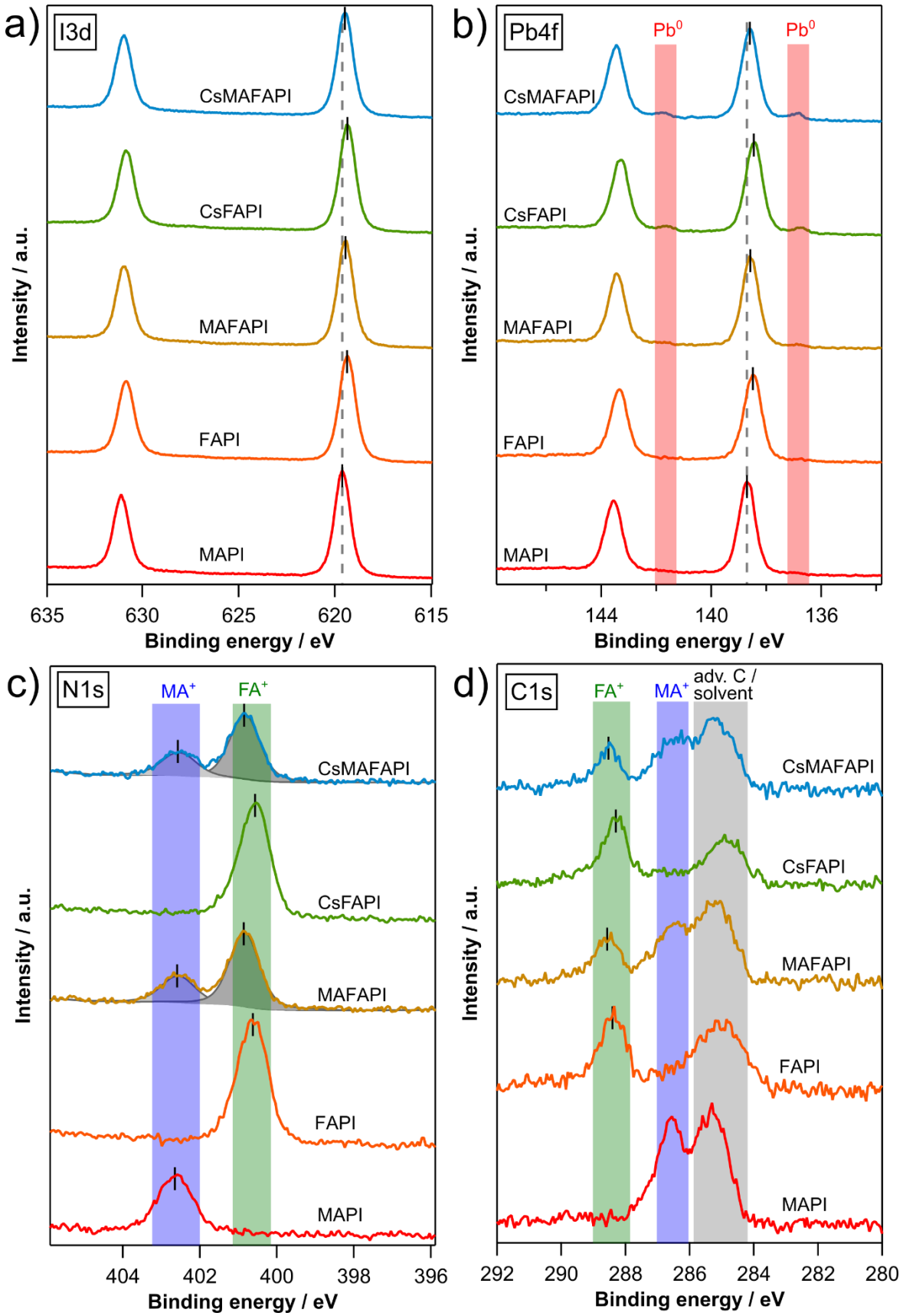

Figure 3.13: a) I3d emission lines, b) Pb4f emission lines, c) N1s emission lines and d) C1s emission lines of MAPI, FAPI, MAFAPI, CsFAPI and CsMAFAPI perovskite films deposited by spin-coating on top of p-type NiO_x. For a better comparison, the intensities of all spectra are aligned with respect to the I3d emission line.

and a reduction of Pb^{2+} to Pb^0 [157]. Since a degraded perovskite sample might show a decreased SPV, light measurements have always been performed before the dark measurements. For improved comprehension, the dark measurements are still discussed first. The light measurements will be discussed in chapter 3.4.6. All binding energy values of the core emission lines along with all differences between the core emission lines and the VBM are given in Table 9.5 in the Appendix. From the logarithmic valence band plots, VBM to Fermi level differences of around 1.45 eV, 1.23 eV, 1.31 eV, 1.23 eV, and 1.31 eV can be extracted for MAPI, FAPI, MAFAPI, CsFAPI, and CsMAFAPI, respectively. These VBM values are in the same range as for the perovskites deposited on top of SnO_2 (1.39 eV to 1.50 eV, see Figure 3.9) and are therefore representative for n-type perovskite as well. Perovskites grown on p-type substrate showing n-type doping are contradicting the theory of a "substrate effect", which has been proposed in literature several times before [127,132–134]. According to the substrate effect one would expect intrinsic or slightly p-doped perovskites when they are deposited on a p-type substate like NiO_x, which would position the VBM to Fermi level difference into a range of 0.7 eV to 0.9 eV. This range is significantly lower than the observed values of 1.23 eV to 1.45 eV.

When looking at the $I3d_{5/2}$ emission lines, shown in Figure 3.13 a), they appear at binding energy values of 619.61 eV, 619.36 eV, 619.46 eV, 619.34 eV, and 619.48 eV and therefore at an average value of 619.45 eV. This average binding energy of the $I3d_{5/2}$ emission line of 619.45 eV is 0.09 meV lower compared to the average binding energy of the $I3d_{5/2}$ emission lines of the perovskites deposited on SnO_2 (619.54 eV). The average energy difference between the $I3d_{5/2}$ emission lines and the VBMs are almost identical with 618.15 eV for perovskite deposited on SnO_2 and 618.13 eV on NiO_x. Thus, the above-mentioned difference in the absolute binding energy values of the $I3d_{5/2}$ emission lines of 0.09 meV should be caused by a slightly stronger unintentional n-doping for the perovskite deposited on SnO_2 compared to the perovskite on NiO_x. However, the doping difference on the n-type and p-type substrate of 0.09 eV is much lower compared to the values that are usually reported in the literature: for example 0.7 eV [133], 0.59 eV [136], 0.66 eV [135], or 0.62 eV [132]. Therefore, one can conclude that the perovskites on NiO_x are also n-doped, just slightly less n-doped as compared to those on SnO_2.

The Pb4f emission lines are presented in Figure 3.13 b): binding energy values of 138.69 eV, 138.47 eV, 138.57 eV, 138.44 eV, and 138.59 eV can be identified for the $Pb4f_{7/2}$ emission lines. This results in an average binding energy value of 138.55 eV for the $Pb4f_{7/2}$ emission lines, which is 0.08 meV lower than the average binding energy of the $Pb4f_{7/2}$ emission lines when the perovskites are deposited on top of SnO_2. As already observed for the $I3d_{5/2}$ emissions, the average difference between the $Pb4f_{7/2}$ emissions and the VBMs of all five perovskites is with a value of 137.23 eV almost identical to the average difference of the perovskites deposited on top of SnO_2 (137.24 eV). The two low-intensity peaks at binding energies of around 136.7 eV and 141.7 eV (here highlighted in red) correspond most likely to metallic lead [157,163], which has been observed in XPS measurements in the literature as well. Literature studies have shown that metallic lead is caused by prolonged exposure of metal halide perovskites to ultra-high vacuum and simultaneous exposure to electromagnetic radiation like X-rays, UV light, or visible light [157,162,164]. Since the dark measurement have been performed after the light measurements, the observed metallic lead is most likely caused by the light measurements.

The N1s emission lines for the five different perovskite absorbers deposited on top of NiO_x are shown in Figure 3.13 c). As already shown in chapter 3.4.3 when discussing the XPS measurements of the perovskites deposited on SnO_2 (see Figure 3.10 b), the N1s emission line of the MA^+ and FA^+ cation can be distinguished easily. Average binding energies of 402.59 eV and 400.78 eV can be calculated for the MA^+ and the FA^+ cation, which are again 0.07 eV and 0.09 eV lower than the average binding energy values of the perovskites deposited on SnO_2. The average difference between the N1s emission lines and the VBMs is 401.23 eV for the MA^+ cation and 399.49 eV for the FA^+ cation. Both values are comparable to what has been observed for the perovskite on SnO_2: 401.22 eV for MA^+ and 399.48 eV for FA^+. The slight difference in the absolute N1s binding energy values between the perovskites deposited on NiO_x and SnO_2 may be caused by a slightly less n-doping of the perovskites deposited on NiO_x. By individually fitting the N1s emission lines of the MA^+ and the FA^+ cation of MAFAPI and CsMAFAPI, MA^+ to FA^+ ratios of 0.83 and 0.85 are determined, respectively. Both perovskite samples are thus showing a slight MA^+-deficit compared to the 1:1 ratio of MA^+ to FA^+ in the precursor solution used during the spin-coating of the perovskite films. These small variations may result from the light measurements that have been performed before the dark measurements (see the first paragraph of this chapter), which may lead to a partial loss of MA^+. For multiple-cation perovskites, MA^+ has indeed shown to be the weakest link [41].

In Figure 3.13 d) the C1s emission lines for the five perovskite absorbers deposited on top of NiO_x are presented. A broad feature appears for all perovskites between 284 eV and 286 eV, here highlighted in black, which originates from leftover solvent of the spin-coating process and/or adventitious carbon contaminations. The C1s emissions line of the MA^+ cations and the FA^+ cations appears at binding energies of around 286.6 eV and 288.6 eV, respectively, which agree to the observations of perovskites deposited on top of SnO_2 (see Figure 3.10 d).

In summary, it has been demonstrated that all five perovskite absorbers grow unintentionally n-doped when they are deposited on top of p-type NiO_x, with VBM values ranging from 1.23 eV to 1.45 eV. This can be further confirmed when looking at the core level emission lines: When comparing the absolute binding energy positions of the core emission lines of the perovskites on NiO_x to those deposited on SnO_x, they appear shifted to lower binding energies by 0.08 eV on average for the NiO_x samples. This shift is consistent for the I3d (0.09 eV), the Pb4f (0.08 eV), the N1s emission lines (0.08 eV), and the VBM values (0.07 eV). The material-specific energy differences between the core emission lines and the VBM values are almost identical for both substrates: for $I3d_{5/2}$, $Pb4f_{7/2}$, and N1s they differ by 0.02 eV, 0.01 eV, and 0.02 eV, respectively, and are therefore below the XPS resolution. It is concluded that the perovskite absorbers are n-doped when deposited on SnO_2 and NiO_x substrates, meaning the substrate does not influence the doping of the perovskite. To further investigate the origin of the claim that the substrate will affect the doping of the perovskite, the following chapter will discuss XPS measurements while the sample is being illuminated. This will allow the identification of possible SPVs, which can shift peaks from their equilibrium binding energy position. If an SPV remains unnoticed, XPS spectra can be misinterpreted, resulting in a wrong determination of the doping level.

3.4.6. Comparison of photovoltage measurements on n- and p-substrates

The XPS measurements of the two previous chapters have demonstrated, that the five different investigated perovskite absorbers are growing n-doped on n-type SnO_2 and p-type NiO_x. Since this contradicts the idea of a substrate effect, XPS measurements under illumination have been performed on the same samples. XPS measurements, while the sample is illuminated, will allow identifying possible SPVs since they will result in a shift of the emission lines from their equilibrium position. Consequently, misinterpretation of the spectra may occur, if the SPV remains unnoticed. A more detailed discussion regarding the cause of SPVs, their influence on PES spectra, and experimental procedures is given in chapter 1.6.3. For the light measurements, a 50 W ECONLUX SolarRaptor tungsten high-intensity discharge (HID)-lamp was attached to one of the glass viewports of the measurement chamber with a 45° angle at a distance of around 50 cm. For the dark measurements, the vacuum viewports were covered with aluminum foil and all light sources inside the measurement chamber were turned off. This included the hot-filament ionization gauge, which emits an amount of light that is not negligible during its operation. Since the heated cathode of the X-ray source will emit visible light as well, an aluminum window, which absorbs most of the visible light but will let the X-ray radiation pass, has been installed in between the cathode and the sample (see chapter 2.6).

Since it has been reported that the exposure of metal halide perovskite to light and ultra-high vacuum conditions can result in degradation [157,164], exposure times to light have been kept as short as possible. For this reason, only the I3d and the Pb4f emission line have been recorded. Figure 3.14 shows the $I3d_{5/2}$ emission lines of the five different perovskite absorbers in the dark (black lines) and

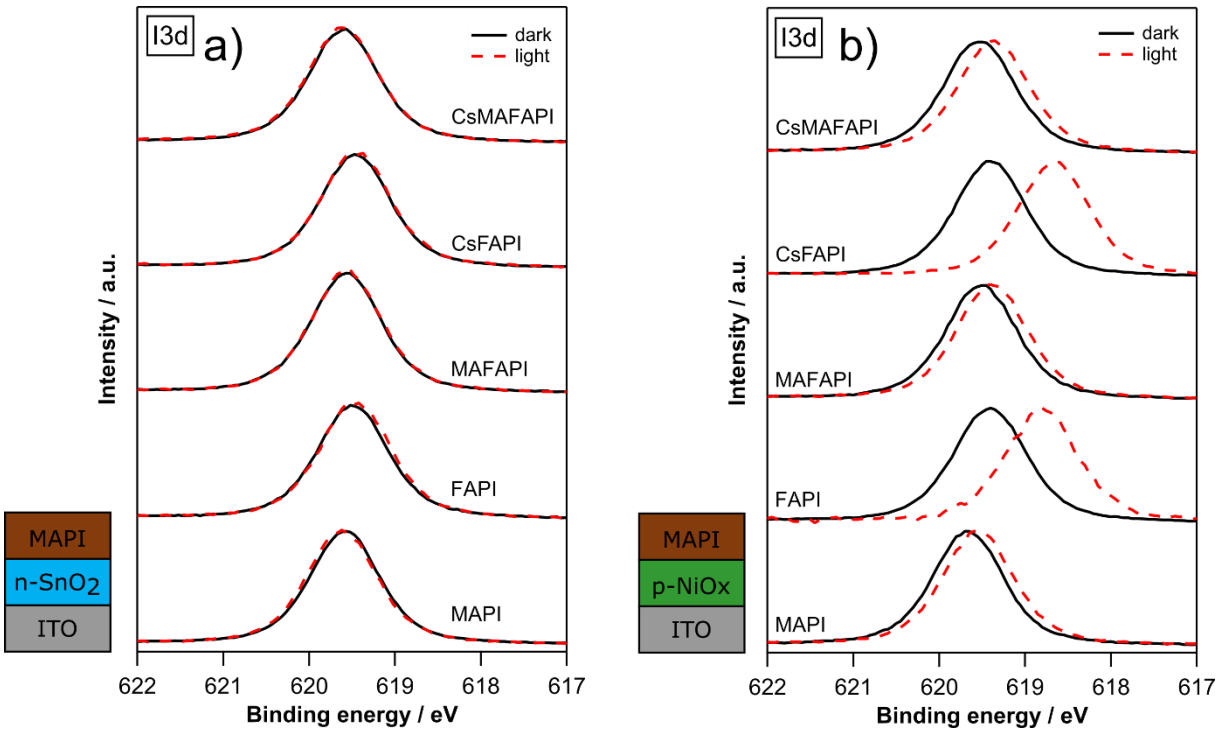

Figure 3.14: a) I3d emission lines of the spin-coated perovskite absorbers deposited on top of SnO_2 and b) on top of NiO_x. The black solid line represents the dark measurement and the red broken line the light measurement. Light measurements have always been performed before the dark measurements.

under illumination (red broken lines) with the classical architecture devices on n-SnO_2 substrates on the left (Figure 3.14 a) and the inverted architecture devices with p-NiO_x as a substrate on the right (Figure 3.14 b). For the classical architecture devices, there is no shift or only a negligible shift observable for all five perovskite absorbers: MAPI, FAPI, MAFAPI, CsFAPI, and CsMAFAPI are showing light-induced binding energy shifts of 0.04 eV, -0.02 eV, -0.02 eV, -0.01 eV, and 0.01 eV, respectively. A positive value means a shift to higher binding energies while a negative value indicates a shift to lower binding energies. The average binding energy shift of all five perovskite absorbers is with a value of -0.0012 eV far below the resolution of the XPS setup. It can therefore be concluded that in the case of SnO_2 as a substrate no light-induced shift and therefore no SPV is observed.

When looking at the I3d emission lines of the perovskite absorbers on NiO_x in Figure 3.14 b), a clear binding energy shift towards lower binding energies can be observed for all five perovskite absorbers when they are being illuminated. The I3d emission line of the illuminated MAPI, MAFAPI, and CsMAFAPI samples are shifted by -0.11 eV, -0.13 eV, and -0.16 eV, respectively. For the methylammonium-free perovskites FAPI and CsFAPI, the binding energy shifts are clearly larger with values of -0.62 eV and even -0.74 eV. When the samples were re-measured in the dark, the emission lines were shifted back to their original binding energy positions, as one would expect it. The light-induced binding energy shifts to lower binding energies are a clear indication for a negative SPV for perovskite absorbers that are deposited on top of p-type NiO_x. Especially the SPV-induced shifts for the methylammonium-free perovskites (-0.62 eV and -0.74 eV) are comparable to the reported doping differences between perovskites on n-type and p-type substrates (for example -0.7 eV [133], -0.59 eV [136], -0.66 eV [135] or -0.62 eV [132]). In these literature reports it is claimed that the doping differences are caused by the substrate (n-type vs. p-type). Any influence of light, possible SPVs, or the conditions of the sample, whether it is illuminated or not, are not addressed and have probably been ignored.

It is emphasized that for the measured perovskite absorbers, even vanishingly small intensities of background light would result in a partial SPV. The issue that the perovskite samples are too light-sensitive to be treated like “normal samples” is discussed in more detail in chapter 3.4.3, where an SPV-active sample is exposed to different light sources and measured with XPS. This experiment basically proves that even low light intensities like the light emitted from the cathode of the X-ray source or the hot-filament ionization gauge which measures the pressure inside the XPS chamber, can emit enough light to unintentionally induce an SPV in the perovskite samples and therefore result in a binding energy shift of all XPS spectra. More intense light sources like the chamber light or the lightning from the room illumination shining through uncovered glass viewports can result in SPVs that are almost as high as the maximum SPV that was observed when illuminating the samples with the HID-lamp used in the light measurements. It is therefore concluded that studies that report a substrate-influenced doping of the perovskite absorber probably suffer from unnoticed SPVs for perovskites on p-type substrates. If the SPV is not considered, a perovskite absorber will appear intrinsic on p-type substrates. However, this is just caused by the SPV-induced binding energy shift and therefore a non-equilibrium state of the perovskite surface, while the perovskite itself is still n-doped.

Even though all perovskite absorbers on p-type substrates are showing a positive SPV, the amount of SPV is lower for the methylammonium-containing perovskites. Possible explanations for this could be i) the fact that the deposition process by spin-coating has not been optimized for the NiO_x substrates or ii) an increased degradation of the methylammonium-containing perovskites during the transport to the vacuum system or inside of it. As already mentioned in the experimental section in chapter 3.2, the process parameters of the spin-coating process of the perovskite absorbers have been optimized so that devices with SnO_2 as a substrate achieve maximum PCEs (see Figure 3.7 for JV-measurements of record devices). However, this does not necessarily mean that the same process parameters will result in high-quality for NiO_x substrates as well, considering that a different surface will have a different surface energy and the precursor solution will therefore show a different wetting. A reasonable high quality of the absorber layer is required to be able to see an SPV in XPS measurements since the V_{OC} is directly connected to the SPV. The second possible explanation, increased degradation of the methylammonium-contain seems reasonable as well. A recent study that focused on comparing the thermal stability of perovskite absorbers with different cation compositions did identify the methylammonium ion as the weakest link [41]. Even though this study focused on thermal degradation in nitrogen atmosphere, the same trend of methylammonium being most vulnerable might also be true for vacuum degradation, especially since MAI has a higher vapor pressure than FAI and CsI, making it more likely that it leaves the perovskite [204]. Besides this, several other publications discuss the low stability of perovskites with methylammonium even though they are not directly comparing them to methylammonium-free perovskites [42,205–207].

To summarize, the presented light experiments are a strong indication that there is no substrate-determined doping of the perovskite absorber and that literature reports of such effects may suffer from unnoticed SPVs. While the perovskites absorbers deposited on top of n-SnO_2 did not show any light-induced shifts, a shift to lower binding energies was observed for all samples on p-NiO_x, indicating the formation of a negative SPV. Since the observed SPVs were rather low for the methyl-ammonium-containing perovskite absorbers, further light experiments with more suitable perovskite samples will be presented in chapter 4 of this work.

3.5. Stoichiometry calculation of the perovskites using XPS

So far, the XPS data presented in chapters 3.4.3 and 3.4.5 have only been analyzed regarding the binding energy position of their emission lines and the differences between the VBM and the Fermi level. The stoichiometry of the perovskite films is worth to be looked at as well since literature reports have shown quite frequently that the doping of metal halide perovskites can be controlled by their stoichiometry. PbI_2-rich perovskite films tend to be n-doped and MAI-rich films p-doped [118,121–123,126,208]. In chapter 3.4.1, XRD and UV/Vis measurements showed that for all investigated perovskite films residual PbI_2 is present, which matches with the n-doping determined by XPS in chapters 3.4.3 and 3.4.5.

Three different atomic ratios are calculated for the perovskite samples: the I to Pb ratio, the I to N ratio, and the Pb to N ratio. For an ideal stoichiometric perovskite, the I to Pb ratio is exactly 3. Values higher than 3 indicate an MAI-excess while values lower than 3 mean that there is an excess of PbI_2. The I to N and Pb to N ratios are varying for each perovskite material since the nitrogen content is different for each perovskite absorber. However, large values indicate a PbI_2-rich and low values an MAI-rich material. In chapter 3.3 reference measurements of thermally evaporated and *in-vacuo* measured MAI, FAI, and PbI_2 films were analyzed, and modified PICSs were calculated so that the measured stoichiometries of these thermally evaporated films are matching their expected ideal stoichiometries. The atomic ratios of the perovskite absorbers will be calculated using both the Scofield PICSs and the modified PICSs. All stoichiometries are given in a tabular form in the Appendix in Table 9.6. For a clearer representation, the atomic ratios are shown here as a graphic in Figure 3.15. Each dot represents the atomic ratio of a perovskite sample, with orange dots being atomic ratios calculated

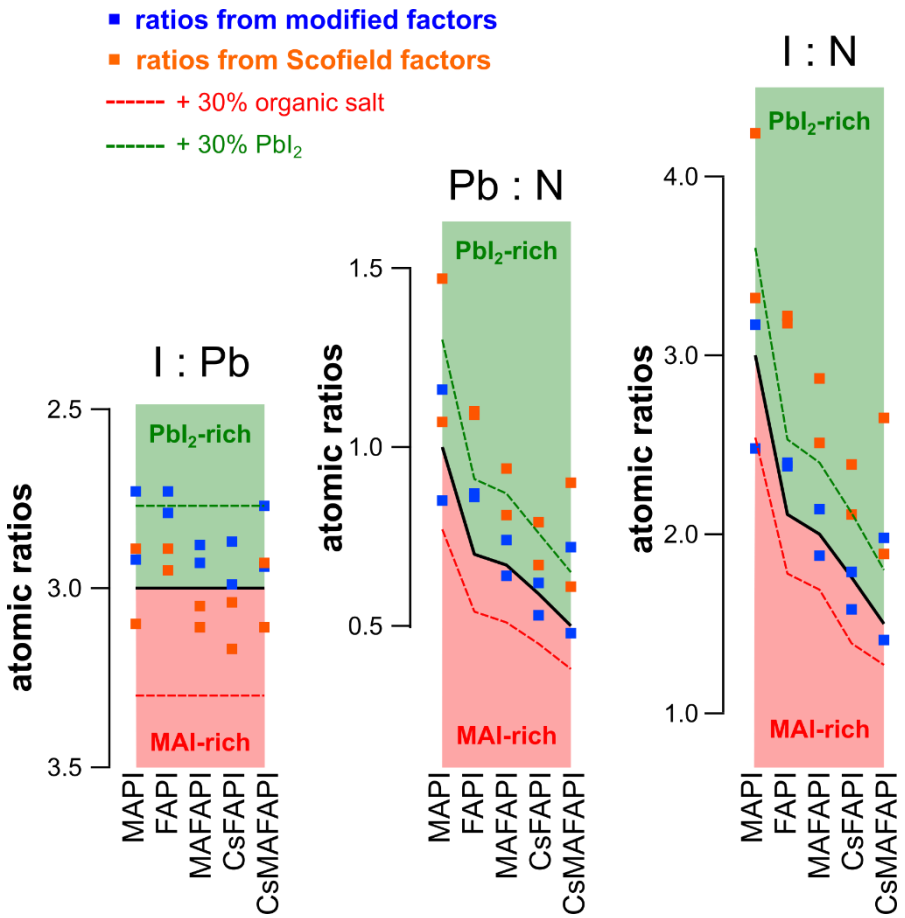

Figure 3.15: Calculated I to Pb, I to N and Pb to N ratios for all ten perovskites films discussed in the previous chapters. The orange dots represent atomic ratios calculated by Scofield PICSs and the blue dots by the modified PICSs that were determined from reference measurements of evaporated MAI, FAI and PbI_2 films (see Chapter 3.3). The black lines represent the ratios for ideal stoichiometric perovskite films. Since the nitrogen content varies between the different perovskite absorbers, the I to N and Pb to N ratios are varying as well. The dotted red and green lines show the atomic ratios of perovskites with 30% excess of the organic salt and 30% excess of PbI_2, respectively. Perovskites are MAI-rich when they are positioned in the red areas and PbI_2-rich when they lie inside the green areas.

with the classical Scofield PICSs and the blue dots with the modified PICSs. The green and red areas are the regions where the perovskite absorbers are expected to be PbI_2-rich and MAI-rich, respectively, based on their atomic ratios. The black solid lines in the middle between the green and red areas represent ideal stoichiometric perovskites. The red and green dotted lines indicate atomic ratios with a 30% excess of organic salt or PbI_2, respectively.

Looking at the I to Pb ratios on the left, the atomic ratios calculated by Scofield PICSs are scattered across both regions, while the atomic ratios calculated by modified PICSs are all positioned in the PbI_2--rich area. The lower I to Pb ratio for the modified PICSs is a result of the slightly smaller modified PICSs of Pb. For the I to N and the Pb to N ratio, the atomic ratios calculated by Scofield PICSs are all positioned inside the PbI_2-rich region. Especially the I to N ratios are deviating quite a lot from the ideal stoichiometries (solid black line) since they are all positioned above the green dotted reference line, which indicates a perovskite with 30% excess of PbI_2. An excess PbI_2 of more than 30%, in some cases even 50% or higher, seems unlikely, considering that the observed PbI_2 peaks in the XRD of those samples were rather low in intensity (see Figure 3.5). The calculations with the modified PICSs are resulting in lower I to N and lower Pb to N ratios, which is a result of the modified nitrogen PICSs being smaller than the Scofield nitrogen PICSS. Even though not all atomic ratios calculated by the modified PICSs are positioned inside the PbI_2-rich regions, the atomic ratios seem to be more reasonable overall. As already mentioned earlier, an excess of PbI_2 is expected since i) the excess of PbI_2 has already been observed in the XRD and UV/Vis measurements (see Figure 3.5 and Figure 3.6) and ii) an excess of PbI_2 is reported to result in an n-doped perovskites. All presented perovskites films were n-doped, based on the previous XPS valence band measurements (see Figure 3.9 and Figure 3.12). It is therefore concluded, that by using the modified PICSs more reasonable atomic ratios can be calculated for metal halide perovskites. However, the modified PICSs are machine-specific and should only be applied for measurements taken at the Escalab 250 system at DAISY-SOL. In any case, the stoichiometry calculations by XPS are confirming the results of the XRD measurements and the UV/Vis measurements: All the investigated perovskite absorbers seem to have an excess of PbI_2. This excess of PbI_2 would explain the strong n-doping which has been observed in XPS valence band measurements since literature reports have repeatedly shown that an excess of PbI_2 will n-dope the perovskite.

3.6. Summary and outlook

In this chapter, five different perovskite absorbers materials (MAPI, FAPI, $MA_{0.5}FA_{0.5}PI$, $Cs_{0.15}FA_{0.85}PI$, and $Cs_{0.05}MA_{0.475}FA_{0.475}PI$) have been investigated by XPS measurements in the dark and under illumination on two different substrate materials (n-type SnO_2 and p-type NiO_x) to i) investigate the influence of the substrate on the doping of the perovskite and ii) identify potential surface photovoltages. XRD and UV/Vis measurements of the same materials have been analyzed as well, to prove that the perovskite phases have been synthesized successfully. Furthermore, reference measurements of the precursor materials to deposit said perovskites (MAI, FAI, PbI_2, and CsI) have been discussed.

With the reference measurements of the precursor materials, it has been demonstrated that XPS can be used to distinguish between the methylammonium cation (MA^+, $CH_3NH_3^+$) and formamidinium cation (FA^+, $CH_5N_2^+$), by comparing their N1s or C1s emission lines (see chapter 3.3). This was verified with the XPS measurements of the perovskite absorbers, where a similar binding energy difference between the N1s and C1s emissions of the MA^+ and FA^+ cations has been observed (see chapters 3.4.3 and 3.4.5). Besides this, the reference measurements have been used to determine modified PICSs, so that the atomic ratios of the reference measurements match the ideal atomic ratios, as they are expected from the stoichiometry of the respective molecules (see chapter 3.3). The modified PICSs are later compared to the Scofield PICSs when the atomic ratios of the five different perovskite absorbers are calculated.

Initial results presented in the motivation part of this work (see chapter 2.6) have shown that during PES measurements metal halide perovskite absorbers are extremely sensitive to light. Since even exceedingly small amounts of light can cause an SPV, the influence of light sources that are commonly appearing in XPS measurements chambers was systematically investigated (see chapter 3.4.3). It has been demonstrated that for example, the light emitted from the cathode of the X-ray source and the X-ray radiation itself can induce significant SPVs.

The XPS measurements of the perovskite absorbers showed that without illumination all investigated perovskite absorbers appear n-type, independent of the substrate they are deposited on (n-type SnO_2 or p-type NiO_x, see chapter 3.4.3 and 3.4.5). The n-doping of the perovskite materials is explained with residual PbI_2, which is visible in the XRD and UV/Vis measurements (see chapter 3.4.1). The atomic ratios determined by XPS did show an excess of PbI_2 as well. When comparing the Scofield PICSs to the modified PICSs it becomes clear, that the results obtained with the modified PICSs are more reliable (see chapter 3.5). Furthermore, in the XRD measurements, the perovskite phases are identified and with UV/Vis the expected bandgaps are determined for the perovskite absorbers. Devices prepared with the respective perovskite absorbers showed reasonable PCE between 13.5% and 19.2% (see chapter 3.4.2). XRD, UV/Vis and JV-measurements were performed by Dr. Jonas Schwenzer.

The most interesting and surprising result is the substrate-independent n-doping of the perovskite absorbers (see chapters 3.4.4 and 3.4.5) since this directly contradicts literature reports of a so-called substrate effect: perovskites on n-type materials like SnO_2 are usually reported n-type,

while they appear intrinsic or slightly p-type on p-type substrates like NiO_x. It is therefore proposed that literature reports of such a substrate effect might be suffering from wrong data interpretation, due to an unnoticed surface photovoltage for perovskite absorbers on top of p-type substrates. For the presented XPS measurements with light illumination, the perovskite absorbers deposited on p-type NiO_x did show a negative surface photovoltage that makes that perovskite *appear* to be slightly p-type (see 3.4.6). While for FAPI and CsFAPI the shifts induced by the surface photovoltage did match very well to the doping difference that is usually attributed to the substrate effect, MAPI, MAFAPI, and CsMAFAPI showed a lower surface photovoltage. Possible reasons for the lower surface photovoltage values for these perovskites might be a degradation of the perovskites in the vacuum during the XPS measurement or an insufficient optimization of the spin-coating process of the perovskite materials on the NiO_x substrates. Also, an SPV already induced by the UV source of the UPS measurements cannot be excluded.

To arrive at a more definitive conclusion of SPV disturbances in PES surface studies, the following chapter will therefore focus on additional light-dependent XPS measurements of MAPI layers and different device stacks of MAPI solar cells. A measurement method will be presented which allows to unambiguously determine the doping of MAPI, measure surface photovoltages, and identify the interfaces at which the photovoltages appear. To overcome the problems of the results presented in this chapter, i.e., a too low SPV in the case of some perovskites, vacuum-deposited MAPI samples will be used for the following experiments. Furthermore, the deposition process of the MAPI perovskites discussed in the following chapter is optimized for SnO_2 as well as NiO_x substrates.

4. Photovoltage experiments on different device stacks

4.1. Motivation and chapter overview

In the previous chapter, XPS measurements in the dark and under the illumination of several different perovskite absorbers on top of n-type SnO_2 and p-type NiO_x were presented. It has been demonstrated that the underlying substrate has no dominant effect on the doping level of the perovskite. Furthermore, for the perovskite absorbers on p-type NiO_x, a negative surface photovoltage was observed when the samples were illuminated during the XPS measurements. It has been proposed, that if the surface photovoltage remains unnoticed, XPS spectra will be misinterpreted, which might be the reason why several publications report an influence of the substrate on the doping of the perovskite absorber.

The focus of this chapter will lie on i) confirming the idea of a substrate-independent doping of the perovskite absorber and ii) investigating different device stacks of perovskite solar cell devices to identify at which interfaces in the device SPVs are created. Since the SPV is equivalent to the open-circuit voltage of the device, the knowledge about where in the device the surface photovoltage is formed will give a better understanding of the device physics and therefore help to identify strategies to further improve the device performance. Throughout this chapter, it will be confirmed that the doping of the substrates does not influence the doping of the perovskite absorber. XPS measurements will show, that the vacuum-deposited MAPI films are n-doped on n-type SnO_2 (classical architecture) as well as on p-type NiO_x (inverted architecture). By investigating the different devices stacks it will be demonstrated that for both architectures the surface photovoltage is formed at the n-MAPI | p-HEL contact, which is the n-MAPI | p-spiro-MeOTAD interface for the classical architecture and the p-NiO_x | n-MAPI interface for the inverted architecture, as preliminary mentioned in chapter 3.4.3. XRD and UV/Vis measurements of the vacuum-deposited MAPI films along with JV-measurements of devices employing the MAPI absorbers will be briefly discussed as well. The here-presented experiments were done in collaboration with the research group of Ulrich W. Paetzold at the Light Technology Institute at the Karlsruhe Institute of Technology. The perovskite sample preparation was performed by Tobias Abzieher, who already optimized the vacuum deposition process of the MAPI perovskite absorbers during his Ph.D. work.

4.2. Experimental procedure

Synthesis of the different device stacks

The synthesis of the different device stacks was performed by Tobias Abzieher from the Light Technology Institute at the Karlsruhe Institute of Technology. The deposition processes will be discussed only briefly here. For the detailed experimental procedure, the reader is referred to chapter 3.1 of the Ph.D. work of Abzieher [209].

Pre-patterned ITO substrates were cleaned in acetone and isopropanol in an ultrasonic bath for 10 min each. Before the deposition of the charge extracting layers, the substrates were exposed to an oxygen plasma for 3 minutes. For the classical architecture, the SnO_2 layers were spin-coated from a colloidal dispersion containing SnO_2 nanoparticles on top of the ITO glass substrates. For the inverted architecture, magnetron-sputtered NiO_x was deposited on top of the ITO front electrode. The sputtering process was performed in a PVD 75 PRO-Line system (Kurt J. Lesker). The deposition of the MAPI absorbers was done by a co-evaporation process inside a home-built vacuum chamber. PbI_2 and MAI were evaporated simultaneously onto the SnO_2 and NiO_x substrates. The rate of PbI_2 was controlled with a quartz crystal microbalance, the rate of MAI through the pressure inside the evaporation chamber. The thickness of the MAPI films was set to 350 nm. After the deposition process, the samples were removed from the vacuum chamber and introduced into a nitrogen-filled glovebox. During the transfer process, the samples were exposed for a short time to ambient atmosphere. To remove excess MAI from the surface of MAPI films, the samples were shortly immersed into isopropanol. This technique has proven to increase the efficiency and reproducibility of devices [209]. Devices in the classical architecture were continued with a spiro-MeOTAD layer prepared by spin-coating. Details regarding the spin-coating process of spiro-MeOTAD are given in chapter 3.2. For the inverted architecture, a 30 nm thick C_{60} film, followed by a 3 nm thick BCP layer was deposited on top of MAPI. A commercial Spectros evaporation system from Kurt J. Lesker was used. Both architectures were finally completed with a 25 nm thick gold back electrode, which was thermally evaporated.

Characterization techniques

The *XRD, UV/Vis, and JV-measurements* were performed at the Karlsruhe Institute of Technology. Details are given in the experimental procedure of the previous chapter (see chapter 3.2). The measurements were performed by Dr. Tobias Abzieher at the Karlsruhe Institute of Technology.

For the *XPS measurements,* the samples were sealed in an air-tight container and shipped from Karlsruhe to Darmstadt. The container was then opened inside a nitrogen-filled glovebox, the samples were mounted on the XPS holder, and finally transferred to the XPS measurement chamber. XPS measurements were performed at an Physical Electronics VersaProbe 5000 at the cluster tool DAISY-BAT. Exposure to ambient atmosphere for around five to ten minutes could not be avoided. More details regarding the XPS measurements are given in chapter 3.2.

4.3. XRD, UV/Vis, and JV-measurements of devices with the vacuum-deposited MAPI layers

Before the photovoltage experiments, XRD and UV/Vis measurements of the vacuum-deposited MAPI films will be discussed. The XRD measurements will allow confirming that the deposited MAPI films crystallize in the cubic perovskite phase and might reveal residual precursor materials. The UV/Vis measurements will be used to determine the bandgap of MAPI and might provide evidence of residual PbI_2. JV-measurements of devices employing the vacuum-deposited MAPI absorbers will be presented as well. As mentioned in the experimental part (see chapter 4.2) the XRD, UV/Vis, and JV-measurements were performed by Dr. Tobias Abzieher at the Karlsruhe Institute of Technology and were already published in his Ph.D. thesis.

The XRD measurements of the vacuum-deposited MAPI films are presented in Figure 4.1 with the red diffractogram being MAPI on top of SnO_2 and the blue diffractogram MAPI on NiO_x. Both perovskite films crystallize in the cubic perovskite phase, which becomes evident when looking at the red shaded area at around 23.5°, where an additional reflection would appear for the tetragonal perovskite phase (see chapter 3.4.1 for a more detailed discussion on the comparison of the cubic and the tetragonal perovskite phase). Since the relative intensities of the cubic perovskite reflections differ for both substrates, it can be concluded that MAPI shows a substrate-dependent texture. For SnO_2 the (100) and (200) reflections show a larger intensity, for NiO_x the (111) and (222) reflections are enhanced. A substrate-dependent orientation of thermally evaporated perovskite films as it is observed here has been reported in the literature before and was correlated to the surface polarity of the respective substrate [209]. The reflections at 12.6° and 23.0° (yellow shaded bars) indicate small amounts of residual PbI_2.

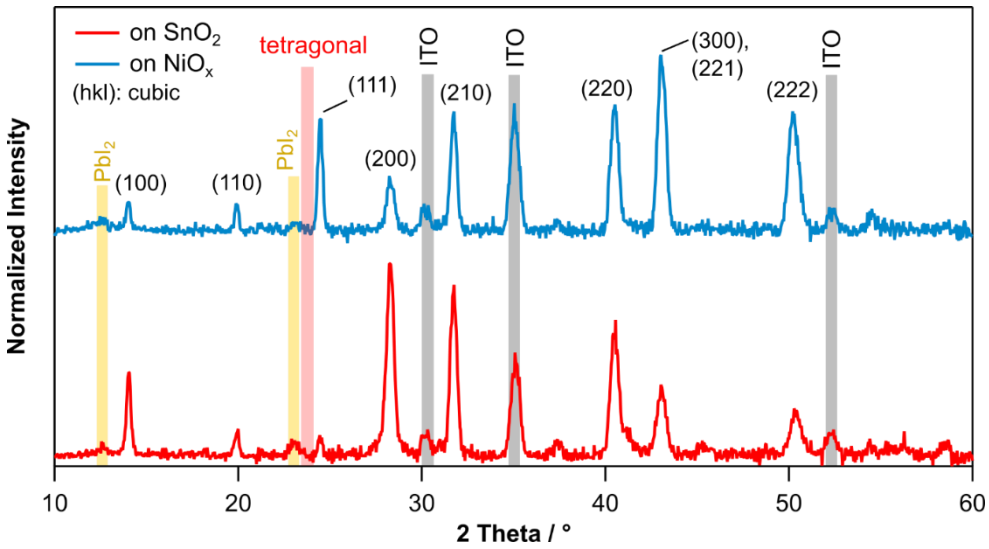

Figure 4.1: XRD measurements of the vacuum-deposited MAPI films on top of SnO_2 (classical architecture, red curve) and NiO_x substrates (inverted architecture, blue curve). Both diffractograms have been normalized to 1. The black indices represent the cubic MAPI perovskite phase. Measurements performed by Dr. Tobias Abzieher.

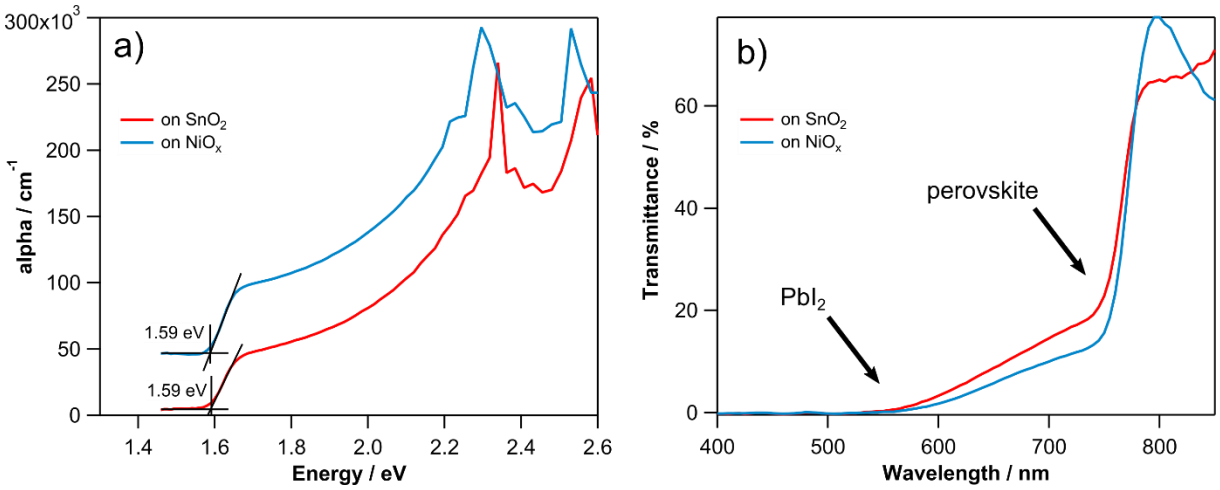

Figure 4.2: UV/Vis spectra of the vacuum-deposited MAPI films on top of SnO_2 (classical architecture, red curve) and NiO_x substrates (inverted architecture, blue curve). a) The absorption coefficient α calculated from the measured transmittance and reflectance data after equation X plotted against the photon energy and b) the recorded transmittance against the wavelength of the incident light. Measurements performed by Dr. Tobias Abzieher.

The UV/Vis measurements are illustrated in Figure 4.2 with the absorption coefficient α plotted against the photon energy in a) and the recorded transmittance versus the wavelength of the incident light in b). For both substrates, a bandgap of 1.59 eV is determined, which is identical to the determined bandgap value of the spin-coated MAPI film from chapter 3.4.1 (see Figure 3.6). This value is also in agreement with literature reports of the bandgap of MAPI [24,135,179]. The transmittance plots in Figure 4.2 b) reveals that besides the absorption feature at around 780 nm, which corresponds to the perovskite phase, another absorption feature at around 560 nm (≈ 2.32 eV) is present. This second absorption feature belongs to residual PbI_2, for which a bandgap of 2.35 eV has been reported [180]. The UV/Vis data confirm therefore what has already been shown by the XRD measurements: the deposited thin films are mainly MAPI with small amounts of residual PbI_2.

The classical architecture devices uses the stack sequence ITO | SnO_2 | MAPI | spiro-MeOTAD | Au and the inverted architecture devices the stack sequence ITO | NiO_x | MAPI | C_{60} | BCP | Au. The JV-measurements are shown on the left in Figure 4.3 a). For SnO_2 a hysteresis is observed whereas the device with NiO_x as substrate is hysteresis-free. Figure 4.3 b) shows the efficiency measured over 300 seconds, to determine the stabilized value that is not influenced by the hysteresis. PCE values of 11.6% and 13.7% are determined for the classical and inverted architecture, respectively. The PCE values are summarized along with the short-circuit current and open-circuit voltage values in Table 4.1. It is emphasized that the presented efficiency values are from average-performing devices and not champion devices. Considering that the reported PCE values for devices with vacuum-deposited perovskite absorbers are usually lower compared to devices where the perovskite has been spin-coated, the PCE values of 11.6% and 13.7% demonstrate a high quality of the vacuum-deposited perovskite films.

In summary, the presented XRD and UV/Vis measurements have demonstrated that MAPI perovskite films have been successfully deposited by co-evaporation of PbI_2 and MAI onto SnO_2 as well as onto NiO_x substrates. A substrate-dependent texture was observed for both materials: on SnO_2 MAPI grows with a preferred (100) texture and on NiO_x with a preferred (111) texture. Like the spin-coated perovskite films investigated in chapter 3, small amounts of residual PbI_2 have been observed in XRD. Devices incorporating the perovskite absorbers achieved PCEs of up to 11.6% and 13.7% for the SnO_2 and NiO_x substrates. The following two chapters will now focus on building up devices of both architectures layer-by-layer and performing SPV measurements for each intermediate step to identify where the SPV of the device develops.

Table 4.1: Stabilized PCE values, short-circuit current density and open-circuit voltage values for the devices with SnO_2 and NiO_x as substrate below the MAPI perovskite absorber.

substrate	stabilized PCE	forward J_{SC} in $\frac{mA}{cm^2}$	reverse J_{SC} in $\frac{mA}{cm^2}$	forward V_{OC} in V	reverse V_{OC} in V
SnO_2	11.6%	19.2	19.2	1.01	1.09
NiO_x	13.7%	20.3	20.7	1.03	1.04

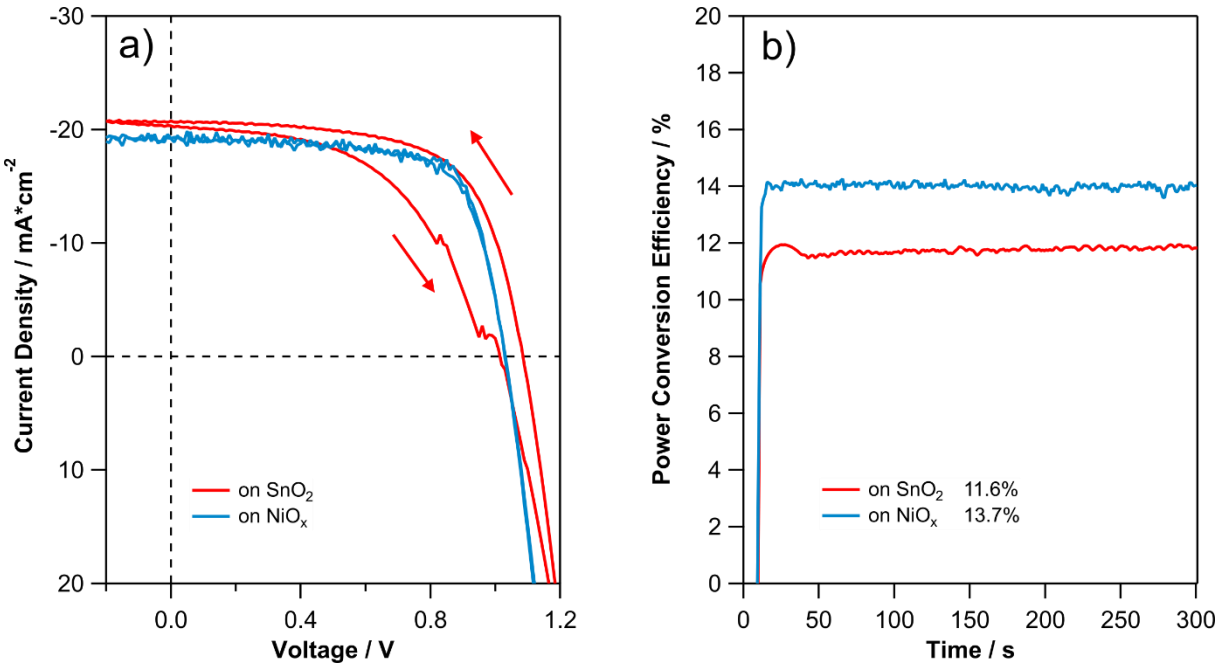

Figure 4.3: Characteristics of devices employing the vacuum-deposited MAPI perovskite absorbers. For the classical architecture devices (red curves) the stack sequence ITO | SnO_2 | MAPI | spiro-MeOTAD | Au is used. The inverted architecture device (blue curves) uses the following layers: ITO | NiO_x | MAPI | C_{60} | BCP | Au. a) is showing the JV-curves of the devices and b) the efficiency measured over a duration of 300 seconds to determine stabilized PCE values. Measurements performed by Dr. Tobias Abzieher.

4.4. SPV measurements of MAPI on n-SnO_2 and p-NiO_x

The following photovoltage measurements aim to i) confirm that the substrate does not influence the doping of MAPI and that the supposed substrate-dependent doping effects are rather due to unrecognized SPVs and ii) identify at which interfaces inside the device the photovoltages develop. Classical and inverted architecture devices will be built up consecutively layer-by-layer and XPS measurements in the dark and under illumination will be performed for each intermediate step. Since by this method the surface photovoltage for each stack can be determined, comparing the different measurements will allow identifying the respective interfaces, where the photovoltages develop.

At first, measurements of the perovskite absorbers on n-type SnO_2 (classical architecture) and p-type NiO_x (inverted architecture) will be discussed (see Figure 4.4). The measurements for SnO_2 are shown in red on top, those for NiO_x at the bottom in blue. The light bulbs indicate whether a measurement was performed in the dark or under illumination. This color code will be kept and used for all following measurements as well. From the valence band measurements in the dark (see Figure 4.4 e) and g) the vacuum-deposited MAPI perovskite appears n-doped for both architectures: a VBM of 1.35 eV and 1.43 eV is determined for SnO_2 and NiO_x, respectively. The absolute binding energy positions of the $Pb4f_{7/2}$ and the $I3d_{5/2}$ emission lines indicate n-doping as well. The $Pb4f_{7/2}$ emission lines appear at 138.56 eV and 138.70 eV for the classical and inverted architecture, respectively, which is comparable to the spin-coated MAPI film (138.65 eV) discussed in chapter 3.4.4 and 3.4.5. The same is true for the $I3d_{5/2}$ emission line: for the classical architecture, it appears at 619.50 eV, and for the inverted architecture at 619.63 eV. The value observed for the spin-coated MAPI perovskite was 619.58 eV. The differences between the core emission lines and the VBM values are also close to those observed for the spin-coated MAPI film: 137.21 eV (classical, vacuum) and 137.27 eV (inverted, vacuum) compared to 137.21 eV (spin-coated) for the $Pb4f_{7/2}$ emission line and 618.15 eV (classical, vacuum) and 618.20 eV (inverted, vacuum) compared to 618.14 eV (spin-coated) for the $I3d_{5/2}$ emission line.

When comparing the dark measurements to the illuminated measurements, almost no change is observed for the MAPI films in the classical architecture: the $Pb4f_{7/2,}$ the $I3d_{5/2}$ emission, and the VBM differ only by 0.01 eV, 0.05 eV, and 0.04 eV, respectively (see Figure 4.4 a), b), e). Since no light-induced shift is observed for the perovskite in the classical architecture, it can be concluded that no SPV is forming at the n-SnO_2 | n-MAPI contact. An SPV under illumination requires the presence of a built-in potential in the dark. Even though the exact amount of band bending can only be verified with an interface experiment, the work function difference can be considered as a first approximation of the built-in potential between two materials (see Anderson's rule in chapter 1.4). UPS measurements of SnO_2 and the respective MAPI sample will be presented in chapter 7.2 and show work function values of 4.15 eV (SnO_2) and 4.02 eV (MAPI on SnO_2) and therefore a rather low work function difference of only 0.13 eV (see Figure 7.3).

Compared to the classical architecture, the spectra of the inverted architecture are showing a significant shift to lower binding when the sample is illuminated: the $Pb4f_{7/2,}$ the $I3d_{5/2}$ emission lines, and the VBM shift by 0.71 eV, 0.70 eV, and by 0.67 eV, respectively (see Figure 4.4 d), e) and g). The

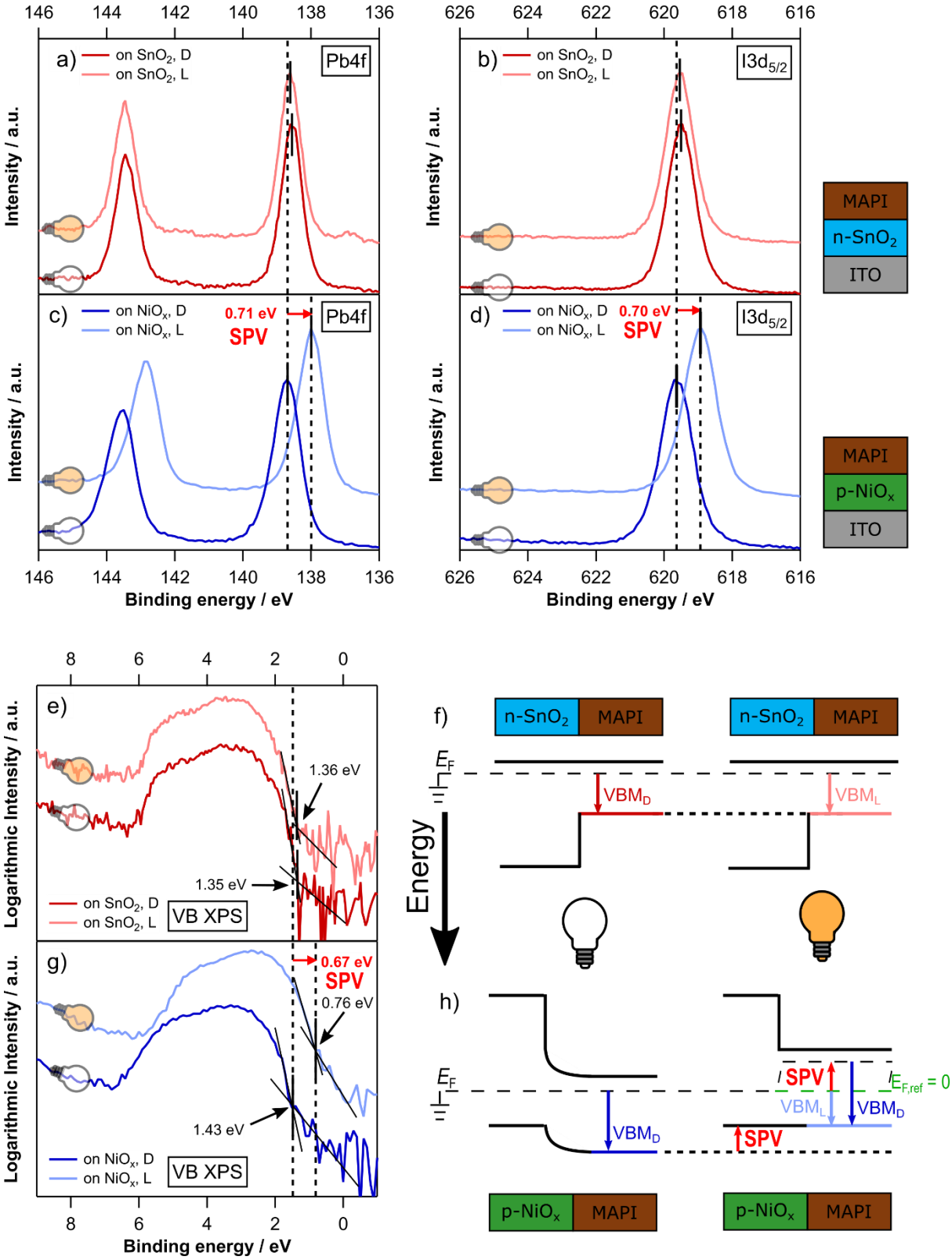

Figure 4.4: The photovoltage measurements using PES of vacuum-deposited MAPI surfaces on SnO_2 and NiO_x substrates. a–c) (red curves) Detailed Pb4f scans, $I3d_{5/2}$ scans, and valence band scans of MAPI films grown on SnO_2 in the classical architecture and d–f) (blue curves) on NiO_x in the inverted architecture. The indices "D" and "L" and the light bulbs indicate whether the measurement was performed in the dark or under illumination. In g) and h) the effect of the light-induced SPV on the respective interface is shown. It is emphasized that the band diagrams in g) and h) are not to scale.

amount of the light-induced shifts are comparable to the shifts observed for the spin-coated FAPI (0.62 eV) and CsFAPI (0.74 eV) perovskites on NiO_x from chapter 3.4.6 (see Figure 3.14). As already discussed in chapter 3.4.6, the light-induced shifts to lower binding energies are attributed to the formation of a negative SPV at the p-NiO_x | n-MAPI interface. The work function difference between NiO_x (5.41 eV) and MAPI (4.16 eV) is high enough to enable the formation of a built-in potential in the dark (see Figure 7.3 in chapter 7.2 for the work function measurements). Figure 4.4 f) and h) are showing schematically the SnO_2 | MAPI and NiO_x | MAPI interfaces in the dark and under illumination. It is emphasized that the presented band diagrams are not to scale and should only visualize how the SPV affects the band diagrams and the PES measurements.

Since no SPV is present for the classical architecture (see Figure 4.4 f), there is no change between the dark case on the left and the illuminated case on the right. In case of the inverted architecture (see Figure 4.4 h), a built-in potential must be present in the dark at the interface between NiO_x and MAPI. As a simplification, the amount of built-in potential, SPV, and quasi-Fermi level splitting is set to the same value here. The light-induced SPV results in a quasi-Fermi level splitting located inside the perovskite absorber. Since the Fermi level of the substrate is fixed to the electrical ground ($E_F = E_{F,ref} = 0$), the SPV shifts all emission lines including the VBM upwards, i.e. to lower binding energies, and the perovskite surface appears to be intrinsic (VBM_L).

In summary, the photovoltage measurements on the vacuum-deposited perovskite absorbers have confirmed the results for the spin-coated perovskite absorbers from chapter 3.4.6: MAPI is n-doped, independent of the substrate it is deposited on. Under illumination, a negative SPV of around 0.70 eV is formed for the MAPI film deposited on top of NiO_x, resulting in a shift of all emission lines including the VBM to lower binding energies. The perovskite appears now to be intrinsic and if the SPV remains unnoticed a wrong doping level will be determined. The presence of an SPV for MAPI on NiO_x fits nicely to the large work function difference between MAPI and NiO_x since this would indicate the presence of a built-in potential in the dark. For SnO_2 and MAPI the work function values differ only by 0.13 eV and no SPV is observed for the MAPI film deposited on top of SnO_2.

4.5. Device measurements

The device stacks are now further continued with the next charge extraction layer and finally completed with the Au back electrode. For the classical architecture devices spiro-MeOTAD is used as HEL. The inverted architecture is continued with C_{60} and BCP, which both function as the EEL. The light-dependent PES measurements for all four device stacks are presented in Figure 4.5. The measurements of device stacks in the classical architecture are shown in red, those for device stacks in the inverted architecture in blue. Dark colors indicate measurements in the dark, brighter colors measurements under illumination.

For the device stack SnO_2 | MAPI | spiro-MeOTAD (see Figure 4.5 a), the VBM appears in the dark at 0.64 eV and shifts by 0.66 eV to higher binding energies when the sample is illuminated. This light-induced shift indicates the presence of a positive SPV at the n-MAPI | p-spiro-MeOTAD interface. It can be excluded that the SPV arises at another interface below since for the SnO_2 | MAPI stack no light-induced SPV was observed (see Figure 4.4). The amount of the SPV is comparable to what is

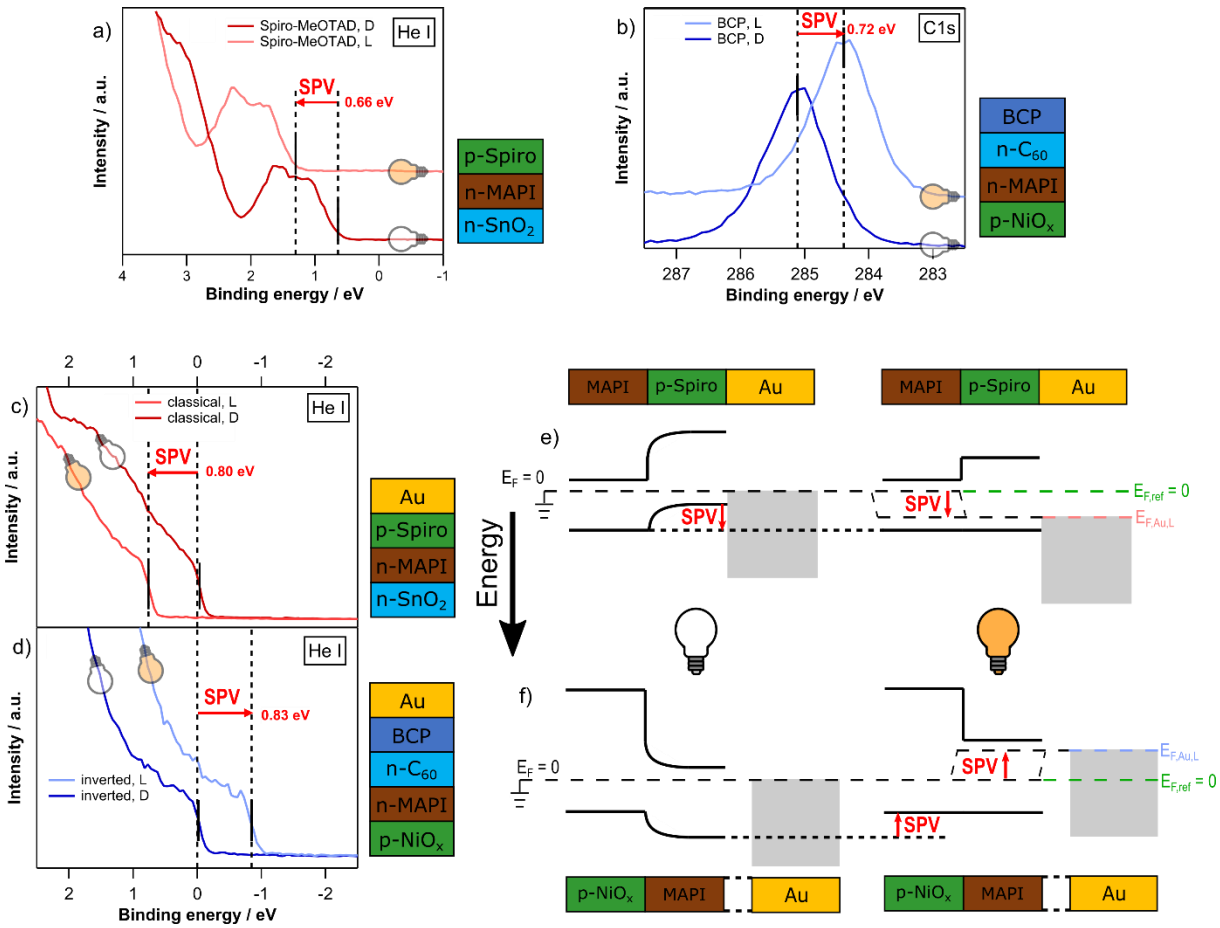

Figure 4.5: The photovoltage measurements of the HEL / EEL surfaces on top of MAPI and of the completed devices with the Au back electrodes. a) He I measurements of spiro-MeOTAD on top of MAPI, b) C1s scans of BCP and He I measurements of the Au back electrode for the c) classical and d) inverted architecture. In e) and f) the effect of the light-induced SPV on the respective interface is shown. It is emphasized that the band diagrams in e) and f) are not to scale. The indices “D” and “L” and the light bulbs indicate whether the measurement was performed in the dark or under illumination.

observed for MAPI on top of NiO_x (0.70 eV, see Figure 4.4). For both architectures, an SPV of around 0.70 eV has been observed at the n-MAPI | p-HEL interface: in case of the inverted architecture at the p-NiO_x | n-MAPI interface and at the n-MAPI | p-spiro-MeOTAD interface for the classical architecture. Considering that the light-induced binding energy shifts appear once to higher (classical architecture) and once to lower binding energies (inverted architecture), it can be concluded that the SPVs are of opposite polarities. This is to be expected since the p-type HEL is positioned once below (inverted architecture) and once above MAPI (classical architecture), which means that the charge carriers excited inside the perovskite absorber are separated in opposite directions at the n-MAPI | p-HEL interface.

For the NiO_x | MAPI | C_{60} | BCP device stack, a light-induced shift of 0.72 eV to lower binding energies is observed (see Figure 4.5 b). Since the amount of this shift is almost identical to what has been observed for the NiO_x | MAPI stack (0.70 eV, see Figure 4.4 a), b) and e), it is concluded that no additional SPV forms at the MAPI | C_{60} or the C_{60} | BCP interfaces. It is therefore confirmed that the classical and inverted architecture devices are working according to the same principle: the photovoltage appears in both devices at the interface between the n-type perovskite absorber and the p-type HEL. The presented devices seem to function as n-n-p (classical architecture) and p-n-n devices (inverted architecture), opposed to the commonly accepted idea of n-i-p and p-i-n devices. To further verify the proposed idea of the photovoltage appearing at the n-MAPI | p-HEL interface, chapters 5 and 6 will focus on analyzing the n-MAPI | p-spiro-MeOTAD and the p-NiO_x | n-MAPI interfaces, respectively.

After finally completing the devices with the gold back electrode, the light-induced shifts are slightly increasing. For the classical architecture, a light-induced shift of 0.80 eV to higher binding and for the inverted architecture a shift of 0.83 eV to lower binding energies can be observed (see Figure 4.5 c) and d). Since in the dark the Fermi levels of the metal surfaces appear at -0.04 eV (classical architecture) and -0.02 eV (inverted architecture), it can be assumed that there is no SPV induced by the UV light of the UV-source used for the UPS measurement. Figure 4.5 e) and f) are showing the dark and illuminated n-MAPI | p-HEL interfaces for both architectures, with the Au contact on top and for simplicity without the EEL. Detailed energy band diagrams of the complete device will be discussed in chapter 7. The light absorption inside the MAPI perovskite leads to a quasi-Fermi level splitting and an SPV at the n-MAPI | p-HEL interfaces. Since the Fermi level of the substrate is fixed to the electrical ground ($E_F = E_{F,ref} = 0$), the Fermi levels of the gold electrode on top appear now shifted to higher/lower binding energies for the classical/inverted architecture. For both architectures, the observed SPVs of the full device stacks are lower compared to the V_{OC} values determined from the J-V measurements using a solar simulator. The classical architecture device showed an V_{OC} of 1.03 V, the inverted architecture device 1.05 V (see Table 4.1). The differences between the SPVs in PES and the open-circuit voltages from the solar simulator measurement is most likely caused by the fact that during the light measurements in the XPS chamber less light will reach the perovskite absorber, as described in the following chapter.

To summarize, the photovoltage measurements of the different device stacks have unambiguously shown that for both architectures the photovoltage appears at the n-MAPI | p-HEL

interface, which is the n-MAPI | p-spiro-MeOTAD interface for the classical and the p-NiOx | n-MAPI interface for the inverted architecture. In contrast, no photovoltage was observed at the n-MAPI | n-EEL interface.

4.6. Comparing the light intensity of the SPV and the solar simulator measurements (AM 1.5G)

In the previous chapters, the photovoltages of full solar cell device stacks in classical and inverted architecture were measured using PES. For both architectures, the SPVs of the devices were around 0.80 V, which is roughly 0.25 V less than the V_{OC} values determined from JV-measurements using a solar simulator. This deviation was attributed to the lower light intensity that will reach the perovskite absorber when it is measured inside the XPS measurement chamber. Ideally, one would now record a JV-curve of the device when it is positioned inside the XPS chamber and illuminated in the same way as the sample during the SPV measurements. Such an experiment would allow verifying that the lower SPV in PES compared to the V_{OC} from the JV-measurements results from a lower light intensity. However, with the given setup it was not possible at this time to put electrical contacts on samples inside the XPS chamber. The following chapter will therefore focus on i) estimating the light intensity that reaches the perovskite absorber when it is measured inside the XPS chamber and ii) discuss how the V_{OC} is affected by the lower light intensity.

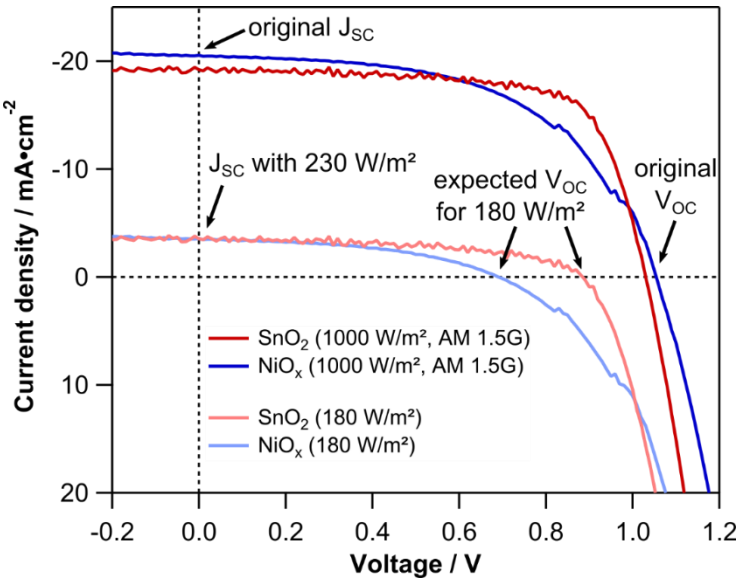

Figure 4.6: The recorded JV-measurements of devices in the classical (dark red) and inverted architecture (dark blue) from solar simulator measurements at 1000 W·m^{-2}. For simplification, only an average between the forward and the reverse scan is shown. The light red and light blue curves are identical to the recorded curves, but shifted upwards, so that the new short-circuit currents are equivalent to a light intensity of 180 W·m^{-2}. It is assumed that the short-circuit current depends linearly on the intensity of the incident light.

The light source used for the illuminated PES measurements is a 50 W ECONLUX SolarRaptor HID-lamp that was attached directly in front of one of the glass viewports of the vacuum chamber. The angle of illumination is 45° with respect to the surface normal of the top of the sample and the distance between the lamp and the sample was approximately 50 cm. At first, the light intensity that will reach the top of the sample surface, which is in this case the gold back electrode, will be determined. To do so, a pyranometer was positioned inside a dark box and an identical glass viewport was positioned on top. The HID-lamp was fixed directly in front of the glass viewport. The pyranometer was then tilted to an angle of 45° and the distance between the pyranometer and the lamp was set to 50 cm so that the illumination conditions inside the box resemble those of the XPS measurement chamber. A power density of 1540 W·m^{-2} was determined. To now calculate the amount of light that will reach the perovskite absorber, it must be considered that some of the photons will be reflected at the vacuum | gold interface and absorbed inside the 25 nm thick gold film. For a gold film with a thickness of 25 nm, it is reported that around 25% of the light will be reflected at the Au | vacuum interface. Inside the gold layer, around 55% of the light will be absorbed, which would then result in a transmittance value of around $T_M = 1 - A - R = 0.2$. These values were reported for light with a wavelength of 492 nm [210]. Another publication that directly measured the transmittance of thin gold films using light with a wave length of 500 nm, reported values of the same order of magnitude with 0.13 and 0.20 for a gold film thickness of 33.0 nm and 11.5 nm, respectively [211]. The transmittance of the 25 nm gold film can therefore be roughly estimated to be 0.18, which would mean that the power density of the light reaching the perovskite absorber during the illuminated measurements is around 180 W·m^{-2} and therefore much lower than the 1000 W·m^{-2} used in the solar simulator measurements.

In the next step, the V_{OC} of the device when it is illuminated with 180 W·m^{-2} will be estimated. In general, the J_{SC} will increase linearly and the V_{OC} logarithmically with increasing incident light intensity (see Equation 1.12) [212]. This is only true when it is assumed that the quantum efficiency is independent of the intensity of the incident light. This is not necessarily the case since with increasing light intensity defects states inside the perovskite absorbers might be filled, which will then decrease Shockley-Read-Hall recombination. Furthermore, the conductivity of layers inside the device stack might increase during the illumination due to a photoconductivity effect, which would then affect the shape of the JV-curve. Nevertheless, the expected V_{OC} at 230 W·m^{-2} can be roughly estimated by shifting the recorded JV-curve to lower photocurrent values so that the new J_{SC} value is equivalent to $\frac{1000\ W \cdot m^{-2}}{180\ W \cdot m^{-2}} = 18\%$ of the original value. This shift results in V_{OC} values 0.88 V and 0.69 V for the classical and inverted architecture, respectively (see Figure 4.6). These estimated open-circuit voltages are comparable to the SPV values determined by the PES measurements (0.80 V and 0.83 V for the classical and inverted architecture, respectively). The lower intensity of the incident light during the XPS measurements might therefore very well be the reason for the SPVs being lower than the open-circuit voltages determined by the solar simulator measurements.

4.7. Summary and conclusion

Chapter 4 focused on determining at which interface in classical and inverted device architecture the photovoltage is formed. The used layers stacks were SnO_2 | MAPI | spiro-MeOTAD | Au for the classical architecture and NiO_x | MAPI | C_{60} | BCP | Au for the inverted architecture. The MAPI perovskites have been deposited by co-evaporation from PbI_2 and MAI.

Initial XRD measurements showed that on both substrates (SnO_2 and NiO_x) the perovskite phase could be synthesized with small amounts of residual PbI_2 (see chapter 4.3). While MAPI on SnO_2 shows a (100) texture, a preferred (111) growth was observed for the NiO_x substrate. UV/Vis measurements revealed a bandgap of 1.59 eV, which is almost identical to the bandgap of 1.58 eV observed for the previously-investigated MAPI deposited by spin-coating in chapter 3.4.1. When used in devices, efficiencies of 11.6% and 13.7% and V_{OC} values of 1.05 V and 1.04 V could be achieved, for SnO_2 and NiO_x, respectively.

The SPV measurements of the MAPI perovskites on n-SnO_2 and p-NiO_x confirmed the result already shown for the spin-coated perovskite absorbers in chapter 3: i) MAPI is n-doped, independent of the underlying substrate and ii) for the inverted architecture a negative SPV 0.72 V is measured at the p-NiO_x | n-MAPI interface (see chapter 4.4). This negative SPV shifts all emission lines including the valence band to lower binding energies making the perovskite appear to be p-type. For the classical architecture, an SPV of 0.66 V is determined at the n-MAPI | p-spiro-MeOTAD. Both architectures are therefore showing a major part of their SPV at the n-MAPI | p-HEL interface.

When the SPVs of the complete devices after the deposition of the Au back electrode are measured, values of 0.80 V and 0.82 V are determined for the classical and inverted architecture, respectively. The deviation to the open-circuit voltages determined from solar simulator measurements (1.05 V and 1.04 V) is explained with a lower light intensity reaching the absorber in the measured samples inside the XPS chamber during the SPV measurements. A rough estimate gives a value of 180 $W \cdot m^{-2}$ for the power density of the light in the XPS chamber compared to the 1000 $W \cdot m^{-2}$ of the AM 1.5 G spectrum used in the solar simulator.

Since the n-MAPI | p-spiro-MeOTAD and the p-NiO_x | n-MAPI have been identified as the interfaces, where the majority of the photovoltage drops, both interfaces will be investigated in the following two chapters in more detail.

5. The MAPI | LiTFSI-doped spiro-MeOTAD interface

5.1. Motivation and chapter overview

The results of the previous chapters have shown that for the investigated perovskite solar cells the photovoltages are located at the n-MAPI | p-HEL interfaces, which is the n-MAPI | p-spiro-MeOTAD interface in case of the classical architecture devices. This chapter will aim to investigate this interface in more detail by a classical step-by-step interface experiment. Through a stepwise deposition of spiro-MeOTAD on top of MAPI and consecutive XPS measurements in the dark, the presence of a built-in potential (a band bending) can be verified. Under illumination this band bending should change to a flat band situation and an SPV should form. Nevertheless, some experimental challenges come along with such an interface experiment. Since it is a necessity to have a depositions process that can deposit layers down to a thickness of 1 nm, spiro-MeOTAD can only be deposited by thermal evaporation. A solution-based deposition technique, like for example spin-coating, is not suitable for a controlled deposition of films with such low thicknesses. When spin-coated spiro-MeOTAD layers are used in perovskite solar cells, there are usually additives inside the precursor solution like lithium bis(trifluoromethanesulfonyl)imide (LiTFSI) and 4-tert-butylpyridine (tBP). While spiro-MeOTAD is a small molecule and the additive LiTFSI is a salt, meaning that both can be deposited by thermal evaporation inside the vacuum, the additive tBP is a liquid at ambient atmosphere, making it much more challenging to control tBP in a vacuum process. Unfortunately, both additives seem to be necessary to achieve homogeneously doped spiro-MeOTAD layers with a high enough conductivity. LiTFSI is reported to act as p-dopant to increase the hole mobility of spiro-MeOTAD and therefore also its conductivity [213–215]. Adding tBP seems to avoid the aggregation of LiTFSI, resulting in more homogeneous films [216,217].

Initial PES measurements presented in this chapter will therefore focus on i) investigating the role of LiTFSI and tBP to confirm their effects reported in literature and ii) record reference measurements of the spin-coated LiTFSI-doped spiro-MeOTAD films. In the next step, LiTFSI-doped spiro-MeOTAD films will be deposited by thermal evaporation of LiTFSI and spiro-MeOTAD. By comparing these vacuum-deposited samples to the spin-coated reference samples, it will be demonstrated that spiro-MeOTAD can effectively be doped with LiTFSI in a thermal evaporation process in the vacuum. Furthermore, it will be shown that due to the vacuum deposition process the dopant LiTFSI does not form large precipitates and tBP can be omitted. An interface characterization between spiro-MeOTAD and tBP will give more insight into the doping process. Finally, the developed vacuum deposition process of LiTFSI-doped spiro-MeOTAD will be used to perform a detailed interface characterization of the MAPI | LiTFSI-doped spiro-MeOTAD interface. The results of the interface experiment with LiTFSI-doped spiro-MeOTAD will provide evidence of a built-in potential in the dark and an SPV under illumination, which will therefore confirm the importance of the n-MAPI | p-HEL interface.

5.2. Experimental procedure

Pre-cut Pilkington NSG TEC™ 15A FTO glass substrates with a thickness of 2.2 mm and dimensions of 20 mm x 20 mm were used. Prior to the deposition of spiro-MeOTAD the FTO substrates were consecutively cleaned with DI water and dishwashing soap, isopropanol, DI water and finally dried under the flow of nitrogen gas.

Synthesis of the spiro-MeOTAD thin films by spin-coating:

The spin-coating process was performed inside a nitrogen-filled glovebox with oxygen and water concentrations below 0.5 ppm. All solutions were freshly prepared immediately before the respective experiment. For the series with varying LiTFSI concentration 64 mg spiro-MeOTAD (Borun Technology, 99.9% purity, CAS: 207739-72-8) was dissolved in 800 µl chlorobenzene (Merck, 99.8% purity, CAS: 108-90-7) along with 22.8 µl tBP (Merck, 98.0% purity, CAS: 3978-81-2). 100 µl of this solution was used to spincoat the first sample without any LiTFSI. The solution was pipetted onto an FTO substrate and after a waiting period of 20 seconds, the substrates were rotated for 30 seconds at 23 rps. The spin-coating process was kept the same for all following samples. For the LiTFSI-containing spiro-MeOTAD films, a second solution was prepared by dissolving 10 mg LiTFSI (Merck, 99.0% purity, CAS: 90076-65-6) in 500 µl acetonitrile (Merck, 99.8% purity, CAS: 75-05-8). The concentration of LiTFSI inside the spiro-MeOTAD solution was then consecutively increased by adding certain amounts of the LiTFSI solution to the spiro-MeOTAD solution, always followed by using 100 µl to spincoat the next sample. The samples with varying tBP concentrations were prepared in the same way, by consecutively adding tBP and using 100 µl of the solution in between to spin-coat the next sample. The spin-coated samples were then transported with a nitrogen-filled shuttle to the XPS measurement chamber to avoid exposure to ambient atmosphere. All XPS measurements were performed with a monochromatic XR6 X-ray source (Al Kα) at a Thermo Fisher Escalab 250 at the cluster tool DAISY-SOL., except for the undoped spiro-MeOTAD sample without LiTFSI. Since the undoped sample exhibit charging during the measurement using the Escalab 250 system, the measurement was repeated at a VersaProbe 5000 system using a neutralizer. Details regarding the XPS measurements are given in chapter 3.2.

Synthesis of the spiro-MeOTAD thin films by vacuum evaporation:

The vacuum deposition of the LiTFSI-doped spiro-MeOTAD films was performed by simultaneously evaporating both materials using home-built evaporation sources equipped with Al_2O_3 crucibles. The crucibles had a length of 30 mm and inner and outer diameters of 5 mm and 8 mm, respectively. Evaporation temperatures of roughly 300 °C and 120 °C were used for spiro-MeOTAD and LiTFSI. The distance between the substrate and the evaporation sources was fixed to 19 cm. The base pressure of the deposition chamber was around $6.0 \cdot 10^{-8}$ mbar and would increase to around $2.5 \cdot 10^{-7}$ mbar during the deposition process. For the vacuum doping series and the interface experiment between spiro-MeOTAD and LiTFSI (chapters 5.4 and 5.5), FTO substrates were used. For

the interface experiment between MAPI and spiro-MeOTAD (chapter 5.6), a vacuum-deposited MAPI film grown on SnO_2 supplied by Tobias Abzieher from the Light Technology Institute at the Karlsruhe Institute of Technology was used. More details on the preparation of the perovskite sample and the transport to Darmstadt are given in chapter 3.2. Details on the XPS measurements, especially regarding the illumination conditions, are given in chapter 3.2. The LiTFSI and spiro-MeOTAD evaporation sources were kept at the evaporation temperatures during the whole interface experiment to maintain a constant evaporation rate. Accumulated evaporation times of 2.5 min, 5 min, 10 min, 20 min, 40 min, 80 min, and 120 min were used. In between each deposition step and XPS measurement, the sample was kept under UHV conditions at a pressure $5.0 \cdot 10^{-8}$ mbar or lower.

5.3. The role of LiTFSI and tBP in spiro-MeOTAD films

At first, the influence of the amount of LiTFSI on spin-coated spiro-MeOTAD films will be investigated. LiTFSI is reported to act as a p-dopant for spiro-MeOTAD, increasing its hole concentration and mobility and therefore also the conductivity of the spiro-MeOTAD films [213–215]. The spiro-MeOTAD films employed in the devices discussed in chapters 3.4.2 and 4.3 were fabricated from a solution with a spiro-MeOTAD to LiTFSI molar ratio of 1 to 0.49, which will also be referred to as the standard concentration. Samples with spiro-MeOTAD to LiTFSI molar ratios of 1 : 0 (undoped), 1 : 0.02, 1 : 0.05, 1 : 0.10, 1 : 0.25, and 1 : 0.75 will be investigated along with the standard concentration sample (1 : 0.49). In addition, the precursor solution contained a spiro-MeOTAD to tBP molar ratio of 1 : 3, which is the standard tBP amount used for the fabrication of spiro-MeOTAD films in solar cells.

For reference, the molecular structures of spiro-MeOTAD, LiTFSI and tBP are displayed in Figure 5.1. The C1s and F1s core level emission lines along with He I measurements of the valence band of the prepared spiro-MeOTAD samples with varying LiTFSI to spiro-MeOTAD molar ratios are presented in Figure 5.2. The N1s, the O1s, the S2p emission lines, and He I measurements with an applied bias of -6V to determine the work function are shown in Figure 9.4 in the Appendix. The absolute binding energy values of all emission lines along with the VBM values and the work function are given in Table 9.7 in the Appendix. When looking at the C1s emission line in Figure 5.2 a), a broad asymmetric peak between 284 eV and 288 eV is observed for all samples which decreases in intensity with increasing LiTFSI amount. This peak belongs to the spiro-MeOTAD molecule and is composed of five different contributing emissions belonging to the different carbon species inside spiro-MeOTAD molecule [218] (see Figure 5.12 b). The shape of the C1s emission is in agreement with literature reports of XPS measurements of spiro-MeOTAD [214,218–220]. With increasing LiTFSI amount, a second peak which belongs to the $-CF_3$ species of the LiTFSI molecule begins to appear at around 293 eV and increases in intensity. According to the PES database of organic polymers published by Briggs *et al.*, the C1s

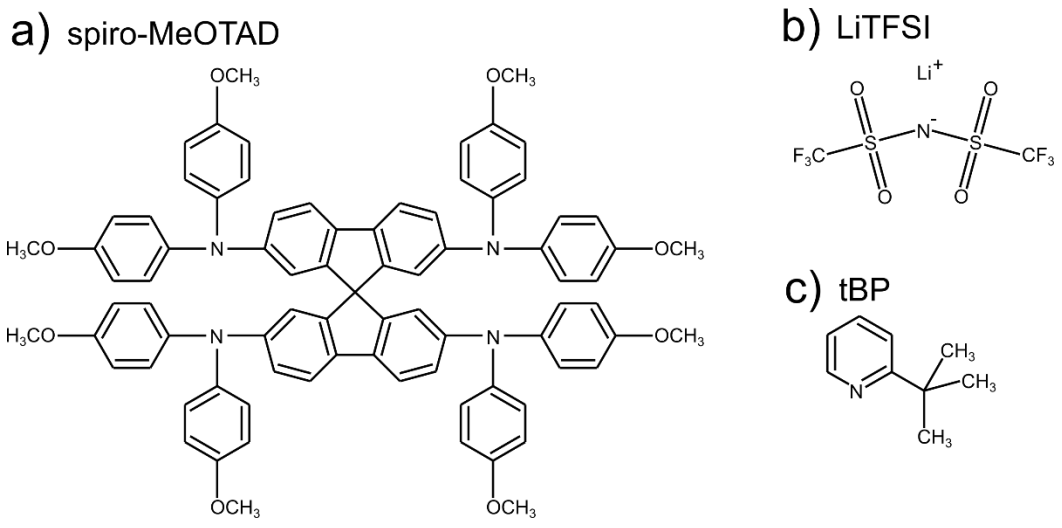

Figure 5.1: The molecular structure of a) spiro-MeOTAD, b) LiTFSI and c) tBP.

emission line for a $-CF_3$ functional group is expected at a binding energy of 292.7 eV [159], which is close to the here-observed value.

The C1s emission line of the undoped spiro-MeOTAD layer appears at 284.91 eV (see Figure 5.2 a), which is comparable to reported literature values of 285.20 eV [214] and 282.25 eV [218]. After the additions of LiTFSI, the C1s emission line of spiro-MeOTAD is gradually shifting to lower binding energies until it appears at 284.29 eV for the sample with the standard LiTFSI concentration (spiro-MeOTAD : LiTFSI of 1 : 0.49). This shift to lower binding energies indicates a p-doping of the spiro-MeOTAD molecule. When a material is p-doped, its Fermi level is shifted towards the VBM. Since in PES the Fermi level is fixed at $E_B = 0\ eV$, the p-doping will be visible as a shift of all emission lines including the VBM to lower binding energies. After further increasing the spiro-MeOTAD : LiTFSI ratio to 1 : 0.75, the C1s emission line does not shift any further and remains at 284.29 eV, indicating that the doping limit has already been achieved for the standard LiTFSI concentration. The F1s emission are displayed in Figure 5.2 b). No F1s peak is visible for the undoped spiro-MeOTAD sample, as fluorine is only present inside LiTFSI. Upon adding LiTFSI to the spiro-MeOTAD film, the F1s peak appears at 689.39 eV and shifts gradually to lower binding energies, while increasing in intensity. The VBM values determined by UPS (see Figure 5.2 c) are showing a similar behavior as the C1s and F1s emission lines: for the undoped spiro-MeOTAD film the highest VBM value of 1.09 eV is observed. With increasing

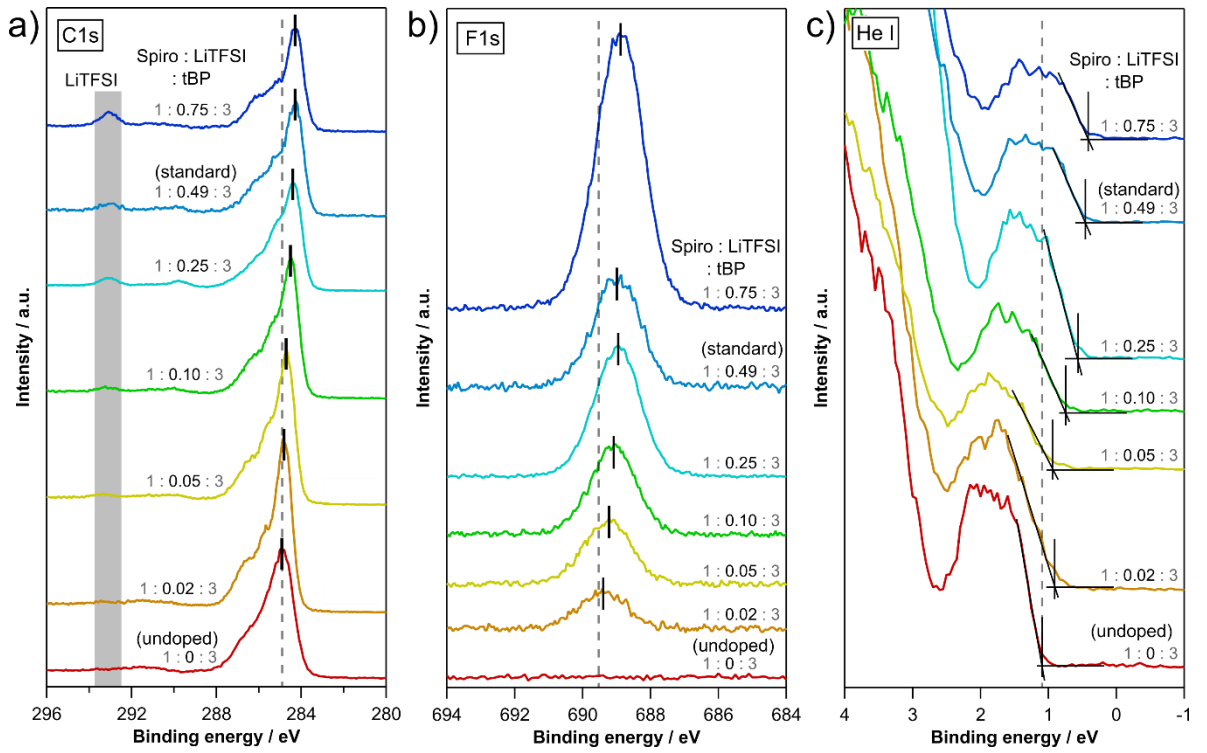

Figure 5.2: a) XPS C1s, b) F1s emission lines and c) He I UPS measurements of spin-coated spiro-MeOTAD samples with varying LiTFSI to spiro-MeOTAD molar ratios. The given molar ratios are the molar ratios used in the precursor solution for the spin-coating. From bottom to top the molar ratios are increasing from 1 : 0 (undoped) until the highest LiTFSI concentration corresponding to a LiTFSI to spiro-MeOTAD molar ratio of 1 : 0.75. The grey dotted lines represent the binding energy positions for the undoped samples (1 : 0 molar ratio). For the F1s emission line the binding energy position of the undoped sample was extrapolated using an exponential fit (see Figure 5.3).

LiTFSI concentration, the VBM is shifting to lower binding energy values until it is positioned at 0.41 eV for the spiro-MeOTAD sample with the highest LiTFSI concentration.

For a better comparison of the binding energy shifts of the C1s, the F1s emission line, and the VBM values, they are summarized in Figure 5.3 a) along with the variation of the work function and the ionization potential changes. The curved broken lines are exponential fits. Details regarding the fitting method are given in Table 4.1 in the Appendix. The binding energy shift of the F1s emission lines has been extrapolated to a LiTFSI to spiro-MeOTAD molar ratio of 1 : 0 using the fit function. The C1s (red), the F1s emission lines (black), and the VBM values (green) are shifting almost parallel with increasing LiTFSI to spiro-MeOTAD molar ratio, verifying the p-doping effect of LiTFSI. Total binding energy shifts between the undoped and the highest doped sample of 0.62 eV, 0.66 eV, and 0.68 eV are determined for C1s, F1s, and the VBM values, respectively. A doping limit of 0.65 eV is determined for the spiro-MeOTAD:LiTFSI system by taking the average of the C1s, the F1s, and the VBM shift, sketched in Figure 5.3 by the black horizontal broken line. The LiTFSI concentration of spiro-MeOTAD films of devices used in this work (grey vertical broken line) lies therefore beyond the doping limit. The variation of the work function, determined from He I measurement with an applied bias of -6V is displayed in Figure 5.3 a) in light blue. The respective spectra are shown in the Appendix in Figure 9.4 d). For the undoped spiro-MeOTAD sample, a work function of 4.00 eV is determined, which increases to 5.33 eV for the sample with the highest LiTFSI concentration. Even though the work function is increasing as it is expected in case of a p-doping, the amount of increase of the work function (1.33 eV) is higher compared to binding energy shifts of the C1s emission line (0.62 eV), the F1s emission line (0.66 eV) and the VBM values (0.68 eV, see Figure 5.3 a). The difference between the

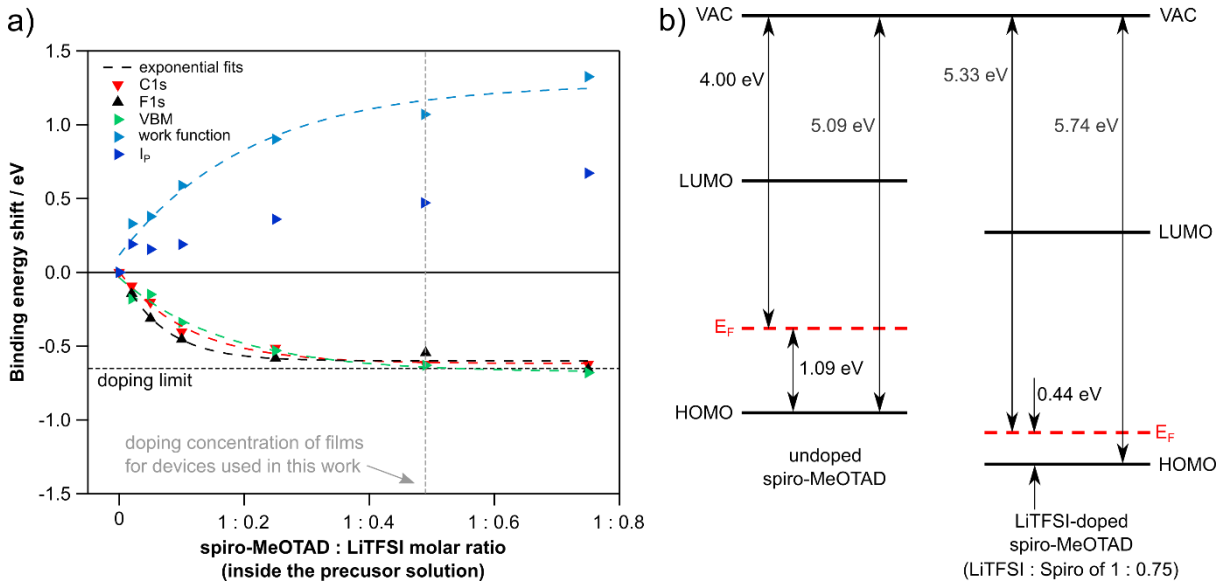

Figure 5.3: a) Binding energy shifts of the C1s, the N1s, the O1s, the F1s emission lines, the VBM values determined from He I measurements and the work function values for spin-coated spiro-MeOTAD samples with varying spiro-MeOTAD to LiTFSI molar ratios. The dotted lines are exponential fits of the measured values. The doping limit of 0.65 eV was determined by taking the average of the binding energy shifts of C1s, F1s and the VBM. b) Comparison of the energy levels of the undoped and the highest doped spiro-MeOTAD sample with a LiTFSI : spiro-MeOTAD molar ratio of 1 : 0.75 of the shown LiTFSI doping series.

work function and VBM variation is given by an increase of the ionization potential (see Figure 5.3, dark blue dots) The stronger increase of the work function might be related to an accumulation of LiTFSI molecules at the sample surface, as it has been reported by Schölin *et al.* [214]. Due to the higher surface sensitivity of the work function measurements compared to the XPS core level measurements, a surface accumulation of LiTFSI will have a stronger influence on the work function. The work function value determined for the highest doped spiro-MeOTAD sample (5.33 eV) is comparable to the work function of a pure thermally evaporated LiTFSI film (5.51 eV, see Appendix Figure 9.9 d) and Table 9.11), suggesting such an enrichment of LiTFSI on the surface. The determined energy levels for an undoped spiro-MeOTAD and the highest achieved doped spiro-MeOTAD film are summarized in Figure 5.2 b). The bandgap value of spiro-MeOTAD was determined to be 2.97 eV from a UV/Vis measurement shown in Figure 9.5 in the Appendix.

In the next step, the role of tBP will be investigated. For that purpose, several samples with different LiTFSI and tBP concentrations were produced and measured with XPS and UPS (see Figure 5.4). From bottom to top the spectra represent a spiro-MeOTAD film without any tBP or LiTFSI (red), only with tBP (orange) and only with LiTFSI (yellow). The following four spectra (green to black) are samples containing both LiTFSI and tBP with increasing tBP content. The absolute binding energy positions of all emission lines are summarized in the Appendix in Table 9.9. The O1s, the N1, and the

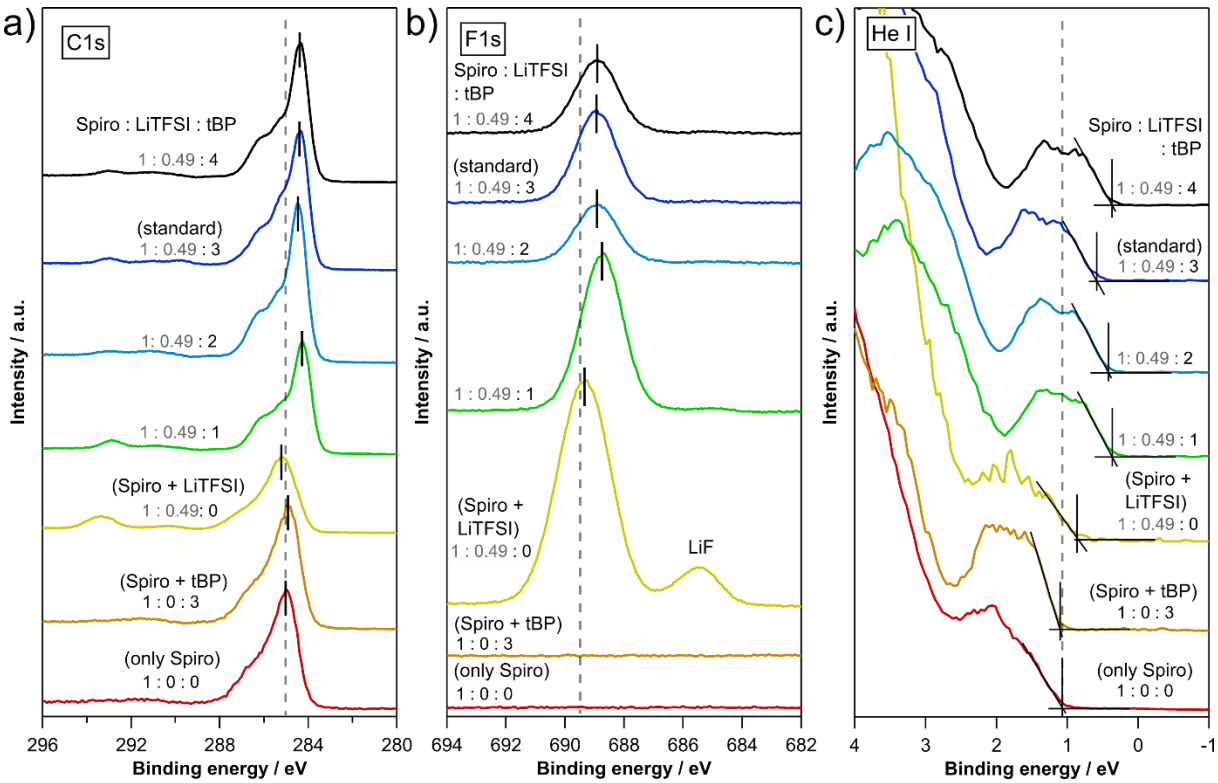

Figure 5.4: a) C1s, b) F1s emission lines and c)) He I measurements of spin-coated spiro-MeOTAD samples with varying LiTFSI and tBP amounts. The here-given molar ratios are the molar ratios used in the precursor solution for the spin-coating. The three curves at the bottom represent pure spiro-MeOTAD, spiro-MeOTAD only with tBP and only spiro-MeOTAD with LiTFSI. The four curves at the top are for show a series of samples with increasing tBP amount. The grey dotted lines represent the binding energy positions for the spiro-MeOTAD sample without tBP and without LiTFSI.

S2p emission lines along with the work function measurements (He I with an applied bias of -6V) are shown in Figure 9.6 in the Appendix.

For the pure spiro-MeOTAD film without any LiTFSI or tBP (red curve in Figure 5.4), the C1s emission line appears at 285.02 eV and the VBM is positioned at 1.07 eV. After adding tBP (orange curve in Figure 5.4), the C1s emission line and the VBM appear at 284.91 eV and 1.09 eV, indicating that tBP itself does not affect the energy levels of spiro-MeOTAD. The spiro-MeOTAD film without tBP but with LiTFSI (yellow curve in Figure 5.4) shows a C1s emission at slightly higher binding energies of 285.21 eV, therefore indicating that without the addition of tBP to the precursor solution LiTFSI does not p-dope spiro-MeOTAD. LiTFSI is still observed in the XPS measurements, indicated by the C1s emission line at around 293 eV, which corresponds to the $-CF_3$ species of LiTFSI and the F1s emission line of LiTFSI at 689.34 eV. However, an additional F1s peak appears at 685.48 eV, which corresponds to LiF, a decomposition product of LiTFSI. The decomposition of LiTFSI is also visible in the S2p emission line (see Figure 9.6 in the Appendix), which appears broader, indicating the presence of different oxidation states of sulfur. A possible decomposition product could be Li_2SO_3, which has also been reported in the literature. Based on the relatively high intensities of the C1s and F1s emission lines of LiTFSI (see Figure 5.4 a) and b) and the lower intensity of the C1s emission line of spiro-MeOTAD (see Figure 5.4 a), it can be concluded that the sample without tBP has a LiTFSI accumulation at its surface. Adding tBP to the precursor solution seems therefore to result in a more homogeneous distribution of LiTFSI inside the spiro-MeOTAD film. The LiTFSI-dissolving effect of tBP is also visible by comparing two precursor solutions with and without tBP as depicted in Figure 5.6. Without the addition of tBP on the left, LiTFSI precipitates are visible at the bottom of the glass vial, which is not the case for the tBP-containing solution on the right. The solvent of spiro-MeOTAD, chlorobenzene, is not polar enough to efficiently dissolve the LiTFSI salt. The pyridine group of tBP leads to a higher polarity as compared

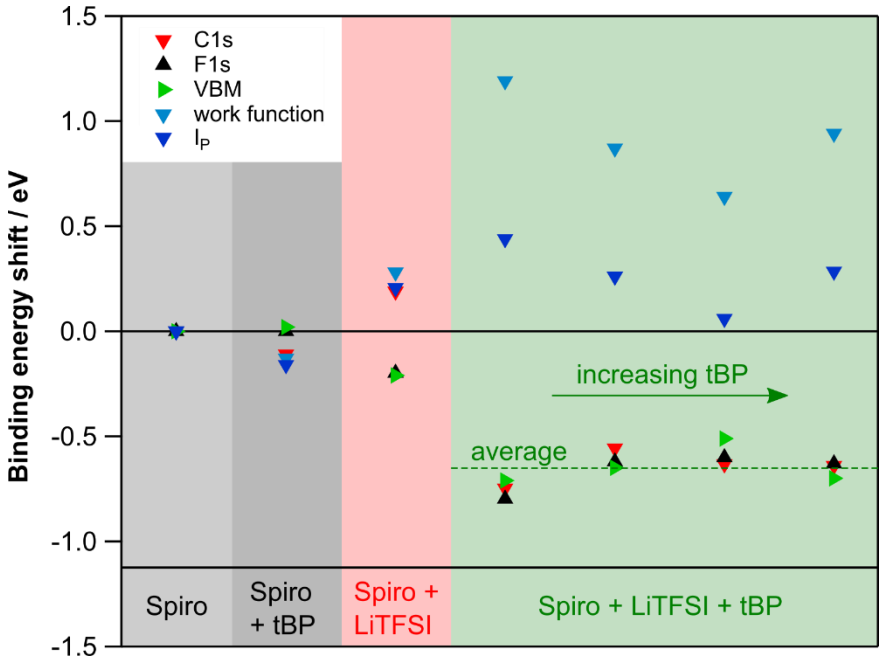

Figure 5.5: Binding energy shifts of the C1s emission line, the F1s emission line, the VBM values determined from He I measurements and the work function values for the samples with varying LiTFSI and tBP content presented in Figure 5.4.

to chlorobenzene, resulting in a better solubility of LiTFSI. By simply comparing the dielectric constants of chlorobenzene (5.62) and pyridine (12.9), the higher polarity of tBP becomes evident as well.

For the spiro-MeOTAD films containing LiTFSI as well as tBP (green to black curves in Figure 5.4) the C1s emission lines of spiro-MeOTAD appear shifted to higher binding energies at 284.28 eV, 294.47 eV, 294.39 eV, and 284.39 eV, for spiro-MeOTAD to tBP molar ratios of 1 : 1, 1 : 2, 1 : 3, and 1 : 4, respectively. The addition of tBP facilitates the solubility of LiTFSI inside the precursor solution, resulting in increased p-doping of spiro-MeOTAD. The F1s emission lines and the VBM values determined by He I are shifting parallel to the C1s emission line to lower binding energies (see summarized binding energy shifts in Figure 5.5). With increasing tBP concentration no obvious trend is observable, the C1s emission, F1s emission and the VBM maximum are scattered around a shift of 0.65 eV which is identical to the determined doping limit in Figure 5.3. tBP has therefore no direct effect on the energy levels of spiro-MeOTAD and only helps to increase the solubility of LiTFSI, avoiding segregation in the spin-coated film. This is also evident from the changes of work function and ionization potentials which tend to be smaller with tBP added.

To summarize, it has been demonstrated that LiTFSI can effectively p-dope spiro-MeOTAD. The doping limit is reached at a spiro-MeOTAD to LiTFSI molar ratio of around 1 : 0.40, corresponding to a shift of the Fermi level of around 0.65 eV. In the LiTFSI-doped spiro-MeOTAD films prepared by spin-coating, LiTFSI seems to diffuse to the surface. The addition of tBP to the precursor solution (spiro-MeOTAD dissolved in chlorobenzene) increases the solubility product of LiTFSI, avoiding its segregation inside the solution. The better solubility of LiTFSI inside chlorobenzene after adding tBP to the solution was explained by the molecular structure of the solvents: the pyridine group of tBP makes it a more polar solvent compared to chlorobenzene, facilitating the solution of LiTFSI. Instead of using a combination of chlorobenzene and tBP, both could be replaced by a single solvent having an intermediate polarity. tBP results therefore in spiro-MeOTAD films with a more homogeneous LiTFSI distribution. Without adding tBP to the precursor solution, LiTFSI showed no p-doping effect on spiro-MeOTAD. The necessity of tBP for an effective p-doping of spiro-MeOTAD through LiTFSI may result in a more complex interface experiment between MAPI and LiTFSI-doped spiro-MeOTAD, since the controlled deposition of a liquid like tBP is experimentally challenging. The following experiments will therefore investigate whether tBP is also required to reach a homogeneous distribution of LiTFSI in a co-evaporation process of LiTFSI and spiro-MeOTAD.

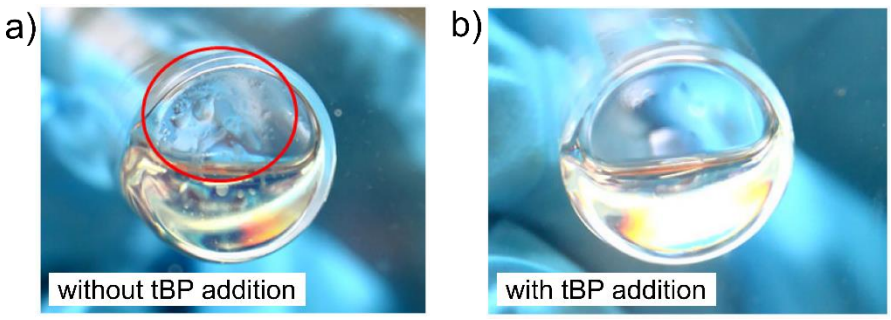

Figure 5.6: Comparison of a solution containing spiro-MeOTAD and LiTFSI a) without the addition of tBP and b) with the addition of tBP. For the solution without the addition of tBP, precipitations of LiTFSI are visible at the bottom of the glass vials. Picture taken by Chandra Prabowo.

5.4. LiTFSI-doped spiro-MeOTAD by thermal evaporation

In the previous chapter is has been demonstrated that LiTFSI acts as a p-dopant for spiro-MeOTAD and that tBP is required for a homogeneous distribution of LiTFSI, when LiTFSI-doped spiro-MeOTAD films are deposited by spin-coating. In the following, LiTFSI-doped spiro-MeOTAD films will be deposited in the vacuum by thermal co-evaporation of LiTFSI and spiro-MeOTAD to investigate whether i) spiro-MeOTAD can be doped with LiTFSI in a vacuum process and ii) a vacuum process requires the addition of tBP for a successful doping as well. Since tBP only results in a more homogeneous distribution of LiTFSI inside the spiro-MeOTAD film, it is reasonable to assume that tBP is not required in a vacuum process. The co-evaporation process itself provides already a more uniform mixing of the precursor materials compared to a spin-coating process. Three different spiro-MeOTAD thin films have been prepared by thermal evaporation of LITFSI and spiro-MeOTAD: i) a spiro-MeOTAD sample without any LiTFSI, ii) a medium doped sample (spiro-MeOTAD to LiTFSI of 1 : 0.7) and iii) a highly doped sample (spiro-MeOTAD to LiTFSI of 1 : 5.3). In the following, these vacuum-deposited thin films are compared to spin-coated spiro-MeOTAD films: one without LiTFSI and two that are similarly doped as the vacuum-deposited films (spiro-MeOTAD to LiTFSI ratios of 1 : 0.8 and 1 : 5.3). It is emphasized here that the given spiro-MeOTAD to LiTFSI ratios were determined from XPS measurements. The C1s and F1s peaks of spiro-MeOTAD and LiTFSI were integrated, normalized as described in chapter 1.3.4, and divided by the number of C and F atoms inside the respective molecules. The presented spiro-MeOTAD to LiTFSI ratios are therefore not directly comparable to the ratios given in Figure 5.3, which are the molar ratios that were used inside the precursor solution.

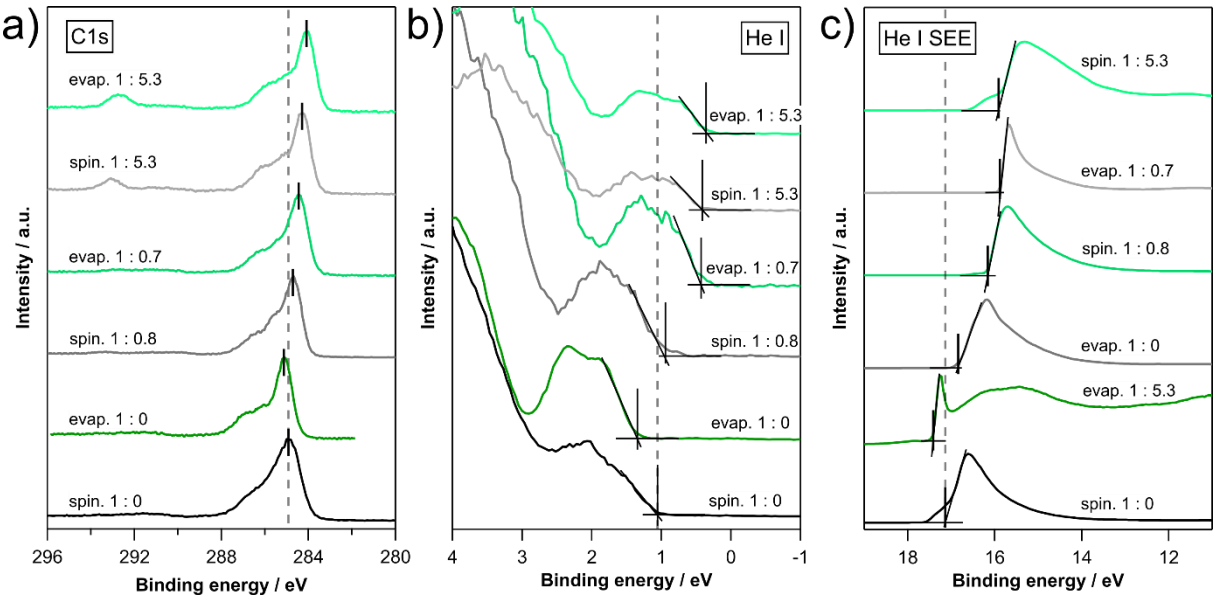

Figure 5.7: C1s emission, He I without bias and He I measurements with an applied bias of -6V to determine the work function of spin-coated and vacuum-deposited undoped an LiTFSI-doped spiro-MeOTAD films. The evaporated doped samples were synthesized by co-evaporation of LiTFSI and spiro-MeOTAD. The spiro-MeOTAD : LiTFSI ratios at the bottom were calculated by comparing the intensities of the C1s emission line belonging to spiro-MeOTAD and the F1s emission line of LiTFSI. The ratios are therefore not comparable to the values given in Figure 5.3, which are molar ratios inside the precursor solution. For a better comparison, all spectra have been normalized to 1.

Figure 5.8 summarizes the binding energy shifts of all emission lines of the vacuum-deposited spiro-MeOTAD samples in comparison to the spin-coated spiro-MeOTAD films. The C1s emission lines, He I measurements without bias, and He I measurements with an applied bias to determine the work function are presented in Figure 5.7. The C1s emission line (see Figure 5.7 a) of the spin-coated spiro-MeOTAD film without LiTFSI addition (bottom curve) appears at a binding energy of 284.91 eV. In comparison, the C1s emission line of the vacuum-deposited sample without any LiTFSI is positioned at 285.10 eV, and therefore shifted to higher binding energies by 0.19 eV. Similar binding energy shifts between both samples are also observed for the N1s emission lines (0.17 eV) as well as for the O1s emission lines (0.09 eV). The absolute binding energy values and the spectra of the N1s and O1s emission lines are shown in Table 9.10 and Figure 9.7 in the Appendix. The VBM of the vacuum-deposited spiro-MeOTAD without addition LiTFSI sample appears at 1.34 eV and therefore shifted by 0.25 eV to higher binding energies compared to the VBM of the spin-coated sample without LiTFSI (1.09 eV). The fact that all core level emission lines and the VBM of the spin-coated sample appear shifted to lower binding energies by around 0.18 eV, indicates that the spin-coated sample is slightly p-doped, even though no LiTFSI was added to the precursor solution during the spin-coating process. Such doping could be caused by short exposures to oxygen in the ambient atmosphere while transporting the sample to the XPS system [221,222] or by impurities inside the precursor solution during spin-coating.

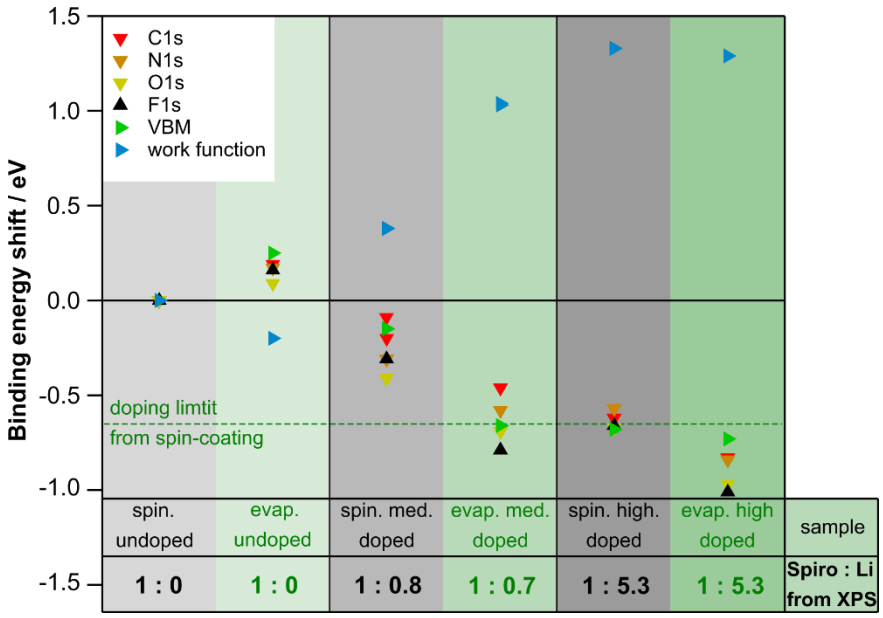

Figure 5.8: Binding energy shifts of the C1s, the N1, the O1s and the F1s emission lines along with the VBM values and work function values determined from He I measurement and the ionization potential values of spin-coated and vacuum-deposited LiTFSI-doped spiro-MeOTAD films. The spiro-MeOTAD : LiTFSI ratios at the bottom were calculated by comparing the intensities of the C1s emission line belonging to spiro-MeOTAD and the F1s emission line of LiTFSI. The integrated peak areas were normalized as described in the experimental section of chapter X and divided by the number of C atoms and F atoms inside spiro-MeOTAD and LiTFSI, respectively. The ratios are therefore not comparable to the values given in Figure 5.3, which are molar ratios inside the precursor solution.

The two curves in the middle represent two LiTFSI-doped spiro-MeOTAD samples with similar spiro-MeOTAD to LiTFSI ratios, one being prepared from solution (ratio 1 : 0.8) and the other prepared by thermal co-evaporation (ratio 1 : 0.7). In both cases, the C1s emission is shifted to lower binding energies, indicating a successful p-doping by LiTFSI. For the co-evaporated spiro-MeOTAD sample the shift to lower binding energies of the C1s emission line is stronger (284.45 eV compared to 284.71 eV for the spin-coated), suggesting that the doping is more efficient for the vacuum process. Likewise, the VBM of the co-evaporated spiro-MeOTAD samples appears at lower binding energies (0.43 eV) compared to the spin-coated one (0.94 eV). The more efficient doping in the case of the vacuum deposition could be related to a more homogeneous distribution of LiTFSI in the spiro-MeOTAD matrix. In case of an agglomeration of the LITFSI dopant, some LiTFSI molecules in the center of an agglomerate would not contribute to the doping process since they do not have any spiro-MeOTAD molecules in their near vicinity. Agglomeration of dopants is a known issue when doping organic semiconductor, especially at higher doping concentrations [223–226]. The fact that the vacuum-deposited spiro-MeOTAD films can be doped with LiTFSI, even without the addition of tBP, confirms the improved mixing of spiro-MeOTAD and LiTFSI for the vacuum process compared to sample preparation by spin-coating.

The top two curves represent a spin-coated and a vacuum-deposited LiTFSI-doped spiro-MeOTAD sample, both with spiro-MeOTAD to LiTFSI ratios of 1 : 5.3 and therefore a higher LiTFSI content as the previously discussed samples. For the spin-coated sample the C1s emission line and the VBM appear at 284.29 eV and 0.41 eV, which is the doping limit for the LiTFSI-doped spiro-MeOTAD samples deposited by spin-coating. Compared to that, the C1s emission and the VBM of the vacuum-deposited are positioned at 284.09 eV and 0.36 eV indicating a stronger p-doping compared to the spin-coating process even beyond the determined doping limit determined for the spin-coated samples in chapter 5.3.

To summarize the results of this chapter, it has been demonstrated that spiro-MeOTAD can be doped with LiTFSI in a co-evaporation process without the use of tBP. Compared to the doping of spiro-MeOTAD by spin-coating, the vacuum process seems to result in a more homogeneous distribution of the LiTFSI dopant inside the spiro-MeOTAD film and therefore a more efficient doping for the same LiTFSI concentration. The doping of spiro-MeOTAD in a vacuum process allows performing a detailed interface characterization between MAPI and LiTFSI-doped spiro-MeOTAD in a classical step-by-step interface experiment. Since for perovskite solar cells in classical architecture, a majority of the photovoltage has been identified at the interface between MAPI and spiro-MeOTAD, such an interface experiment is of high interest. Before investigating the interface between MAPI and LiTFSI-doped spiro-MeOTAD, the doping mechanism of spiro-MeOTAD with LiTFSI will be investigated further by performing an interface experiment between both materials.

5.5. The interface between spiro-MeOTAD and LiTFSI

To systematically investigate the doping process of spiro-MeOTAD with LITFSI, a detailed interface experiment between both materials has been performed by stepwise depositing LiTFSI onto a vacuum-deposited undoped spiro-MeOTAD film with *in-vacuo* XPS and UPS measurements in between each deposition step. There are no indications of source-induced SPVs in these experiments as usually expected for semiconductors with no photovoltaic performance. At first, the band energy diagrams of both materials, deduced from XPS and UPS measurements of thick vacuum-deposited films, are compared in Figure 5.9. The bandgap value of spiro-MeOTAD (2.97 eV) has been determined from the UV/Vis measurement shown in Figure 9.5 in the Appendix. The bandgap value of LiTFSI of 5.34 eV has been taken from He *et al.* [227]. Even though the LUMO level of LiTFSI is positioned above the HOMO level of spiro-MeOTAD, which may lead to the conclusion that an electron transfer from spiro-MeOTAD to LiTFSI is not possible, LiTFSI can still act as a p-dopant for spiro-MeOTAD as shown in the previous chapters. A charge transfer from the HOMO level of spiro-MeOTAD to possible defects states of LiTFSI is one possible mechanism. Another explanation might be given by Salzmann *et al.* [228], who proposed a charge transfer complex model in which hybridization of the HOMO of the matrix molecule and the

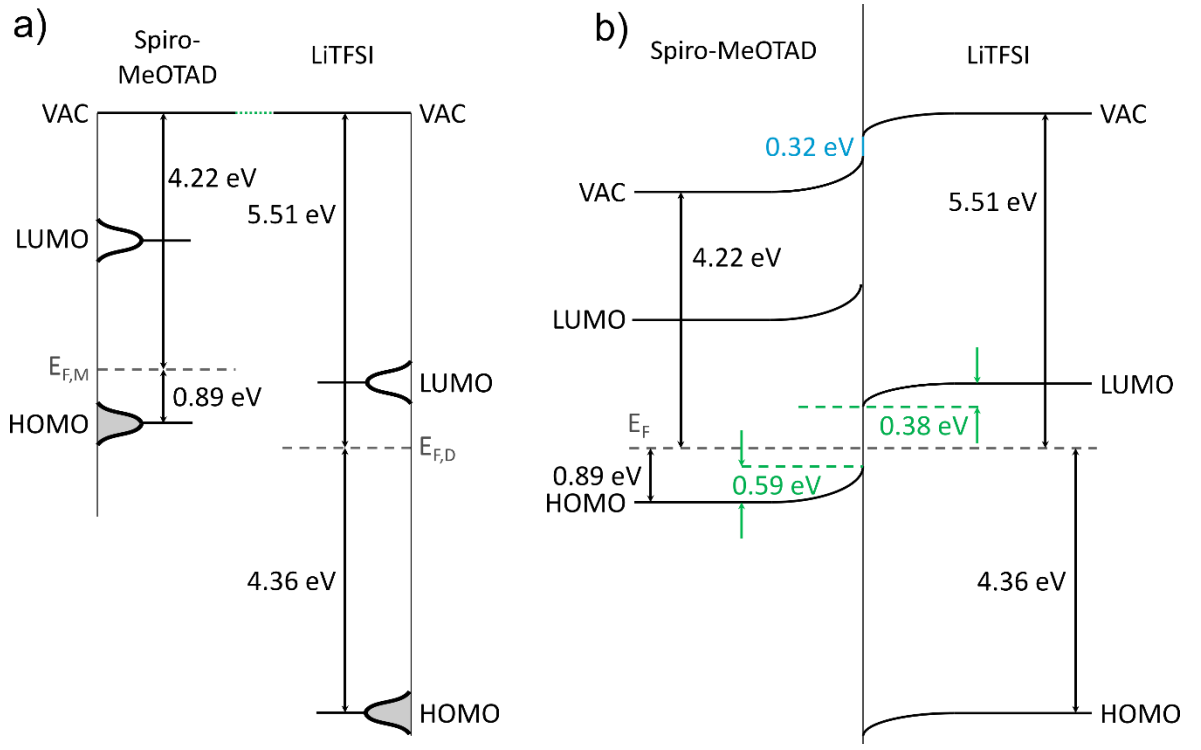

Figure 5.9: a) Energy levels of a thick spiro-MeOTAD film (left) and a thick LiTFSI film (right), aligned by their vacuum levels. Since the HOMO level of spiro-MeOTAD is positioned below the LUMO level of LiTFSI an electron transfer from spiro-MeOTAD to LiTFSI is not expected from the classical point of view where single LiTFSI dopant molecules are dissolved inside a spiro-MeOTAD matrix. b) The determined band diagram between spiro-MeOTAD and LiTFSI. The work function difference of 1.29 eV between both materials is compensated by an interface dipole $\delta = 0.32\ eV$ and band bending inside the matrix material and dopant of $V_{bb,M} = 0.59$ eV and $V_{bb,D} = 0.38$ eV, respectively. The observed band bending inside the matrix material fits nicely to the doping limit of 0.65 eV which was determined in Chapter 5.3 from spin-coated spiro-MeOTAD films with varying LiTFSI concentration.

LUMO of the dopant forms a complex with changed energy levels. Mayer *et al.* [226] propose the internal interface charge transfer doping model to address this issue. They argue that the dopant molecules form large enough precipitations so that they cannot be considered as single molecules anymore, meaning they must be described as a second phase with its own Fermi level. The charge transfer is now determined by the thermodynamic equalization of the Fermi level of matrix and the precipitations. At the "internal interface" between the dopant precipitations and the matrix, the formation of an electrical dipole is expected, which will in general take up part of the Fermi level difference between matrix and dopant. The magnitude of this dipole can be approximated by a classical step-by-step interface experiment between the matrix and dopant material. The doping limit of the matrix molecule can then be determined by the work function difference of the pure materials (matrix and dopant molecule) minus the determined interface dipole. Since the formation of LiTFSI precipitations is not only expected but has been shown in the literature and this work (see chapter 5.3), the internal interface charge transfer doping model will be applied.

During the discussion of the spiro-MeOTAD | LiTFSI interface the C1s emission line of spiro-MeOTAD and the F1s emission line of LiTFSI will be used to determine the matrix (spiro-MeOTAD) and dopant (LiTFSI) band bending values, respectively. Furthermore, the change of the shape of the C1s emission lines of spiro-MeOTAD with increasing LiTFSI thickness will be used to take a closer look at the charge transfer between both molecules. The N1s, O1s, and S2p emission lines will not be treated to determine band bending values, since either the contributions of matrix and dopant are overlapping, making an independent determination of the binding energy values complicated (N1s and

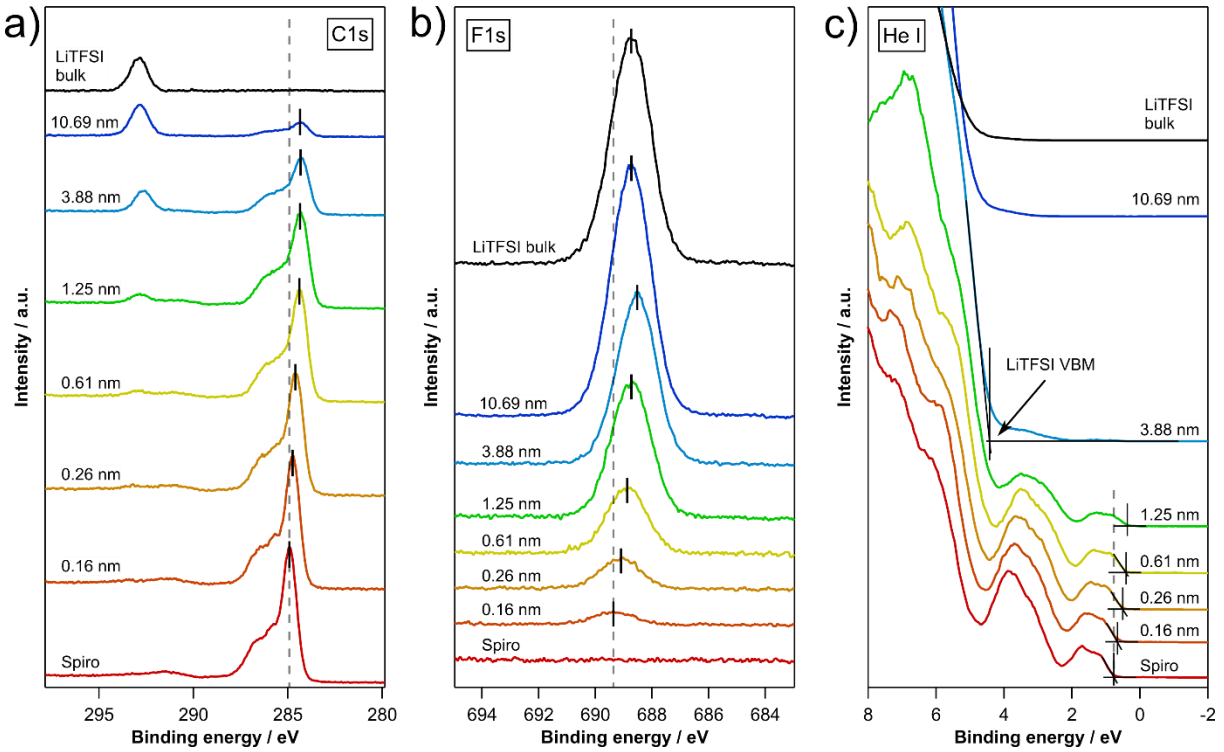

Figure 5.10: a) C1s, b) F1s emission lines and He I measurements to determine the VBM values of spiro-MeOTAD (red curve at the bottom) and step-wise deposited LiTFSI with increasing thickness from bottom to top. The LiTFSI thickness values have been determined from the damping of the C1s emission line of spiro-MeOTAD through equation 1.19 in chapter 1.3.3.

O1s), or their signal-to-noise ratio is too poor (S2p). For completeness, all spectra are presented in the Appendix in Figure 9.9 along with the He I measurements with an applied bias of -6 V to determine the work function values. Figure 5.10 presents the C1s emission lines, the F1s emission lines, and the He I measurements for the pure undoped spiro-MeOTAD substrate (red curve at the bottom) and increasing LiTFSI thicknesses when going from bottom to top. The LiTFSI thicknesses have been calculated from the damping of the C1s signal of the spiro-MeOTAD substrate following equation 1.19. For the spiro-MeOTAD substrate the C1s emission line appears at 284.91 eV and shifts gradually to lower binding energies until it appears at 284.34 eV (dark blue curve), indicating an upward band bending inside spiro-MeOTAD towards the interface. The F1s emission of LiTFSI appears after the first deposition step (0.16 nm) at a binding energy of 689.36 eV and is gradually shifting to lower binding energies as well until it appears at 688.52 eV for a LiTFSI thickness of 3.88 nm. For the last two deposition steps (10.69 nm and the LiTFSI bulk) the F1s emission lines appear at 699.72 eV and 699.73 eV, respectively, and are therefore shifted back to higher binding energies. This shift to higher binding energies is related to a charging of the sample, which can be caused by a too low electrical conductivity of the LiTFSI adsorbate layer [229]. The charging becomes more evident when comparing the He I work function measurements (see Appendix Figure 9.9). The last two deposition steps are therefore not considered for the interface analysis. The binding energy shifts of the C1s and F1s emission lines in dependence of the LiTFSI thickness are summarized in Figure 5.11, referenced to the binding energy position corresponding to a LiTFSI thickness of 0 nm. For F1s, the reference value at

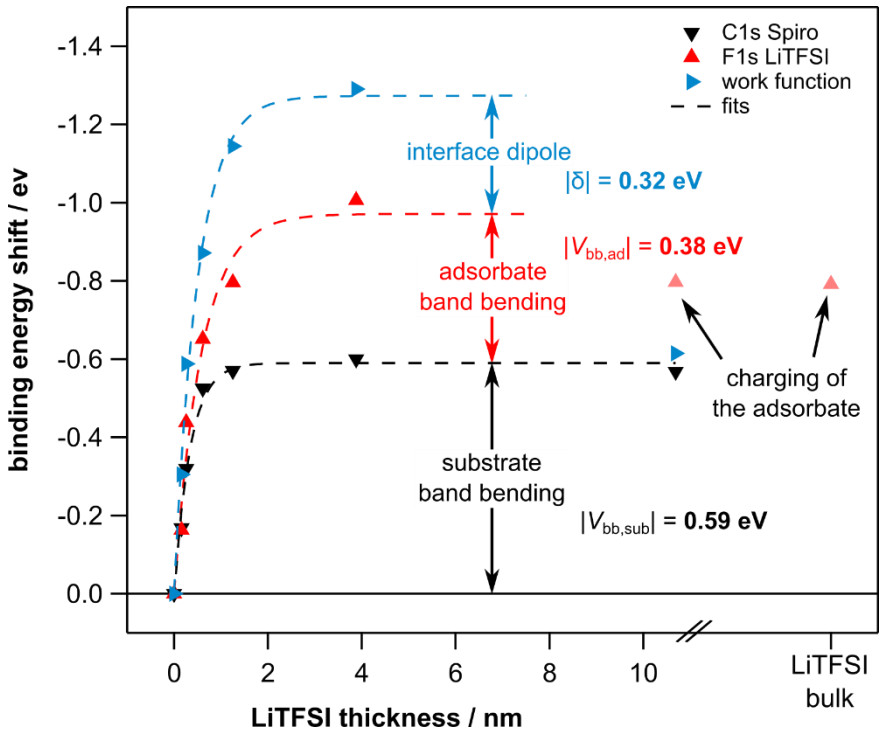

Figure 5.11: The binding energy shifts of the C1s emission line of spiro-MeOTAD and the F1s of LiTFSI to determine the band bending inside the substrate and the adsorbate. The blue horizontal line represents the work function difference between spiro-MeOTAD and LiTFSI and is used to determine the strength of the interface dipole. For simplicity, absolute values of the band bendings and the interface dipole are given.

0 nm has been determined by an extrapolation based on an exponential fit (see Figure 9.8 in the Appendix).

The formulas that are used in the following define the band bending values coming from the bulk of the substrate/adsorbate and going towards the interface. Since in PES the binding energy is increasing when going from the Fermi level towards the core levels, an upward band bending corresponds to a decrease and a downward band bending to an increase in binding energy. A more detailed explanation is given in the fundamentals in chapter 1.6.1.

Since the C1s emission line of spiro-MeOTAD is showing a total shift of $\Delta E_{sub} = -0.59\ eV$ eV to lower binding energies it can be concluded that an upward band bending of

$$V_{bb,sub} = \Delta E_{sub} = -0.59\ \text{eV}$$

towards the interface is present inside spiro-MeOTAD (see Figure 5.9 b). The F1s emission line of LiTFSI is shifted to lower binding energies as well, but the shift is larger ($\Delta E_{sub} = -0.97$eV) compared to the shift of the C1s emission of spiro-MeOTAD. LiTFSI is therefore showing a downward band bending towards the interface of

$$V_{bb,ads} = \Delta E_{ads} - \Delta E_{sub} = -0.59\ \text{eV} - (-0.97\text{eV}) = 0.38\ \text{eV}.$$

Along with the work functions of n spiro-MeOTAD and LiTFSI, the interface dipole is determined to be

$$\delta = \varphi_{sub} - \varphi_{ads} - V_{bb,sub} + V_{bb,ads} = 4.22\ eV - 5.51eV - (-0.59\ eV) + 0.38\ eV = -0.32\ \text{eV}.$$

The corresponding band diagram between spiro-MeOTAD and LiTFSI is presented in Figure 5.9. Based on the internal interface charge transfer doping model a doping limit of 0.59 eV is predicted (amount of band bending inside the matrix material), which fits nicely to the doping limit of 0.65 eV determined in chapter 5.3 from spin-coated spiro-MeOTAD films with varying LiTFSI concentrations.

By looking at the change of the shape of the C1s emission line with increasing LiTFSI thickness, the carbon atom which transfers the electron in the doping process to LiTFSI can be identified. Therefore, the C1s emission lines of spiro-MeOTAD for the different LiTFSI overlayer thicknesses are summarized in Figure 5.12 a). XPS measurements by Hock *et al.* [230] of the C1s emission line of two different spiro-MeOTAD films along with a proposed fitting model to distinguish the different carbon species inside the spiro-MeOTAD molecule are presented in Figure 5.12 b). For each LiTFSI deposition step in Figure 5.12 a), more charges are being transferred from spiro-MeOTAD to LiTFSI, resulting in a stronger p-doping of spiro-MeOTAD with increasing LiTFSI thickness. The charge transfer has two effects on the C1s emission line of spiro-MeOTAD: i) an overall shift of the C1s emission lines to lower binding energies (which is in principle the doping-induced Fermi level shift) and ii) a shift of the oxidized spiro-MeOTAD carbon species from, which the transferred electron originates, to higher binding energies. To accommodate for the doping-induced Fermi level shift inside the spiro-MeOTAD, the spectra are shifted on the binding energy axis so that their maxima are aligned at the position of

undoped spiro-MeOTAD. In addition, the C1s spectra have been normalized with respect to the area under the curve. The normalization with respect to the integrated area allows to compare the relative intensities of the different carbon species inside the spiro-MeOTAD molecule and therefore identify which carbon species is being oxidized due to the charge transfer to LiTFSI. Looking at Figure 5.12 a), a decrease of the intensity around the main peak at 284.9 eV (blue peak I in Figure 5.12 b) can be observed, which leads to the conclusion that during the doping of spiro-MeOTAD with LiTFSI the electrons are being transferred from the carbon atoms positioned at the benzol ring at the core of the spiro-MeOTAD molecule (position I in Figure 5.12 b). After the charge transfer to LiTFSI, the oxidized carbon species add to the emission at a binding energy range between 285.7 eV and 286.8 eV, which means that the local electron density of the oxidized species is comparable to carbon atoms located in the outer benzol rings of spiro-MeOTAD (red peak III and green peak IV in Figure 5.12 b).

To conclude, a first comparison of the energy levels of the matrix material spiro-MeOTAD and the dopant molecule LiTFSI showed that the LUMO level of LiTFSI is positioned above the HOMO level of spiro-MeOTAD which would indicate that an electron transfer from spiro-MeOTAD to LiTFSI and therefore a p-doping is not possible. However, based on the internal interface charge transfer doping model, p-doping of spiro-MeOTAD with LiTFSI becomes possible if one assumes that LiTFSI forms large

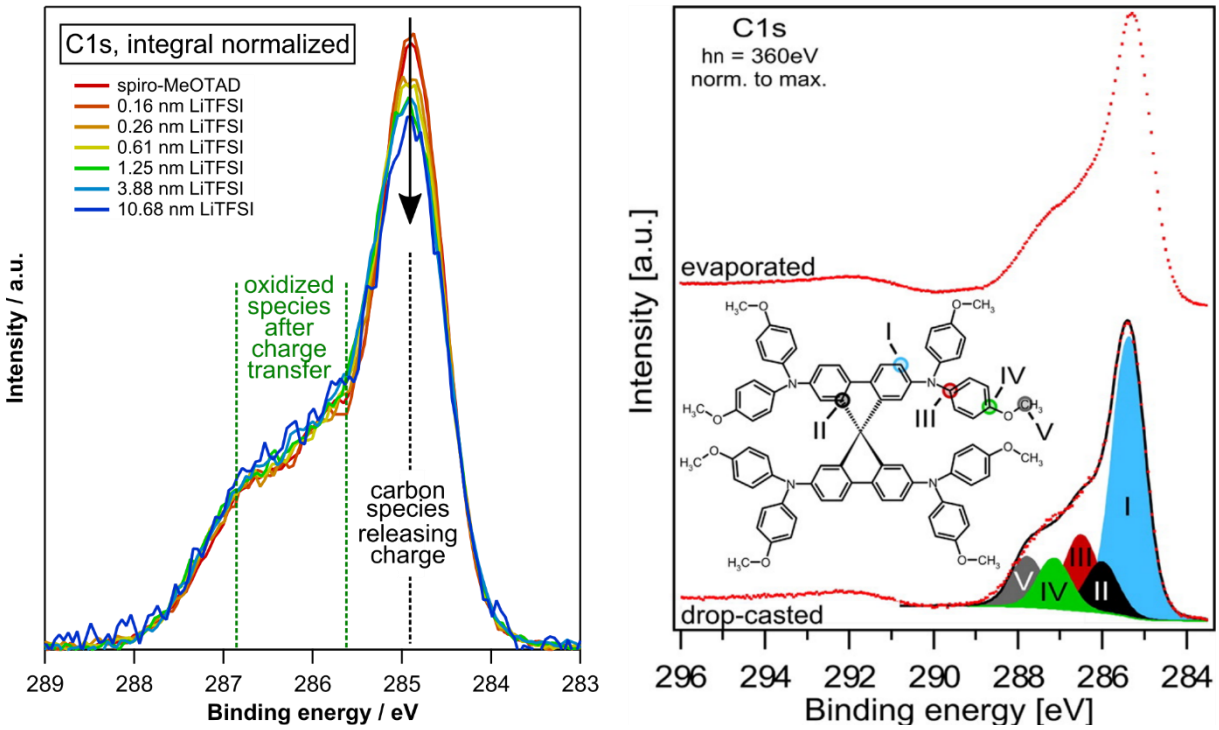

Figure 5.12: a) The change of the C1s emission line of spiro-MeOTAD during the spiro-MeOTAD | LiTFSI interface experiment. A Shirley background subtraction has been performed. All spectra are normalized with respect to the integrated area below the respective curve and shifted in the binding energy axis so that their maxima coincide with the maximum of the undoped spiro-MeOTAD. b) C1s emission line of spiro-MeOTAD films measured by Hock *et al.* and their proposed fitting model for the different carbon species inside the spiro-MeOTAD molecule.

enough precipitations so that they can be considered as a second phase with its own Fermi level. Based on the results in chapter 5.3 and several literature reports [214,216,217] the formation of LiTFSI precipitations seems reasonable. The interface experiment between spiro-MeOTAD and LiTFSI revealed a band bending of 0.59 eV inside spiro-MeOTAD, which fits very well to the doping limit of 0.65 eV determined in chapter 5.3. Finally, it has been demonstrated that while p-doping spiro-MeOTAD with LiTFSI, the electrons are being transferred from carbon atoms positioned at the inner benzol rings at the core of the spiro-MeOTAD molecule to LiTFSI.

5.6. MAPI | LiTFSI-doped spiro-MeOTAD interface

Since it has been demonstrated in chapters 5.3 and 5.4 that spiro-MeOTAD can be p-doped by LiTFSI in a vacuum process through co-evaporation of spiro-MeOTAD and LiTFSI, the framework for an interface experiment between MAPI and LiTFSI-doped spiro-MeOTAD has been set. Investigating the MAPI | LiTFSI-doped spiro-MeOTAD interface in detail is of high interest since it has been identified as the origin of the majority of the photovoltage for perovskite solar cell devices in classical architecture (see chapter 4.4). A detailed interface characterization by stepwise deposition of LiTFSI-doped spiro-MeOTAD on top of a pre-deposited MAPI film and subsequent XPS and UPS measurements will allow verifying the presence of a band bending under dark conditions. Illuminated PES measurements will help to determine the amount of photovoltage. The interface between MAPI and *undoped*

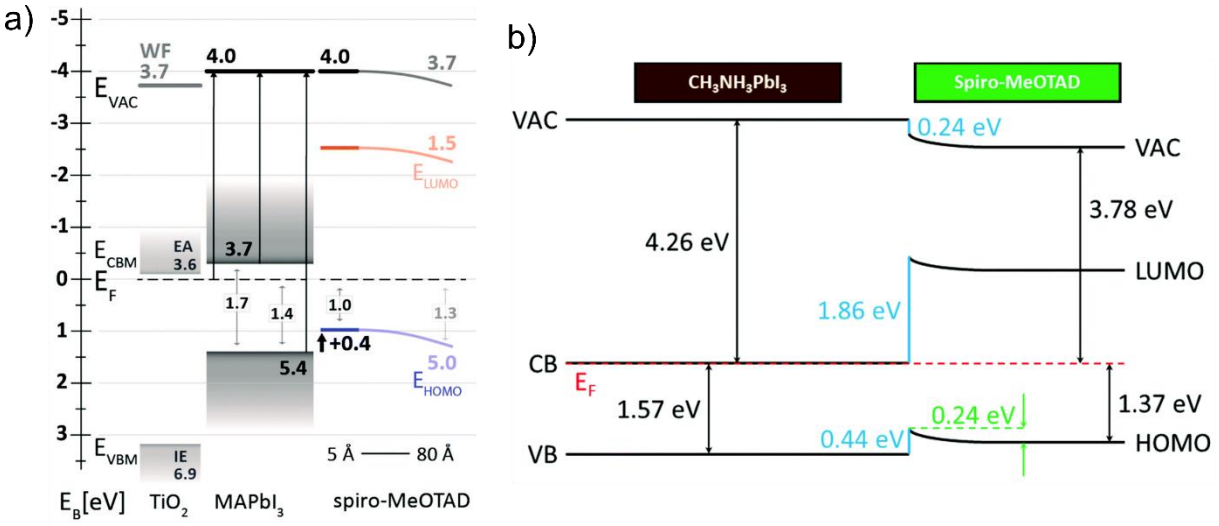

Figure 5.13: The energy band diagram between MAPI and undoped spiro-MeOTAD as it has been determined by a) Schulz *et al.* and b) Hellmann *et al.*

spiro-MeOTAD has been characterized before by Schulz *et al.* [198] in 2014. The authors reported a flat band inside MAPI and inside spiro-MeOTAD an upward band bending towards the interface of 0.3 eV, which should in principle impede the extraction of holes from MAPI into the HOMO of spiro-MeOTAD (see Figure 5.13 a). A similar band energy diagram has been determined by the author of this Ph.D. thesis in 2019 (see Figure 5.13 b). In both cases, a valence band offset of around 0.4 eV between the VBM of MAPI and the HOMO level spiro-MeOTAD was determined. Under the assumption that the VBM offset does not change when spiro-MeOTAD is differently doped, the lower VBM of the p-doped spiro-MeOTAD should change the direction of the band bending inside the spiro-MeOTAD. To the best of the author's knowledge, a detailed interface characterization between MAPI and LiTFSI-doped spiro-MeOTAD has not been reported in the literature before and was only discussed in the supplementary information of our publication [231].

The N1s emission lines for the different deposition steps of the interface are presented in Figure 5.14 a). For the pre-deposited MAPI film, the N1s emission line appears at 402.59 eV. Since the N1s emission line of MAPI and spiro-MeOTAD are positioned about 2 eV away from each other, the N1s region can be used to determine the band bending of both the substrate as well as the adsorbate. Upon deposition of LiTFSI-doped spiro-MeOTAD, the N1s emission line of MAPI is shifting to lower binding energies by a total amount of 0.10 eV. Similar binding energies shifts are determined for the $Pb4f_{7/2}$ (0.08 eV) as well as the $I3d_{5/2}$ emission line (0.10 eV) (see Figure 9.12 in the Appendix). The N1s emission line of spiro-MeOTAD is shifting to lower binding energies as well, with a total binding energy

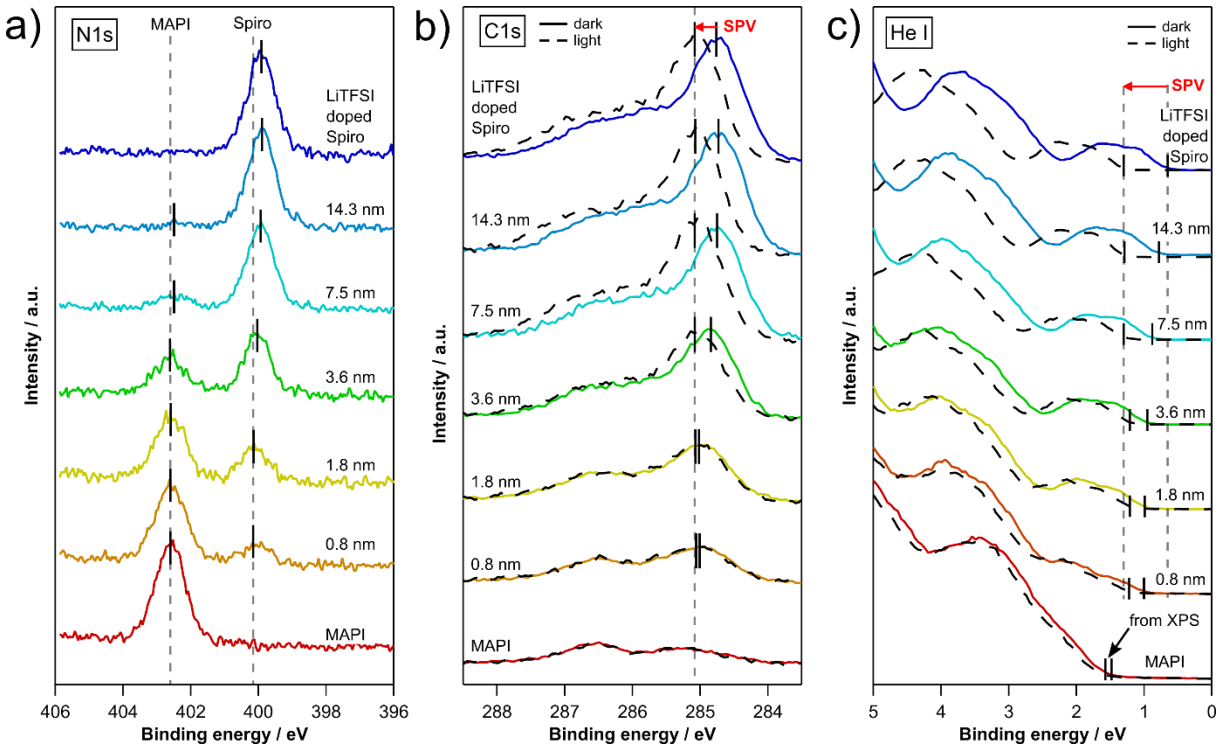

Figure 5.14: a) N1s emission lines, b) C1s emission lines and c) He I measurements to determine the VBM values of a MAPI film (red curve at the bottom) and step-wise deposited LiTFSI-doped spiro-MeOTAD with increasing thickness from bottom to top. The spiro-MeOTAD thickness values have been determined from the damping of the Pb4f and I3d emissions line of MAPI through equation 1.19 in chapter 1.3.3.

shift of 0.31 eV. It is therefore assumed that MAPI, as well as spiro-MeOTAD, shows band bending towards the interface.

The C1s emission lines for the different deposition steps of the interface are presented in Figure 5.14 b). To make the binding energy shifts more noticeable only the binding energy range from 283 eV to 289 eV is shown. For completeness, the full binding energy range of the C1s emission line is shown in the Appendix in Figure 9.12. The solid and broken lines in Figure 5.14 b) represent measurement in the dark and under illumination, respectively. Since the C1s signal of MAPI and spiro-MeOTAD are overlapping, the binding energy positions of the C1s emission of spiro-MeOTAD at thicknesses of 0.8 nm, 1.8 nm, and 3.6 nm have been determined from difference spectra. Details regarding the difference spectra are given in the Appendix in Figure 9.10. Looking at the dark measurements (solid lines) a shift to lower binding energies with increasing spiro-MeOTAD thickness can be observed. The total shift of 0.24 eV is comparable to the shift of 0.31 eV that has been observed for the N1s emission line (see Figure 5.13). In case of the light measurements, the C1s emission lines of spiro-MeOTAD are all appearing at around 285 eV, indicating that the band bending which is present in the dark is changing to a flat-band situation upon illumination. The difference between the C1s emission line in the dark and under illumination for each interface step is equal to the light-induced SPV. The light-induced SPV is therefore increasing while the interface is being built up, until a maximum SPV value of 0.32 eV for the last spiro-MeOTAD deposition step is reached.

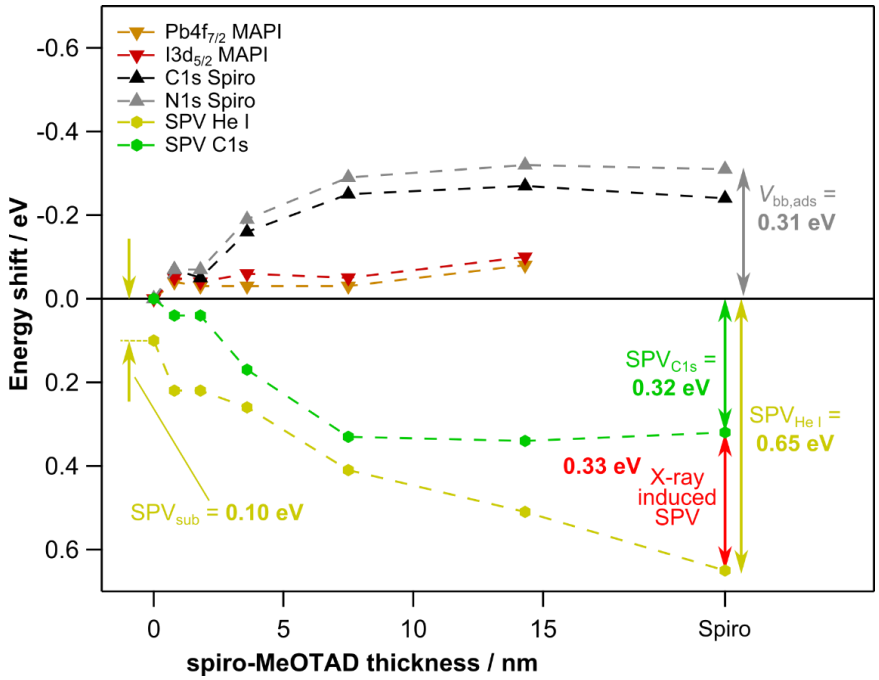

Figure 5.15: The binding energy shifts of the Pb4f, I3d, C1s and N1s emission lines along with the increase of the SPV values determined from C1s and He I in dependence of the spiro-MeOTAD thickness. From the core level shifts determined by the XPS measurements in the dark, substrate and adsorbate band bending values of 0.09 eV and 0.22 eV are determined, resulting in a total band bending of 0.31 eV. Under illumination, SPV values of 0.32 eV and 0.65 eV are determined by XPS and UPS, respectively. It is therefore assumed that an X-ray induced SPV of 0.65 eV – 0.32 eV = 0.33 eV is present for the XPS dark measurements. Due to the X-ray induced SPV determining the band bending from the core level shifts results in an underestimation of the total band bending.

Figure 5.14 c) presents the He I measurements. Similar to the C1s emission lines, the solid and broken lines represent measurement in the dark and under illumination, respectively. For the pre-deposited MAPI substrate, the VBM values were determined from logarithmic XPS measurements of the valence band region to account for the low DOS region at the valence band onset. In the dark, the VBM of MAPI appears at 1.30 eV and is shifting to a value of 1.40 eV upon exposure to light. The MAPI perovskite seems to form already a minor photovoltage of 0.10 V, which should originate from the SnO_2 | MAPI interface. With increasing spiro-MeOTAD, the light-induced SPV is gradually increasing until a maximum value of 0.65 V for the bulk of the LiTFSI-doped spiro-MeOTAD.

The VBM values for the illuminated measurements are all positioned in between 0.90 eV and 1.0 eV, indicating a flat band situation as it has already been observed for the C1s emission lines in Figure 5.14 b). Compared to the observed SPV values determined from the C1s emission lines (maximum SPV of 0.31 eV), the SPV values determined from the He I VBM measurements are considerably higher (maximum SPV of 0.65 eV, see also Figure 5.15). The different SPV values observed in the XPS and the UPS measurements are explained by the presence of an X-ray induced SPV. The formation of a X-ray-induced SPV has been proven before for a MAPI | LiTFSI-doped spiro-MeOTAD sample in chapter 3.4.3 (see Figure 3.8), where the spiro-MeOTAD film was deposited by spin-coating. The XPS measurements in the dark are therefore resembling a non-equilibrium situation, where already some SPV is present. Consequently, the additional SPV that can be induced for the XPS measurements by turning on the light is lowered compared to the UPS measurements. The different development of the SPV values determined by XPS and UPS measurements is depicted in Figure 5.15. From the difference between SPV from UPS and XPS for the bulk spiro-MeOTAD film, the X-ray-induced SPV is determined to be 0.33 eV.

Since the XPS dark measurements are affected by an X-ray-induced SPV, the shift of the core levels will not reveal the full substrate and adsorbate band bending values. As an alternative approach, it can be assumed that for the formation of an SPV under illumination a band bending of the same magnitude or higher must be present in the dark. Considering that the SPV increased from 0.10 eV (for the pre-deposited MAPI substrate) up to a maximum value of 0.65 eV for the bulk of the LiTFSI-doped spiro-MeOTAD film, it is assumed that a total band bending of at least 0.55 eV exists at the MAPI | LiTFSI-doped spiro-MeOTAD film in the dark, which appears completely on the spiro-MeOTAD side.

The resulting band diagrams for the MAPI | LiTFSI-doped spiro-MeOTAD interface are sketched in Figure 5.16 with a) showing the dark and b) the illuminated situation. Since an SPV of 0.1 eV has been observed for MAPI without any spiro-MeOTAD deposition, a band bending of 0.1 eV is drawn towards the SnO_2 substrate. At the MAPI | spiro-MeOTAD interface a band bending of 0.55 eV appears at the spiro-MeOTAD side. Given the work function values of 4.40 eV and 4.80 eV for MAPI and spiro-MeOTAD, an interface dipole of 0.15 eV arises. Upon illumination, an SPV of 0.65 V is formed, which results in a quasi-Fermi level splitting inside the perovskite absorber. It is emphasized here that the maximum observed SPV value of 0.65 V is remarkably high. Previous SPV measurements of an identical sample stack, where the deposition processes of all layers were optimized so that the full photovoltaic devices achieved PCE values of up to 11.6%, shows a similar SPV of 0.68 V (see chapter

4.5, Figure 4.5). Due to the formation of the SPV of 0.65 V, the band bending disappears and a flat-band situation is achieved. The light grey horizontal extension of the Fermi level ($E_{F,ref}$) in Figure 5.16 b) indicates the grounded Fermi level which is the reference energy for the PES measurements. By comparing the HOMO level of spiro-MeOTAD to the reference Fermi level it becomes evident that the HOMO level and the core levels measured in PES are shifted to higher binding energies, due to the formation of the SPV. Under illumination, work function values of 4.32 eV and 4.19 eV are determined for MAPI and LiTFSI-doped spiro-MeOTAD, resulting in an interface dipole of 0.13 eV which is close to the value of 0.15 eV determined for the dark situation. The illumination does therefore not affect the interface dipole at the MAPI | LiTFSI-doped spiro-MeOTAD interface. The fact, that the band bending at the MAPI | spiro-MeOTAD interface appears completely at the spiro-MeOTAD side raises the question how the generated holes can be separated. Due to the large band of spiro-MeOTAD of 2.97 eV, absorption will only take place in the MAPI layer. Extraction of the holes into the spiro-MeOTAD can therefore only take place through diffusion since the electric field of the space charge region (the band bending) is completely located on the spiro-MeOTAD side. Since metal halide perovskite absorbers like MAPI are showing excellent charger carrier lifetimes and extremely long diffusion lengths (see chapter 1.1) a purely diffusion-controlled charge carrier separation seems reasonable. As for silicon solar cells, the charge carrier lifetime in the perovskite absorber layer allows them to reach the charge extraction layers by diffusion.

To summarize, the presence of a band bending in the dark and the formation of an SPV under illumination at the MAPI | LiTFSI-doped spiro-MeOTAD interface has been demonstrated through a classical step-by-step interface experiment. These findings agree with the SPV measurements presented in chapter 4.5 (see Figure 4.5). The amount of SPV (0.65 V) is comparable to an identical device stack employing an optimized spiro-MeOTAD film deposited through spin-coating. The total band bending of 0.31 eV that is observed with XPS for the dark measurements is smaller than the UPS SPV due to an X-ray induced SPV of 0.33 eV.

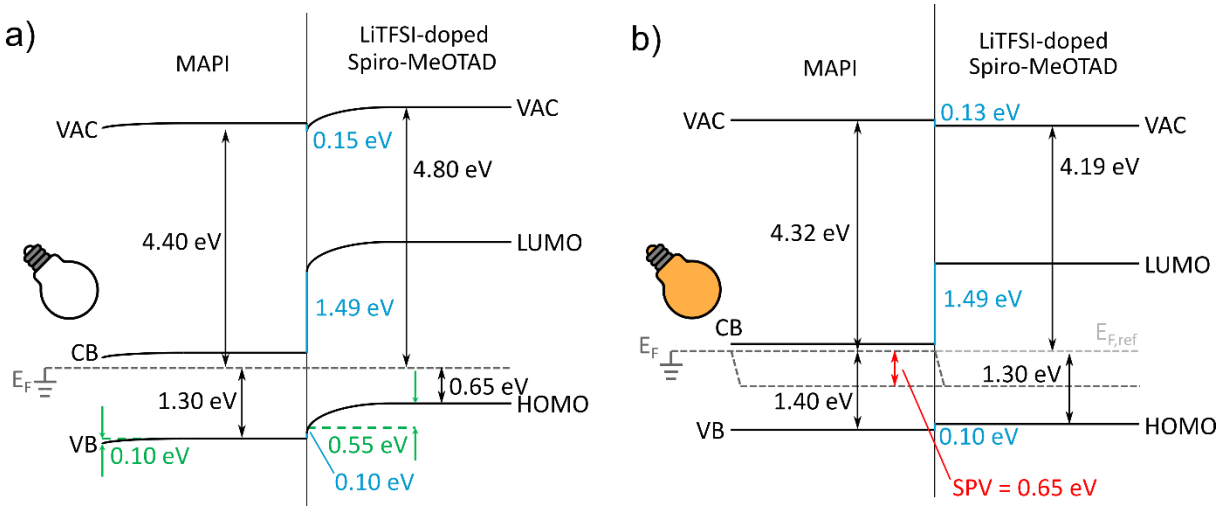

Figure 5.16: The determined band energy diagram between MAPI and LiTFSI-doped spiro-MeOTAD a) in the dark and b) under illumination. In the dark a total band bending of 0.10 eV (between SnO_2 and MAPI) + 0.55 eV (between MAPI and spiro-MeOTAD) = 0.65 eV is present. The full band bending of 0.55 eV observed at the MAPI | spiro-MeOTAD interface appears on the spiro-MeOTAD side. Upon illumination an SPV of 0.65 V is formed.

5.7. Summary and conclusion

In this chapter, the commonly used p-doping process of spiro-MeOTAD with LiTFSI as dopant and tBP as additional additive was studied to i) develop an understanding of the doping process and the roles of LiTFSI and tBP, ii) transfer the p-doping process of spiro-MeOTAD from a spin-coating technique to a vacuum-deposition and finally iii) use the developed vacuum-deposition process to investigate the interface between MAPI and p-doped spiro-MeOTAD concerning the presence of a band bending in the dark and an SPV under illumination.

Through the initial experiments on the role of LiTFSI and tBP it was demonstrated that while LiTFSI can act as a p-dopant for spiro-MeOTAD, the addition of tBP is required in the spin-coating process as well since tBP guarantees a homogeneous distribution of the LiTFSI inside the spiro-MeOTAD film (see chapter 5.3). Without adding tBP to the precursor solution, no p-doping of spiro-MeOTAD through LiTFSI could be achieved. The doping limit was determined for a spiro-MeOTAD to LiTFSI molar ratio of 1 : 0.4, resulting in a Fermi level shift of 0.65 eV towards the VBM of spiro-MeOTAD for the highest doped sample compared to the undoped sample.

Furthermore, it was shown that by a co-evaporation of spiro-MeOTAD and LiTFSI it is possible to p-dope spiro-MeOTAD with LITFSI without the addition of tBP (see chapter 5.4). An interface experiment between spiro-MeOTAD and LiTFSI by a step-wise deposition of LiTFSI on top of spiro-MeOTAD revealed a band bending of 0.59 eV inside the spiro-MeOTAD (see chapter 5.5). This band bending of 0.59 eV is comparable to the Fermi level shift of 0.65 eV of the highest doped sample which was prepared by spin-coating. In addition, it has been shown that the electron that is transferred from the spiro-MeOTAD molecule to the LiTFSI molecule during the doping process is transferred from a carbon atom positioned at the benzol ring at the core of the spiro-MeOTAD molecule.

Finally, the interface experiment between MAPI and LiTFSI-doped spiro-MeOTAD revealed a band bending inside the spiro-MeOTAD in the dark which has changed to a flat band situation under illumination, giving rise to an SPV (see chapter 5.6). For the thick spiro-MeOTAD film outside the influence of any space charge region, an SPV of 0.65 eV is observed, which is comparable to the SPV value compared for an identical device stack employing an optimized spiro-MeOTAD layer which was deposited by spin-coating (0.68 eV). For the dark measurements, an X-ray induced SPV was observed as well, which limits the amount of band bending that could be measured from the core level shifts.

6. The NiO_x | MAPI interface using tapered cross-section analysis

6.1. Motivation and chapter overview

The results of chapter 4.4 have shown that for the investigated perovskite solar cells the photovoltages are located at the n-MAPI | p-HEL interfaces, which is the p-NiO_x | n-MAPI interface in case of the inverted architecture devices. This chapter will aim to investigate this interface between NiO_x and MAPI in more detail, to verify the presence of a band bending at this interface in the dark. Compared to the n-MAPI | p-spiro-MeOTAD interface discussed in the previous chapter, the interface analysis between NiO_x and MAPI is more challenging since for a classical step-by-step interface experiment it is necessary to deposit films of the adsorbate material (in this case MAPI) with thicknesses of only 1 nm.

Even though MAPI can be deposited by co-evaporation from its precursor materials PbI_2 and MAI, the controlled deposition of stoichiometric films with thicknesses of less than 10 nm is not possible, due to the high vapor pressure and low sticking coefficient of MAI [204]. During a co-evaporation of MAPI, the deposition rate is therefore often not directly measured with a quartz crystal microbalance but is controlled by monitoring the pressure inside the vacuum chamber [209,232–235]. In fact, it has been shown that a stoichiometric MAPI film can be synthesized even when a shutter is placed in between the substrate and the MAI effusion cell [209]. The co-evaporation process of MAPI is therefore often described as a CVD process rather than a PVD process with reported chamber pressures in the range $1.0 \cdot 10^{-5}$ mbar $1.0 \cdot 10^{-3}$ mbar to during the deposition process [209,232–235]. While the sample is being transferred out of the deposition chamber, the formation of a thin MAI film on top of the sample surface is therefore inevitable. Such a MAI surface layer will affect the interface energetics and therefore the energy band diagram determined with a step-by-step interface experiment. The inverse interface experiment – a step-by-step deposition of NiO_x by sputtering on top of a pre-deposited MAPI film – will most likely damage the perovskite film, due to the high energy of the sputtered species [236]. As a result, no reliable data can be extracted from such an experiment.

An alternative approach to determine the energy band diagram at the MAPI | NiO_x interface is through preparing and measuring a so-called small-angle tapered cross-section [110,111]. While the cross-section of a typical perovskite solar cell normal to the surface has a thickness of around 1 µm, meaning that it is much smaller than the spatial resolution of typical XPS measurements [237], tapered cross-section XPS (TCS-XPS) aims to extend the cross-section from 1 µm to several mm by preparing a low angle wedge through mechanically polishing the sample. TCS-XPS has been proven to be able to determine energy band diagrams of full perovskite solar cell devices which are similar to the energy band diagrams determined from classical step-by-step interface experiments [110,111].

The TCS-XPS measurements on the NiO_x | MAPI sample will provide evidence of a built-in potential in the dark inside the MAPI layer and will therefore be in agreement with the results of chapter 4.4, where under illumination an SPV was identified at the NiO_x | MAPI interface. The tapered cross-section experiments were performed in collaboration with Dr. Chittaranjan Das.

6.2. Experimental procedure

Preparation of the NiOx | MAPI sample:

The synthesis of the NiO_x | MAPI sample was performed by Tobias Abzieher from the Light Technology Institute at the Karlsruhe Institute of Technology. The NiO_x film was deposited on top of an ITO substrate by sputtering. The deposition of the MAPI absorbers was done by co-evaporation process inside a home-build vacuum chamber. More details regarding the manufacturing process are given in the experimental procedure of chapter 4.2.

Preparation of the tapered cross-section and XPS analysis:

After the deposition of the MAPI layer on top of the ITO | NiO_x substrate, the sample was removed from the vacuum chamber and introduced into a nitrogen-filled glovebox. During the transfer process, the samples were exposed for a short time to ambient atmosphere. To remove excess MAI from the surface of MAPI films, the samples were shortly immersed into isopropanol. This technique has proven to increase the efficiency and reproducibility of devices. After the immersion into isopropanol, the sample was sealed in an airtight box and transported to another glovebox. The preparation of the tapered cross-section was performed with a "multifunction rotary tool" (also called "Dremel") equipped with a felt polishing attachment. After preparing the tapered cross-section, the prepared sample was introduced into the XPS measurement chamber without exposure to ambient atmosphere. The tapered cross-section experiments were performed in collaboration with Dr. Chittaranjan Das.

The XPS measurements were performed at a Thermo Fisher Scientific K-Alpha+ system equipped with a monochromatic XR6 X-ray source (Al Kα) with an excitation energy of around 1486.6 eV. A line scan over 1855 µm with a step size of 103.1 µm was performed, resulting in 19 measurements points in total. The acquisition was performed at a pass energy of 50 eV using a 2D channel plate detector, a step size of 0.10 eV, and a dwell time of 50 ms per measurement point. All measurements were performed in the dark with all light sources in the measurement chamber switched off.

6.3. The interface between NiO_x and MAPI by TCS-XPS

Figure 6.1 a) – c) shows the $I3d_{5/2}$, the $Pb4f_{7/2,}$ and the Ni2p emission lines from an XPS line scan starting at a region with a thin MAPI layer and going towards the bulk of MAPI. The scan direction, going from NiO_x towards the bulk of MAPI, is indicated with a blue arrow and is further described in subfigure d), where a sketch of the prepared wedge is shown. The $Pb4f_{7/2}$ and $I3d_{5/2}$ emission lines appear at 138.41 eV and 619.20 eV (NiO_x side) and are shifting towards higher binding energies until they appear at 138.85 eV and 619.68 eV for the bulk of the MAPI perovskite. Total binding energy shifts of 0.49 eV and 0.44 eV are therefore observed for $Pb4f_{7/2}$ and $I3d_{5/2}$, respectively, indicating a band bending inside MAPI. The fact that even at the NiO_x side (beginning of the scan direction) iodine and lead species are visible indicates that some of the perovskite layer could not be removed during the preparation of the tapered cross-section. The incomplete removal of MAPI is indicated in the sketch of the prepared tapered cross-section in Figure 6.1 d) with the "thin MAPI" region. For the Ni2p emission lines shown in subfigure c), no binding energy shift is observed, indicating a flat-band situation inside the NiO_x substrate. The total band bending that is observed for the NiO_x | MAPI interface is therefore determined to be 0.46 eV and occurs completely in the MAPI layer.

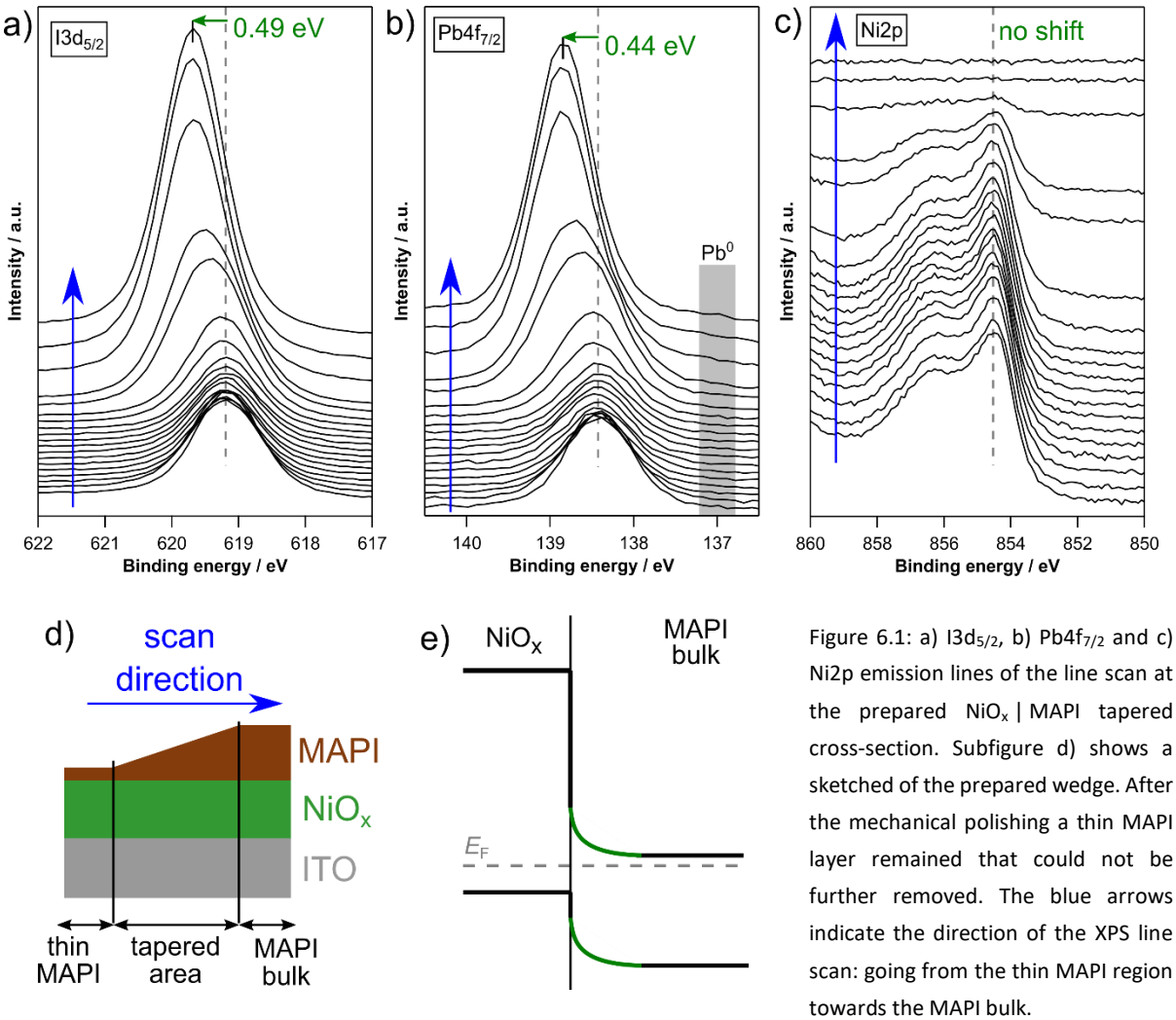

Figure 6.1: a) $I3d_{5/2}$, b) $Pb4f_{7/2}$ and c) Ni2p emission lines of the line scan at the prepared NiO_x | MAPI tapered cross-section. Subfigure d) shows a sketched of the prepared wedge. After the mechanical polishing a thin MAPI layer remained that could not be further removed. The blue arrows indicate the direction of the XPS line scan: going from the thin MAPI region towards the MAPI bulk.

In chapter 4.4 of this work, SPV measurements on a NiO_x | MAPI sample showed a light-induced SPV of 0.70 V, which would require a band bending of the same magnitude or higher at the NiO_x | MAPI interface. The here-determined band bending is with a value of 0.46 eV lower compared to the observed SPV of 0.70 V. The lower band bending is most likely caused by the tapered edge cross-section approach, which will eventually result in some minor damage and/or contamination of the sample during the polishing process. Similar to the discrepancies discussed here, Wussler *et al.* observed a total band bending of 0.74 eV when investigating the tapered cross-section of a full classical architecture perovskite solar cell device, even though an open-circuit voltage of 1.10 V was achieved in solar simulator measurements [110]. The obtained band bending of 0.46 eV at the NiO_x | MAPI is a proof of principle, verifying the results of the SPV measurements discussed in chapter 4.4. The resulting energy band diagram between NiO_x with the flat band situation inside NiO_x and the downward band bending inside MAPI is sketched in Figure 6.1 e).

The absolute binding energy positions of the $I3d_{5/2}$, the $Pb4f_{7/2}$, the Ni2p, and the O1s emission lines along with the VBM values are summarized in the Appendix in Table 9.14. A comparison of the VBM to core level differences of the MAPI perovskite used for the tapered cross-section experiment and the identically-prepared MAPI perovskites discussed in chapter 4.3 that achieved efficiencies of up to 15.9% when used in a solar cell is shown in Table 9.15 in the Appendix as well. Core level to VBM differences of 137.35 eV and 618.18 eV are determined for the $Pb4f_{7/2}$ and the $I3d_{5/2}$ emission lines, respectively, for the bulk of the tapered perovskite. The reference perovskite discussed in chapter 4.3 showed similar differences of 137.24 eV and 618.16 eV for the $Pb4f_{7/2}$ and the $I3d_{5/2}$ emission lines, respectively. The C1s and O1s emission lines are shown in the Appendix in Figure 9.14 as well. For the O1s emission line of NiO_x no binding energy shift is observed, indicating that no band bending is present inside the NiO_x layer.

Additional experiments are needed to completely analyze the interfacial contact properties of inverted perovskite solar cells applying the tapered edge technique. However, due to the complexity of these experiments they have been transferred to additional studies after this thesis.

6.4. Summary and conclusion

To summarize, it has been demonstrated that the TCS-XPS method established by Wussler *et al.* [110] is a viable technique for determining energy band diagrams at material interfaces and therefore a promising alternative to classical step-by-step interface experiments. TCS-XPS measurements are especially useful when the investigated materials cannot be evaporated or be evaporated stoichiometrically with thicknesses down to 1 nm since such a controlled deposition is necessary for performing classical step-by-step interface experiments.

For the presented NiO_x | MAPI interface, the presence of a band bending of 0.46 eV in the MAPI layer under dark conditions was proven by the TCS-XPS measurements, i.e. again at the p-HEL | n-MAPI interface. The band bending confirms the results of the SPV measurements presented in chapter 4.4, where an SPV of 0.70 V was identified as the NiO_x | MAPI interface. This band bending appears completely inside the MAPI layer. The fact that the band bending is lower compared to the SPV presented in chapter 4.4 is most likely caused by the tapered edge cross-section approach, which will eventually result in some minor damage and/or contamination of the sample during the polishing process, or due to the effect of X-ray source induced SPV.

In the following chapter, the conclusions from the detailed interface analysis of the MAPI | LiTSFI-doped spiro-MeOTAD and the NiO_x | MAPI interfaces along with the results obtained from the SPV measurements will be combined to develop energy band diagrams of full perovskite solar cell devices in classical and inverted architecture for the dark and the illuminated case.

7. Full energy band diagrams of perovskite solar cells

7.1. Motivation and chapter overview

The final chapter of this Ph.D. thesis will summarize the results of all previous chapters and combine them to construct full energy band diagrams of classical and inverted architecture devices both in the dark and under illumination. At first, some additional measurements like VBM and work function measurements of the EEL and HEL layers used in the devices along with a step-by-step interface experiment between MAPI and C_{60} are presented. Then, the energy band diagrams are constructed step by step for both architectures and compared with each other. Also already described earlier, the built-in potential in the dark and the SPV under illumination is drawn at the n-MAPI | p-HEL interface. However, in case of the classical architecture, the band bending appears inside the HEL (spiro-MeOTAD) and for the inverted architecture on the perovskite side (MAPI). To explain this different position of the band bending, the charge carrier concentration values of the perovskite absorbers and spiro-MeOTAD are estimated. It is then proposed that for the MAPI | spiro-MeOTAD interface the band bending appears on the spiro-MeOTAD side due to i) the lower charge carrier concentration compared to MAPI or ii) pinning of the Fermi level inside MAPI. For the NiO_x | MAPI interface it is assumed that the Fermi level inside the nickel oxide is pinned to defect states at the NiO_x surface or bulk.

7.2. Additional measurements

Determination of additional VBM values

For all charge extraction layers incorporated in the classical and inverted architecture devices, the VBM to Fermi level energy difference must be determined. Figure 7.1 a) shows XPS valence band measurements of a SnO_2 film deposited by spin-coating and a NiO_x film deposited by sputtering with ITO as a substrate in both cases. The samples were prepared outside of the vacuum and transported through air before introducing them into the vacuum chamber for the XPS measurement. VBM values of 3.85 eV and 0.53 eV are determined for SnO_2 and NiO_x, respectively. Additional information regarding the preparation of both layers is given in the Experimental Procedure of chapter 4.2. Figure 7.1 b) shows He I measurements of a C_{60} and a BCP surface, both deposited by thermal evaporation on top of an ITO substrate and measured without breaking the vacuum. VBM values of 1.51 eV and 1.96 eV are determined for C_{60} and BCP, respectively.

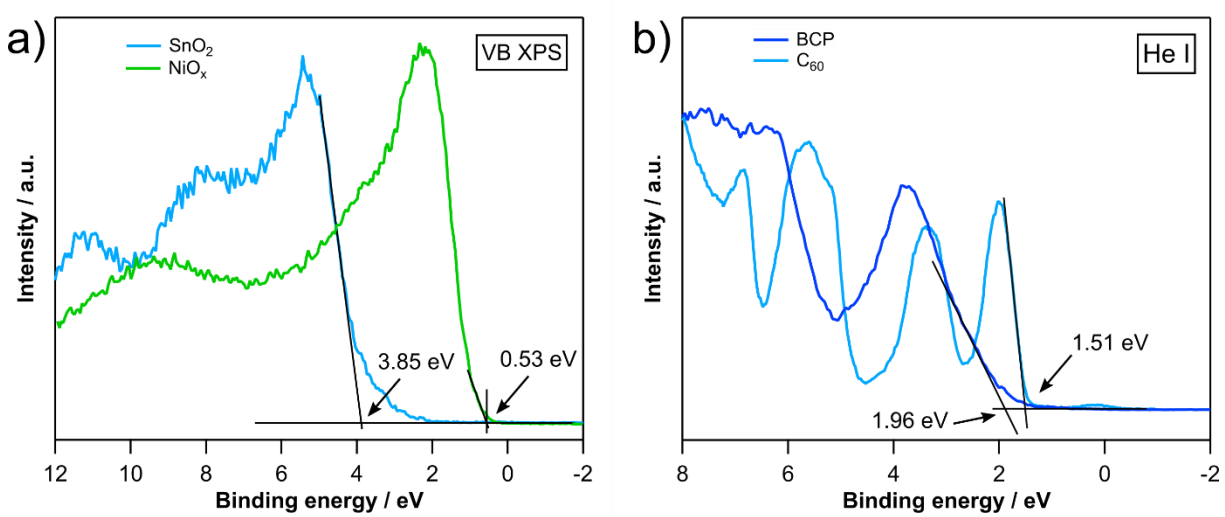

Figure 7.1: a) XPS measurements of the valence band region of a spin-coated SnO_2 and a NiO_x film from sputter deposition and b) He I measurements of C_{60} and BCP surfaces deposited by thermal evaporation and *in-vacuo* measured.

Energy band alignment at the MAPI | C_{60} interface

An additional step-by-step interface experiment between MAPI and C_{60} was performed. The interface experiment was performed on an ITO | NiO_x | MAPI sample. Details regarding the synthesis of the NiO_x and the MAPI layer are given in the Experimental Procedure of chapter 4.2. The deposition of the C_{60} layer was performed by thermal evaporation using a home-built evaporation source equipped with an Al_2O_3 crucible at the DAISY-BAT cluster tool. A deposition temperature of roughly 320 °C was chosen. The XPS measurements were performed with a Physical Electronics VersaProbe 5000. More details regarding the XPS measurements are given in the Experimental Procedure of chapter 3.2.

The I3d, Pb4f, and C1s emission lines for different deposition steps are presented in Figure 7.2. Due to an issue with the autofocus of the XPS machine some samples were measured out of focus, meaning that the absolute intensities of the different deposition steps cannot be compared. All absolute binding energy positions are summarized in Table 9.16 in the Appendix. Since no binding energy shift can be observed for any of the emission lines, it is assumed that no band bending is present at the MAPI | C_{60} interface.

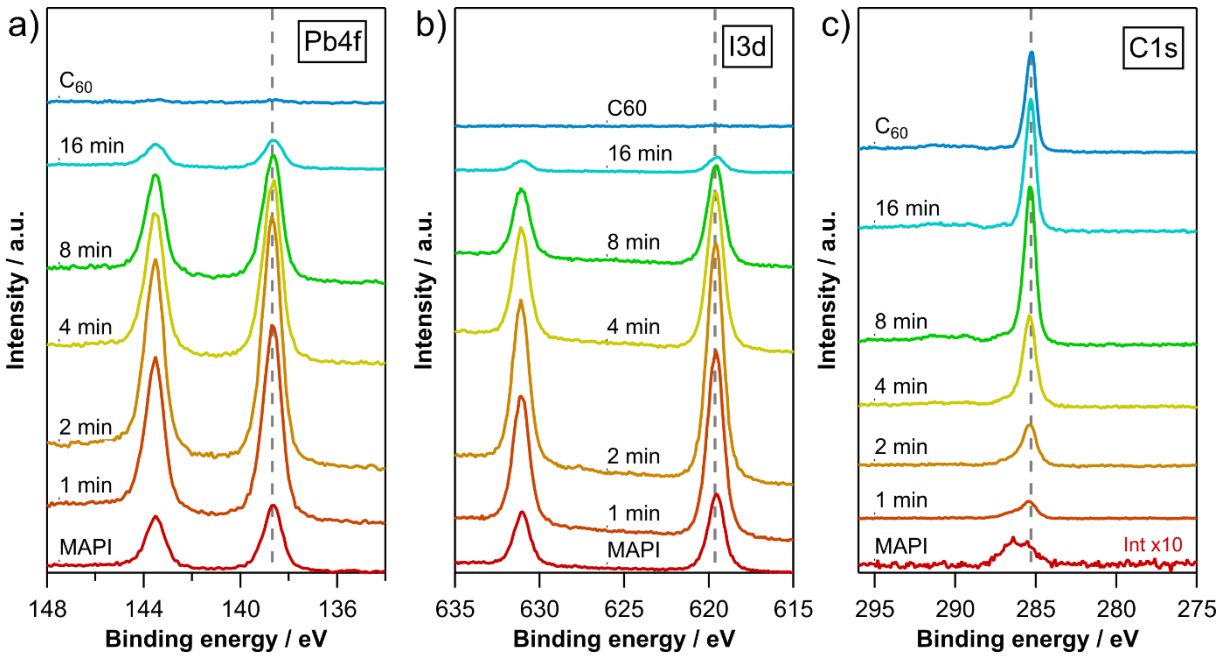

Figure 7.2: a) Pb4f, b) I3d and c) C1s emission lines of the step-by-step interface experimental between MAPI and C_{60}. Due to an issue with the auto-focus of the XPS machine some samples were measured out of focus, meaning that the absolute intensities of the different deposition steps cannot be compared. The thickness of the C_{60} adsorbate layer can therefore not be determined from the damping of a substrate emission line. The deposition steps are therefore labelled with the accumulated C_{60} deposition time.

Determination of additional work function values:

Additional work function values were determined from He I measurements with an applied bias of -6 V (see Figure 7.3). The SnO_2 and NiO_x films were deposited by spin-coating and sputtering, respectively, and spiro-MeOTAD was p-doped with LiTFSI and deposited spin-coated. The perovskite absorbers were deposited by co-evaporation from PbI_2 and MAI. Additional information on the preparation of the different layers is given in chapter 4.2. Work function values of 4.15 eV, 4.02 eV, and 4.72 eV are determined for SnO_2, MAPI on SnO_2, and MAPI on spiro-MeOTAD, respectively. For NiO_x and MAPI on NiO_x values of 5.41 eV and 4.16 eV are determined.

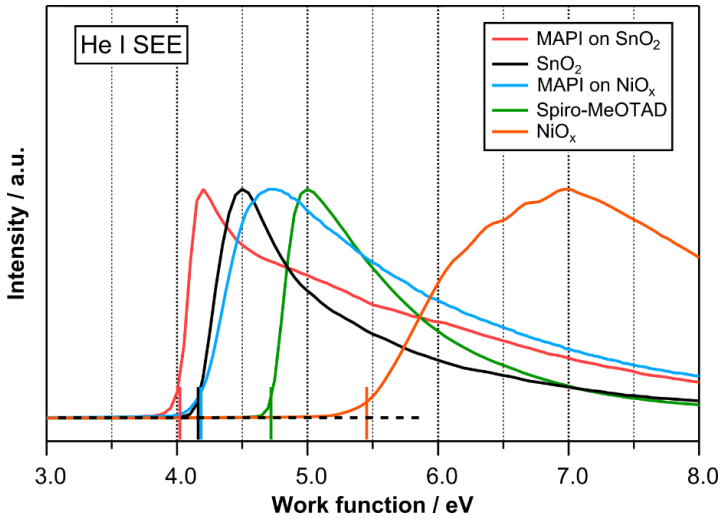

Figure 7.3: He I measurements with an applied bias of -6 V to determine the work function of MAPI on SnO_2, MAPI on NiO_x and different charge extraction layers.

7.3. Drawing the dark and illuminated energy band diagrams

All formulas for calculating the valence and conduction band offsets that are used in the following were defined in chapter 1.6.1 of this work. At first, the energy band diagram of the classical architecture device with the layers stack ITO | SnO_2 | MAPI | spiro-MeOTAD | Au will be investigated. For SnO_2 and MAPI, VBM values of $E_{VBM,MAPI} = 1.35\ eV$ (see Figure 4.4 e) and $E_{VBM,SnO2} = 3.85\ eV$ (see Figure 7.1) were determined. Since the SPV measurements revealed, that no SPV is present at this interface, it is assumed that no band bending exists in the dark. The work functions of SnO_2 ($\varphi_{SnO2} = 4.15\ eV$) and MAPI on SnO_2 ($\varphi_{MAPI} = 4.02\ eV$) are close to each other, indicating as well that no band bending should form at this interface in the dark. From the difference of the VBM values of SnO_2 and MAPI, the valence band offset between both materials is calculated to be

$$\Delta E_{VB,SnO2-MAPI} = E_{VBM,MAPI} - E_{VBM,SnO2} = 1.35\ eV - 3.85\ eV = -2.50\ eV,$$

demonstrating an efficient blocking of holes. After the deposition of spiro-MeOTAD on top of the perovskite absorber, the SPV measurements revealed a light-induced SPV of 0.66 V (see Figure 4.5 a), which increased further to 0.80 V when the device is completed with the Au back electrode (see Figure 4.5 c). The full photovoltage of 0.80 V is here addressed to the MAPI | spiro-MeOTAD interface since photovoltage at the spiro-MeOTAD | Au interface would require a quasi-Fermi level splitting inside the spiro-MeOTAD layer, which due to the large bandgap of 2.97 eV is not expected. The step-by-step interface experiment of the MAPI | spiro-MeOTAD confirmed the presence of a band bending at this

interface in the dark and confirmed as well that under illumination the band bending will change to a flat band situation, giving rise to an SPV. It is therefore concluded that in the dark a band bending of at least $V_{bb,Spiro} = 0.80\ eV$ exists at the MAPI | spiro-MeOTAD interface. With the bandgap values of MAPI ($E_{g,MAPI} = 1.58\ eV$, see Figure 3.6 a) and spiro-MeOTAD ($E_{g,Spiro} = 2.97\ eV$, see Figure 9.5 in the Appendix) and their VBM and HOMO values, the CBM and LUMO values with respect to the Fermi level can be calculated.

$$E_{CBM,MAPI} = E_{VBM,MAPI} - E_{g,MAPI} = 1.58\ eV - 1.35\ eV = -0.23\ eV$$
$$E_{LUMO,Spiro} = E_{HOMO,Spiro} - E_{g,Spiro} = 2.97\ eV - 0.64\ eV = -2.33\ eV$$

From the CBM and LUMO values the offset between the CBM of MAPI and the LUMO of spiro-MeOTAD is determined to be

$$\Delta E_{CB,MAPI-Spiro} = E_{LUMO,Spiro} - E_{CBM,MAPI} + V_{bb,Spiro} = -2.33\ eV - (-0.23\ eV) + 0.80\ eV = -1.30\ eV,$$

which is sufficient to guarantee an efficient blocking of electrons. The offset between the VBM of MAPI and the HOMO of spiro-MeOTAD is calculated to be

$$\Delta E_{VB,MAPI-Spiro} = E_{HOMO,Spiro} - E_{VBM,MAPI} + V_{bb,Spiro} = 0.64\ eV - 1.35\ eV + 0.80\ eV = 0.09\ eV,$$

which is low enough so that the thermal energy of holes trying to enter the spiro-MeOTAD from MAPI is sufficient to overcome the offset barrier. The corresponding energy band diagram for the full classical architecture device without illumination is depicted in Figure 7.4 a). Under illumination (see Figure 7.4 b), the absorption of light results in a generation of electron-hole pairs inside the perovskite absorber and therefore a splitting of the electron and hole quasi-Fermi levels. The generated charge carriers are separated by the hole-filter mechanism of the MAPI | spiro-MeOTAD interface, and the formed SPV lowers the built-in potential until, ideally, a flat-band situation is reached. The generated SPV is the open-circuit voltage of the device.

In accordance with the classical architecture, the energy band diagram of the inverted architecture device with the device stack ITO | NiO_x | MAPI | C_{60} | BCP | Au is constructed in the following. The VBM values of NiO_x and MAPI deposited on NiO_x are determined to be $E_{VBM,NiOx} = 0.53\ eV$ (see Figure 9.4) and $E_{VBM,MAPI} = 1.43\ eV$ (see Figure 4.4 g). SPV measurements revealed that a photovoltage of 0.70 V is present at the NiO_x | MAPI interface, which increased to 0.83 V for the full device with the C_{60} EEL, the BCP buffer layer, and the Au back electrode on top. Like the classical architecture, the full SPV is addressed to the p-contact at the NiO_x | MAPI interface ($V_{bb,MAPI} = -0.83\ eV$). For the VBM offset between NiO_x and MAPI a value of

$$\Delta E_{VB,NiOx-MAPI} = E_{VBM,MAPI} - E_{VBM,NiOx} - V_{bb,MAPI} = 1.43\ eV - 0.53\ eV - 0.83\ eV = -0.09\ eV$$

is therefore calculated, which is only a slight voltage loss for holes moving from MAPI to NiO_x. With the bandgap values of NiO_x ($E_{g,NiOx} = 3.60\ eV$) [209] and MAPI ($E_{g,MAPI} = 1.58\ eV$, see Figure 3.6 a) the CBM positions of NiO_x and MAPI with respect to the Fermi level can be calculated.

$$E_{CBM,NiOx} = E_{VBM,NiOx} - E_{g,NiOx} = 0.51\ eV - 3.60\ eV = -3.09\ eV$$
$$E_{CBM,MAPI} = E_{VBM,MAPI} - E_{g,MAPI} = 1.43\ eV - 1.58\ eV = -0.15\ eV$$

Using the CBM values of NiO_x and MAPI, the offset between the conduction band of both materials is determined to be

$$\Delta E_{CB,NiOx-MAPI} = E_{CBM,MAPI} - E_{CBM,NiOx} + V_{bb,MAPI} = -0.15\ eV - (-3.09\ eV) + (-0.83\ eV) = 2.11\ eV,$$

which will efficiently block electrons from the CB of MAPI to the CB of NiO_x. For the CBM of C_{60} with respect to the Fermi level, a value of

$$E_{CBM,C60} = E_{VBM,C60} - {E_{g,C60}}^{a)} = 1.67\ eV - 1.51\ eV = -0.16\ eV$$

is determined. Since the CBM values of MAPI and C_{60} differ only by 0.01 eV, it is assumed that the conduction bands are aligned and that there is no barrier for an electron moving from MAPI to C_{60}. Given the LUMO of BCP of

$$E_{LUMO,BCP} = E_{HOMO,BCP} - {E_{g,BCP}}^{a)} = 1.96\ eV - 3.50\ eV = -1.54\ eV$$

a large offset between the LUMO of C_{60} and BCP is determined.

$$\Delta E_{LUMO,C60-BCP} = E_{LUMO,BCP} - E_{LUMO,C60} = -1.54\ eV - (-0.16\ eV) = -1.38\ eV$$

However, this will not block the electrons from entering the LUMO of BCP, since the BCP buffer layer has only a thickness of 3 nm, therefore allowing electrons to tunnel through it. The tunneling of electrons mediated by gap states of the BCP has also been described in literature before [238–240]. The complete band diagram for the inverted architecture is presented in Figure 7.4 c) and d).

In both devices (classical and inverted architecture), the band bending in the dark and therefore also the photovoltage under illumination is formed at the n-MAPI | p-HEL interface, which means that any device optimization should focus on improving the energy alignment at these interfaces, to further increase the V_{OC} and therefore also the PCE of the device. In fact, a recent strategy to further improve the PCE of perovskite solar cells involves the use of passivation layers at the perovskite | HEL interface [241–245]. Until now, the exact mechanism of PCE improvement of such passivation strategies is still not clarified. The fact that the photovoltage of the device has been identified at the perovskite | HEL

a) The values for the energy gaps of C_{60} and BCP were taken from Chiu *et al.* [246] and Yoshida *et al.* [238], respectively.

has given some hints regarding the role of such passivation layers. While for the classical architecture, the built-in potential appears inside the HEL (spiro-MeOTAD), it is formed inside the perovskite absorber in case of the inverted architecture. To explain the different positions of the band bending in both architectures, the charge carrier concentrations are estimated for both MAPI (on SnO_2 and NiO_x) perovskites, depending on the Fermi level to VBM differences. Wang *et al.* reported charge carrier concentrations values from Hall measurements and valence band to Fermi level differences from XPS measurements for differently doped MAPI perovskites, which are summarized in Figure 7.5. By applying an exponential fit to the data points determined by Wang and extrapolating it, charge carrier concentration values of $n_{MAPI,SnO2} = 3.2 \cdot 10^{20} cm^{-3}$ and $n_{MAPI,NiOx} = 1.1 \cdot 10^{21} cm^{-3}$ are determined for the MAPI perovskites investigated in this work. However, the charge carrier concentration values determined from the fit based on the data of Wang *et al.* should only be taken as a rough estimate, as Hall measurements of MAPI perovskite films are challenging, due to MAPIs low dark conductivity [247,248]. In addition, the determination of the VBM in UPS or XPS is inaccurate due to the low density of states near the onset of the valence band [199]. Since the charge carrier concentration depends exponentially on the Fermi level position inside the bandgap, a variation of only 100 meV of

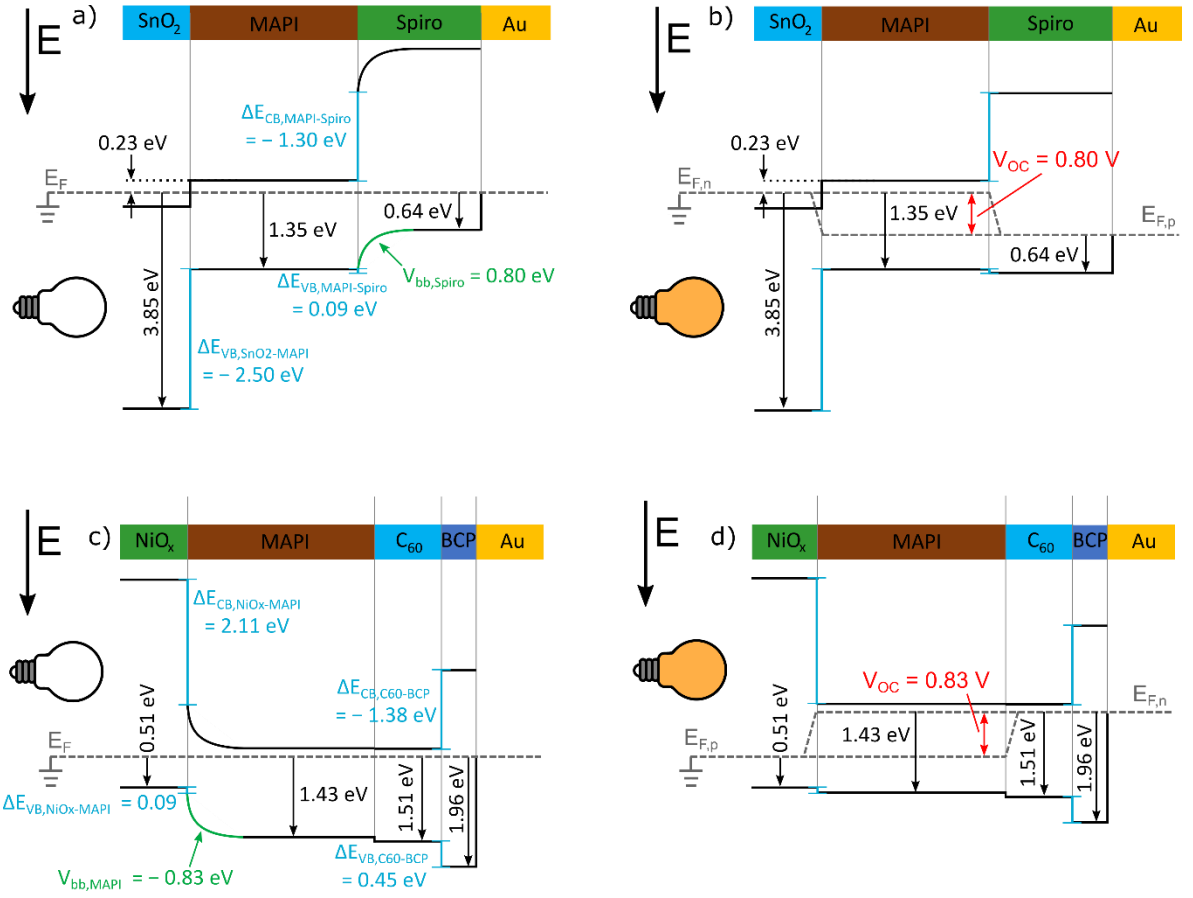

Figure 7.4: Derived Band diagrams for a complete perovskite solar cell in classical architecture a) The dark case with a band bending at the MAPI | spiro-MeOTAD interface and b) under illumination with the band bending changing to a flat-band situation, which results in the formation of an SPV. The subfigures c) and d) show the same for the inverted architecture. . The black labelled arrows are VBM to Fermi level differences, the blue lines valence / conduction band offsets and the green highlighted lines built-in potentials (band bending).

the VBM positions results in a change of the charge carrier concentration of almost one order of magnitude [249]. A direct comparison of charge carrier concentrations determined by Hall measurements, PES, and resistivity measurements of MAPI thins films, and ideally, also single crystals is therefore needed in the future.

For the charge carrier concentrations of MAPI on SnO_2 and NiO_x substrates a difference of a factor around 3.5 has been determined, which cannot explain the fact that the band bending appears inside MAPI for the NiO_x | MAPI interface and inside the spiro-MeOTAD for the MAPI | spiro-MeOTAD interface. In fact, the determined doping level and therefore the charge carrier concentration of MAPI on NiO_x is even larger compared to MAPI on SnO_2, meaning that one would expect less band bending inside the MAPI layer grown on NiO_x. However, another explanation could be pinning of the NiO_x Fermi level at defects states existing at the nickel oxide surface and bulk [250–252]. These defects states result from deviations of the NiO stoichiometry, leading to defect levels and related defect bands. The reason why the band bending appears on the spiro-MeOTAD for the classical architecture devices might be related to the lower hole concentration inside spiro-MeOTAD compared to the electron concentration inside MAPI. For a similarly doped spiro-MeOTAD film as it was used in this work, Li *et al.* [253] reported a hole concentration of $p = 2.8 \cdot 10^{19} cm^{-3}$, which is one order of magnitude lower than the here estimated electron concentration of MAPI on SnO_2 ($n_{MAPI,SnO2} = 3.2 \cdot 10^{20} cm^{-3}$). The distribution of the band bending on the p- and n-side can be calculated using Equation 7.1 [75]. For the above-mentioned charge carrier concentrations on MAPI and spiro-MeOTAD, 92% of the band bending would appear on the spiro-MeOTAD side and 9% on the MAPI side.

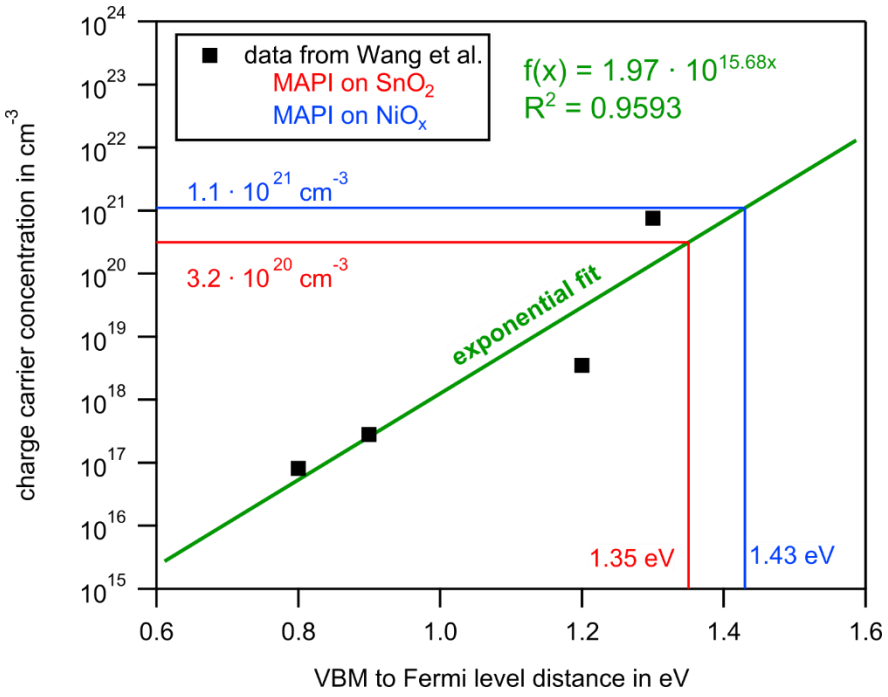

Figure 7.5: Logarithmic plot of the charge carrier concentration values in cm^{-3} plotted against the VBM to Fermi level difference in eV. The black dots represent the data from Wang *et al.* The green exponential fit was performed with the data points of Wang *et al.* The red and blue lines represent the VBM values of MAPI on SnO_2 and NiO_x of this work and the expected charge carrier concentration values based on the VBM values.

$$\frac{V_{bb,p}}{V_{bb,total}} = \frac{N_D}{N_A + N_D} \quad (7.1)$$

7.4. Summary and conclusion

In this chapter, the results of the SPV measurements (see chapter 4), the classical step-by-step interface experiment between MAPI and LiTFSI-doped spiro-MeOTAD (see chapter 5), and the TCS-XPS measurements on a NiO_x | MAPI sample (see chapter 6) have been summarized and combined with additional measurements to derive band diagrams for classical and inverted architecture perovskite solar cell devices in the dark and under illumination. For both architectures, a band bending in the dark and an SPV under illumination was identified at the MAPI | HEL interface. The fact that most of the device's photovoltage has been identified at the interface to the HEL might explain why recently a lot of studies are introducing passivation layers in between the perovskite absorber and the HEL [241–245]. Even though the band bending has been identified at the MAPI | HEL interface for both architectures, the space charge region is formed inside the MAPI layer for the inverted architecture and inside the spiro-MeOTAD layer for the classical architecture. In case of the classical architecture, the position of the band bending could be explained by the higher charge carrier concentration inside the MAPI perovskite compared to spiro-MeOTAD. Pinning of the Fermi level inside MAPI, which is causing the band bending to be located on the spiro-MeOTAD side is a possibility as well. For the classical architecture, it is proposed that the Fermi level inside the nickel oxide is pinned to defect states at the NiO_x bulk and surface.

8. Final conclusion and outlook

The goal of this thesis was to determine the working principle of perovskite solar cells in classical and inverted architecture, by deriving energy band diagrams of the full solar cells in the dark and under illumination. Such band energy diagrams allow concluding at which interface the photovoltage of the devices is forming, which will be an important piece of information for developing new strategies to further increase the PCE of the device. Literature reports have often described perovskite solar cell devices as "*n-i-p-devices*" (classical architecture) or "*p-i-n-devices*" (inverted architecture). In addition, it was reported that the doping of the perovskite absorber is determined by its underlying substrate: on an n-type substrate, metal halide perovskites would show an n-doping, on p-type substrates they are claimed to be intrinsic or slightly p-doped. Since such a *substrate effect* contradicts basic semiconductor physics, the first chapter of the results part focused on investigating perovskite absorbers on n-type and on p-type substrates.

Five different perovskite absorbers materials (MAPI, FAPI, MAFAPI, CsFAPI, and CsMAFAPI) deposited by the most applied process of spin-coating were investigated in **chapter 3** to determine whether the underlying substrate influences the doping level of the perovskite materials. The actually shifted Fermi level was identified as SPVs that may form during the doping level measurement, due to unintentional illumination. While the initial UV/Vis and XRD measurements showed that the perovskite phase was successfully synthesized for all five materials, solar simulator measurements verified that PCEs of up to 19.2% can be achieved when the absorber materials are used in devices. Thermally evaporated and *in-vacuo* PES-measured precursor materials were used to determine modified photoionization cross-sections values, allowing to improve the stoichiometry determination of the perovskite absorbers. PES measurements of the five perovskite absorbers in the dark showed that for both investigated substrates (n-type SnO_2 and p-type NiO_x) the on-top deposited perovskite absorbers exhibit a strong n-doping. During illumination, an SPV was observed for all perovskite absorbers grown on p-type NiO_x. Additional SPV measurements with controlled illumination conditions have shown that metal halide perovskite absorbers are extremely light-sensitive. Even the room lights shining through the glass viewports of the vacuum chamber or the visible light from the cathode of the X-ray source resulted in significant SPVs. Since the magnitude of the observed SPVs is in the same range as the substrate-related doping differences for MAPI on n-type and p-type substrates discussed in the literature, it was concluded that literature reports of a substrate-dependent doping of the perovskite are most likely suffering from an unnoticed SPV due to unintentional light illumination.

In **chapter 4** the classical and inverted architecture devices with perovskite absorbers deposited by co-evaporation were built up layer-by-layer and SPV measurements were performed on each intermediate device stack. The majority of the photovoltage of both architectures was identified at the n-MAPI | p-HEL interface, which is the *n-MAPI | p-spiro-MeOTAD interface* for the classical architecture and the *p-NiO_x | n-MAPI interface* in case of the inverted architecture. The slightly lower SPVs of 0.80 V (classical) and 0.82 V (inverted) compared to the open-circuit voltages of the devices (1.05 V and 1.04 V) were explained with the lower light intensity during the SPV measurements in the

XPS chamber compared to the AM1.5G spectrum used during the solar simulator measurements. Solar simulator measurements of perovskite solar cell devices employing the vacuum-deposited perovskite absorbers showed PCE values of 13.7% (classical) and 11.6% (inverted).

To corroborate and further detail these findings, the investigation of the n-MAPI | p-spiro-MeOTAD interface, at which the majority of the photovoltage for the classical architecture devices was identified, has been the focus of **chapter 5**. A prerequisite for these step-by-step interface experiments was to develop a vacuum deposition process of LiTFSI-doped spiro-MeOTAD. Therefore, at first, the role of tBP and LiTFSI, two commonly used additives inside the precursor solution used for spin-coating spiro-MeOTAD films, were studied. It was shown that LiTFSI acts as p-dopant for spiro-MeOTAD and that tBP is required for a more homogeneous distribution of LiTFSI inside the liquid-processed spiro-MeOTAD film. For the doping limit, a Fermi level shift of 0.65 eV was observed. Without the addition of tBP, no p-doping of spiro-MeOTAD with LiTFSI could be achieved. The deposition of LiTFSI-doped spiro-MeOTAD films was successfully transferred from the previously-used spin-coating process to a vacuum deposition technique by thermal co-evaporation of spiro-MeOTAD and LiTFSI. The vacuum process allowed a doping of spiro-MeOTAD through LiTFSI even in the absence of tBP, indicating that a more homogeneous mixing of spiro-MeOTAD and LiTFSI is possible with the vacuum deposition process. The interface formation of LiTFSI with spiro-MeOTAD was studied in more detail by performing a classical step-by-step interface experiment between both materials. The observed band bending of 0.59 eV inside the spiro-MeOTAD layer fits nicely to the determined doping limit from the previous experiments and is therefore in agreement with the internal interface charge transfer doping model developed for small dopant precipitates forming in the matrix semiconductor material [226]. By comparing the shape of the C1s emission line spiro-MeOTAD for increasing LiTFSI thicknesses, it was demonstrated that by the p-doing of spiro-MeOTAD electrons are being transferred from the inner benzol ring of the spiro-MeOTAD core to the LiTFSI molecules. Finally, a step-by-step interface experiment between MAPI and spiro-MeOTAD was performed and analyzed in the dark and under illumination. XPS measurements revealed a band bending of 0.31 eV in the dark at the spiro-MeOTAD side, that would change into a flat-band situation upon illumination, giving rise to an SPV of the same magnitude. From UPS measurements the observed SPV was much higher with up to 0.65 eV for thick layers of spiro-MeOTAD. The different SPV values determined from XPS and UPS were explained with an X-ray source-induced SPV that limits the XPS-observable band bending in the dark.

Chapter 6 focused on studying the hole contact interface where the majority of the photovoltage was found for the inverted architecture: the p-NiO_x | n-MAPI interface. Instead of a classical step-by-step interface experiment as it was performed for the MAPI | spiro-MeOTAD interface, a tapered cross-section-XPS approach was chosen for the NiO_x | MAPI interface. In the dark, a bend bending of 0.46 eV was determined on the perovskite, verifying the results of the SPV measurements of chapter 4. Interestingly, and opposed to the MAPI | LiTFSI-doped spiro-MeOTAD interface, the band bending was found in MAPI, while the Fermi level of NiO_x was pinned.

The results of the SPV measurements presented in chapter 4 and the detailed interface characterizations in chapter 5 and chapter 6 were summarized in **chapter 7** to construct band energy

diagrams of full perovskite solar devices in classical and inverted architecture both in the dark and under illumination. For both architectures, the band bending in the dark and therefore also the photovoltage under illumination appears at the n-MAPI | p-HEL interface. For the classical architecture device, the band bending was measured inside the HEL and therefore on the spiro-MeOTAD side. Compared to that, the band bending appeared on the MAPI perovskite side for the inverted architecture. For the classical architecture, the position of the band bending could be explained by the lower charge carrier concentration of spiro-MeOTAD compared to MAPI, although pinning of the Fermi level inside MAPI as a cause of the location of the band bending is a possibility as well. For the inverted architecture, it is assumed that the Fermi level inside the nickel oxide is pinned to defect states at the NiO_x surface or bulk so that the space charge layer develops in the MAPI layer.

To further increase the V_{OC} and therefore also the PCE of classical and inverted perovskite solar cell devices, strategies must be developed for improving the energy alignment at the MAPI | HEL interface, since the photovoltage of the perovskite solar cell devices has been identified here. In fact, several publications have recently been introducing passivation layers between the perovskite absorber and the HEL into the device stacks. So far, the exact mechanism behind such passivation strategies is not well understood and the selection of materials used as passivation layers is usually purely empirically. The findings in this thesis may suggest that the passivation layer at the MAPI | spiro-MeOTAD interface leads to unpinning of MAPI, allowing the band bending and the photovoltage to form on the MAPI side. Future experiments could therefore try to clarify the exact role of the passivation layer by performing detailed interface characterization through classical step-by-step interface experiments or by the tapered-cross-section-XPS approach and comparing the results for devices with and without a passivation layer. In addition, the influence of the passivation layers should also be studied by SPV measurements.

Another scientific question that should be addressed in the future is how the position of photovoltage changes with the doping level of the perovskite absorber. Since it has been shown that by changing the PbI_2 to MAI-ratio from a PbI_2-rich perovskite to an MAI-rich perovskite, the doping of the perovskite should change from n-doped to p-doped, one would also expect, that the photovoltage will move from the n-MAPI | p-HEL interface to the (now) p-MAPI | n-EEL interface. For a perfectly stoichiometric and therefore intrinsic perovskite absorber, the photovoltage should in principle be evenly split between the i-MAPI | n-EEL and the i-MAPI | p-HEL interface. However, throughout this thesis, numerous different perovskite samples prepared in different laboratories (from the Technical University of Darmstadt, the Karlsruhe Institute of Technology, the Helmholtz Center for Materials and Energy in Berlin, the Jülich Research Centre, and the University of Wuppertal) and by different deposition methods (one-step and two-step spin-coating, co-evaporation, close space sublimation, and chemical vapor deposition) were investigated. Even though not all measurements were presented in this thesis, all samples without exception were always measured n-doped by XPS and UPS valence band measurements. The question remains whether the n-doping of the perovskite absorbers is a natural cause of the device optimization, meaning that PCE-optimized devices are eventually n-doped, or if it is related to the PES technique. To corroborate the general experimentally found n-doping of metal halide perovskite absorbers, a dedicated study on determining the doping level of perovskite

samples using not only PES but also Hall measurements and conductivity measurements is therefore recommended. Ideally, thin films and single crystals must both be compared, to minimize the effect of grain boundaries.

In addition to the in this work primarily investigated metal iodide perovskite absorbers, the SPV measurements and interface characterizations could also be performed for Sn-based or Br-based perovskites absorbers. Even though Sn-based perovskites have much lower stability compared to the classical Pb-containing materials, making their processing much more challenging, recent advances have pushed their PCE above 13.2% [51]. Systems with a mixture of lead and tin have even achieved PCE values of up to 21% [56]. The substitution of lead with tin is especially interesting due to tins lower toxicity and the lower bandgap of Sn-perovskites, which means that based on the Shockley-Queisser limit they can in principle achieve higher PCEs. Sn-perovskites have often been reported as p-doped instead of n-doped so it would be of interest to investigate whether the photovoltage would form at the interface between the p-perovskite and the n-EEL instead. Br-based perovskites are mainly interesting due to their large bandgap, which opens a potential application as wide bandgap material for tandem devices or as absorber material for direct water splitting. Initial results of SPV measurements performed on $CH_3NH_3PbBr_3$ perovskite absorbers are shown in chapter 9.2 of the Appendix.

9. Appendix

9.1. FAPI and CsFAPI through co-evaporation

In addition to the SPV measurements and interface characterizations presented in chapters 3 to 7, which are more fundamental research, part of this thesis focused also on device fabrication and optimization. The results will only be shortly summarized here and the reader is referred to the Advanced Research Lab report [254] and the master report of Waqas Zia [255], who worked under the supervision of the author of this Ph.D. thesis. Figure 9.1 a) shows representative XRD measurements of a FAPI and CsFAPI perovskite film deposited by co-evaporation of PbI_2, FAI, and additionally CsI in the case of CsFAPI on top of FTO | SnO_2 substrates. For both perovskite materials, a strong (100) texture is observed. For the FAPI perovskites, small amounts of the yellow phase (δ-phase) are observed and residual PbI_2 are observed. Figure 9.1 b) shows the normalized and enlarged (100) reflection of both perovskite materials. Due to the incorporation of the smaller Cs^+ cations (compared to FA^+) into the perovskite lattice, the unit cell gets slightly smaller, and the reflection is shifted to larger angles. Figure 9.2 shows achieved record efficiencies when the perovskite absorbers are incorporated into devices. All devices were prepared in the classical architecture with either SnO_2 or TiO_2 as EEL, spiro-MeOTAD as HEL, and gold as a back electrode and a device area of 3.25 mm x 10 mm (32.5 mm^2). Details regarding the preparation of the different layers are given in the reports of Zia. Record efficiencies of 14.0% were achieved for FAPI on SnO_2 as well as on TiO_2 substrates. Devices with CsFAPI as absorber material were only built on FTO | SnO_2 substrates. Record efficiencies of 11.0% were achieved.

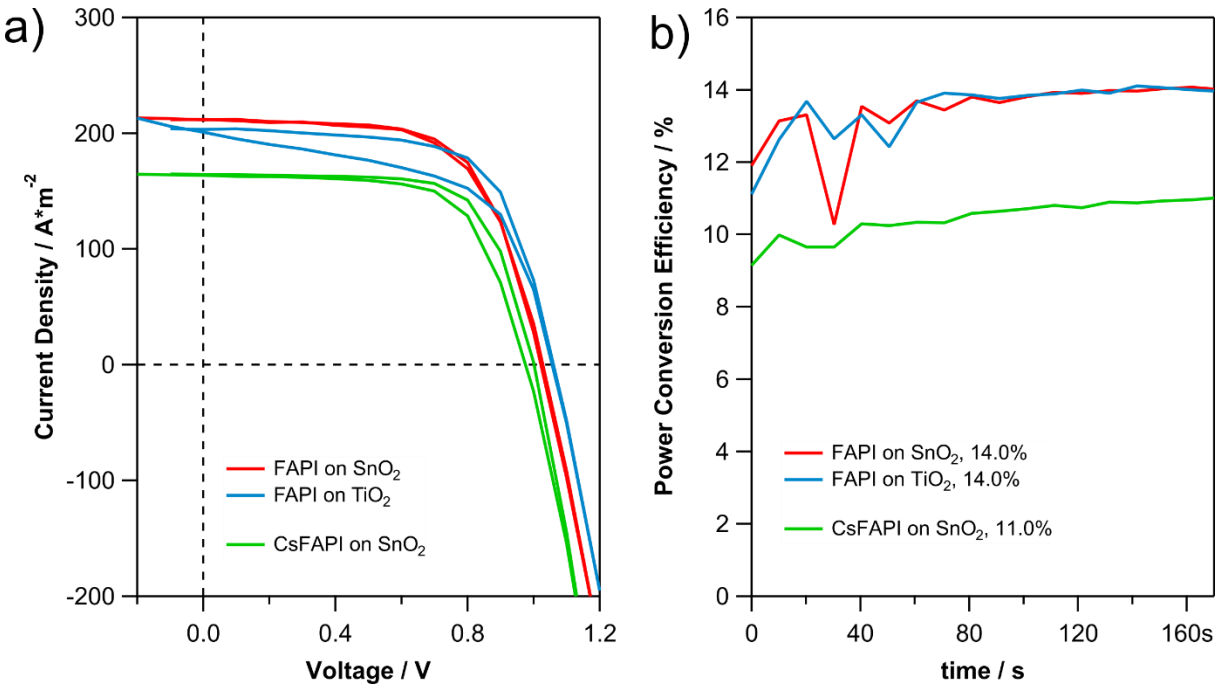

Figure 9.2: a) JV-curves of champion devices of FAPI perovskite solar cells on SnO_2 (red) and TiO_2 (blue) substrates and CsFAPI perovskites on SnO_2 substrates (green). Subfigure b) shows the MPP-tracked PCE over a duration of 170 s. Stabilized PCE values of 14.0% were achieved for both FAPI devices and 11.0% for the CsFAPI device. A cell area of 32.5 mm² (3.25 mm x 10 mm) was used for the devices.

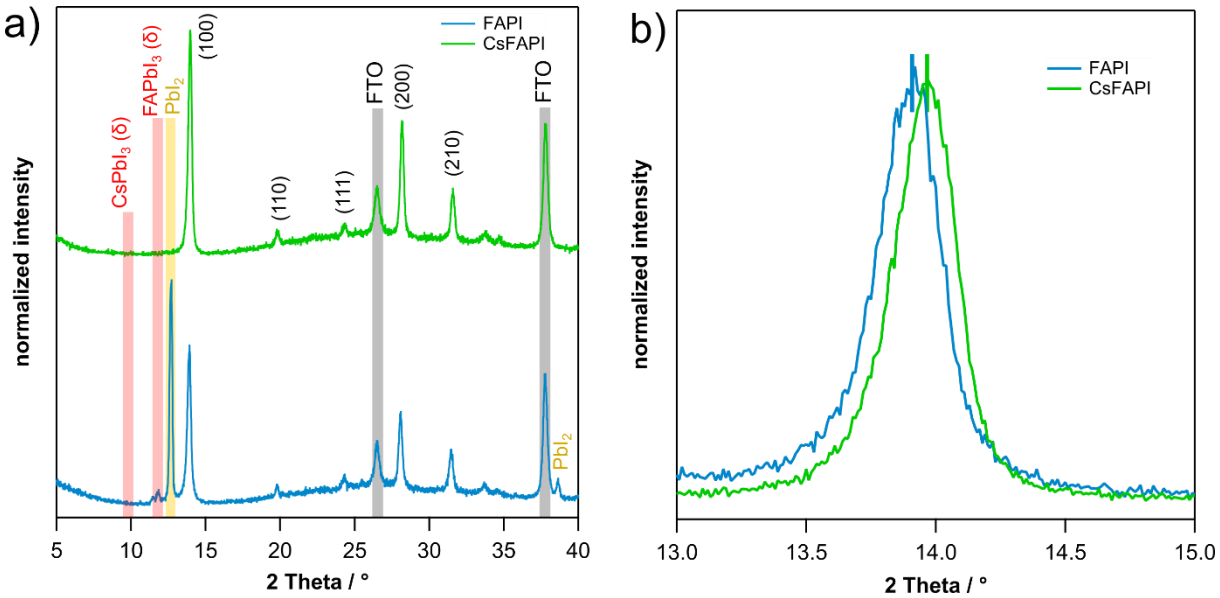

Figure 9.1: a) XRD measurements of a FAPI and a CsFAPI perovskite deposited by co-evaporation of Pb_2, FAI and additionally CsI in the case of CsFAPI. Both perovskite materials crystallize in the cubic perovskite structure with a strong (100) texture. For FAPI, usually small amounts of the undesired delta phase and large amounts of unreacted PbI_2 were observed. Subfigure b) shows a comparison of the (100) reflection of both perovskite materials. Due to the incorporation of Cs^+ into the perovskite lattice, the (100) reflection of CsFAPI is shifted to higher angles.

9.2. SPV experiments on $CH_3NH_3PbBr_3$

Initial SPV measurements on $MAPbBr_3$ perovskites have already been performed throughout this work, although the measurements are not presented here, since the first gathered data are not fully conclusive. Some of the samples showed strong X-ray source-induced SPVs which makes an interpretation of the spectra more complicated. The shown $MAPbBr_3$ films are all deposited by spin-coating on top of TiO_2 substrates and are therefore in the classical architecture. The samples were prepared by a Ph.D. student of the research group of Prof. Michael Saliba of the Jülich Research Centre and shipped to Darmstadt. Similar to the I-containing perovskites materials, $MAPbBr_3$ was measured n-doped in the dark, as depicted by the XPS valence band measurements shown in Figure 9.3 a). The CBM value shown in Figure 9.3 a) has been positioned based on the bandgap of $MAPbBr_3$ which was reported to be 2.29 eV. Measurements of the Pb4f emission line in the dark and under illumination show that no SPV is present for the TiO_2 | $MAPbBr_3$ device stack (see Figure 9.3 b). After the deposition of the spiro-MeOTAD HEL, valence band measurements by UPS showed remarkably high SPVs of up to 1.25 V (see Figure 9.3 c).

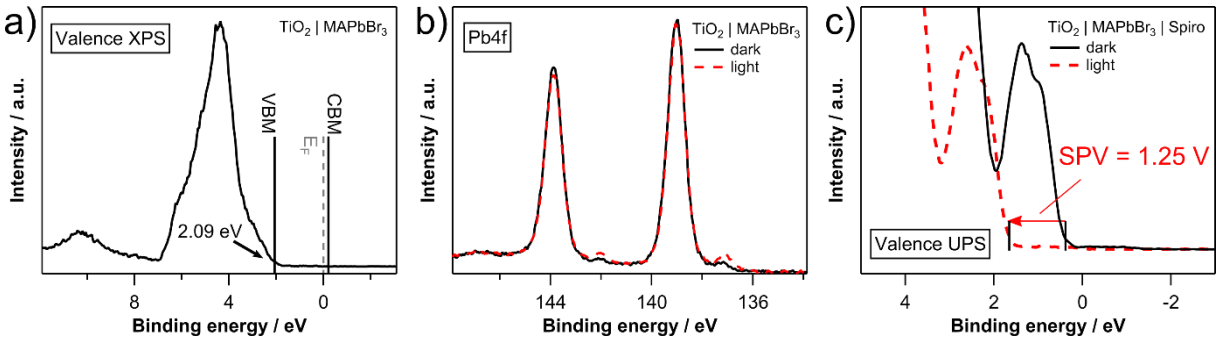

Figure 9.3: a) XPS valence band measurements and b) Pb4f emissions lines of a TiO_2 | $MAPbBr_3$ sample. The dark and light measurements show that no SPV is present. After the deposition of the spiro-MeOTAD layer the dark and light UPS valence band measurements in c) are showing an SPV of 1.25 V. Based on the VBM positions of the spiro-MeOTAD film in the dark, there is most likely no X-ray induced SPV present.

9.3. Supplementary information for chapter 1

Extended table of the charge carrier transport properties of MAPI

In chapter 1.1 different charge carrier transport properties for MAPI were tabularized, but only a range was given for each value. Table 9.1 and Table 9.2 below are showing all values including the references that they were taken from and the respective measurement technique used to determine the value.

Table 9.1: Extended table for charge carrier transport property values reported in the literature for single-crystalline MAPI samples.

Charge carrier	Mobility μ / $\frac{cm^2}{Vs}$	Carrier lifetime τ / µs	Diffusion length L / µm	reference
e^- h^+	24[a] and 105[b] 24.8[c] and 164[c]	82[d] and 95[e]	175[h]	[138]
e^- h^+	2.5[c]	0.02[fg] (sf) and 1[fg] (b)	2 to 8[h]	[137]
e^- h^+	67[c]	0.02[fg] (sf) and 0.6[fg] (b)	1.8 [h] (sf) and 10 [h] (b)	[256]
e^- h^+	66[b]	-	-	[31]

Table 9.2: Extended table for charge carrier transport property values reported in the literature for poly-crystalline thin MAPI samples.

Charge carrier	Mobility μ / $\frac{cm^2}{Vs}$	Carrier lifetime τ / µs	Diffusion length L / µm	reference
e^- h^+	1.4[g] 0.9[g]	0.0045[f] and 0.0056[g]	0.13[h] 0.09[h]	[257]
e^- h^+	0.7[f] 0.4[f]	0.0096[f]	0.13[f] 0.11[f]	[258]
e^- h^+	-	-	1.9[i] 1.5[i]	[259]

[a] = from time-of-flight measurements (TOF)
[b] = from Hall measurements
[c] = from the space charge limit current (SCLC) regime of JV measurements
[d] = from transient photovoltaic measurements (TPV)
[e] = from impedance spectroscopy measurements
[f] = from photoluminescence quenching (PLQ)
[g] = from transient absorption measurements (TA)
[h] = calculated from mobility and carrier lifetime
[i] = from electron-beam-induced current
sf = surface and b = bulk

9.4. Supplementary information for chapter 3

Modified PICS, extended table

Table 9.3 contains additional information on the determination of the modified photoionization cross-section (PICS) values of chapter 3.5. Four different precusor materials were thermally evaporated and *in-vacuo* measured by XPS. Atomic percentages were calculated using Scofield PICSs according to equation 1.19 given in chapter 1.3.4. Modified PICS were then determined so that the atomic percentages calculated by these modified PICS match the ideal, expected atomic percentages.

Table 9.3: Extended table for calculating the modified photoionization cross-section (PICS) values. TXFN stands for the transmission function and $KE^{0.6}$ for the energy correction.

Material	Emission Line	Area in cps	TXFN	$KE^{0.6}$	Scofield PICS	Norm. Area in cps	Calculated Atomic %	Ideal Atomic %	Mod. PICS
FAI	$Pb4f_{7/2}$	5.51E4	191.74	75.47	12.73	0.317	32.1	33.3	12.0
	$I3d_{5/2}$	1.85E5	252.98	57.92	19.87	0.634	67.9	67.7	19.87
MAI	C1s	5.91E3	207.36	70.34	1	0.405	26.0	20	0.844
	N1s	1.77E4	220.84	66.31	1.8	0.671	43.1	40	1.26
	$I3d_{5/2}$	1.40E5	252.83	57.95	19.87	0.480	30.8	20	19.87
PbI_2	C1s	1.27E3	207.19	70.40	1	0.087	34.1	33.3	0.929
	N1s	1.96E3	221.07	66.25	1.8	0.074	29.2	33.3	1.43
	$I3d_{5/2}$	2.72E4	252.89	57.94	19.87	0.093	36.7	33.3	19.9
CsI	$Cs3d_{5/2}$	2.05E5	272.33	53.53	23.76	0.5927	51.57	50	25.3
	$I3d_{5/2}$	1.62E5	253.16	57.88	19.87	0.5565	48.43	50	19.87

Fitting parameters for determining the stabilized PCE of the CsMAFAPI device

Since the efficiency of the device with CsFAPI as an absorber material presented in chapter 3.4.2 did not stabilize within the recorded 300 seconds, the curve of CsFAPI was fitted using an exponentially decaying function, to determine the stabilized PCE value. The fitting parameters are given in Table 9.4 below.

The following fit function was used: $f(x) = y_0 + A \cdot exp\left(\frac{-(x-x_0)}{\tau}\right)$

Table 9.4: Fitting parameters for the exponential decay function used to determine the stabilized PCE values for the CsMAFAPI perovskite.

parameter	value
y_0	13.47
A	-2.343
x_0	12.2
τ	146.18

Absolute binding energy positions of the perovskite absorbers investigated in chapter 3:

The following Table 9.5 shows all bandgap values and binding energy values of the core levels of the measured precursor materials and perovskites absorbers discussed in chapter 3.

Table 9.5: Absolut core level binding energy positions and core level to VBM differences of the thermally evaporated precursor materials and the five different perovskite absorbers (MAPI, FAPI, MAFAPI, CsFAPI, CsMAFAPI) on SnO_2 and NiO_x substrates, determined by XPS. The bandgap values were determined from UV/Vis measurements.

Sub.	Pero.	Bandgap	Binding Energy Positions in eV						Core Level to VBM Differences in eV					
			N1s MA^+	N1s FA^+	$I3d_{5/2}$	$Pb4f_{7/2}$	$Cs3d_{5/2}$	VBM	N1s MA^+	N1s FA^+	$I3d_{5/2}$	$Pb4f_{7/2}$	$Cs3d_{5/2}$
FTO	MAI	x	401.88	x	619.01	x	x	2.00	400.43	x	617.56	x	x
	FAI	x	x	400.14	618.58	x	x	1.87	x	398.74	617.18	X	x
	PbI_2	x	x	x	619.56	138.57	X	1.93	x	x	617.63	136.64	x
	CsI	x	x	x	618.24	x	723.86	1.49	x	x	616.75	x	722.37
SnO_2	MAPI	1.59	402.60	x	619.58	138.65	x	1.50	401.16	x	618.14	137.21	x
	FAPI	1.51	x	400.85	619.49	138.60	x	1.39	x	399.52	618.16	137.27	x
	MAFAPI	1.53	402.66	400.91	619.58	138.67	x	1.50	401.22	399.47	618.14	137.23	x
	CsFAPI	1.53	x	400.81	619.46	138.56	x	1.39	x	399.48	618.13	137.23	x
	CsMAFAPI	1.54	402.71	400.90	619.60	138.68	x	1.50	401.27	399.46	618.16	137.24	x
	average	1.54	402.66	400.87	619.54	138.63	x	1.47	401.22	399.48	618.15	137.24	x
NiO_x	MAPI	1.59	402.64	x	619.61	138.69	x	1.45	401.19	x	618.16	137.24	x
	FAPI	1.51	x	400.62	619.36	138.47	x	1.23	x	399.39	618.13	137.24	x
	MAFAPI	1.53	402.57	400.84	619.46	138.57	x	1.31	401.26	399.53	618.15	137.26	x
	CsFAPI	1.53	x	400.83	619.34	138.44	x	1.23	x	399.60	618.11	137.21	x
	CsMAFAPI	1.54	402.56	400.84	619.48	138.59	x	1.31	401.25	399.53	618.17	137.28	x
	average	1.54	402.59	400.78	619.45	138.55	x	1.30	401.23	399.51	618.14	137.25	x

Atomic concentrations of the perovskite absorbers investigated in chapter 3

The following Table 9.6 shows the atomic concentrations of the MAPI, FAPI, MAFAPI, CsFAPI, and CsMAFAPI perovskite absorbers investigated in chapter 3, calculated with Scofield PICSs and modified PICSs using equation 1.19 given in chapter 1.3.4.

Table 9.6: Atomic concentrations of the five different perovskite absorbers (MAPI, FAPI, MAFAPI, CsFAPI, CsMAFAPI) on SnO_2 and NiO_x substrates, determined by XPS with standard Scofield PICS and the modified PICS.

Substrate	Perovskite	Atomic concentrations with Scofield PICS					Atomic concentrations with modified PICS				
		N1s MA^+	N1s FA^+	$I3d_{5/2}$	$Pb4f_{7/2}$	$Cs3d_{5/2}$	N1s MA^+	N1s FA^+	$I3d_{5/2}$	$Pb4f_{7/2}$	$Cs3d_{5/2}$
on SnO_2 (classical)	MAPI	18.55	x	61.57	19.88	x	23.11	x	57.29	19.59	x
	FAPI	x	28.62	54.02	17.36	x	x	34.60	48.79	16.61	x
	MAFAPI	7.73	15.41	58.13	18.72	x	9.49	18.94	53.36	18.20	x
	CsFAPI	x	25.83	54.52	17.21	2.44	x	31.54	49.74	16.63	2.09
	CsMAFAPI	6.35	12.41	59.67	20.67	0.90	7.91	15.45	55.49	20.36	0.79
on NiO_x (inverted)	MAPI	14.91	x	63.2	21.89	x	18.77	x	59.43	21.80	x
	FAPI	x	23.94	57.26	18.81	x	x	29.34	52.42	18.24	x
	MAFAPI	6.10	14.70	59.65	19.55	x	7.55	18.19	55.12	19.14	x
	CsFAPI	x	21.69	57.45	19.6	1.26	x	26.78	52.98	19.15	1.09
	CsMAFAPI	5.55	13.12	60.03	20.32	0.97	6.91	16.35	55.86	20.03	0.85
Expected from precursor ratio	MAPI	20	x	60	20	x	20	x	60	20	x
	FAPI	x	33.3	50	16.7	x	x	33.3	50	16.7	x
	MAFAPI	9.1	18.2	54.5	18.2	x	9.1	18.2	54.5	18.2	x
	CsFAPI	x	29.1	51.3	17.1	2.6	x	29.1	51.3	17.1	2.6
	CsMAFAPI	8.7	17.4	54.8	18.3	0.9	8.7	17.4	54.8	18.3	0.9

9.5. Supplementary information for chapter 4

Absolute binding energy positions of the LiTFSI variation series

In chapter 5.3 the role of LiTFSI in LiTFSI-doped spiro-MeOTAD films with tBP as an additive was investigated. Table 9.7 below shows the binding energy positions of the core levels of spiro-MeOTAD samples prepared by spin-coating with varying LiTFSI concentrations.

Table 9.7: C1s, N1s, O1s, F1s, VBM values from He I and work function values of the spin-coated spiro-MeOTAD films with varying LiTFSI concentrations. The values marked with a circle "°" indicate extrapolated values.

Spiro : LiTFSI molar ratio	C1s	N1s	O1s	F1s	VBM from UPS	WF	I_P
1 : 0 (undoped)	284.91	400.09	533.76	689.54°	1.09	4.00	5.09
1 : 0.02	284.82	399.94	533.49	689.39	0.91	4.33	5.24
1 : 0.05	284.71	399.78	533.35	689.22	0.94	4.38	5.32
1 : 0.10	284.51	399.59	533.14	689.08	0.75	4.59	5.34
1 : 0.25	284.40	399.51	533.04	688.95	0.56	4.90	5.46
1 : 0.49 (standard)	284.29	399.46	533.0	688.99	0.46	5.07	5.53
1 : 0.75	284.29	399.52	533.08	688.88	0.41	5.33	5.74

Fitting parameters for the core level shifts of the LiTFSI variation series

In chapter 5.3 XPS measurements of LiTFSI-doped spiro-MeOTAD samples with varying LiTFSI concentrations were performed. In Figure 5.5 the binding energy shift of the core levels in dependence of the LiTFSI : spiro-MeOTAD molar ratio were fitted using exponentially decaying function. The fitting parameters are shown below in Table 9.8.

Table 9.8: Fitting parameters for fitting the binding energy shifts of the C1s, the F1s emission lines, the VBM values and the work function values of the spin-coated spiro-MeOTAD films with varying LiTFSI concentrations.

fitted values	y_0	A	x_0	τ
C1s	-0.618	0.622	0	0.112
F1s	-0.60	0.454	0.02	0.0691
VBM	-0.677	0.642	0	0.168
WF	1.28	-1.16	0	0.211

The following fit function was used: $f(x) = y_0 + A \cdot exp\left(\frac{-(x-x_0)}{\tau}\right)$

XPS core levels measurements of the LiTFSI variation series

In chapter 5.3 the role of LiTFSI in LiTFSI-doped spiro-MeOTAD films with tBP as an additive was investigated. Figure 9.6 below shows XPS core levels of spiro-MeOTAD samples prepared by spin-coating with varying LiTFSI concentrations.

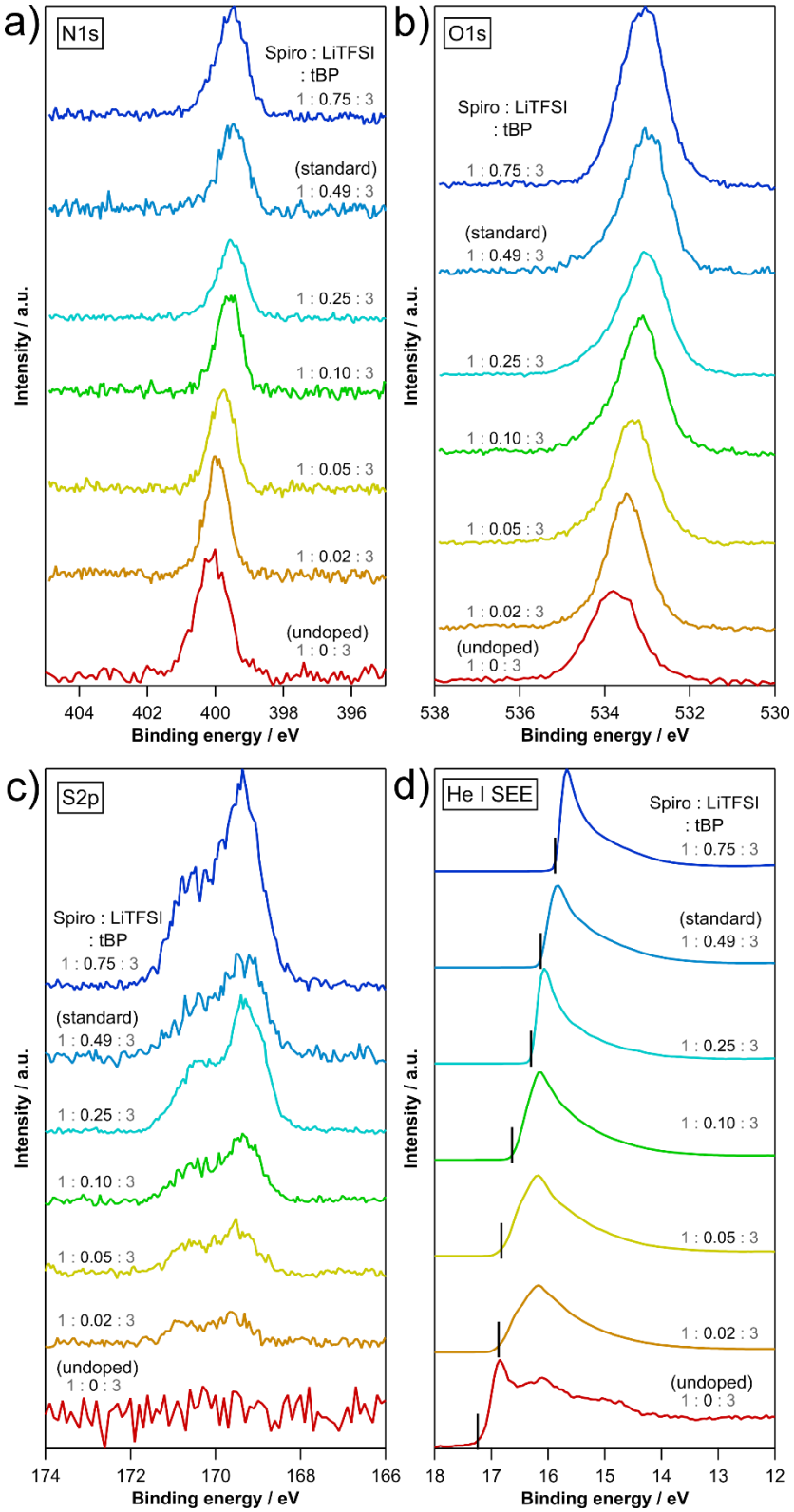

Figure 9.4: a) N1s emission lines, b) O1s emission lines, c) S2p emission lines and d) He I measurement with an applied bias of -6V for spin-coated spiro-MeOTAD samples with varying LiTFSI to spiro-MeOTAD molar ratios.

UV/Vis measurements of spiro-MeOTAD to determine its bandgap

For the spiro-MeOTAD | LiTFSI and MAPI | LiTFSI-doped spiro-MeOTAD interfaces drawn in chapters 5.5 and 5.6 the bandgap value of spiro-MeOTAD is required. Figure 9.5 shows the UV/Vis measurements that were performed to determine the bandgap of spiro-MeOTAD.

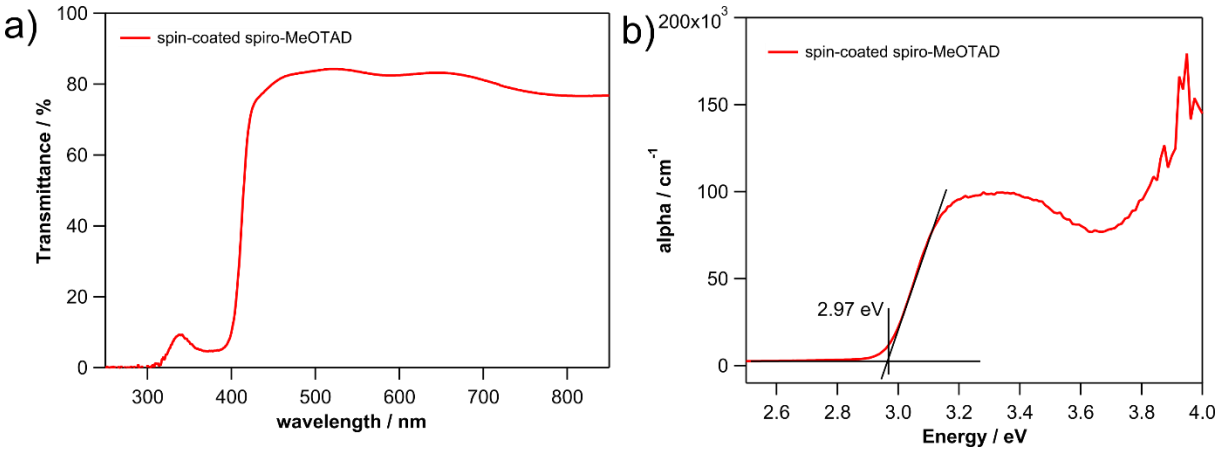

Figure 9.5: UV/Vis spectra of a spin-coated undoped spiro-MeOTAD film on a FTO substrate. a) The recorded transmittance plotted against the wavelength of the incident light and b) the absorption coefficient α, calculated from the measured transmittance and reflectance data after equation 1.9 plotted against the photon energy.

Absolute binding energy positions of the tBP variation series

In chapter 5.3 the role of tBP in LiTFSI-doped spiro-MeOTAD films with tBP as an additive was investigated. Table 9.9 below shows the binding energy positions of the core levels, the work function values, and ionization potentials of spiro-MeOTAD samples prepared by spin-coating with varying tBP concentrations.

Table 9.9: C1s, N1s, O1s, F1s, VBM values from He I and work function values of the spin-coated spiro-MeOTAD films with varying LiTFSI concentrations.

Spiro : LiTFSI : tBP molar ratio	C1s	N1s	O1s	F1s	VBM from UPS	WF	I_P
1 : 0 : 0	285.02	400.13	533.81	-	1.07	4.13	5.20
1 : 0 : 2.98	284.91	400.09	533.76	-	1.09	4.00	5.09
1 : 0:49 : 0	285.212	400.07	533.49	689.34	0.86	4.41	5.27
1 : 0.49 : 1	284.276	399.40	532.95	688.74	0.36	5.32	5.68
1 : 0.49 : 2	284.466	399.48	533.05	688.92	0.42	5.00	5.42
1 : 0.49 : 3	284.391	399.47	533.01	688.94	0.56	4.77	5.33
1 : 0.49 : 4	284.383	399.49	533.05	688.91	0.37	5.07	5.44

Absolute binding energy positions of the vacuum doping series

In chapter 5.4 LiTFSI-doped spiro-MeOTAD films prepared by thermal evaporation were investigated. Table 9.10 below shows the binding energy positions of the core levels, the work function values, and ionization potentials of vacuum-deposited LiTFSI-doped spiro-MeOTAD samples prepared by spin-coating with varying LiTFSI concentrations.

Table 9.10: C1s, N1s, O1s, F1s, VBM values from He I and work function values of the spin-coated spiro-MeOTAD films with varying LiTFSI concentrations. The values marked with a circle "°" indicate extrapolated values.

deposition method	Spiro : LiTFSI	C1s	N1s	O1s	F1s	VBM from UPS	WF	I_P
spin-coating	1 : 0 (undoped)	284.91	400.09	533.76	689.54°	1.09	4.00	5.09
	1 : 0.8	284.71	399.78	533.35	689.22	0.94	4.38	5.32
	1 : 5.3	284.29	399.52	533.09	688.88°	0.41	5.33	5.74
co-evaporation	1 : 0 (undoped)	285.10	400.26	533.85	689.69	1.34	3.80	5.14
	1 : 0.7	284.45	399.51	533.07	688.75	0.43	5.04	5.47
	1 : 5.3	284.09	399.25	532.79	688.53	0.36	5.29	5.65

XPS core levels measurements of the tBP variation series

In chapter 5.3 the role of LiTFSI in LiTFSI-doped spiro-MeOTAD films with tBP as an additive was investigated. Figure 9.6 below shows XPS core levels of spiro-MeOTAD samples prepared by spin-coating with varying LiTFSI concentrations.

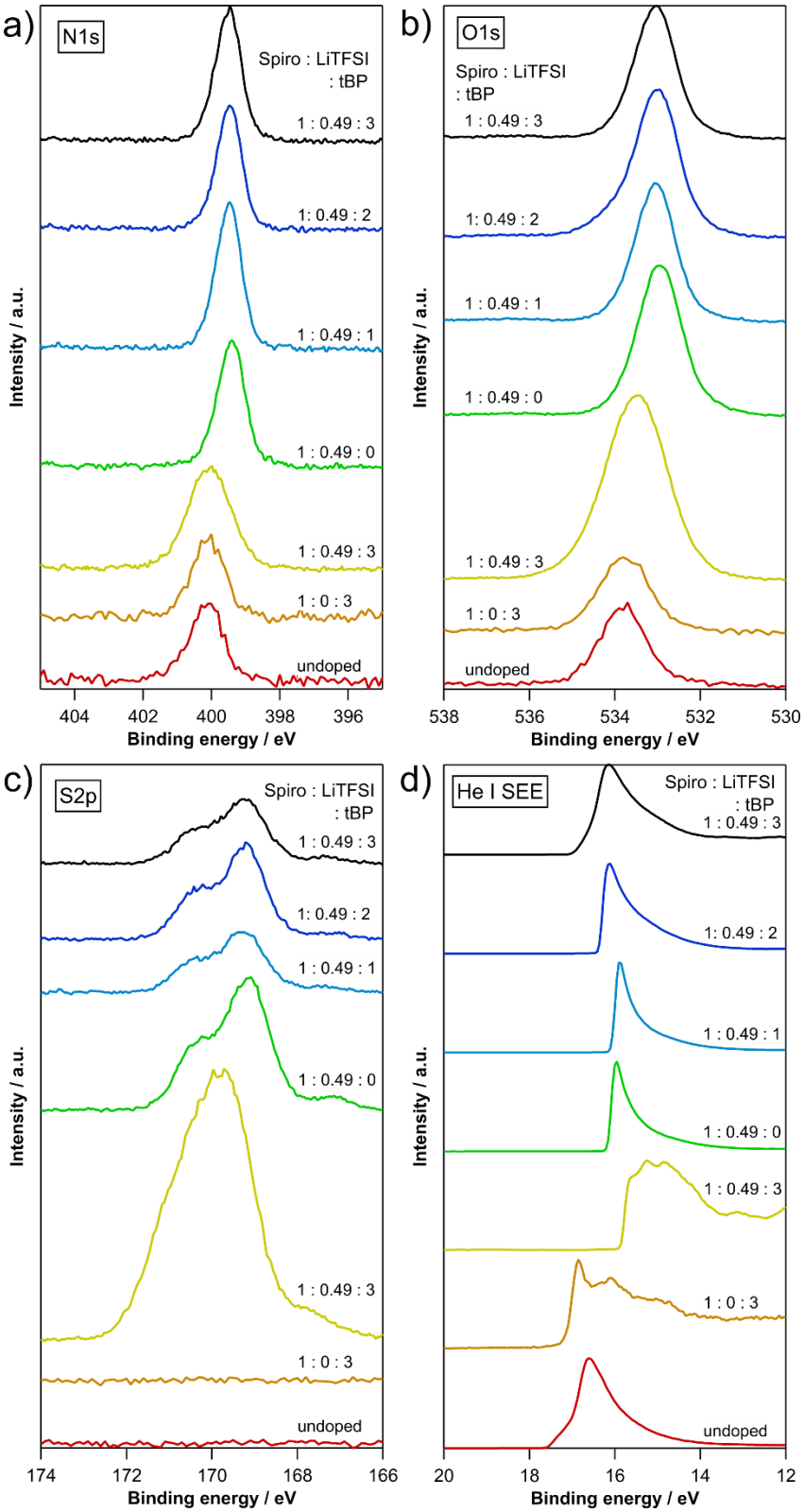

Figure 9.6: a) N1s emission lines, b) O1s emission lines, c) S2p emission lines and d) He I measurement with an applied bias of -6V for spin-coated spiro-MeOTAD samples with fixed LiTFSI and varying tBP to spiro-MeOTAD molar ratios.

XPS core levels measurements of the vacuum doping series

In chapter 5.4 LiTFSI-doped spiro-MeOTAD films prepared by thermal evaporation were investigated. Figure 9.7 below shows XPS core levels of spiro-MeOTAD samples prepared by spin-coating with varying LiTFSI concentrations.

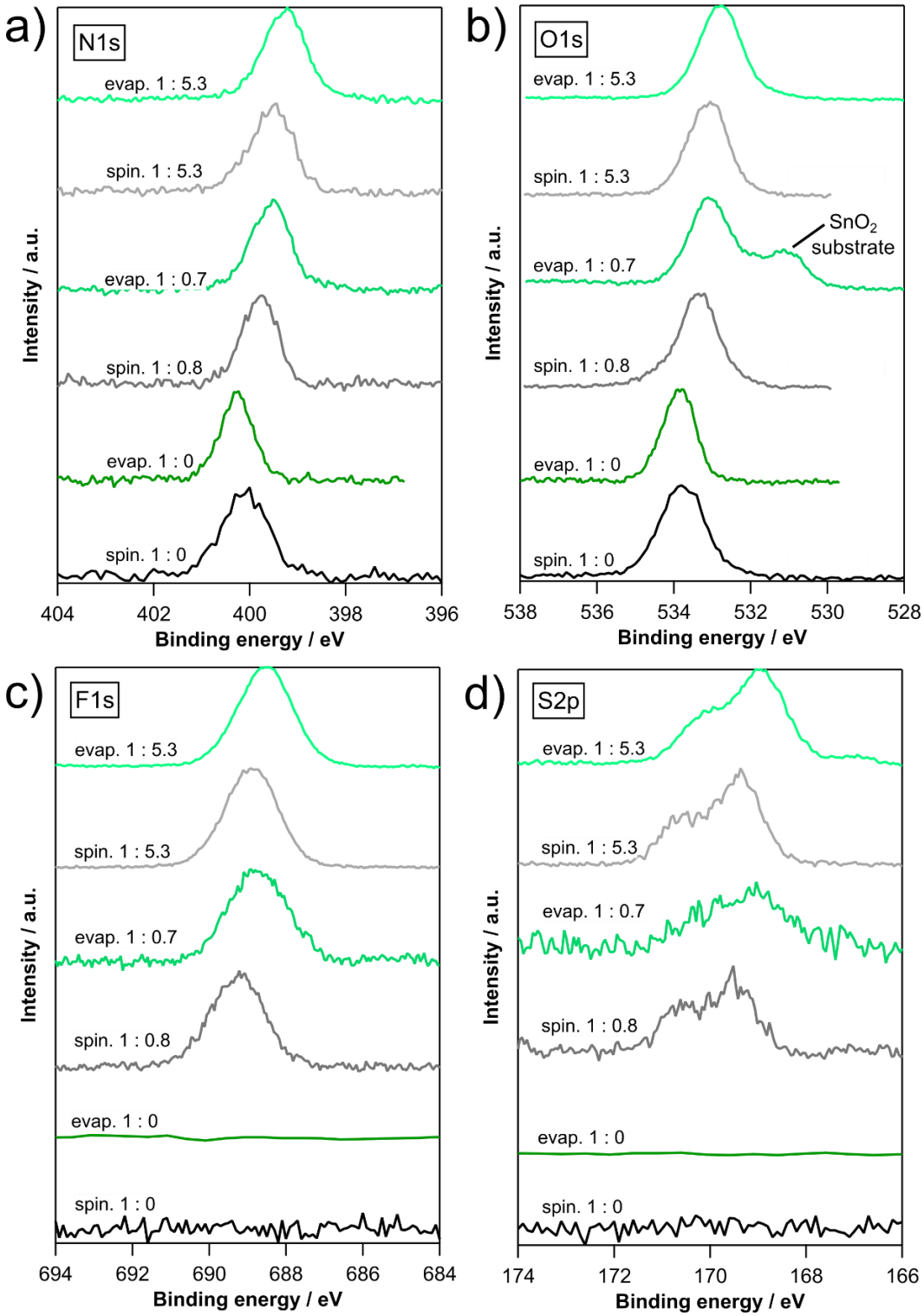

Figure 9.7: a) N1s, b) O1s, c) F1s and d) S2p emission lines of spin-coated and vacuum-deposited LiTFSI-doped spiro-MeOTAD films. The evaporated doped samples were synthesized by co-evaporation of LiTFSI and spiro-MeOTAD. The spiro-MeOTAD : LiTFSI ratios at the bottom were calculated by comparing the intensities of the C1s emission line of spiro-MeOTAD and the F1s emission line of LiTFSI. Spin-coated samples contain tBP.

Absolute binding energy positions spiro-MeOTAD | LiTFSI interface

In chapter 5.5 the spiro-MeOTAD | LiTFSI interface was investigated. Table 9.11 below shows the binding energy positions of the core levels and the work function values for different LiTFSI thicknesses.

Table 9.11: C1s, N1s, O1s, F1s, VBM values from He I and work function values of the spiro-MeOTAD | LiTFSI interface. The lines "-" indicate that no value could be determined because the signal of the emission line was too low. The grey written values marked with a star "*" indicate a charging due to too high LiTFSI thicknesses. The values marked with a circle "°" indicate extrapolated values.

Sample / LiTFSI thickness	C1s (Spiro)	N1s (both)	O1s (both)	F1s (LiTFSI)	VBM (Spiro)	VBM (LiTFSI)	WF
Spiro substrate	284.91	400.04	533.64	689.52°	0.79	-	4.22
0.16 nm	284.74	399.88	533.46	689.36	0.66	-	4.52
0.26 nm	284.59	399.68	533.28	689.08	0.50	-	4.80
0.61 nm	284.39	399.50	533.07	688.87	0.40	-	5.09
1.25 nm	284.34	399.47	532.98	688.73	0.37	-	5.36
3.88 nm	284.31	399.42	532.87	688.52	-	4.36	5.51
10.69 nm	284.34*	399.70*	533.10*	688.72	-	4.93*	4.83*
LiTFSI bulk	-	399.64*	533.08*	688.73	-	5.43*	3.90*

Fit functions for the spiro-MeOTAD | LiTFSI interface

In chapter 5.5 the spiro-MeOTAD | LiTFSI interface was investigated. In Figure 5.11 the binding energy shift of the core levels in dependence of the LiTFSI thickness were fitted using an exponentially decaying function. The fitting parameters are shown below in Table 9.12.

The following fit function was used: $f(x) = y_0 + A \cdot exp\left(\frac{-(x-x_0)}{\tau}\right)$

Table 9.12: Fitting parameters for fitting the binding energy shifts of the F1s emission lines, the C1s emission lines and the work function values used during the analysis of the spiro-MeOTAD films | LiTFSI interface.

fitted values	y_0	A	x_0	τ
F1s	688.550	0.743	0.155	0.580
C1s	-0.590	0.608	0	0.336
WF	-1.273	1.270	0	0.505

Extrapolation of the F1s binding energy position at the spiro-MeOTAD | LiTFSI interface

In chapter 5.5 the spiro-MeOTAD | LiTFSI interface was investigated. Figure 9.8 below shows the variation of the binding energy of the F1s emission line with increasing LiTFSI thickness. The data points were fitted with an exponentially decaying function (see Table 9.12 on the previous page) and extrapolated back to 0 nm to determine the full band bending inside LiTFSI.

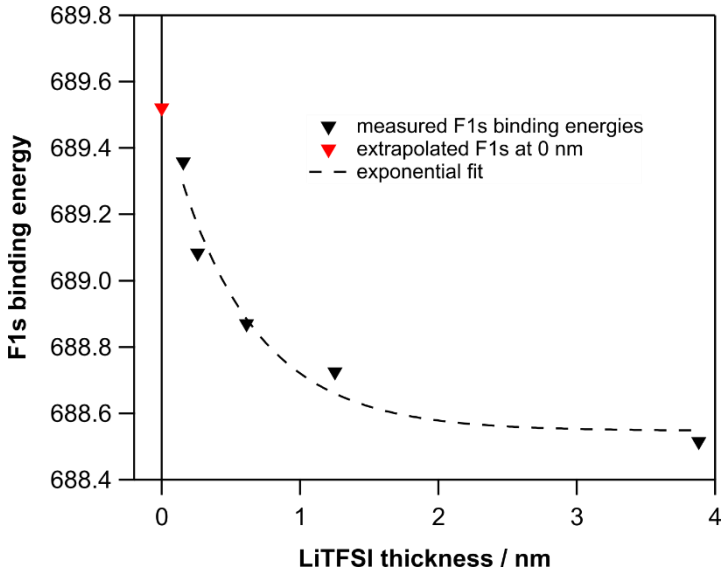

Figure 9.8: Variation of the F1s binding energy of LiTFSI during the spiro-MeOTAD | LiTFSI interface (black triangle) and the fit to extrapolate the hypothetical F1s binding energy positions for a LiTFSI thickness of 0 nm (red triangle) to determine the full band bending inside LiTFSI.

XPS core levels measurements of the spiro-MeOTAD | LiTFSI interface

In chapter 5.5 the spiro-MeOTAD | LiTFSI interface was investigated. Figure 9.9 below shows XPS core levels for different LiTFSI thicknesses.

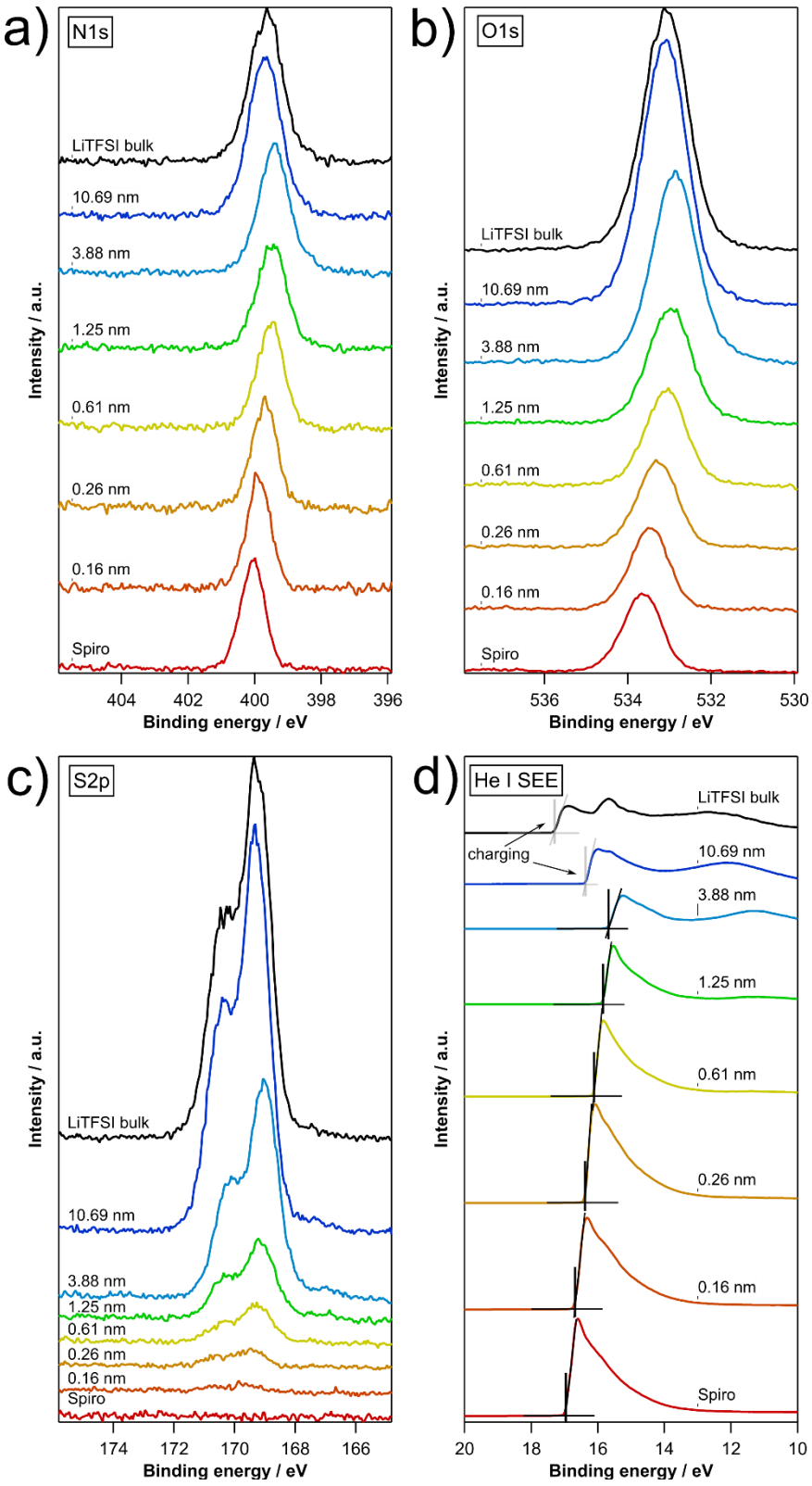

Figure 9.9: a) N1s, b) O1s, c) S2p emission lines and d) He I measurements with an applied bias of -6V to determine the work function values of the spiro-MeOTAD | LiTFSI interface.

Absolut binding energy positions of the MAPI | LiTFSI-doped spiro-MeOTAD interface:

In chapter 5.6 the MAPI | LiTFSI-doped spiro-MeOTAD interface was investigated. Table 9.13 below shows the binding energy positions of the core levels for different spiro-MeOTAD thicknesses.

Table 9.13: Core levels, VBM values from He I and work function values of the MAPI | LiTFSI-doped spiro-MeOTAD interface. The lines "-" indicate that no value could be determined because the signal of the emission line was too low. The values marked with a circle "°" indicate extrapolated values. The letter "D" and "L" indicate whether a measurement was performed in the dark or in the light.

Sample / Spiro thickness	N1s D (MAPI)	$Pb4f_{7/2}$ D (MAPI)	$I3d_{5/2}$ D (MAPI)	C1s D (Spiro)	C1s L (Spiro)	N1s (Spiro)	O1s (Spiro)
MAPI	402.59	138.65	619.58	285.00°	-	400.22°	-
0.8 nm	402.60	138.61	619.53	284.93	284.97	400.15	-
1.8 nm	402.59	138.61	619.54	284.95	284.99	400.14	533.68
3.6 nm	402.61	138.61	619.53	284.84	285.01	400.03	533.60
7.5 nm	402.55	138.62	619.53	284.75	285.08	399.93	533.49
14.3 nm	-	138.58	619.49	284.73	285.07	399.89	533.45
Spiro bulk	-	-	-	284.76	285.08	399.91	533.47
Sample / Spiro thickness	F1s (Spiro)	VBM D	VBM L	WF D			
MAPI	-	1.30	1.40	4.40			
0.8 nm	-	1.00	1.22	4.31			
1.8 nm	689.65	0.99	1.21	4.39			
3.6 nm	689.50	0.95	1.21	4.52			
7.5 nm	689.31	0.88	1.30	4.64			
14.3 nm	689.22	0.78	1.29	4.68			
Spiro bulk	689.27	0.65	1.30	4.81			

Difference spectra of the C1s emission line for the MAPI | LiTFSI-doped spiro-MeOTAD interface

In chapter 5.6 the MAPI | LiTFSI-doped spiro-MeOTAD interface was investigated. Since the C1s emission line of MAPI and spiro-MeOTAD are overlapping, difference spectra were used to determine the C1s positions of spiro-MeOTAD. The C1s emission line of pure MAPI (0 nm spiro-MeOTAD) was subtracted from the spectra where contributions of MAPI and spiro-MeOTAD are overlapping (0.8 nm, 1.8 nm, and 3.6 nm spiro-MeOTAD). The resulting spectra are shown below in Figure 9.10.

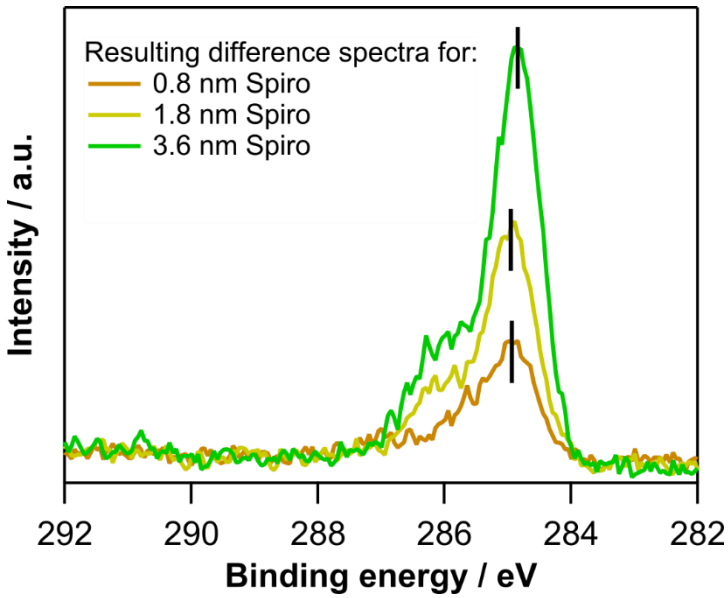

Figure 9.10: Difference spectra to determine the C1s positions of spiro-MeOTAD for the MAPI | LiTFSI-doped spiro-MeOTAD interface. The difference spectra were obtained by subtracting the C1s spectrum of pure MAPI (red curve in Figure 5.14) from the measured C1s spectra at spiro-MeOTAD thickness of 0.8 nm, 1.8 nm and 3.6 nm. Minor intensity scaling and shifts on the binding energy axis were applied to the C1s spectrum of pure MAPI so that the shape of the final spectrum looks like C1s of pure spiro-MeOTAD.

Extrapolation of the C1s and F1s binding energy position at the MAPI | spiro-MeOTAD interface

In chapter 5.6 the MAPI | LiTFSI-doped spiro-MeOTAD interface was investigated. Figure 9.11 below shows the variation of the binding energy of the C1s and F1s emission line with increasing LiTFSI thickness. The data points were fitted with an exponentially decaying function and extrapolated back to 0 nm to determine the full band bending inside spiro-MeOTAD.

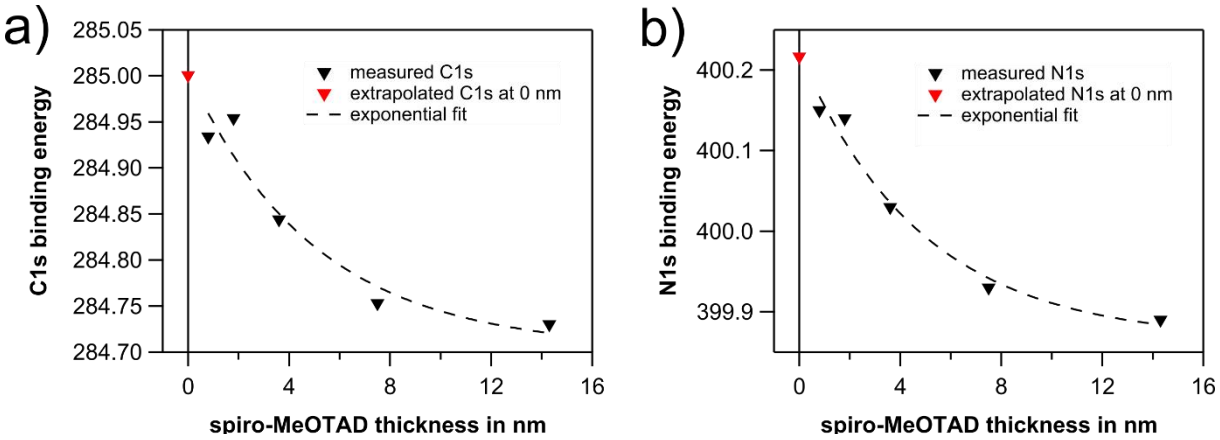

Figure 9.11: Variation of the a) C1s binding energy and b) N1s binding energy values of spiro-MeOTAD during the MAPI | LiTFSI-doped spiro-MeOTAD interface and the fits to extrapolate the hypothetical C1s and N1s binding energy positions for a spiro-MeOTAD thickness of 0 nm.

XPS core levels measurements of the MAPI | LiTFSI-doped spiro-MeOTAD interface

In chapter 5.6 the MAPI | LiTFSI-doped spiro-MeOTAD interface was investigated. Figure 9.12 below shows XPS core levels for different spiro-MeOTAD thicknesses.

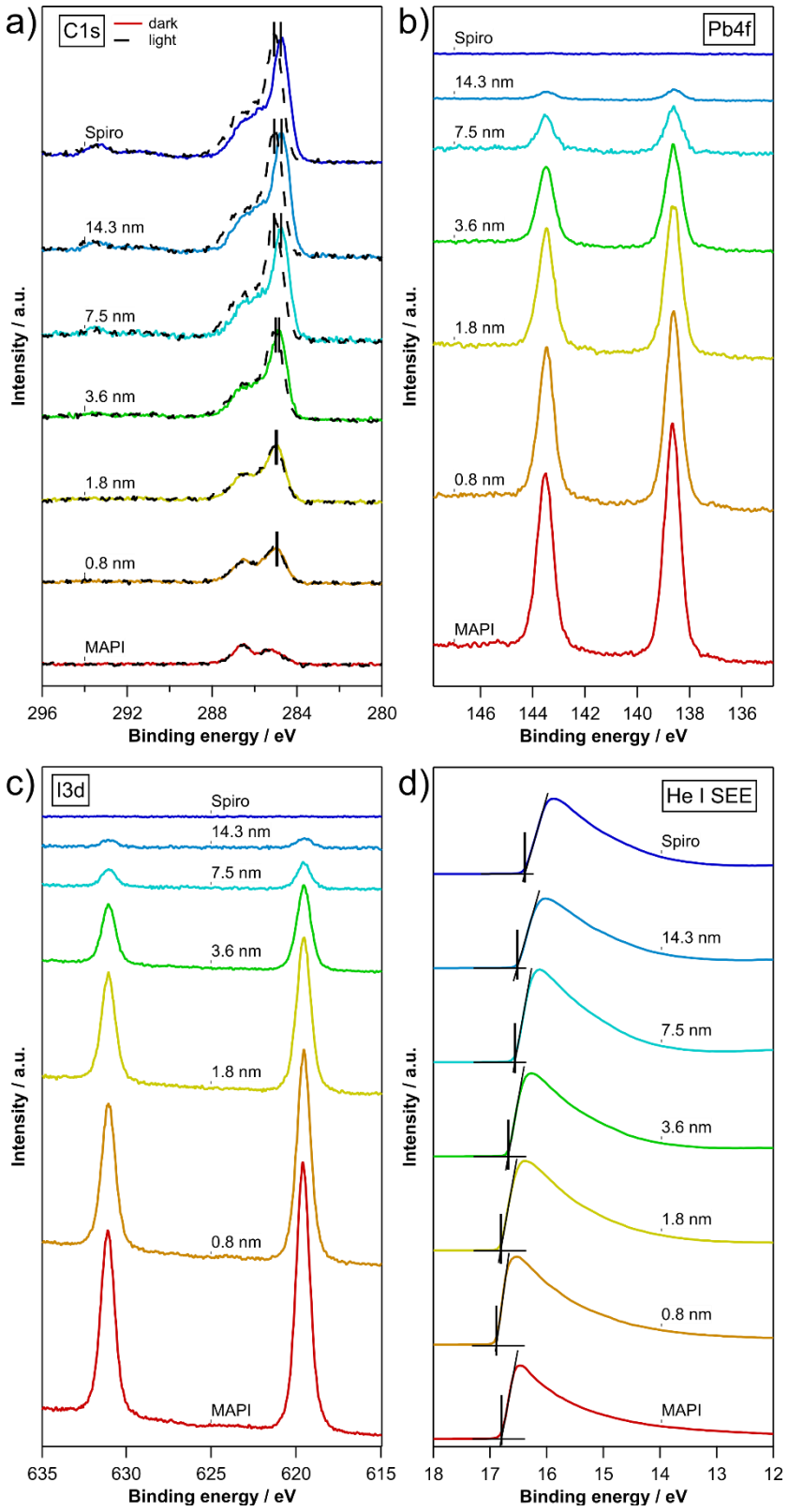

Figure 9.12: a) C1s, b) Pb4f, c) I3d emission lines and d) He I measurements with an applied bias of -6V to determine the work function values of the MAPI | LiTFSI-doped spiro-MeOTAD interface.

XPS core levels measurements of the MAPI | LiTFSI-doped spiro-MeOTAD interface

In chapter 5.6 the MAPI | LiTFSI-doped spiro-MeOTAD interface was investigated. Figure 9.13 below shows XPS core levels for different spiro-MeOTAD thicknesses.

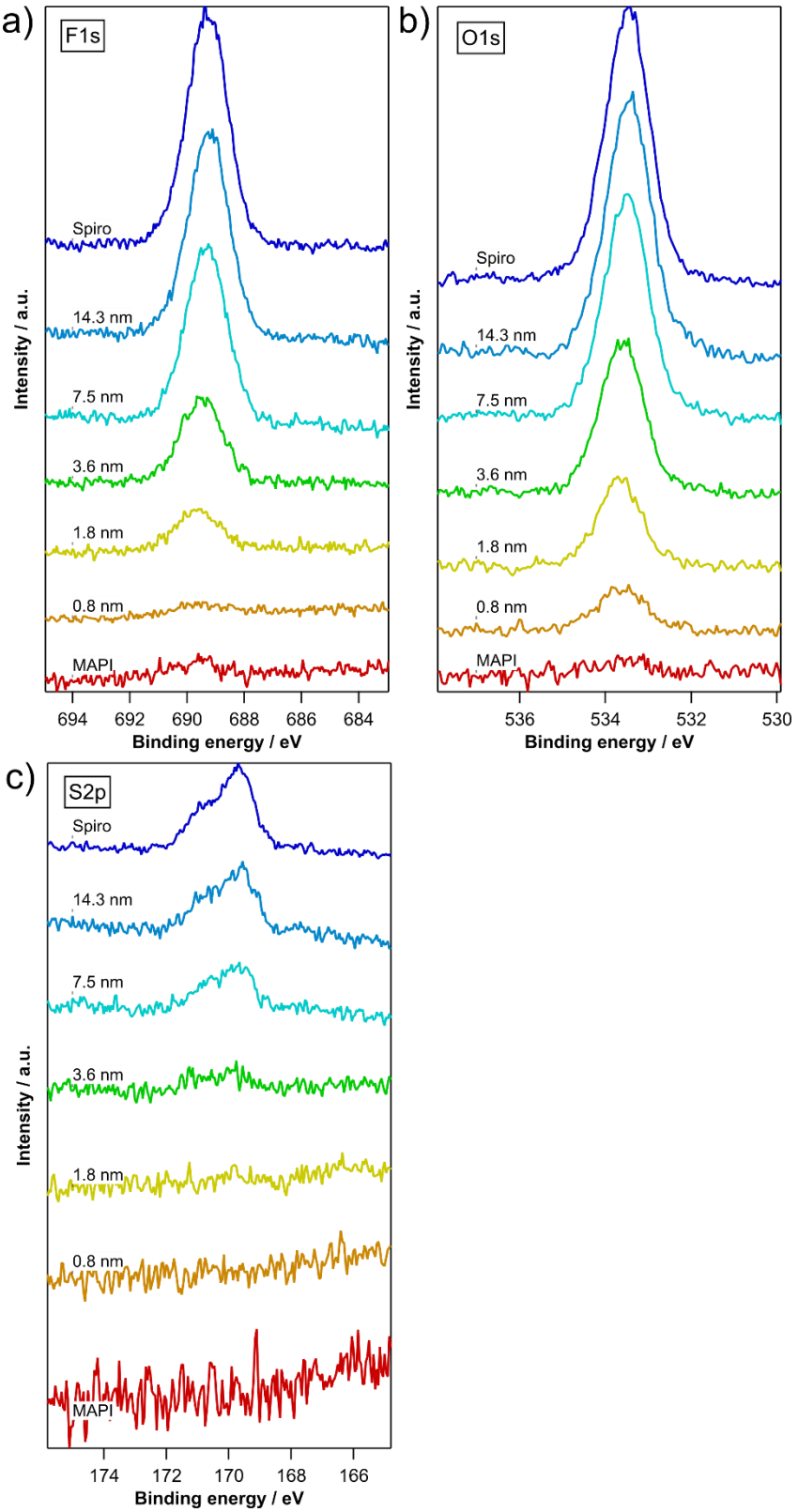

Figure 9.13: a) F1s, b) O1s and c) S2p emissions lines of the MAPI | LiTFSI-doped spiro-MeOTAD interface.

9.6. Supplementary information for chapter 6

Absolute binding energy positions of the NiO_x | MAPI tapered cross-section

In chapter 6.3 the NiO_x | MAPI interface was investigated by TCS-XPS. Table 9.14 shows the core level positions at the interface and at the bulk of MAPI. Table 9.15 compares the core level binding energy of the MAPI perovskite used for the TCS-XPS experiment to the MAPI perovskite investigated in chapter 3.

Table 9.14: Pb4f7/2, I3d5/2, Ni2p3/2, O1s and VBM values for the NiO_x | MAPI tapered cross-section experiment.

Position	$Pb4f_{7/2}$ (MAPI)	$I3d_{5/2}$ (MAPI)	$Ni2p_{3/2}$ (NiO_x)	O1s (NiO_x)	VBM
thin MAPI area	138.41	619.20	854.56	530.04	1.50
MAPI bulk	138.85	619.68	854.53	530.03	0.68
Total shift	0.44	0.49	-0.03	-0.01	-

Table 9.15: Comparison of the MAPI perovskite used for the tapered cross-section experiment and the MAPI perovskites studied in chapter 3 (here labeled as MAPI reference).

Sample	absolute positions			core level to VBM distances	
-	$Pb4f_{7/2}$	$I3d_{5/2}$	VBM	$Pb4f_{7/2}$	$I3d_{5/2}$
MAPI tapered	138.85	619.68	1.5	137.35	618.18
MAPI reference	138.69	619.61	1.45	137.24	618.16

C1s and O1s core levels measurements of the NiO_x | MAPI tapered cross-section

In chapter 6.3 the NiO_x | MAPI interface was investigated by TCS-XPS. Figure 9.14 below shows the C1s and O1s emission lines for different NiO_x thicknesses. Going from bottom to top means moving along the wedge from the NiO_x side to the MAPI side.

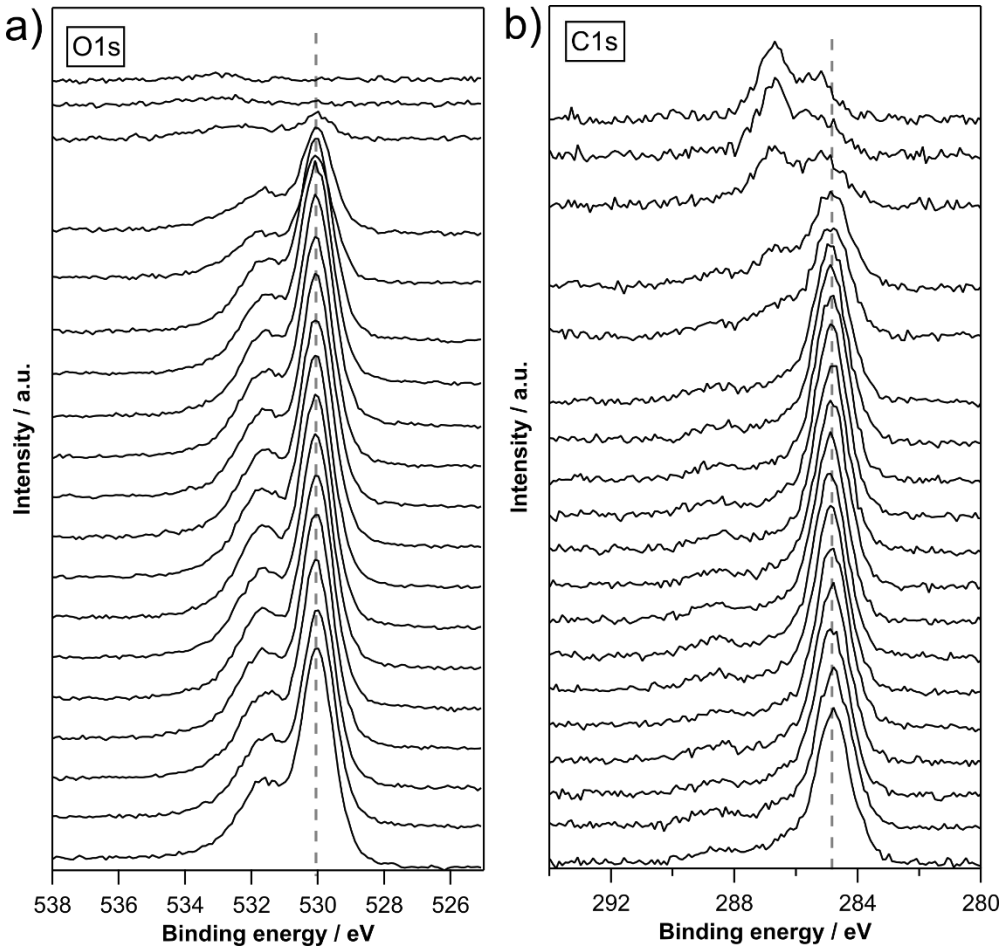

Figure 9.14: a) C1s and b) O1s spectra of an XPS line scan on a NiO_x | MAPI tapered cross-section. Going from bottom to top means moving along the wedge from the NiO_x side to the MAPI side.

9.7. Supplementary information for chapter 7

Absolut binding energy positions of the MAPI | C_{60} interface

In chapter 7.2 the MAPI | C_{60} interface was investigated. Table 9.16 below shows the binding energy positions of the core levels for different spiro-MeOTAD thicknesses.

Table 9.16: Absolute binding energy positions of the $Pb4f_{7/2}$, $I3d_{5/2}$, C1s emission lines, and the VBM values of the MAPI | C_{60} interface.

Sample / C_{60} deposition time	$Pb4f_{7/2}$ (MAPI)	$I3d_{5/2}$ (MAPI)	C1s (C_{60})	VBM (both)
MAPI substrate	138.64	619.54	-	1.51
1 min	138.67	619.59	-	-
2 min	138.69	619.61	285.38	-
4 min	138.67	619.60	285.38	-
8 min	138.66	619.58	285.34	-
16 min	138.62	619.52	285.31	-
C_{60} bulk	-	-	285.29	1.49

10. Literature

[1] G. Rose, Ueber einige neue Mineralien des Urals, *Journal fuer Praktische Chemie*, **1840**, *19*, 459.

[2] V. M. Goldschmidt, Die Gesetze der Krystallochemie, *Naturwissenschaften*, **1926**, *14*, 477.

[3] W. Travis, E. N. K. Glover, H. Bronstein, D. O. Scanlon, R. G. Palgrave, On the application of the tolerance factor to inorganic and hybrid halide perovskites: a revised system, *Chemical science*, **2016**, *7*, 4548.

[4] A. Kojima, K. Teshima, Y. Shirai, T. Miyasaka, Organometal halide perovskites as visible-light sensitizers for photovoltaic cells, *Journal of the American Chemical Society*, **2009**, *131*, 6050.

[5] D.-Y. Son, J.-W. Lee, Y. J. Choi, I.-H. Jang, S. Lee, P. J. Yoo, H. Shin, N. Ahn, M. Choi, D. Kim, N.-G. Park, Self-formed grain boundary healing layer for highly efficient CH3NH3PbI3 perovskite solar cells, *Nature Energy*, **2016**, *1*.

[6] B. Brunetti, C. Cavallo, A. Ciccioli, G. Gigli, A. Latini, On the Thermal and Thermodynamic (In)Stability of Methylammonium Lead Halide Perovskites, *Scientific reports*, **2016**, *6*, 31896.

[7] A. Ciccioli, A. Latini, Thermodynamics and the Intrinsic Stability of Lead Halide Perovskites CH3NH3PbX3, *The journal of physical chemistry letters*, **2018**, *9*, 3756.

[8] E. J. Juarez-Perez, L. K. Ono, M. Maeda, Y. Jiang, Z. Hawash, Y. Qi, Photodecomposition and thermal decomposition in methylammonium halide lead perovskites and inferred design principles to increase photovoltaic device stability, *Journal of Materials Chemistry A*, **2018**, *6*, 9604.

[9] E. J. Juarez-Perez, Z. Hawash, S. R. Raga, L. K. Ono, Y. Qi, Thermal degradation of CH 3 NH 3 PbI 3 perovskite into NH 3 and CH 3 I gases observed by coupled thermogravimetry–mass spectrometry analysis, *Energy & environmental science*, **2016**, *9*, 3406.

[10] A. F. Akbulatov, S. Y. Luchkin, L. A. Frolova, N. N. Dremova, K. L. Gerasimov, I. S. Zhidkov, D. V. Anokhin, E. Z. Kurmaev, K. J. Stevenson, P. A. Troshin, Probing the Intrinsic Thermal and Photochemical Stability of Hybrid and Inorganic Lead Halide Perovskites, *The journal of physical chemistry letters*, **2017**, *8*, 1211.

[11] B. Philippe, B. Park, R. Lindblad, J. Oscarsson, S. Ahmadi, E. M. J. Johansson, H. Rensmo, Chemical and Electronic Structure Characterization of Lead Halide Perovskites and Stability Behavior under Different Exposures—A Photoelectron Spectroscopy Investigation, *Chemistry of Materials*, **2015**, *27*, 1720.

[12] M. O. Reese, S. A. Gevorgyan, M. Jørgensen, E. Bundgaard, S. R. Kurtz, D. S. Ginley, D. C. Olson, M. T. Lloyd, P. Morvillo, E. A. Katz, A. Elschner, O. Haillant, T. R. Currier, V. Shrotriya, M. Hermenau, M. Riede, K. R. Kirov, G. Trimmel, T. Rath, O. Inganäs, F. Zhang, M. Andersson, K. Tvingstedt, M. Lira-Cantu, D. Laird, C. McGuiness, S. Gowrisanker, M. Pannone, M. Xiao, J. Hauch, R. Steim, D. M. DeLongchamp, R. Rösch, H. Hoppe, N. Espinosa, A. Urbina, G. Yaman-Uzunoglu, J.-B. Bonekamp, A. J. van Breemen, C. Girotto, E. Voroshazi, F. C. Krebs, Consensus stability testing protocols for organic photovoltaic materials and devices, *Solar Energy Materials and Solar Cells*, **2011**, *95*, 1253.

[13] M. V. Khenkin, E. A. Katz, A. Abate, G. Bardizza, J. J. Berry, C. Brabec, F. Brunetti, V. Bulović, Q. Burlingame, A. Di Carlo, R. Cheacharoen, Y.-B. Cheng, A. Colsmann, S. Cros, K. Domanski, M. Dusza, C. J. Fell, S. R. Forrest, Y. Galagan, D. Di Girolamo, M. Grätzel, A. Hagfeldt, E. von Hauff, H. Hoppe, J. Kettle, H. Köbler, M. S. Leite, S. Liu, Y.-L. Loo, J. M. Luther, C.-Q. Ma, M. Madsen, M. Manceau, M.

Matheron, M. McGehee, R. Meitzner, M. K. Nazeeruddin, A. F. Nogueira, Ç. Odabaşı, A. Osherov, N.-G. Park, M. O. Reese, F. de Rossi, M. Saliba, U. S. Schubert, H. J. Snaith, S. D. Stranks, W. Tress, P. A. Troshin, V. Turkovic, S. Veenstra, I. Visoly-Fisher, A. Walsh, T. Watson, H. Xie, R. Yıldırım, S. M. Zakeeruddin, K. Zhu, M. Lira-Cantu, Consensus statement for stability assessment and reporting for perovskite photovoltaics based on ISOS procedures, *Nature Energy*, **2020**, *5*, 35.

[14] M. Hada, M. Abdullah Al Asad, M. Misawa, Y. Hasegawa, R. Nagaoka, H. Suzuki, R. Mishima, H. Ota, T. Nishikawa, Y. Yamashita, Y. Hayashi, K. Tsuruta, A mechanistic investigation of moisture-induced degradation of methylammonium lead iodide, *Applied Physics Letters*, **2020**, *117*, 253304.

[15] Z. Song, N. Shrestha, S. C. Watthage, G. K. Liyanage, Z. S. Almutawah, R. H. Ahangharnejhad, A. B. Phillips, R. J. Ellingson, M. J. Heben, Impact of Moisture on Photoexcited Charge Carrier Dynamics in Methylammonium Lead Halide Perovskites, *The journal of physical chemistry letters*, **2018**, *9*, 6312.

[16] S.-W. Lee, S. Kim, S. Bae, K. Cho, T. Chung, L. E. Mundt, S. Lee, S. Park, H. Park, M. C. Schubert, S. W. Glunz, Y. Ko, Y. Jun, Y. Kang, H.-S. Lee, D. Kim, UV Degradation and Recovery of Perovskite Solar Cells, *Scientific reports*, **2016**, *6*, 38150.

[17] N. H. Nickel, F. Lang, V. V. Brus, O. Shargaieva, J. Rappich, Unraveling the Light-Induced Degradation Mechanisms of CH 3 NH 3 PbI 3 Perovskite Films, *Advanced Electronic Materials*, **2017**, *3*, 1700158.

[18] T. Leijtens, G. E. Eperon, S. Pathak, A. Abate, M. M. Lee, H. J. Snaith, Overcoming ultraviolet light instability of sensitized TiO_2 with meso-superstructured organometal tri-halide perovskite solar cells, *Nature communications*, **2013**, *4*, 2885.

[19] J. Yang, K. M. Fransishyn, T. L. Kelly, Comparing the Effect of Mesoporous and Planar Metal Oxides on the Stability of Methylammonium Lead Iodide Thin Films, *Chemistry of Materials*, **2016**, *28*, 7344.

[20] S. W. Glunz, R. Preu, D. Biro, in *Comprehensive Renewable Energy*, Elsevier, **2012**, p. 353.

[21] R. Wang, M. Mujahid, Y. Duan, Z.-K. Wang, J. Xue, Y. Yang, A Review of Perovskites Solar Cell Stability, *Advanced Functional Materials*, **2019**, *29*, 1808843.

[22] P. Holzhey, P. Yadav, S.-H. Turren-Cruz, A. Ummadisingu, M. Grätzel, A. Hagfeldt, M. Saliba, A chain is as strong as its weakest link – Stability study of MAPbI3 under light and temperature, *Materials Today*, **2019**, *29*, 10.

[23] D. C. Jordan, S. R. Kurtz, K. VanSant, J. Newmiller, Compendium of photovoltaic degradation rates, *Progress in Photovoltaics: Research and Applications*, **2016**, *24*, 978.

[24] G. E. Eperon, S. D. Stranks, C. Menelaou, M. B. Johnston, L. M. Herz, H. J. Snaith, Formamidinium lead trihalide: a broadly tunable perovskite for efficient planar heterojunction solar cells, *Energy & environmental science*, **2014**, *7*, 982.

[25] T. M. Koh, K. Fu, Y. Fang, S. Chen, T. C. Sum, N. Mathews, S. G. Mhaisalkar, P. P. Boix, T. Baikie, Formamidinium-Containing Metal-Halide: An Alternative Material for Near-IR Absorption Perovskite Solar Cells, *The Journal of Physical Chemistry C*, **2014**, *118*, 16458.

[26] W. Shockley, H. J. Queisser, Detailed Balance Limit of Efficiency of p-n Junction Solar Cells, *Journal of Applied Physics*, **1961**, *32*, 510.

[27] G. E. Eperon, G. M. Paternò, R. J. Sutton, A. Zampetti, A. A. Haghighirad, F. Cacialli, H. J. Snaith, Inorganic caesium lead iodide perovskite solar cells, *Journal of Materials Chemistry A*, **2015**, *3*, 19688.

[28] E. J. Juarez-Perez, L. K. Ono, Y. Qi, Thermal degradation of formamidinium based lead halide perovskites into sym -triazine and hydrogen cyanide observed by coupled thermogravimetry-mass spectrometry analysis, *Journal of Materials Chemistry A*, **2019**, *7*, 16912.

[29] R. J. Sutton, G. E. Eperon, L. Miranda, E. S. Parrott, B. A. Kamino, J. B. Patel, M. T. Hörantner, M. B. Johnston, A. A. Haghighirad, D. T. Moore, H. J. Snaith, Bandgap-Tunable Cesium Lead Halide Perovskites with High Thermal Stability for Efficient Solar Cells, *Advanced Energy Materials*, **2016**, *6*, 1502458.

[30] F. Ma, J. Li, W. Li, N. Lin, L. Wang, J. Qiao, Stable α/δ phase junction of formamidinium lead iodide perovskites for enhanced near-infrared emission, *Chemical science*, **2017**, *8*, 800.

[31] C. C. Stoumpos, C. D. Malliakas, M. G. Kanatzidis, Semiconducting tin and lead iodide perovskites with organic cations: phase transitions, high mobilities, and near-infrared photoluminescent properties, *Inorganic chemistry*, **2013**, *52*, 9019.

[32] O. J. Weber, D. Ghosh, S. Gaines, P. F. Henry, A. B. Walker, M. S. Islam, M. T. Weller, Phase Behavior and Polymorphism of Formamidinium Lead Iodide, *Chemistry of Materials*, **2018**, *30*, 3768.

[33] S. Jiang, Y. Luan, J. I. Jang, T. Baikie, X. Huang, R. Li, F. O. Saouma, Z. Wang, T. J. White, J. Fang, Phase Transitions of Formamidinium Lead Iodide Perovskite under Pressure, *Journal of the American Chemical Society*, **2018**, *140*, 13952.

[34] C. K. MØLLER, Crystal Structure and Photoconductivity of Cæsium Plumbohalides, *Nature*, **1958**, *182*, 1436.

[35] J. Borchert, R. L. Milot, J. B. Patel, C. L. Davies, A. D. Wright, L. Martínez Maestro, H. J. Snaith, L. M. Herz, M. B. Johnston, Large-Area, Highly Uniform Evaporated Formamidinium Lead Triiodide Thin Films for Solar Cells, *ACS Energy Letters*, **2017**, *2*, 2799.

[36] T. Chen, B. J. Foley, C. Park, C. M. Brown, L. W. Harriger, J. Lee, J. Ruff, M. Yoon, J. J. Choi, S.-H. Lee, Entropy-driven structural transition and kinetic trapping in formamidinium lead iodide perovskite, *Science advances*, **2016**, *2*, e1601650.

[37] C. Wang, A. S. R. Chesman, J. J. Jasieniak, Stabilizing the cubic perovskite phase of CsPbI3 nanocrystals by using an alkyl phosphinic acid, *Chemical communications*, **2016**, *53*, 232.

[38] C. Yang, Q. Han, S. Liu, J. Liao, C. Long, Y. Li, G. Dai, J. Yang, X. Liu, Can Vacuum Deposition Apply to Bismuth-Doped γ-CsPbI3 Perovskite? Revealing the Role of Bi3+ in the Formation of Black Phase, *The journal of physical chemistry letters*, **2021**.

[39] Z. Li, M. Yang, J.-S. Park, S.-H. Wei, J. J. Berry, K. Zhu, Stabilizing Perovskite Structures by Tuning Tolerance Factor: Formation of Formamidinium and Cesium Lead Iodide Solid-State Alloys, *Chemistry of Materials*, **2016**, *28*, 284.

[40] B. Charles, M. T. Weller, S. Rieger, L. E. Hatcher, P. F. Henry, J. Feldmann, D. Wolverson, C. C. Wilson, Phase Behavior and Substitution Limit of Mixed Cesium-Formamidinium Lead Triiodide Perovskites, *Chemistry of Materials*, **2020**, *32*, 2282.

[41] J. A. Schwenzer, T. Hellmann, B. A. Nejand, H. Hu, T. Abzieher, F. Schackmar, I. M. Hossain, P. Fassl, T. Mayer, W. Jaegermann, U. Lemmer, U. W. Paetzold, Thermal Stability and Cation Composition of Hybrid Organic-Inorganic Perovskites, *ACS applied materials & interfaces*, **2021**, *13*, 15292.

[42] S.-H. Turren-Cruz, A. Hagfeldt, M. Saliba, Methylammonium-free, high-performance, and stable perovskite solar cells on a planar architecture, *Science*, **2018**, *362*, 449.

[43] I. R. Benmessaoud, A.-L. Mahul-Mellier, E. Horváth, B. Maco, M. Spina, H. A. Lashuel, L. Forró, Health hazards of methylammonium lead iodide based perovskites: cytotoxicity studies, *Toxicology research*, **2016**, *5*, 407.

[44] A. Babayigit, D. Duy Thanh, A. Ethirajan, J. Manca, M. Muller, H.-G. Boyen, B. Conings, Assessing the toxicity of Pb- and Sn-based perovskite solar cells in model organism Danio rerio, *Scientific reports*, **2016**, *6*, 18721.

[45] G. Schileo, G. Grancini, Lead or no lead? Availability, toxicity, sustainability and environmental impact of lead-free perovskite solar cells, *Journal of Materials Chemistry C*, **2021**, *9*, 67.

[46] L. Serrano-Lujan, N. Espinosa, T. T. Larsen-Olsen, J. Abad, A. Urbina, F. C. Krebs, Tin- and Lead-Based Perovskite Solar Cells under Scrutiny: An Environmental Perspective, *Advanced Energy Materials*, **2015**, *5*, 1501119.

[47] A. Abate, Perovskite Solar Cells Go Lead Free, *Joule*, **2017**, *1*, 659.

[48] J. Li, H.-L. Cao, W.-B. Jiao, Q. Wang, M. Wei, I. Cantone, J. Lü, A. Abate, Biological impact of lead from halide perovskites reveals the risk of introducing a safe threshold, *Nature communications*, **2020**, *11*, 310.

[49] H. Hoshi, N. Shigeeda, T. Dai, Improved oxidation stability of tin iodide cubic perovskite treated by 5-ammonium valeric acid iodide, *Materials Letters*, **2016**, *183*, 391.

[50] K. P. Marshall, R. I. Walton, R. A. Hatton, Tin perovskite/fullerene planar layer photovoltaics: improving the efficiency and stability of lead-free devices, *Journal of Materials Chemistry A*, **2015**, *3*, 11631.

[51] C. Wang, Y. Zhang, F. Gu, Z. Zhao, H. Li, H. Jiang, Z. Bian, Z. Liu, Illumination Durability and High-Efficiency Sn-Based Perovskite Solar Cell under Coordinated Control of Phenylhydrazine and Halogen Ions, *Matter*, **2021**, *4*, 709.

[52] M. H. Kumar, S. Dharani, W. L. Leong, P. P. Boix, R. R. Prabhakar, T. Baikie, C. Shi, H. Ding, R. Ramesh, M. Asta, M. Graetzel, S. G. Mhaisalkar, N. Mathews, Lead-free halide perovskite solar cells with high photocurrents realized through vacancy modulation, *Advanced Materials*, **2014**, *26*, 7122.

[53] K. J. Savill, A. M. Ulatowski, M. D. Farrar, M. B. Johnston, H. J. Snaith, L. M. Herz, Impact of Tin Fluoride Additive on the Properties of Mixed Tin-Lead Iodide Perovskite Semiconductors, *Advanced Functional Materials*, **2020**, *30*, 2005594.

[54] F. Hao, C. C. Stoumpos, R. P. H. Chang, M. G. Kanatzidis, Anomalous band gap behavior in mixed Sn and Pb perovskites enables broadening of absorption spectrum in solar cells, *Journal of the American Chemical Society*, **2014**, *136*, 8094.

[55] C. Wang, Z. Song, C. Li, D. Zhao, Y. Yan, Low-Bandgap Mixed Tin-Lead Perovskites and Their Applications in All-Perovskite Tandem Solar Cells, *Advanced Functional Materials*, **2019**, *29*, 1808801.

[56] R. Lin, K. Xiao, Z. Qin, Q. Han, C. Zhang, M. Wei, M. I. Saidaminov, Y. Gao, J. Xu, M. Xiao, A. Li, J. Zhu, E. H. Sargent, H. Tan, Monolithic all-perovskite tandem solar cells with 24.8% efficiency exploiting comproportionation to suppress Sn(ii) oxidation in precursor ink, *Nature Energy*, **2019**, *4*, 864.

[57] P. Umari, E. Mosconi, F. de Angelis, Relativistic GW calculations on CH3NH3PbI3 and CH3NH3SnI3 perovskites for solar cell applications, *Scientific reports*, **2014**, *4*, 4467.

[58] N. V. Sidgwick, The Electronic Theory Of Valency, Clarendon Press, **1927**.

[59] I. Kopacic, B. Friesenbichler, S. F. Hoefler, B. Kunert, H. Plank, T. Rath, G. Trimmel, Enhanced Performance of Germanium Halide Perovskite Solar Cells through Compositional Engineering, *ACS Applied Energy Materials*, **2018**, *1*, 343.

[60] S. A. Kulkarni, T. Baikie, P. P. Boix, N. Yantara, N. Mathews, S. Mhaisalkar, Band-gap tuning of lead halide perovskites using a sequential deposition process, *Journal of Materials Chemistry A*, **2014**, *2*, 9221.

[61] S. Tao, I. Schmidt, G. Brocks, J. Jiang, I. Tranca, K. Meerholz, S. Olthof, Absolute energy level positions in tin- and lead-based halide perovskites, *Nature communications*, **2019**, *10*, 2560.

[62] F. Brivio, C. Caetano, A. Walsh, Thermodynamic Origin of Photoinstability in the CH3NH3Pb(I1-xBrx)3 Hybrid Halide Perovskite Alloy, *The journal of physical chemistry letters*, **2016**, *7*, 1083.

[63] F. Lehmann, A. Franz, D. M. Többens, S. Levcenco, T. Unold, A. Taubert, S. Schorr, The phase diagram of a mixed halide (Br, I) hybrid perovskite obtained by synchrotron X-ray diffraction, *RSC Advances*, **2019**, *9*, 11151.

[64] E. H. Jung, N. J. Jeon, E. Y. Park, C. S. Moon, T. J. Shin, T.-Y. Yang, J. H. Noh, J. Seo, Efficient, stable and scalable perovskite solar cells using poly(3-hexylthiophene), *Nature*, **2019**, *567*, 511.

[65] M. Saliba, T. Matsui, K. Domanski, J.-Y. Seo, A. Ummadisingu, S. M. Zakeeruddin, J.-P. Correa-Baena, W. R. Tress, A. Abate, A. Hagfeldt, M. Grätzel, Incorporation of rubidium cations into perovskite solar cells improves photovoltaic performance, *Science*, **2016**, *354*, 206.

[66] T. M. Brenner, D. A. Egger, L. Kronik, G. Hodes, D. Cahen, Hybrid organic—inorganic perovskites: low-cost semiconductors with intriguing charge-transport properties, *Nature Reviews Materials*, **2016**, *1*.

[67] L. M. Herz, Charge-Carrier Mobilities in Metal Halide Perovskites: Fundamental Mechanisms and Limits, *ACS Energy Letters*, **2017**, *2*, 1539.

[68] M. H. Du, Efficient carrier transport in halide perovskites: theoretical perspectives, *Journal of Materials Chemistry A*, **2014**, *2*, 9091.

[69] M. R. Filip, G. E. Eperon, H. J. Snaith, F. Giustino, Steric engineering of metal-halide perovskites with tunable optical band gaps, *Nature communications*, **2014**, *5*, 5757.

[70] E. Mosconi, P. Umari, F. de Angelis, Electronic and optical properties of MAPbX3 perovskites (X = I, Br, Cl): a unified DFT and GW theoretical analysis, *Physical chemistry chemical physics*, **2016**, *18*, 27158.

[71] F. Brivio, K. T. Butler, A. Walsh, M. van Schilfgaarde, Relativistic quasiparticle self-consistent electronic structure of hybrid halide perovskite photovoltaic absorbers, *Physical Review B*, **2014**, *89*.

[72] K. Tanaka, T. Takahashi, T. Ban, T. Kondo, K. Uchida, N. Miura, Comparative study on the excitons in lead-halide-based perovskite-type crystals CH3NH3PbBr3 CH3NH3PbI3, *Solid State Communications*, **2003**, *127*, 619.

[73] L. C. Barcus, A. Perlmutter, J. Callaway, Effective Mass of Electrons in Gallium Arsenide, *Physical Review*, **1958**, *111*, 167.

[74] D. T. F. Marple, Effective Electron Mass in CdTe, *Physical Review*, **1963**, *129*, 2466.

[75] S. M. Sze, K. K. Ng, Physics of semiconductor devices, John Wiley & Sons, **2007**.

[76] R. J. Nelson, R. G. Sobers, Minority-carrier lifetimes and internal quantum efficiency of surface-free GaAs, *Journal of Applied Physics*, **1978**, *49*, 6103.

[77] H. Buckley, The whitened cube as a precision integrating photometer, *Journal of the Institution of Electrical Engineers*, **1921**, *59*, 143.

[78] J. M. Palmer, B. G. Grant, The art of radiometry, SPIE, Bellingham, Wash. (1000 20th St. Bellingham WA 98225-6705 USA), **2010**.

[79] R. Dachauer, Fabrication of methylammonium lead iodide thin films via sequential closed space sublimation, Doctoral Thesis, Technische Universität Darmstadt, **2019**.

[80] W. Shockley, The Theory of p-n Junctions in Semiconductors and p-n Junction Transistors, *Bell System Technical Journal*, **1949**, *28*, 435.

[81] J. A. Schwenzer, Thermische Stabilität von Metall-Halogenid-Perowskit-Solarzellen, Doctoral Thesis, Karlsruher Institut für Technologie, **2020**.

[82] S. Rühle, Tabulated values of the Shockley–Queisser limit for single junction solar cells, *Solar Energy*, **2016**, *130*, 139.

[83] A. Einstein, Über einen die Erzeugung und Verwandlung des Lichtes betreffenden heuristischen Gesichtspunkt, *Annalen der Physik und Chemie*, **1905**, *322*, 132.

[84] C. Nordling, E. Sokolowski, K. Siegbahn, Precision Method for Obtaining Absolute Values of Atomic Binding Energies, *Physical Review*, **1957**, *105*, 1676.

[85] K. Siegbahn, K. Edvarson, β-Ray spectroscopy in the precision range of 1 105, *Nuclear Physics*, **1956**, *1*, 137.

[86] K. Siegbahn, ESCA applied to free molecules, North-Holland Publishing Company, Amsterdam, **1971**.

[87] W. E. Spicer, Photoemissive, Photoconductive, and Optical Absorption Studies of Alkali-Antimony Compounds, *Physical Review*, **1958**, *112*, 114.

[88] P. A. M. Dirac, The quantum theory of the emission and absorption of radiation, *Proceedings Of The Royal Society A*, **1927**, *114*, 243.

[89] E. Fermi, Nuclear physics, University of Chicago Press, **1974**.

[90] M. T. Anthony, M. P. Seah, XPS: Energy calibration of electron spectrometers. 1—An absolute, traceable energy calibration and the provision of atomic reference line energies, *Surface and Interface Analysis*, **1984**, *6*, 95.

[91] I. S. Gilmore, J. C. Vickerman, Surface analysis: The principal techniques, John Wiley & Sons, **2009**.

[92] J. F. Moulder, W. F. Stickle, P. E. Sobol, K. D. Bomben, J. Chastain, R. C. King Jr., Handbook of X-ray photoelectron spectroscopy: A reference book of standard spectra for identification and interpretation of XPS data, Physical Electronics, **1995**.

[93] D. Lützenkirchen-Hecht, Anodic Silver Oxide (AgO) Layers by XPS, *Surface Science Spectra*, **2011**, *18*, 102.

[94] M. P. Seah, W. A. Dench, Quantitative electron spectroscopy of surfaces: A standard data base for electron inelastic mean free paths in solids, *Surface and Interface Analysis*, **1979**, *1*, 2.

[95] Beer, Bestimmung der Absorption des rothen Lichts in farbigen Flüssigkeiten, *Annalen der Physik und Chemie*, **1852**, *162*, 78.

[96] S. Tanuma, C. J. Powell, D. R. Penn, Calculations of electorn inelastic mean free paths. II. Data for 27 elements over the 50-2000 eV range, *Surface and Interface Analysis*, **1991**, *17*, 911.

[97] J. H. Scofield, Hartree-Slater subshell photoionization cross-sections at 1254 and 1487 eV, *Journal of Electron Spectroscopy and Related Phenomena*, **1976**, *8*, 129.

[98] M. B. Trzhaskovskaya, V. G. Yarzhemsky, Dirac–Fock photoionization parameters for HAXPES applications, *Atomic Data and Nuclear Data Tables*, **2018**, *119*, 99.

[99] J. J. Yeh, I. Lindau, Atomic subshell photoionization cross sections and asymmetry parameters: 1 ⩽ Z ⩽ 103, *Atomic Data and Nuclear Data Tables*, **1985**, *32*, 1.

[100] C. D. Wagner, L. E. Davis, M. V. Zeller, J. A. Taylor, R. H. Raymond, L. H. Gale, Empirical atomic sensitivity factors for quantitative analysis by electron spectroscopy for chemical analysis, *Surface and Interface Analysis*, **1981**, *3*, 211.

[101] C. K. Jørgensen, H. Berthou, Relative intensities and widths of X-ray induced photo-electron signals from different shells in 72 elements, *Faraday Discussions of the Chemical Society*, **1972**, *54*, 269.

[102] V. I. Nefedov, N. P. Sergushin, I. M. Band, M. B. Trzhaskovskaya, Relative intensities in X-ray photoelectron spectra, *Journal of Electron Spectroscopy and Related Phenomena*, **1973**, *2*, 383.

[103] R. F. Reilman, A. Msezane, S. T. Manson, Relative intensities in photoelectron spectroscopy of atoms and molecules, *Journal of Electron Spectroscopy and Related Phenomena*, **1976**, *8*, 389.

[104] T. Carney, XPS Quantification - Can You Believe the Numbers?: (And why is it difficult?), PowerPoint Presentation, **2000**.

[105] O. Flament, E. Druet, Calibration of VG ESCALAB MkII spectrometer for XPS quantitative analysis, *Journal of Electron Spectroscopy and Related Phenomena*, **1990**, *53*, 141.

[106] M. Schärli, J. Brunner, Experimental study of the energy dependence of transmission in photoelectron spectrometers, *Journal of Electron Spectroscopy and Related Phenomena*, **1983**, *31*, 323.

[107] R. L. Anderson, Germanium-Gallium Arsenide Heterojunctions [Letter to the Editor], *IBM Journal of Research and Development*, **1960**, *4*, 283.

[108] S. Hunklinger, Festkörperphysik, Walter de Gruyter GmbH, **2018**.

[109] P. Wuerfel, Physics of Solar Cells, John Wiley & Sons, **2016**.

[110] M. Wussler, T. Mayer, C. Das, E. Mankel, T. Hellmann, C. Prabowo, I. Zimmermann, M. K. Nazeeruddin, W. Jaegermann, Tapered Cross-Section Photoelectron Spectroscopy of State-of-the-Art Mixed Ion Perovskite Solar Cells: Band Bending Profile in the Dark, Photopotential Profile Under Open Circuit Illumination, and Band Diagram, *Advanced Functional Materials*, **2020**, *30*, 1910679.

[111] C. Das, M. Wussler, T. Hellmann, T. Mayer, I. Zimmermann, C. Maheu, M. K. Nazeeruddin, W. Jaegermann, Surface, Interface, and Bulk Electronic and Chemical Properties of Complete Perovskite Solar Cells: Tapered Cross-Section Photoelectron Spectroscopy, a Novel Solution, *ACS applied materials & interfaces*, **2020**, *12*, 40949.

[112] Schellenberger, Schlaf, Pettenkofer, Jaegermann, Synchrotron-induced surface-photovoltage saturation at intercalated Na/WSe2 interfaces, *Phys. Rev. B*, **1992**, *45*, 3538.

[113] W. Jaegermann, Adsorption of Br2 on n-MoSe2: modelling photoelectrochemistry in the UHV, *Chemical Physics Letters*, **1986**, *126*, 301.

[114] National Renewable Energy Laboratory, Best Research-Cell Efficiency Chart, **2021**, https://www.nrel.gov/pv/assets/pdfs/best-research-cell-efficiencies-rev210726.pdf, Accessed 25 August 2021.

[115] T. Umebayashi, K. Asai, T. Kondo, A. Nakao, Electronic structures of lead iodide based low-dimensional crystals, *Physical Review B*, **2003**, *67*.

[116] S. Olthof, Research Update: The electronic structure of hybrid perovskite layers and their energetic alignment in devices, *APL Materials*, **2016**, *4*, 91502.

[117]S. Béchu, M. Ralaiarisoa, A. Etcheberry, P. Schulz, Photoemission Spectroscopy Characterization of Halide Perovskites, *Advanced Energy Materials*, **2020**, *10*, 1904007.

[118]Q. Wang, Y. Shao, H. Xie, L. Lyu, X. Liu, Y. Gao, J. Huang, Qualifying composition dependent p and n self-doping in CH3NH3PbI3, *Applied Physics Letters*, **2014**, *105*, 163508.

[119]W.-J. Yin, T. Shi, Y. Yan, Unusual defect physics in CH3NH3PbI3 perovskite solar cell absorber, *Applied Physics Letters*, **2014**, *104*, 63903.

[120]J. Kim, S.-H. Lee, J. H. Lee, K.-H. Hong, The Role of Intrinsic Defects in Methylammonium Lead Iodide Perovskite, *The journal of physical chemistry letters*, **2014**, *5*, 1312.

[121]T. G. Kim, S. W. Seo, H. Kwon, J. Hahn, J. W. Kim, Influence of halide precursor type and its composition on the electronic properties of vacuum deposited perovskite films, *Physical chemistry chemical physics*, **2015**, *17*, 24342.

[122]H. Xie, X. Liu, L. Lyu, D. Niu, Q. Wang, J. Huang, Y. Gao, Effects of Precursor Ratios and Annealing on Electronic Structure and Surface Composition of CH3NH3PbI3 Perovskite Films, *The Journal of Physical Chemistry C*, **2016**, *120*, 215.

[123]J. Emara, T. Schnier, N. Pourdavoud, T. Riedl, K. Meerholz, S. Olthof, Impact of Film Stoichiometry on the Ionization Energy and Electronic Structure of CH3NH3PbI3 Perovskites, *Advanced Materials*, **2016**, *28*, 553.

[124]Z. Hawash, S. R. Raga, D.-Y. Son, L. K. Ono, N.-G. Park, Y. Qi, Interfacial Modification of Perovskite Solar Cells Using an Ultrathin MAI Layer Leads to Enhanced Energy Level Alignment, Efficiencies, and Reproducibility, *The journal of physical chemistry letters*, **2017**, *8*, 3947.

[125]P. Fassl, V. Lami, A. Bausch, Z. Wang, M. T. Klug, H. J. Snaith, Y. Vaynzof, Fractional deviations in precursor stoichiometry dictate the properties, performance and stability of perovskite photovoltaic devices, *Energy & environmental science*, **2018**, *11*, 3380.

[126]D. Song, P. Cui, T. Wang, D. Wei, M. Li, F. Cao, X. Yue, P. Fu, Y. Li, Y. He, B. Jiang, M. Trevor, Managing Carrier Lifetime and Doping Property of Lead Halide Perovskite by Postannealing Processes for Highly Efficient Perovskite Solar Cells, *The Journal of Physical Chemistry C*, **2015**, *119*, 22812.

[127]M. Cai, N. Ishida, X. Li, X. Yang, T. Noda, Y. Wu, F. Xie, H. Naito, D. Fujita, L. Han, Control of Electrical Potential Distribution for High-Performance Perovskite Solar Cells, *Joule*, **2018**, *2*, 296.

[128]J. Burschka, N. Pellet, S.-J. Moon, R. Humphry-Baker, P. Gao, M. K. Nazeeruddin, M. Grätzel, Sequential deposition as a route to high-performance perovskite-sensitized solar cells, *Nature*, **2013**, *499*, 316.

[129]J.-H. Im, C.-R. Lee, J.-W. Lee, S.-W. Park, N.-G. Park, 6.5% efficient perovskite quantum-dot-sensitized solar cell, *Nanoscale*, **2011**, *3*, 4088.

[130]P. Docampo, J. M. Ball, M. Darwich, G. E. Eperon, H. J. Snaith, Efficient organometal trihalide perovskite planar-heterojunction solar cells on flexible polymer substrates, *Nature communications*, **2013**, *4*, 2761.

[131]J.-Y. Jeng, Y.-F. Chiang, M.-H. Lee, S.-R. Peng, T.-F. Guo, P. Chen, T.-C. Wen, CH3NH3PbI3 perovskite/fullerene planar-heterojunction hybrid solar cells, *Advanced Materials*, **2013**, *25*, 3727.

[132]E. M. Miller, Y. Zhao, C. C. Mercado, S. K. Saha, J. M. Luther, K. Zhu, V. Stevanović, C. L. Perkins, J. van de Lagemaat, Substrate-controlled band positions in $CH_3NH_3PbI_3$ perovskite films, *Physical chemistry chemical physics*, **2014**, *16*, 22122.

[133]P. Schulz, L. L. Whittaker-Brooks, B. A. MacLeod, D. C. Olson, Y.-L. Loo, A. Kahn, Electronic Level Alignment in Inverted Organometal Perovskite Solar Cells, *Advanced Materials Interfaces*, **2015**, *2*, 1400532.

[134]F. Zu, C. M. Wolff, M. Ralaiarisoa, P. Amsalem, D. Neher, N. Koch, Unraveling the Electronic Properties of Lead Halide Perovskites with Surface Photovoltage in Photoemission Studies, *ACS applied materials & interfaces*, **2019**, *11*, 21578.

[135]Y. Zou, Q. Meng, H. Mao, D. Zhu, Substrate effect on the interfacial electronic structure of thermally-evaporated CH3NH3PbI3 perovskite layer, *Organic Electronics*, **2017**, *41*, 307.

[136]S. Olthof, K. Meerholz, Substrate-dependent electronic structure and film formation of MAPbI3 perovskites, *Scientific reports*, **2017**, *7*, 40267.

[137]D. Shi, V. Adinolfi, R. Comin, M. Yuan, E. Alarousu, A. Buin, Y. Chen, S. Hoogland, A. Rothenberger, K. Katsiev, Y. Losovyj, X. Zhang, P. A. Dowben, O. F. Mohammed, E. H. Sargent, O. M. Bakr, Low trap-state density and long carrier diffusion in organolead trihalide perovskite single crystals, *Science*, **2015**, *347*, 519.

[138]Q. Dong, Y. Fang, Y. Shao, P. Mulligan, J. Qiu, L. Cao, J. Huang, Electron-hole diffusion lengths > 175 μm in solution-grown CH3NH3PbI3 single crystals, *Science*, **2015**, *347*, 967.

[139]M. Stolterfoht, P. Caprioglio, C. M. Wolff, J. A. Márquez, J. Nordmann, S. Zhang, D. Rothhardt, U. Hörmann, Y. Amir, A. Redinger, L. Kegelmann, F. Zu, S. Albrecht, N. Koch, T. Kirchartz, M. Saliba, T. Unold, D. Neher, The impact of energy alignment and interfacial recombination on the internal and external open-circuit voltage of perovskite solar cells, *Energy & environmental science*, **2019**, *12*, 2778.

[140]P. Caprioglio, D. S. Cruz, S. Caicedo-Dávila, F. Zu, A. A. Sutanto, F. Peña-Camargo, L. Kegelmann, D. Meggiolaro, L. Gregori, C. M. Wolff, B. Stiller, L. Perdigón-Toro, H. Köbler, B. Li, E. Gutierrez-Partida, I. Lauermann, A. Abate, N. Koch, F. de Angelis, B. Rech, G. Grancini, D. Abou-Ras, M. K. Nazeeruddin, M. Stolterfoht, S. Albrecht, M. Antonietti, D. Neher, Bi-functional interfaces by poly(ionic liquid) treatment in efficient pin and nip perovskite solar cells, *Energy & environmental science*, **2021**.

[141]K. C. Icli, M. Ozenbas, Fully metal oxide charge selective layers for n-i-p perovskite solar cells employing nickel oxide nanoparticles, *Electrochimica Acta*, **2018**, *263*, 338.

[142]T. Lemercier, L. Perrin, E. Planès, S. Berson, L. Flandin, A Comparison of the Structure and Properties of Opaque and Semi-Transparent NIP/PIN-Type Scalable Perovskite Solar Cells, *Energies*, **2020**, *13*, 3794.

[143]T. Liu, K. Chen, Q. Hu, R. Zhu, Q. Gong, Inverted Perovskite Solar Cells: Progresses and Perspectives, *Advanced Energy Materials*, **2016**, *6*, 1600457.

[144]Z. Liu, A. Zhu, F. Cai, L. Tao, Y. Zhou, Z. Zhao, Q. Chen, Y.-B. Cheng, H. Zhou, Nickel oxide nanoparticles for efficient hole transport in p-i-n and n-i-p perovskite solar cells, *Journal of Materials Chemistry A*, **2017**, *5*, 6597.

[145]S. S. Mali, C. K. Hong, p-i-n/n-i-p type planar hybrid structure of highly efficient perovskite solar cells towards improved air stability: synthetic strategies and the role of p-type hole transport layer (HTL) and n-type electron transport layer (ETL) metal oxides, *Nanoscale*, **2016**, *8*, 10528.

[146]S. S. Mali, H. Kim, H. H. Kim, S. E. Shim, C. K. Hong, Nanoporous p-type NiOx electrode for p-i-n inverted perovskite solar cell toward air stability, *Materials Today*, **2018**, *21*, 483.

[147]C. Momblona, L. Gil-Escrig, E. Bandiello, E. M. Hutter, M. Sessolo, K. Lederer, J. Blochwitz-Nimoth, H. J. Bolink, Efficient vacuum deposited p-i-n and n-i-p perovskite solar cells employing doped charge transport layers, *Energy & environmental science*, **2016**, *9*, 3456.

[148]M. Roß, L. Gil-Escrig, A. Al-Ashouri, P. Tockhorn, M. Jošt, B. Rech, S. Albrecht, Co-Evaporated p-i-n Perovskite Solar Cells beyond 20% Efficiency: Impact of Substrate Temperature and Hole-Transport Layer, *ACS applied materials & interfaces*, **2020**, *12*, 39261.

[149]M. Saliba, J.-P. Correa-Baena, C. M. Wolff, M. Stolterfoht, N. Phung, S. Albrecht, D. Neher, A. Abate, How to Make over 20% Efficient Perovskite Solar Cells in Regular (n–i–p) and Inverted (p–i–n) Architectures, *Chemistry of Materials*, **2018**, *30*, 4193.

[150]J. M. Ball, M. M. Lee, A. Hey, H. J. Snaith, Low-temperature processed meso-superstructured to thin-film perovskite solar cells, *Energy & environmental science*, **2013**, *6*, 1739.

[151]E. Edri, S. Kirmayer, A. Henning, S. Mukhopadhyay, K. Gartsman, Y. Rosenwaks, G. Hodes, D. Cahen, Why lead methylammonium tri-iodide perovskite-based solar cells require a mesoporous electron transporting scaffold (but not necessarily a hole conductor), *Nano letters*, **2014**, *14*, 1000.

[152]V. W. Bergmann, S. A. L. Weber, F. Javier Ramos, M. K. Nazeeruddin, M. Grätzel, D. Li, A. L. Domanski, I. Lieberwirth, S. Ahmad, R. Berger, Real-space observation of unbalanced charge distribution inside a perovskite-sensitized solar cell, *Nature communications*, **2014**, *5*, 5001.

[153]I. M. Hermes, Y. Hou, V. W. Bergmann, C. J. Brabec, S. A. L. Weber, The Interplay of Contact Layers: How the Electron Transport Layer Influences Interfacial Recombination and Hole Extraction in Perovskite Solar Cells, *The journal of physical chemistry letters*, **2018**, *9*, 6249.

[154]M. Stöhr, Deposition and Characterisation of CH3NH3PbI3 Perovskite for Thin Film Solar Cells, Master's thesis, Technische Universität Darmstadt, **2018**.

[155]M. Konstantakou, D. Perganti, P. Falaras, T. Stergiopoulos, Anti-Solvent Crystallization Strategies for Highly Efficient Perovskite Solar Cells, *Crystals*, **2017**, *7*, 291.

[156]S. Paek, P. Schouwink, E. N. Athanasopoulou, K. T. Cho, G. Grancini, Y. Lee, Y. Zhang, F. Stellacci, M. K. Nazeeruddin, P. Gao, From Nano- to Micrometer Scale: The Role of Antisolvent Treatment on High Performance Perovskite Solar Cells, *Chemistry of Materials*, **2017**, *29*, 3490.

[157]C. Das, M. Wussler, T. Hellmann, T. Mayer, W. Jaegermann, In situ XPS study of the surface chemistry of MAPI solar cells under operating conditions in vacuum, *Physical chemistry chemical physics*, **2018**, *20*, 17180.

[158]L. Liu, J. A. McLeod, R. Wang, P. Shen, S. Duhm, Tracking the formation of methylammonium lead triiodide perovskite, *Applied Physics Letters*, **2015**, *107*, 61904.

[159]G. Beamson, D. Briggs, High Resolution XPS of Organic Polymers: The Scienta ESCA300 Database, *Journal of Chemical Education*, **1993**, *70*, A25.

[160]Y. Li, X. Xu, C. Wang, C. Wang, F. Xie, J. Yang, Y. Gao, Investigation on thermal evaporated CH 3 NH 3 PbI 3 thin films, *AIP Advances*, **2015**, *5*, 97111.

[161]B. Conings, L. Baeten, C. de Dobbelaere, J. D'Haen, J. Manca, H.-G. Boyen, Perovskite-based hybrid solar cells exceeding 10% efficiency with high reproducibility using a thin film sandwich approach, *Advanced Materials*, **2014**, *26*, 2041.

[162]Y. Li, X. Xu, C. Wang, B. Ecker, J. Yang, J. Huang, Y. Gao, Light-Induced Degradation of CH3NH3PbI3 Hybrid Perovskite Thin Film, *The Journal of Physical Chemistry C*, **2017**, *121*, 3904.

[163]R. Lindblad, D. Bi, B. Park, J. Oscarsson, M. Gorgoi, H. Siegbahn, M. Odelius, E. M. J. Johansson, H. Rensmo, Electronic Structure of TiO2/CH3NH3PbI3 Perovskite Solar Cell Interfaces, *The journal of physical chemistry letters*, **2014**, *5*, 648.

[164]G. Sadoughi, D. E. Starr, E. Handick, S. D. Stranks, M. Gorgoi, R. G. Wilks, M. Bär, H. J. Snaith, Observation and Mediation of the Presence of Metallic Lead in Organic-Inorganic Perovskite Films, *ACS applied materials & interfaces*, **2015**, *7*, 13440.

[165]X. Tang, M. Brandl, B. May, I. Levchuk, Y. Hou, M. Richter, H. Chen, S. Chen, S. Kahmann, A. Osvet, F. Maier, H.-P. Steinrück, R. Hock, G. J. Matt, C. J. Brabec, Photoinduced degradation of methylammonium lead triiodide perovskite semiconductors, *Journal of Materials Chemistry A*, **2016**, *4*, 15896.

[166]W. E. Morgan, J. R. van Wazer, W. J. Stec, Inner-orbital photoelectron spectroscopy of the alkali metal halides, perchlorates, phosphates, and pyrophosphates, *Journal of the American Chemical Society*, **1973**, *95*, 751.

[167]Triloki, R. Rai, N. Gupta, N. F. Jammal, B. K. Singh, Photoemission and optical constant measurements of a Cesium Iodide thin film photocathode, *Nuclear Instruments and Methods in Physics Research Section A: Accelerators, Spectrometers, Detectors and Associated Equipment*, **2015**, *787*, 161.

[168]T. Baikie, Y. Fang, J. M. Kadro, M. Schreyer, F. Wei, S. G. Mhaisalkar, M. Graetzel, T. J. White, Synthesis and crystal chemistry of the hybrid perovskite (CH3NH3)PbI3 for solid-state sensitised solar cell applications, *Journal of Materials Chemistry A*, **2013**, *1*, 5628.

[169]A. Poglitsch, D. Weber, Dynamic disorder in methylammoniumtrihalogenoplumbates (II) observed by millimeter-wave spectroscopy, *The Journal of Chemical Physics*, **1987**, *87*, 6373.

[170]P. Docampo, F. C. Hanusch, N. Giesbrecht, P. Angloher, A. Ivanova, T. Bein, Influence of the orientation of methylammonium lead iodide perovskite crystals on solar cell performance, *APL Materials*, **2014**, *2*, 81508.

[171]H. E. Swanson, N. T. Gilfrich, G. M. Ugrinic, Circular of the Bureau of Standards No. 539 Volume 5: Standard X-Ray Diffraction Powder Patterns, *NBS Circulars*, **1955**.

[172]F. Fu, L. Kranz, S. Yoon, J. Löckinger, T. Jäger, J. Perrenoud, T. Feurer, C. Gretener, S. Buecheler, A. N. Tiwari, Controlled growth of PbI2 nanoplates for rapid preparation of CH3NH3PbI3 in planar perovskite solar cells, *Physica Status Solidi A*, **2015**, *212*, 2708.

[173]S. M. Jain, B. Philippe, E. M. J. Johansson, B. Park, H. Rensmo, T. Edvinsson, G. Boschloo, Vapor phase conversion of PbI2 to CH3NH3PbI3: spectroscopic evidence for formation of an intermediate phase, *Journal of Materials Chemistry A*, **2016**, *4*, 2630.

[174]M. Schieber, N. Zamoshchik, O. Khakhan, A. Zuck, Structural changes during vapor-phase deposition of polycrystalline-PbI2 films, *Journal of Crystal Growth*, **2008**, *310*, 3168.

[175]P. Terpstra, H. Westenbrink, On the crystal structure of lead-iodide, *Materials Science*, **1925**.

[176]J.-P. Correa-Baena, A. Abate, M. Saliba, W. Tress, T. Jesper Jacobsson, M. Grätzel, A. Hagfeldt, The rapid evolution of highly efficient perovskite solar cells, *Energy & environmental science*, **2017**, *10*, 710.

[177]N. J. Jeon, J. H. Noh, W. S. Yang, Y. C. Kim, S. Ryu, J. Seo, S. I. Seok, Compositional engineering of perovskite materials for high-performance solar cells, *Nature*, **2015**, *517*, 476.

[178]X. Xu, H. Zheng, G. Liu, L. Zhu, D. He, S. Xu, H. Xu, L. Zhang, X. Zhang, X. Pan, Elimination of Yellow Phase: An Effective Method to Achieve High Quality HC(NH2)2 PbI3 -based Perovskite Films, *ChemSusChem*, **2020**, *13*, 956.

[179]T. P. Gujar, T. Unger, A. Schönleber, M. Fried, F. Panzer, S. van Smaalen, A. Köhler, M. Thelakkat, The role of PbI2 in CH3NH3PbI3 perovskite stability, solar cell parameters and device degradation, *Physical chemistry chemical physics*, **2017**, *20*, 605.

[180]R. Dachauer, O. Clemens, K. Lakus-Wollny, T. Mayer, W. Jaegermann, Characterization of Methylammonium Lead Iodide Thin Films Fabricated by Exposure of Lead Iodide Layers to Methylammonium Iodide Vapor in a Closed Crucible Transformation Process, *Physica Status Solidi A*, **2019**, *216*, 1800894.

[181]W. Tress, N. Marinova, T. Moehl, S. M. Zakeeruddin, M. K. Nazeeruddin, M. Grätzel, Understanding the rate-dependent J–V hysteresis, slow time component, and aging in CH3NH3PbI3 perovskite solar cells: the role of a compensated electric field, *Energy & environmental science*, **2015**, *8*, 995.

[182]E. L. Unger, E. T. Hoke, C. D. Bailie, W. H. Nguyen, A. R. Bowring, T. Heumüller, M. G. Christoforo, M. D. McGehee, Hysteresis and transient behavior in current–voltage measurements of hybrid-perovskite absorber solar cells, *Energy & environmental science*, **2014**, *7*, 3690.

[183]C. Liu, J. Fan, X. Zhang, Y. Shen, L. Yang, Y. Mai, Hysteretic Behavior upon Light Soaking in Perovskite Solar Cells Prepared via Modified Vapor-Assisted Solution Process, *ACS applied materials & interfaces*, **2015**, *7*, 9066.

[184]L. K. Ono, S. R. Raga, S. Wang, Y. Kato, Y. Qi, Temperature-dependent hysteresis effects in perovskite-based solar cells, *Journal of Materials Chemistry A*, **2015**, *3*, 9074.

[185]D. H. Song, M. H. Jang, M. H. Lee, J. H. Heo, J. K. Park, S.-J. Sung, D.-H. Kim, K.-H. Hong, S. H. Im, A discussion on the origin and solutions of hysteresis in perovskite hybrid solar cells, *Journal of Physics D: Applied Physics*, **2016**, *49*, 473001.

[186]Y.-C. Wang, X. Li, L. Zhu, X. Liu, W. Zhang, J. Fang, Efficient and Hysteresis-Free Perovskite Solar Cells Based on a Solution Processable Polar Fullerene Electron Transport Layer, *Advanced Energy Materials*, **2017**, *7*, 1701144.

[187]Y. Shao, Z. Xiao, C. Bi, Y. Yuan, J. Huang, Origin and elimination of photocurrent hysteresis by fullerene passivation in CH3NH3PbI3 planar heterojunction solar cells, *Nature communications*, **2014**, *5*, 5784.

[188]E. Mosconi, F. de Angelis, Mobile Ions in Organohalide Perovskites: Interplay of Electronic Structure and Dynamics, *ACS Energy Letters*, **2016**, *1*, 182.

[189]W. Tress, Metal Halide Perovskites as Mixed Electronic-Ionic Conductors: Challenges and Opportunities-From Hysteresis to Memristivity, *The journal of physical chemistry letters*, **2017**, *8*, 3106.

[190]S. van Reenen, M. Kemerink, H. J. Snaith, Modeling Anomalous Hysteresis in Perovskite Solar Cells, *The journal of physical chemistry letters*, **2015**, *6*, 3808.

[191]D. A. Jacobs, Y. Wu, H. Shen, C. Barugkin, F. J. Beck, T. P. White, K. Weber, K. R. Catchpole, Hysteresis phenomena in perovskite solar cells: the many and varied effects of ionic accumulation, *Physical chemistry chemical physics*, **2017**, *19*, 3094.

[192]Z. Xiao, Y. Yuan, Y. Shao, Q. Wang, Q. Dong, C. Bi, P. Sharma, A. Gruverman, J. Huang, Giant switchable photovoltaic effect in organometal trihalide perovskite devices, *Nature materials*, **2015**, *14*, 193.

[193]S. A. L. Weber, I. M. Hermes, S.-H. Turren-Cruz, C. Gort, V. W. Bergmann, L. Gilson, A. Hagfeldt, M. Graetzel, W. Tress, R. Berger, How the formation of interfacial charge causes hysteresis in perovskite solar cells, *Energy & environmental science*, **2018**, *11*, 2404.

[194]Alonso, Cimino, Horn, Surface photovoltage effects in photoemission from metal-GaP(110) interfaces: Importance for band bending evaluation, *Physical review letters*, **1990**, *64*, 1947.

[195]Hecht, Role of photocurrent in low-temperature photoemission studies of Schottky-barrier formation, *Physical Review B*, **1990**, *41*, 7918.

[196]J. P. Long, V. M. Bermudez, Band bending and photoemission-induced surface photovoltages on clean n - and p -GaN (0001) surfaces, *Physical Review B*, **2002**, *66*.

[197]D. Mao, A. Kahn, M. Marsi, G. Margaritondo, Synchrotron radiation induced surface photovoltage at metal/GaAs interfaces, *Applied Surface Science*, **1991**, *48-49*, 324.

[198]P. Schulz, E. Edri, S. Kirmayer, G. Hodes, D. Cahen, A. Kahn, Interface energetics in organo-metal halide perovskite-based photovoltaic cells, *Energy & environmental science*, **2014**, *7*, 1377.

[199]J. Endres, D. A. Egger, M. Kulbak, R. A. Kerner, L. Zhao, S. H. Silver, G. Hodes, B. P. Rand, D. Cahen, L. Kronik, A. Kahn, Valence and Conduction Band Densities of States of Metal Halide Perovskites: A Combined Experimental-Theoretical Study, *The journal of physical chemistry letters*, **2016**, *7*, 2722.

[200]F. Zu, P. Amsalem, D. A. Egger, R. Wang, C. M. Wolff, H. Fang, M. A. Loi, D. Neher, L. Kronik, S. Duhm, N. Koch, Constructing the Electronic Structure of CH3NH3PbI3 and CH3NH3PbBr3 Perovskite Thin Films from Single-Crystal Band Structure Measurements, *The journal of physical chemistry letters*, **2019**, *10*, 601.

[201]A. Klein, T. Mayer, A. Thissen, W. Jaegermann, Photoelectron Spectroscopy in Materials Science and Physical Chemistry: Analysis of Composition, Chemical Bonding, and Electronic Structure of Surfaces and Interfaces, *In Methods in Physical Chemistry (eds R. Schäfer and P.C. Schmidt)*.

[202]L. Li, S. Tong, Y. Zhao, C. Wang, S. Wang, L. Lyu, Y. Huang, H. Huang, J. Yang, D. Niu, X. Liu, Y. Gao, Interfacial Electronic Structures of Photodetectors Based on C8BTBT/Perovskite, *ACS applied materials & interfaces*, **2018**, *10*, 20959.

[203]X. Zhang, Z. Su, B. Zhao, Y. Yang, Y. Xiong, X. Gao, D.-C. Qi, L. Cao, Chemical interaction dictated energy level alignment at the N,N'-dipentyl-3,4,9,10-perylenedicarboximide/CH3NH3PbI3 interface, *Applied Physics Letters*, **2018**, *113*, 113901.

[204]M. J. Bækbo, O. Hansen, I. Chorkendorff, P. C. K. Vesborg, Deposition of methylammonium iodide via evaporation – combined kinetic and mass spectrometric study, *RSC Advances*, **2018**, *8*, 29899.

[205]B. Conings, J. Drijkoningen, N. Gauquelin, A. Babayigit, J. D'Haen, L. D'Olieslaeger, A. Ethirajan, J. Verbeeck, J. Manca, E. Mosconi, F. de Angelis, H.-G. Boyen, Intrinsic Thermal Instability of Methylammonium Lead Trihalide Perovskite, *Advanced Energy Materials*, **2015**, *5*, 1500477.

[206]A. García-Fernández, E. J. Juarez-Perez, S. Castro-García, M. Sánchez-Andújar, L. K. Ono, Y. Jiang, Y. Qi, Benchmarking Chemical Stability of Arbitrarily Mixed 3D Hybrid Halide Perovskites for Solar Cell Applications, *Small Methods*, **2018**, *2*, 1800242.

[207]J.-W. Lee, D.-H. Kim, H.-S. Kim, S.-W. Seo, S. M. Cho, N.-G. Park, Formamidinium and Cesium Hybridization for Photo- and Moisture-Stable Perovskite Solar Cell, *Advanced Energy Materials*, **2015**, *5*, 1501310.

[208]Y. Lu, Q. Han, Y. Zhao, C. Yang, Y. Li, X. Liu, Substrate-dependent Growth of CH3NH3PbI3 Films Deposited by Vacuum Evaporation, *Journal of Physics: Conference Series*, **2020**, *1637*, 12080.

[209]T. B. Abzieher, Thermische Koverdampfung von hybriden Perowskit-Halbleitern für den Einsatz in Solarzellen, Doctoral Thesis, Karlsruher Institut für Technologie, **2020**.

[210]O. Loebich, The optical properties of gold, *Gold Bulletin*, **1972**, *5*, 2.

[211]A. Axelevitch, B. Gorenstein, G. Golan, Investigation of Optical Transmission in Thin Metal Films, *Physics Procedia*, **2012**, *32*, 1.

[212]Z. Liu, S. Niu, N. Wang, Light illumination intensity dependence of photovoltaic parameter in polymer solar cells with ammonium heptamolybdate as hole extraction layer, *Journal of colloid and interface science*, **2018**, *509*, 171.

[213]A. Abate, T. Leijtens, S. Pathak, J. Teuscher, R. Avolio, M. E. Errico, J. Kirkpatrik, J. M. Ball, P. Docampo, I. McPherson, H. J. Snaith, Lithium salts as "redox active" p-type dopants for organic semiconductors and their impact in solid-state dye-sensitized solar cells, *Physical chemistry chemical physics*, **2013**, *15*, 2572.

[214]R. Schölin, M. H. Karlsson, S. K. Eriksson, H. Siegbahn, E. M. J. Johansson, H. Rensmo, Energy Level Shifts in Spiro-OMeTAD Molecular Thin Films When Adding Li-TFSI, *The Journal of Physical Chemistry C*, **2012**, *116*, 26300.

[215]H. J. Snaith, M. Grätzel, Enhanced charge mobility in a molecular hole transporter via addition of redox inactive ionic dopant: Implication to dye-sensitized solar cells, *Applied Physics Letters*, **2006**, *89*, 262114.

[216]E. J. Juarez-Perez, M. R. Leyden, S. Wang, L. K. Ono, Z. Hawash, Y. Qi, Role of the Dopants on the Morphological and Transport Properties of Spiro-MeOTAD Hole Transport Layer, *Chemistry of Materials*, **2016**, *28*, 5702.

[217]S. Wang, Z. Huang, X. Wang, Y. Li, M. Günther, S. Valenzuela, P. Parikh, A. Cabreros, W. Xiong, Y. S. Meng, Unveiling the Role of tBP-LiTFSI Complexes in Perovskite Solar Cells, *Journal of the American Chemical Society*, **2018**, *140*, 16720.

[218]R. Hock, T. Mayer, W. Jaegermann, p-Type Doping of Spiro-MeOTAD with WO 3 and the Spiro-MeOTAD/WO 3 Interface Investigated by Synchrotron-Induced Photoelectron Spectroscopy, *The Journal of Physical Chemistry C*, **2012**, *116*, 18146.

[219]Z. Hawash, L. K. Ono, Y. Qi, Moisture and Oxygen Enhance Conductivity of LiTFSI-Doped Spiro-MeOTAD Hole Transport Layer in Perovskite Solar Cells, *Advanced Materials Interfaces*, **2016**, *3*, 1600117.

[220]Z. Hawash, L. K. Ono, S. R. Raga, M. V. Lee, Y. Qi, Air-Exposure Induced Dopant Redistribution and Energy Level Shifts in Spin-Coated Spiro-MeOTAD Films, *Chemistry of Materials*, **2015**, *27*, 562.

[221]U. B. Cappel, T. Daeneke, U. Bach, Oxygen-induced doping of spiro-MeOTAD in solid-state dye-sensitized solar cells and its impact on device performance, *Nano letters*, **2012**, *12*, 4925.

[222]L. K. Ono, P. Schulz, J. J. Endres, G. O. Nikiforov, Y. Kato, A. Kahn, Y. Qi, Air-Exposure-Induced Gas-Molecule Incorporation into Spiro-MeOTAD Films, *The journal of physical chemistry letters*, **2014**, *5*, 1374.

[223]S. D. Ha, J. Meyer, A. Kahn, Molecular-scale properties of MoO3 -doped pentacene, *Physical Review B*, **2010**, *82*.

[224]J.-H. Lee, H.-M. Kim, K.-B. Kim, J.-J. Kim, Origin of charge generation efficiency of metal oxide p-dopants in organic semiconductors, *Organic Electronics*, **2011**, *12*, 950.

[225]T. Menke, Molecular Doping of Organic Semiconductors: A Conductivity and Seebeck Study, Doctoral Thesis, Technische Universität Dresden.

[226]T. Mayer, C. Hein, E. Mankel, W. Jaegermann, M. M. Müller, H.-J. Kleebe, Fermi level positioning in organic semiconductor phase mixed composites: The internal interface charge transfer doping model, *Organic Electronics*, **2012**, *13*, 1356.

[227]Y. He, Y. Zhang, P. Yu, F. Ding, X. Li, Z. Wang, Z. Lv, X. Wang, Z. Liu, X. Huang, Ion association tailoring SEI composition for Li metal anode protection, *Journal of Energy Chemistry*, **2020**, *45*, 1.

[228]I. Salzmann, G. Heimel, Toward a comprehensive understanding of molecular doping organic semiconductors (review), *Journal of Electron Spectroscopy and Related Phenomena*, **2015**, *204*, 208.

[229]M. Kühn, Heterokontakte organischer Leuchtdioden: Schichtdickenabhängiges Strom-Spannungsverhalten, Doctoral Thesis, Technische Universität Darmstadt, **2017**.

[230]R. Pekkola, Electronic Structure of Solid-State Dye-Sensitized Solar Cells: Synchrotron Induced Photoelectron Spectroscopy on Nanocrystalline TiO2, Newly Developed Dyes and Spiro-MeOTAD, Doctoral Thesis, **2014**.

[231]T. Hellmann, C. Das, T. Abzieher, J. A. Schwenzer, M. Wussler, R. Dachauer, U. W. Paetzold, W. Jaegermann, T. Mayer, The Electronic Structure of MAPI-Based Perovskite Solar Cells: Detailed Band Diagram Determination by Photoemission Spectroscopy Comparing Classical and Inverted Device Stacks, *Advanced Energy Materials*, **2020**, *10*, 2002129.

[232]S.-Y. Hsiao, H.-L. Lin, W.-H. Lee, W.-L. Tsai, K.-M. Chiang, W.-Y. Liao, C.-Z. Ren-Wu, C.-Y. Chen, H.-W. Lin, Efficient All-Vacuum Deposited Perovskite Solar Cells by Controlling Reagent Partial Pressure in High Vacuum, *Advanced Materials*, **2016**, *28*, 7013.

[233]Y. Li, J. K. Cooper, R. Buonsanti, C. Giannini, Y. Liu, F. M. Toma, I. D. Sharp, Fabrication of Planar Heterojunction Perovskite Solar Cells by Controlled Low-Pressure Vapor Annealing, *The journal of physical chemistry letters*, **2015**, *6*, 493.

[234]L. K. Ono, S. Wang, Y. Kato, S. R. Raga, Y. Qi, Fabrication of semi-transparent perovskite films with centimeter-scale superior uniformity by the hybrid deposition method, *Energy & environmental science*, **2014**, *7*, 3989.

[235]J. Teuscher, A. Ulianov, O. Müntener, M. Grätzel, N. Tétreault, Control and Study of the Stoichiometry in Evaporated Perovskite Solar Cells, *ChemSusChem*, **2015**, *8*, 3847.

[236]E. S. Thibau, A. Llanos, Z.-H. Lu, Disruptive and reactive interface formation of molybdenum trioxide on organometal trihalide perovskite, *Applied Physics Letters*, **2017**, *110*, 81604.

[237]I. W. Drummond, Spatial resolution in X-ray photoelectron spectroscopy, *Philosophical Transactions of the Royal Society A*, **1996**, *354*, 2667.

[238]H. Yoshida, Electron Transport in Bathocuproine Interlayer in Organic Semiconductor Devices, *The Journal of Physical Chemistry C*, **2015**, *119*, 24459.

[239]J. Lee, S. Park, Y. Lee, H. Kim, D. Shin, J. Jeong, K. Jeong, S. W. Cho, H. Lee, Y. Yi, Electron transport mechanism of bathocuproine exciton blocking layer in organic photovoltaics, *Physical chemistry chemical physics*, **2016**, *18*, 5444.

[240]T. Sakurai, S. Toyoshima, H. Kitazume, S. Masuda, H. Kato, K. Akimoto, Influence of gap states on electrical properties at interface between bathocuproine and various types of metals, *Journal of Applied Physics*, **2010**, *107*, 43707.

[241]B. Chaudhary, A. Kulkarni, A. K. Jena, M. Ikegami, Y. Udagawa, H. Kunugita, K. Ema, T. Miyasaka, Poly(4-Vinylpyridine)-Based Interfacial Passivation to Enhance Voltage and Moisture Stability of Lead Halide Perovskite Solar Cells, *ChemSusChem*, **2017**, *10*, 2473.

[242]S. Gharibzadeh, B. Abdollahi Nejand, M. Jakoby, T. Abzieher, D. Hauschild, S. Moghadamzadeh, J. A. Schwenzer, P. Brenner, R. Schmager, A. A. Haghighirad, L. Weinhardt, U. Lemmer, B. S. Richards, I. A. Howard, U. W. Paetzold, Record Open-Circuit Voltage Wide-Bandgap Perovskite Solar Cells Utilizing 2D/3D Perovskite Heterostructure, *Advanced Energy Materials*, **2019**, *9*, 1803699.

[243]H. Kanda, N. Shibayama, A. J. Huckaba, Y. Lee, S. Paek, N. Klipfel, C. Roldán-Carmona, V. I. E. Queloz, G. Grancini, Y. Zhang, M. Abuhelaiqa, K. T. Cho, M. Li, M. D. Mensi, S. Kinge, M. K. Nazeeruddin, Band-bending induced passivation: high performance and stable perovskite solar cells using a perhydropoly(silazane) precursor, *Energy & environmental science*, **2020**, *13*, 1222.

[244]N. K. Noel, S. N. Habisreutinger, A. Pellaroque, F. Pulvirenti, B. Wenger, F. Zhang, Y.-H. Lin, O. G. Reid, J. Leisen, Y. Zhang, S. Barlow, S. R. Marder, A. Kahn, H. J. Snaith, C. B. Arnold, B. P. Rand, Interfacial charge-transfer doping of metal halide perovskites for high performance photovoltaics, *Energy & environmental science*, **2019**, *12*, 3063.

[245]L. Zuo, H. Guo, D. W. deQuilettes, S. Jariwala, N. de Marco, S. Dong, R. DeBlock, D. S. Ginger, B. Dunn, M. Wang, Y. Yang, Polymer-modified halide perovskite films for efficient and stable planar heterojunction solar cells, *Science advances*, **2017**, *3*, e1700106.

[246]K.-C. Chiu, J.-S. Wang, C.-Y. Lin, Temperature dependence of the band gap in C 60 crystals, *Journal of Applied Physics*, **1996**, *79*, 1784.

[247]Y. Chen, H. T. Yi, X. Wu, R. Haroldson, Y. N. Gartstein, Y. I. Rodionov, K. S. Tikhonov, A. Zakhidov, X.-Y. Zhu, V. Podzorov, Extended carrier lifetimes and diffusion in hybrid perovskites revealed by Hall effect and photoconductivity measurements, *Nature communications*, **2016**, *7*, 12253.

[248]Y. Song, W. Bi, A. Wang, X. Liu, Y. Kang, Q. Dong, Efficient lateral-structure perovskite single crystal solar cells with high operational stability, *Nature communications*, **2020**, *11*, 274.

[249]A. Many, Y. Goldstein, N. B. Grover, Semiconductor surfaces, North Holland Publishing Company, Amsterdam, **1971**.

[250]A. R. Gonzalez-Elipe, J. P. Holgado, R. Alvarez, G. Munuera, Use of factor analysis and XPS to study defective nickel oxide, *The Journal of Physical Chemistry*, **1992**, *96*, 3080.

[251]M. W. Roberts, R. S. C. Smart, The defect structure of nickel oxide surfaces as revealed by photoelectron spectroscopy, *Journal of the Chemical Society, Faraday Transactions 1: Physical Chemistry in Condensed Phases*, **1984**, *80*, 2957.

[252]M. Tomellini, X-ray photoelectron spectra of defective nickel oxide, *Journal of the Chemical Society, Faraday Transactions 1: Physical Chemistry in Condensed Phases*, **1988**, *84*, 3501.

[253]B. Li, S. Zhang, F. Xia, Y. Huang, X. Ran, Y. Xia, Y. Chen, W. Huang, Insights into the hole transport properties of LiTFSI-doped spiro-OMeTAD films through impedance spectroscopy, *Journal of Applied Physics*, **2020**, *128*, 85501.

[254]W. Zia, Fabrication & Characterization of FAPI Solar Cells by Co-Evaporation, Advanced Research Lab Report, Technische Universität Darmstadt, **2019**.

[255]W. Zia, Fabrication & Characterization of Double Cation CsxFA1-xPbI3 Perovskite Solar Cells by Co-Evaporation, Master's Thesis, Technische Universität Darmstadt, **2019**.

[256]M. I. Saidaminov, A. L. Abdelhady, B. Murali, E. Alarousu, V. M. Burlakov, W. Peng, I. Dursun, L. Wang, Y. He, G. Maculan, A. Goriely, T. Wu, O. F. Mohammed, O. M. Bakr, High-quality bulk hybrid perovskite single crystals within minutes by inverse temperature crystallization, *Nature communications*, **2015**, *6*, 7586.

[257]G. Xing, N. Mathews, S. Sun, S. S. Lim, Y. M. Lam, M. Grätzel, S. Mhaisalkar, T. C. Sum, Long-range balanced electron- and hole-transport lengths in organic-inorganic CH3NH3PbI3, *Science*, **2013**, *342*, 344.

[258]S. D. Stranks, G. E. Eperon, G. Grancini, C. Menelaou, M. J. P. Alcocer, T. Leijtens, L. M. Herz, A. Petrozza, H. J. Snaith, Electron-hole diffusion lengths exceeding 1 micrometer in an organometal trihalide perovskite absorber, *Science*, **2013**, *342*, 341.

[259]E. Edri, S. Kirmayer, S. Mukhopadhyay, K. Gartsman, G. Hodes, D. Cahen, Elucidating the charge carrier separation and working mechanism of CH3NH3PbI(3-x)Cl(x) perovskite solar cells, *Nature communications*, **2014**, *5*, 3461.

A. Publications, conferences contributions and supervised student theses

Publications related to this thesis

- **T. Hellmann**, C. Das, T. Abzieher, J. A. Schwenzer, M. Wussler, R. Dachauer, U. W. Paetzold, W. Jaegermann and T. Mayer, "The Electronic Structure of MAPI-Based Perovskite Solar Cells: Detailed Band Diagram Determination by Photoemission Spectroscopy Comparing Classical and Inverted Device Stacks," Advanced Energy Materials, vol. 10, no. 42, p. 2002129, 2020
- **T. Hellmann**, M. Wussler, C. Das, R. Dachauer, I. El-Helaly, C. Mortan, T. Mayer and W. Jaegermann, "The difference in electronic structure of MAPI and MASI perovskites and its effect on the interface alignment to the HTMs spiro-MeOTAD and CuI," Journal of Materials Chemistry C, vol. 7, no. 18, pp. 5324-5332, 2019
- J. A. Schwenzer, **T. Hellmann**, B. A. Nejand, H. Hu, T. Abzieher, F. Schackmar, I. M. Hossain, P. Fassl, T. Mayer, W. Jaegermann, U. Lemmer and U. W. Paetzold, "Thermal Stability and Cation Composition of Hybrid Organic-Inorganic Perovskites," ACS applied materials & interfaces, vol. 13, no. 13, pp. 15292-15304, 2021
- C. Mortan, **T. Hellmann**, O. Clemens, T. Mayer and W. Jaegermann, "Preparation of Methylammonium Tin Iodide ($CH_3NH_3SnI_3$) Perovskite Thin Films via Flash Evaporation," physica status solidi (a), vol. 216, no. 18, p. 1900209, 2019
- C. Mortan, **T. Hellmann**, M. Buchhorn, M. d'Eril Melzi, O. Clemens, T. Mayer and W. Jaegermann, "Preparation of methylammonium lead iodide ($CH_3NH_3PbI_3$) thin film perovskite solar cells by chemical vapor deposition using methylamine gas (CH_3NH_2) and hydrogen iodide gas," Energy Science & Engineering, vol. 8, no. 9, pp. 3165-3173, 2020.
- C. Das, M. Kot, **T. Hellmann**, C. Wittich, E. Mankel, I. Zimmermann, D. Schmeisser, M. Khaja Nazeeruddin and W. Jaegermann, "Atomic Layer-Deposited Aluminum Oxide Hinders Iodide Migration and Stabilizes Perovskite Solar Cells," Cell Reports Physical Science, vol. 1, no. 7, p. 100112, 2020
- C. Das, M. Wussler, **T. Hellmann**, T. Mayer, I. Zimmermann, C. Maheu, M. K. Nazeeruddin and W. Jaegermann, "Surface, Interface, and Bulk Electronic and Chemical Properties of Complete Perovskite Solar Cells: Tapered Cross-Section Photoelectron Spectroscopy, a Novel Solution," ACS applied materials & interfaces, vol. 12, no. 36, pp. 40949-40957, 2020
- T. Abzieher, T. Feeney, F. Schackmar, Y. J. Donie, I. M. Hossain, J. A. Schwenzer, T. Hellmann, T. Mayer, M. Powalla and U. W. Paetzold, "From Groundwork to Efficient Solar Cells: On the Importance of the Substrate Material in Co-Evaporated Perovskite Solar Cells," Advanced Functional Materials, p. 2104482, 2021
- M. Wussler, T. Mayer, C. Das, E. Mankel, **T. Hellmann**, C. Prabowo, I. Zimmermann, M. K. Nazeeruddin and W. Jaegermann, "Tapered Cross-Section Photoelectron Spectroscopy of

State-of-the-Art Mixed Ion Perovskite Solar Cells: Band Bending Profile in the Dark, Photopotential Profile Under Open Circuit Illumination, and Band Diagram," Advanced Functional Materials, vol. 30, no. 27, p. 1910679, 2020

- Das, M. Wussler, **T. Hellmann**, T. Mayer and W. Jaegermann, "In situ XPS study of the surface chemistry of MAPI solar cells under operating conditions in vacuum," Physical chemistry chemical physics: PCCP, vol. 20, no. 25, pp. 17180-17187, 2018

Additional publications in the period of this thesis

- S. N. Abdollahi, E. Ochoa Martínez, C. Kilchoer, G. Kremer, T. Jaouen, P. Aebi, **T. Hellmann**, T. Mayer, Y. Gu, U. B. Wiesner, U. Steiner, B. D. Wilts and I. Gunkel, "Carbon-Assisted Stable Silver Nanostructures," Advanced Materials Interfaces, vol. 7, no. 23, p. 2001227, 2020
- Chakraborty, S. Kalra, R. Beltrán-Suito, C. Das, **T. Hellmann**, P. W. Menezes and M. Driess, "A Low-Temperature Molecular Precursor Approach to Copper-Based Nano-Sized Digenite Mineral for Efficient Electrocatalytic Oxygen Evolution Reaction," Chemistry, an Asian journal, vol. 15, no. 6, pp. 852-859, 2020
- M. C. Scheuerlein, F. Muench, U. Kunz, **T. Hellmann**, J. P. Hofmann and W. Ensinger, "Electroless Nanoplating of Iridium: Template-Assisted Nanotube Deposition for the Continuous Flow Reduction of 4-Nitrophenol," ChemElectroChem, vol. 7, no. 16, pp. 3496-3507, 2020
- Z. Zhao, M. Widenmeyer, T. Frömling, **T. Hellmann**, R. Yan, Fangmu Qu, G. Homm, J. P. Hofmann, A. Feldhoff, A. Weidenkaff, "A comprehensive comparative study of CO2-resistance and oxygen permeability of 60 wt % $Ce_{0.}8M_{0.2}O_{2-\delta}$ (M = La, Pr, Nd, Sm, Gd) - 40 wt % $La_{0.5}Sr_{0.5}Fe_{0.8}Cu_{0.2}O_{3-\delta}$ dual-phase membranes", Journal of Membrane Science, manuscript number: MEMSCI-D-21-01853R1, accepted

Conference contributions

- Interface Experiments on classical architecture perovskite solar cells, T. Hellmann, C. Das, M. Wussler, C. Mortan, E. Mankel, T. Mayer, W. Jaegermann, *(poster)*, PSCO 2017, Oxford
- Tracking the origin of the photovoltage in $CH_3NH_3PbI_3$ solar cells by PES, T. Hellmann, C. Das, C. Mortan, T. Abzieher, T. Mayer, U. W. Paetzold, W. Jaegermann, *(talk, awarded with graduate student award)*, EMRS 2017, Warsaw
- Photovoltage distribution and Fermi Level position of MAPI films in inverted and classical architectures, T. Hellmann, C. Das, T. Abzieher, T. Mayer, U. W. Paetzold, W. Jaegermann *(poster)*, PSCO 2019

Supervised student theses

- Chandra Prabowo, Photoemission Spectroscopy Studies of p-doped spiro-MeOTAD Prepared from Solution and by Thermal Co-evaporation, *master thesis*, 2020
- Waqas Zia, Fabrication & Characterization of Double Cation $Cs_xFA_{1-x}PbI_3$ Perovskite Solar Cells by Co-Evaporation, *master thesis*, 2019
- Nils Schäfer, Synthesis of $CH_3NH_3PbI_3$ Films Using a Vapour-Assisted Tube Furnace Process for Photovoltaic Applications, *master thesis*, 2018
- Ian Coates, Vacuum Deposition of All-Inorganic Metal-Halide Perovskite Solar Cells, *master thesis,* 2018
- Waqas Zia, Fabrication & Characterization of FAPI Solar Cells by Co-Evaporation, *advanced research lab report*, 2019

B. Acknowledgment

Writing a Ph.D. thesis is an extremely long enduring process, that was only possible with the help of numerous other people, who I would like to acknowledge in the following. I am sorry if forgot to mention your name, just show me this paragraph, and provided that your contribution was worth mentioning, I owe you a beer (or a substitute drink of your choice) as compensation.

First of all, I would like to thank Professor Wolfram Jaegermann for the opportunity to pursue my Ph.D. in his research group, all the scientific discussions, and for giving me a lot of freedom in planning and performing the experiments throughout my Ph.D.

In addition, I would like to thank Professor Wolfgang Ensinger for taking the responsibility of being the second reviewer on such short notice. I am also grateful to Professor Uli Lemmer and Professor Anke Weidenkaff for taking their time to be an examiner for my defense.

I would also like to thank Dr. Thomas Mayer for his scientific input regarding planning experiments and interpreting the results. His extensive proofreading of my Ph.D. thesis and my publications helped is highly appreciated as well. I also enjoyed all the non-science related discussions.

I also would like to thank our cooperation partners at the Karlsruhe Institute of Technology, especially Dr. Tobias Abzieher and Dr. Jonas Schwenzer for supplying me with all the perovskite samples and for helping me with the XRD, UV/Vis, and JV-measurements. Also, many thanks to Professor Ulrich Paetzold for the support while preparing the manuscript for our photovoltage paper.

Furthermore, I would like to thank the “unknown Ph.D. student” of the research group of Prof. Michael Saliba at the Jülich Research Centre for supplying me with the bromine-based perovskite samples and Hans Köbler from the Helmholtz Center for Materials and Energy in Berlin for sending me perovskites samples as well.

Definitely worth mentioning are also Dr. Chittaranjan Das and soon-to-be Dr. Michael Wussler, for their moral and scientific support, even a long time after they had already left the surface science group. In addition, I would also like to thank the rest of the surface science group. Many thanks to Andi for the final proof-reading! Special thanks to the Perosol team: Thanks to Ralph, Claudiu, Clément, Kerstin, Luca, Carolin, Islam, Max, Hans, Nils, Waqas, Ian, Chandra, Marco, and Moritz. Working together with you guys as a team was an amazing time that I enjoyed a lot. Our hiking and camping trips, Feuerzangenbowle and waffle events, and the repeated evenings at “Shotz” were incredible. Also props to the running team; the pre-run beer was always a great motivation for beating the “badger mountain”. Cheers to the Bessy 2021 team, we were definitely “broken at Bessy”. (And Bessy was broken as well…) I haven’t eaten a Kebab since Bessy and guess I won’t be able to do so before the next Bessy trip.

Greetings to the Age of Empires II team! Thanks a lot, to Jorge, Hans, and Max for giving me that extra motivation to be extra efficient in my writing and be able to join in the evening games. HCCC, BE, BE!

During my Ph.D. I supervised several students who hopefully did not have to suffer too much. The research they performed, and their acquired data did not only lead to new ideas and further

experiments but was also partially incorporated into my Ph.D. thesis. Many thanks here to Nils Schäfer, Ian Coates, Waqas Zia and Chandra Prabowo. Not only working together with you was a lot of fun, but also the time we spent outside the lab. Special thanks to Ian for proof-reading my thesis!

I am also grateful to all the people who helped me to keep DAISY-SOL and especially our XPS running. Thanks a lot, to the Mawi workshop, especially Jochen Rank and Michael Weber. They were not only extremely professional in fixing everything that broke (basically everything at least once during these four years…) but also during planning and constructing numerous samples holders, shadow masks, or even complete deposition systems. Thanks a lot also to Kerstin Lakus-Wollny for all the fruitful coffee discussions and her help in the lab even after her contract had already ended. I also would like to mention Jean Thibaut, who gave me a lot of advice on fixing the XPS, often late at night or on weekends. I am quite certain that without his input, our XPS would not be running right now. Thanks as well to Patrick Brehier. The support of Dr. Horst Sjuts and Dr. Wolfgang Winkelnkemper who helped me installing our new channeltrons and construct the new preamplifier is also greatly appreciated. No cross-talk anymore, I guess our modified setup is superior!

In addition, I would like to thank a few friends, who did not get tired of my (I suppose I should say frequent) complaining about how horrible a Ph.D. can be. (I believe most of the time, I was complaining about XPS issues.) Thanks to Nico, Max, Falk, and Hans. I guess you only know how it is to study a Ph.D. if you have been through it yourself.

Finally, I would like to thank my family. I want to mention my parents and my brother who not only supported me throughout my studies but also during my Ph.D. time. I am really grateful to my daughter Zoey for being such a happy and joyful child and for motivating me to finish my Ph.D. early. I also would like to thank my wife Chuqi for all her moral support and especially for taking over the parenting responsibilities in the final phase of my Ph.D. when I was writing my thesis.

C. Curriculum Vitae

Personal Information

Name	Tim Hellmann
Date of Birth	22.09.1991
Place of Birth	Gelnhausen
Nationality	German

Academic Education

2017 – 2021	Ph.D. studies at Technical University of Darmstadt Ph.D. thesis: *Advanced Understanding of the Electronic Properties of Perovskite Solar Cells: Contact Formation, Band Energy Diagrams and resulting Surface Photovoltages*
2014 – 2017	Master of Science in Materials Science at Technical University of Darmstadt Master thesis: *Interface experiments on perovskite solar cells by photoelectron spectroscopy*
2010 – 2013	Bachelor of Science in Materialwissenschaft (materials science) at Technical University of Darmstadt Bachelor thesis: *Optimization of the synthesis of copper and cobalt-nanowires by electroless and electrochemical deposition into track-etched polycarbonate membranes* (german title: *Optimierung der Synthese von metallischen Kupfer- und Kobaltnanoröhren durch stromlose und elektrochemische Abscheidung in ionenspurgeätzte Polykarbonat-Template*)

Additional Experience

2013 - 2014	Stay abroad in Hsinchu, Taiwan • Chinese language class at Chung Hua University, Hsinchu • Internship at Feedback Technology Corporation • Internship at China Quartz TECH. CO., LTD.

School Education

2003 – 2010	Grimmelshausen Gymnasium Gelnhausen *Certificate of general qualification for university entrance* (german: Abitur)
1997 – 2003	Hasela-Schule Altenhaßlau